Controlling Energy-Efficient Buildings in the Context of Smart Grid: A Cyber Physical System Approach

Mehdi Maasoumy Haghighi

Electrical Engineering and Computer Sciences
University of California at Berkeley

Technical Report No. UCB/EECS-2013-244
http://www.eecs.berkeley.edu/Pubs/TechRpts/2013/EECS-2013-244.html

December 28, 2013

Controlling Energy-Efficient Buildings in the Context of Smart Grid:
A Cyber Physical System Approach

by

Mehdi Maasoumy Haghighi

A dissertation submitted in partial satisfaction of the
requirements for the degree of
Doctor of Philosophy

in

Engineering - Mechanical Engineering

and the Designated Emphasis

in

Energy Science and Technology – DEEST

in the

Graduate Division

of the

University of California, Berkeley

Committee in charge:

Professor Alberto Sangiovanni-Vincentelli, Co-Chair
Professor Francesco Borrelli, Co-Chair
Professor David M. Auslander
Professor Seth Sanders

Fall 2013

Controlling Energy-Efficient Buildings in the Context of Smart Grid:
A Cyber Physical System Approach

Abstract

Controlling Energy-Efficient Buildings in the Context of Smart Grid:
A Cyber Physical System Approach

by

Mehdi Maasoumy Haghighi

Doctor of Philosophy in Engineering - Mechanical Engineering

University of California, Berkeley

Professor Alberto Sangiovanni-Vincentelli, Chair

The building sector is responsible for about 40% of energy consumption, 40% of greenhouse gas emissions, and 70% of electricity use in the US. Over 50% of the energy consumed in buildings is directly related to space heating, cooling and ventilation. Optimal control of heating, ventilation and air conditioning (HVAC) systems is crucial for reducing energy consumption in buildings.

We present a physics-based mathematical model of thermal behavior of buildings, along with a novel Parameter Adaptive Building (PAB) model framework to update the model parameters, as new measurements arrive, to reduce the model uncertainties. We then present a Model Predictive Control (MPC), and a Robust Model Predictive Control (RMPC) algorithm and a methodology for selecting a controller type, i.e. RMPC or MPC, versus Rule Based Control (RBC) as a function of model uncertainty.

We then address the "Cyber-Physical" aspect of a building HVAC system in the design flow. We present a co-design framework that analyzes the interaction between the control algorithm and the embedded platform through a set of interface variables, and demonstrate how the design space is explored to optimize the energy cost and monetary cost, while satisfying the constraints for occupant comfort level.

The last part of this dissertation is centered on the role of *smart buildings* in the context of the *smart grid*. Commercial buildings have inherent flexibility in how their HVAC systems consume electricity. We first propose a means to define and quantify the flexibility of a commercial building. We then present a contractual framework that could be used by the building operator and the utility company to declare flexibility on one side and reward structure on the other side. We also present a control mechanism for the building to decide its flexibility for the next contractual period to maximize the reward. We also present a Model Predictive Control (MPC) scheme to direct the ancillary service power flow from buildings to improve upon the classical Automatic Generation Control (AGC) practice. We show how constraints

such as slow and fast ramping rates for various ancillary service providers, and short-term load forecast information can be integrated into the proposed MPC framework. Finally, results from at-scale experiments are presented to demonstrate the feasibility of the proposed algorithm.

To my mother for her unconditional love, my father for his continual support, and my brothers for being my best friends.

Contents

List of Figures

Acknowledgments

I would like to deeply thank my advisor, Professor Alberto Sangiovanni-Vincentelli, for his guidance during my research and study at University of California, Berkeley. His spectacular vision, perpetual energy and enthusiasm for research have motivated all his advisees, including me. Mostly, I thank him for the freedom in thinking and research directions that he provides for his students, which gave me the liberty to explore very interesting subjects within the principal theme of my dissertation. His open and positive approach served my curiosity, and he was my advocate and mentor throughout my PhD. He deserves my utmost gratitude and I hope he remains a guiding presence to steer my way in the future.

I feel fortunate to have had Alessandro Pinto, Qi Zhu, Yang Yang, Pierluigi Nuzzo, Chung Wei, Liangpeng Guo, Alberto Puggelli, Antonio Iannopollo, Mohammad Mostafizur Mozumdar, Piergiuseppe Di Marco, Nikunj Bajaj as my collaborators in Alberto's group. I am humbled and appreciative of the professors near and far who helped me along the way: Catherine Rosenberg, Duncan Callaway, Claire Tomlin, Kameshwar Poolla, Mahdi Shahbakhti, Laurent El Ghaoui, David Culler, Costas Spanos, Tseng King Jet. I thank them all for their time, their precious pieces of research advice, and encouragement. Special thanks to Francesco Borrelli, David M. Auslander and Seth Sanders who agreed to be in my Dissertation committee.

I am also grateful for the fruitful discussions with PhD students at Berkeley: Yudong Ma, Tony Kelman, Maryam Kamgarpour, Jorge Ortiz, Borhan Sanandaji, Francesco Smarra, Forest Landola, Alexandre Donze, Pangun Park, in Berkeley. The collaborations with students from other schools proved invaluable: Marcel Bruelisauer, Forrest Meggers, Cheng Li, researchers whom I met in Singapore during my internship at Singapore-Berkeley Building Efficiency and Sustainability in the Tropics (SinBerBEST), and Meysam Razmara, Barzin Moridian, students from Michigan Technological University.

I enjoyed five great and memorable years in the DOP center, Cory hall. Overall, I probably spent more hours in Cory hall, than I spent at home during these five years. Thanks to the DOP center Jura coffee maker! I will fondly recall sharing DOP center with Sayak Ray, Baruch Sterin, Susmit Jha, Daniel Holcomb, Wenchao Li, Dai Bui, and had brief overlaps with Yang Yang, Xuening Sun.

Above all, I thank my wonderful family, my parents, and my brothers, for their care, patience and endless love. This thesis is dedicated to them.

Chapter 1

Introduction

This dissertation addresses the broad area of energy-efficient buildings within the context of the smart grid. Its overarching theme encompasses subjects such as modeling thermal behavior of buildings using fundamental laws of Thermodynamics and Heat Transfer, development of a parameter-adaptive building model that automatically tune the parameters of the system to adapt to the changing environment, development of optimal control algorithms to efficiently run the Heating Ventilation and Air Conditioning (HVAC) systems of buildings, development of a framework to co-design the control algorithm and the embedded platform, and the role of buildings as significant consumers of energy in the context of the smart grid for providing regulation services as well as development of a novel MPC technique to control the flow of such regulation services to improve upon the classical AGC practice.

1.1 Motivation

Total primary energy consumption in the United States increased from 78.3 quads[1] in 1980 to over 100 quads in 2008, of which the building sector accounts for about 40%. The building sector is also responsible for almost 40% of greenhouse gas emissions and 70% of electricity use. About 50% of the energy consumed in buildings is directly related to space heating, cooling and ventilation (Figure 1.1). Therefore, reducing building energy consumption by designing smart control systems to operate the HVAC system in a more efficient way is critically important to address the worldwide energy and environmental concerns. With the advent of smart, easily-controllable thermostats, smart meters, and two-way communication infrastructure between the buildings as consumers of energy and utility companies as providers of energy, the role of buildings in the operation of the smart grid will be even more

[1] A quad is a unit of energy equal to 1.055×10^{18} joules.

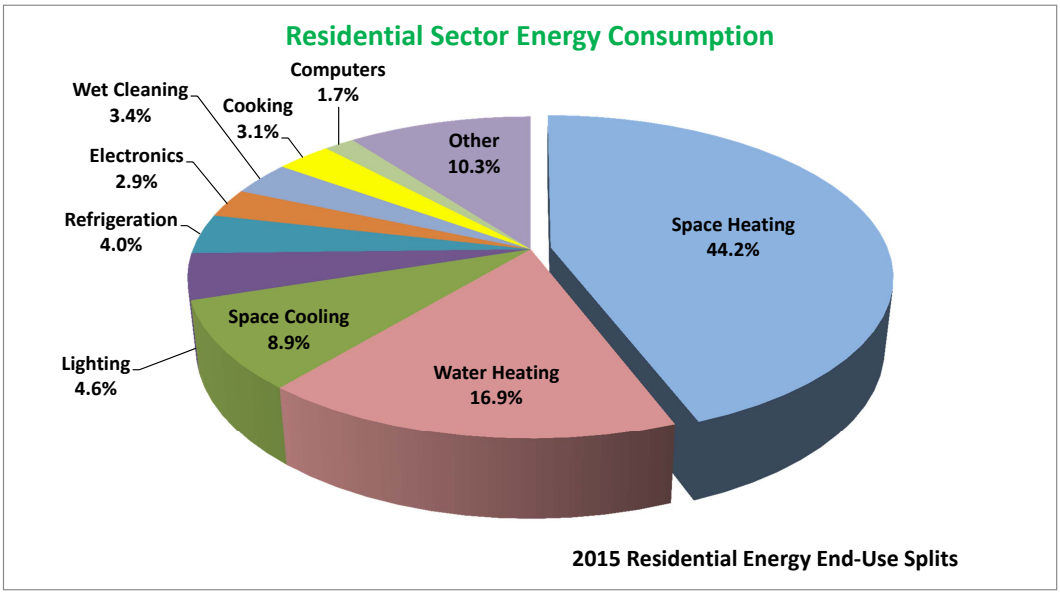

Figure 1.1: Breakdown of energy consumption in a typical building. Over 50% of energy consumption is related to HVAC systems [11].

significant in the near future, compared to the current state-of-the-art.

Advanced control algorithms are considered critical enablers to achieve low energy consumption in commercial buildings. Entire sections of the ASHRAE 90.1 standard [77] are dedicated to the specification of control requirements. Although the optimal control of an HVAC system is a complex multi-variable problem, it is standard practice to rely on simple control strategies that include bang-bang controllers with hysteresis, and PID controllers (Figure 1.2). In most cases, standard sequences of operations for *typical* installations are used by control contractors. Each sequence controls the HVAC equipment during an operation phase such as optimal start, safety shutdown and normal operation. After installation and tuning, the building is inspected by a commissioning agent that mainly verifies that the building satisfies the owner's expectations. The commissioning agent does not only verify the expected performance right after installation, but also after the building has started its operations.

This short snapshot of design and validation practices in the building industry

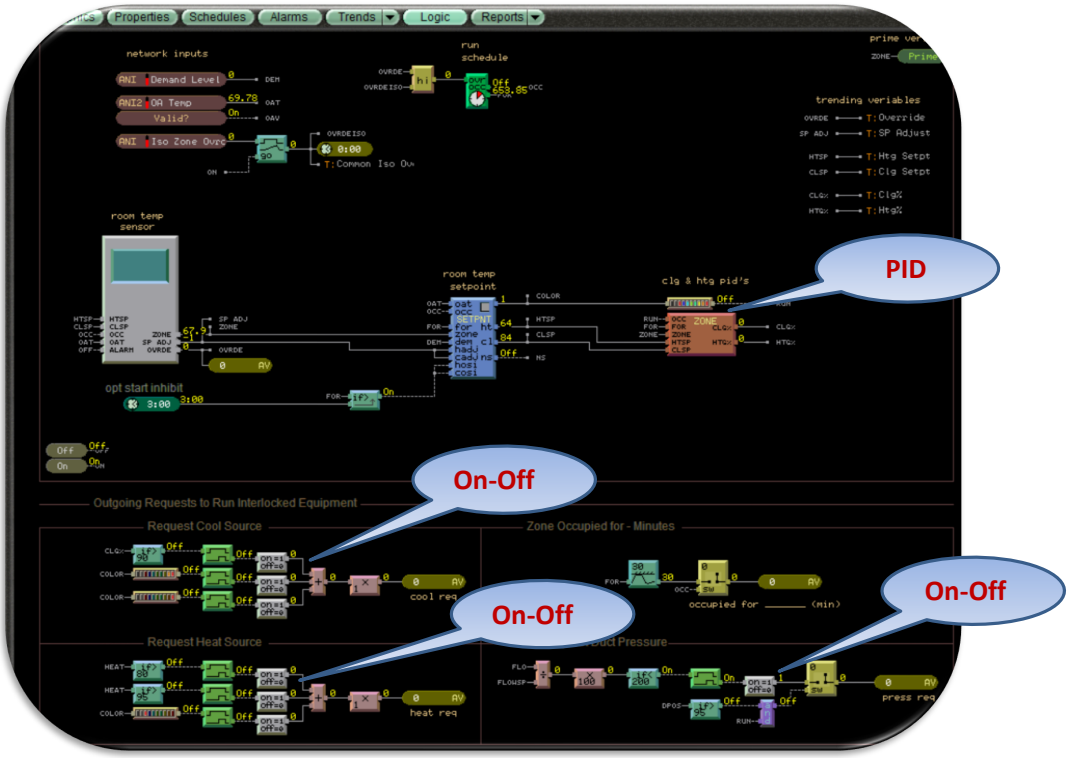

Figure 1.2: Control logic of a typical commercial building. The interaction and interrelation of building sub-systems is not addressed in the state-of-the-art control logic of such systems. This may cause inefficient use of energy, such as simultaneous heating and cooling of air in two different part of the system.

shows the importance of a model-based design flow for building controls. To attain energy efficiency, control algorithms need to be tailored to the physical properties of the building at hand rather than being an adaptation of a standard sequence designed for a typical building. Thus, a thermal model of the building is needed that is also suitable for optimal control design. Once such model is made available, it can be used to design an optimal controller that balances comfort and energy usage. To achieve building-level energy-optimality, the model should be able to capture the interaction between physically connected spaces in the building, occupancy schedules, and state and input constraints.

1.2 Contributions

In recent years, a variety of works in the area of building energy efficiency and smart grid has been done and can be found in the literature. A nonlinear model of the overall cooling system including the chillers, the cooling towers and the thermal storage tank, as well as an MPC framework for minimizing the energy consumption of the building is proposed in [51]. In [67] and [31], the authors use a model of the building which is bilinear between inputs, states and weather parameters and they use Sequential Quadratic Programming (SQP) for solving non-linear problems in which they iteratively linearize the non-convex constraints around the current solution, solve the optimization problem and repeat until a convergence condition is met. Common available methods for wall thermal analysis is proposed in [44]. A building thermal model is proposed in [27] which is based on an Resistor-Capacitor (RC)-network, with a large number of coupled linear differential equations. The authors then reduce the order of the model via aggregation of states. In [35], the authors investigate the potential of building thermal storage inventory, in particular the combined utilization of active and passive inventory, for the reduction of electrical utility cost using common time-of-use rate differentials. In [63], the authors propose a dynamic multinodal lumped-capacitance nonlinear model to describe a building, considering conduction heat fluxes, envelope thermal capacity, lighting and people loads, infiltration, fenestration and thermal inertia of heating systems. A nonlinear disturbance rejection state feedback controller for an HVAC system is proposed in [18].

Buildings are dynamical systems with uncertain and time-varying plant and occupant characteristics. The heat transfer characteristics of a building are highly dependent on the ambient conditions. For instance, heat transfer properties such as convective heat transfer coefficient h, of peripheral walls is dependent on outside temperature, wind speed and direction. Also, unmodelled dynamics of a building [55] is a function of 1) *external factors*: ambient weather conditions such as radiative heat flux into the walls and windows, and cloudiness of the sky, and 2) *internal factors:* such as occupancy level, internal heat generation from lighting, and computers. These quantities are highly time-varying and therefore the dynamics of the building and, consequently, parameters of the mathematical model describing the dynamics of the buildings are constantly changing with time. Accordingly, the estimation algorithms utilized to identify these parameters should take the *time-varying* aspect of buildings into account and be *adaptive* in this respect.

Reliable dynamical models are crucial to model predictive control strategies. Modeling and system identification are the most challenging and time-consuming parts of building predictive control [71]. To address this challenge, over the last few years numerous mathematical models of building thermal dynamics have been proposed in the literature. Resistor-capacitor (RC) models with disturbances to capture un-

modelled dynamics have been proposed in [56, 55, 53]. A bilinear version of an RC model is presented in [67] that takes into account weather predictions to increase building energy efficiency. In [15], the authors discovered that time-varying properties such as occupancy can significantly change the dynamic thermal model and influence how building models are identified. While modeling a multi-zone building, the authors of [15] observed that the experimental data often did not have sufficient quality for system identification and hence, proposed a closed-loop architecture for active system identification using prediction-error identification method (PEM). Other modeling techniques with application in building predictive control include: subspace methods, MPC relevant identification (MRI), deterministic semi-physical modeling (DSPM), and probabilistic semi-physical modeling (PSPM). In a recent work, unscented Kalman filtering has been used for online estimation of building thermal parameter estimation [72].

Optimal control of HVAC components using model-based control techniques has shown promising results for achieving energy efficiency in buildings [55, 66, 85, 51, 67]. However, these control techniques rely heavily on a perfect (or almost perfect) mathematical model of the building or a perfect (or almost perfect) estimation of the unmodelled dynamics of the system [55].

Although a great deal of progress has been made in modeling the thermal behavior of building envelope and HVAC system as mentioned above, the random nature of some components of buildings makes it very hard to predict, with high fidelity, the temperature evolution of the room using mathematical models. These random events and phenomena include building occupancy by people which along with other internal loads such as the heat emitted from electrical devices and lighting, account for the total internal heat generation of the building. The outside environment of the building is also subject to many random and hard-to-accurately-predict phenomena such as the wind speed, solar radiation, cloudiness of the sky and outside air temperature. The aggregate effect of all these factors constitutes the total external heat gain of the building. We call these two heat gains of the building, the "unmodelled dynamics". As mentioned earlier, it is difficult to obtain a *perfect* prediction of the loads in future times. On the other hand, model-based optimal controllers such as Model Predictive Control (MPC) are highly dependent on accurate predictions of these disturbances. In order to account for these modeling deficiencies, it is usually a reasonable assumption to consider an additive norm-bounded uncertainty to the model. The question here is how to integrate this uncertainty information in the control design to achieve the desired comfort level while consuming *minimum* energy. We will discuss this fundamental question in Chapter 4 of this dissertation.

The focus of the papers mentioned above is on physical modeling and control design without taking into account the limitations of the embedded platform. For instance, in [54], weather and occupancy prediction uncertainties are considered in

the control design process, and a robust model predictive control mechanism against prediction uncertainties is derived. However, the uncertainties (errors) from the embedded platform measurements are not addressed. Another set of papers [86, 87] focuses on the design of the embedded software and hardware for a given control algorithm, thus not addressing design space exploration for optimal HVAC system design. Chapter 5 of this dissertation will discuss this problem.

The last two chapters of this dissertation discuss the role of smart buildings in the emerging smart grid. Electricity storage is believed by some to be a solution to the problem of frequency regulation in the new emerging highly Renewable Energy Sources (RESs)-dependent smart grid by absorbing the variability associated with RESs. However, storage has two important drawbacks. It is expensive and it is not environmentally friendly. There is an emerging consensus that flexible loads with thermal storage capabilities such as Thermostatically Controlled Loads (TCLs) will play an important role in regulating the grid frequency and consequently in enabling deep penetration of RESs. It has been reported that about 20% of the total electricity consumption in the United States is used by residential TCLs such as air conditioners, heat pumps, water heaters, and refrigerators [4, 9]. Recently, [75, 33] showed that flexible loads such as TCLs are good candidates for providing ancillary services since their aggregate flexibility has the characteristic of a stochastic battery.

These recent papers also demonstrate that TCLs have a great potential for providing *fast* regulating reserve services; speed is indeed beneficial, especially in the context of recent regulations such as Federal Energy Regulatory Commission (FERC) Order 755 [13]. In fact, these new federal regulations require scheduling coordinators to procure and compensate more for regulation resources with *faster ramping rates*. There is an emerging consensus that future regulation services will be distinguished and compensated by *capabilities* of which ramping rate is one component.

Modeling, estimation, and control of aggregated heterogeneous TCLs for ancillary services have been discussed in [42, 62]. TCLs are particularly well-suited for Direct Load Control (DLC) and Demand Response (DR) programs that require loads to both decrease and increase power consumption because they are capable of storing thermal energy, much like a battery stores chemical energy. Fully responsive load control is highlighted in [24] in the context of TCLs and plug-in Electric Vehicles (EVs). Despite several challenges of using loads for system services, several key advantages include: 1) Reducing overall grid emissions by using loads to provide system services [78]. 2) Instantaneous response of loads to operator requests, versus slow response of generators to make significant output changes [40], and 3) Less variability associated to a very large number of small loads with respect to that of a small number of large generators [40]. It may soon be the case that the only technical impediment to reliable utilization of loads for system services is the development of the necessary load models and control strategies and the development of inexpensive

and scalable communication and sensing infrastructure [83].

This dissertation offers novel algorithms on the modeling, estimation, control, and design of energy-efficient buildings as significant cyber-physical systems within the Smart Grid.

At the conceptual level, the contributions of this dissertation can be summarized as follows:

- **Physics-based Modeling of Thermal Behavior of Buildings:** We present high fidelity models of building thermal dynamics which are obtained using fundamental laws of Thermodynamics and Heat Transfer. We model the conductive and convective heat transfer phenomena which takes place in the walls and between the walls and the environment, respectively. We obtain a RC model of the whole building. Each wall and room in the building is modeled as a node with a designated capacitor, and these nodes are connected using resistances. Historical data is then used to calibrate the parameters of the model. In order to integrate internal (occupancy) and external (sun radiation, etc.) disturbances to the model, we use CO2 concentration level and outside temperature from sensors, respectively. Throughout this dissertation, we call these two quantities *unmodelled dynamics* .

- **Parameter-Adaptive Building (PAB) Model:** Incorporating unmodelled dynamics improves the accuracy of the mathematical model of the building. However, the building is exposed to extremely time-varying phenomena in the environment such as occupancy from inside, and solar radiation and wind from outside. In order to account for such time-varying phenomena, we propose a framework for online parameter adaptation and state estimation for building models. We call the resulting model, Parameter-Adaptive Building (PAB) Model.

- **Model Predictive Control:** Once we obtain a fairly accurate mathematical model of the building, we proceed with performing model predictive control of the HVAC system of buildings. MPC provides a very attractive framework for optimizing a cost function subject to constraints over a prediction horizon. This framework is of utmost advantage to control of building HVAC systems. Optimal control of building HVAC system includes minimizing energy consumption or monetary cost of operating HVAC systems, subject to constraints on the room temperature and on the inputs to the system such as air mass flow input. We propose MPC and Robust Model Predictive Control (RMPC) algorithms. RMPC is designed to account for model uncertainties. We also analyze the performances of MPC, and RMPC for a range of model uncertainties and address the trade-off between cost and comfort.

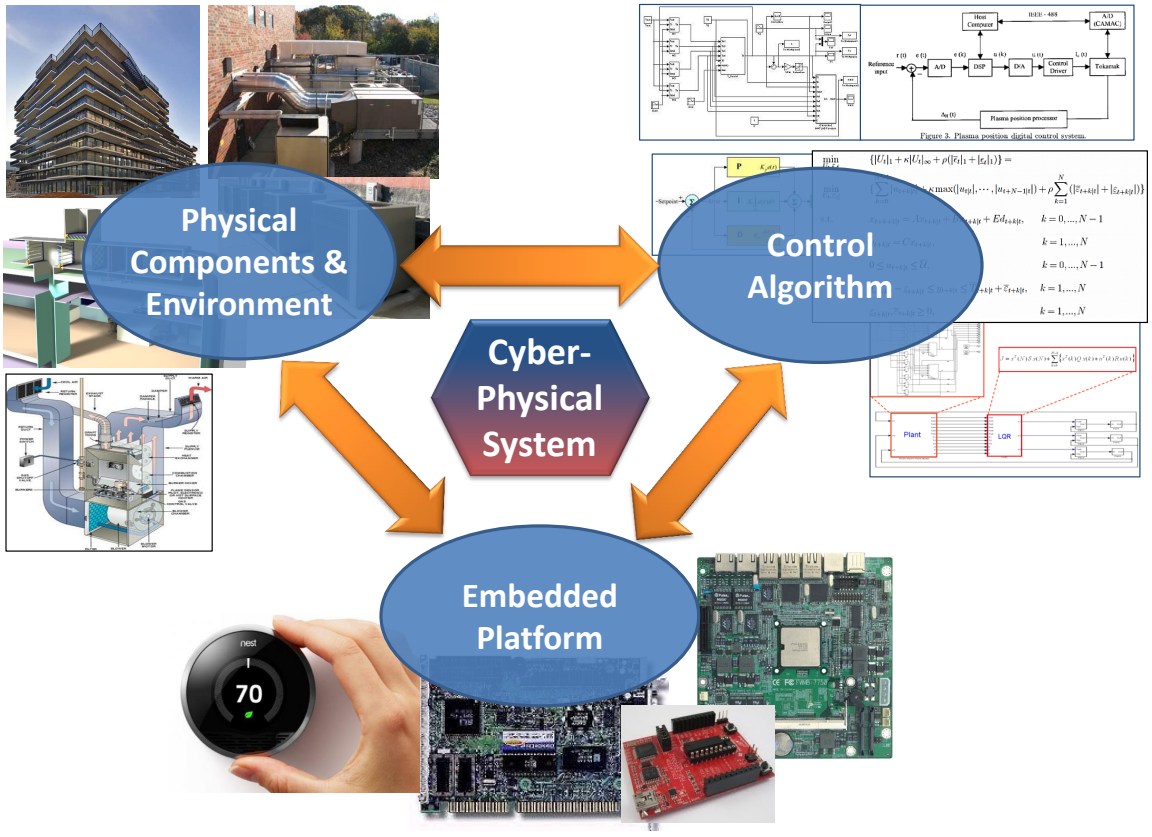

Figure 1.3: As complex cyber-physical systems, HVAC systems involve three closely-related subsystems - the control algorithm, the physical environment and the embedded implementation platform.

- **Co-design of Control Algorithm and Embedded Platform:** Smart buildings today have sophisticated and distributed control systems as part of a Building Automation System (BAS). The task of a BAS is to maintain building climate within a specified range, control the lighting based on the occupancy schedule, and monitor the system performance and failures. To accomplish these tasks, a BAS has to deal with computation and communication non-idealities stemming from the distributed nature of the implementation platform.

  The design of HVAC systems involves three main subsystems – the physical building and its environment, the control algorithm that determines the system operations based on sensing inputs from the building and the environment, and the embedded platform that implements the control algorithm (Figure 1.3). In the traditional top-down approach, the design of the HVAC control algorithm

is done without explicit consideration of the embedded platform. The underlying assumption is that the computation and communication capabilities of the embedded platform are sufficiently performing for any type of control mechanism. However, with the advent of more complex HVAC control algorithms for energy efficiency, the use of distributed networked platforms, and the imposition of tighter requirements for user comfort, this assumption on the embedded platform is no longer valid. Various aspects of the platform, including sensor accuracy and availability, communication channel reliability, and computing power of embedded processors, may have a significant impact on the quality and cost of a BAS. Thus, the design of the control algorithm should take into account the configuration of the implementation platform and *vice versa*, i.e., the control algorithm and the embedded platform should be *co-designed*.

We propose a co-design approach that analyzes the interaction between the control algorithm and the embedded platform through a set of interface variables. We present six control algorithms that take into account the sensing error, and model the relation of control performance and cost versus sensing error. We also capture the relation of embedded platform cost versus sensing error by analysis of the collected data from a testbed. Based on these models, we explore the co-design of the control algorithm and the temperature sensing subsystem of the embedded platform to optimize with respect to energy cost and monetary cost while satisfying the constraints for user comfort level.

- **Flexibility of Buildings for Supply-Following:** Commercial buildings have inherent flexibility in how their HVAC systems consume electricity. We investigate how to take advantage of this flexibility. We first propose a means to define and quantify the flexibility of a commercial building. We then propose a contractual framework that could be used by the building operator and the utility to declare flexibility on the one side and reward structure on the other side. We then design a control mechanism for the building to decide its flexibility for the next contractual period to maximize the reward, given the contractual framework. Finally, we perform at-scale experiments to demonstrate the feasibility of the proposed algorithm.

- **Control of Regulation Services from Buildings to the Smart Grid:** We first demonstrate that the demand-side flexibility of the HVAC system of a typical commercial building can be exploited for providing frequency regulation service to the power grid using at-scale experiments. We then show how this flexibility in power consumption of building HVAC system can be leveraged for providing regulation service. To this end, we consider a simplified model of the power grid with uncertain demand and generation (Figure 1.4). We present

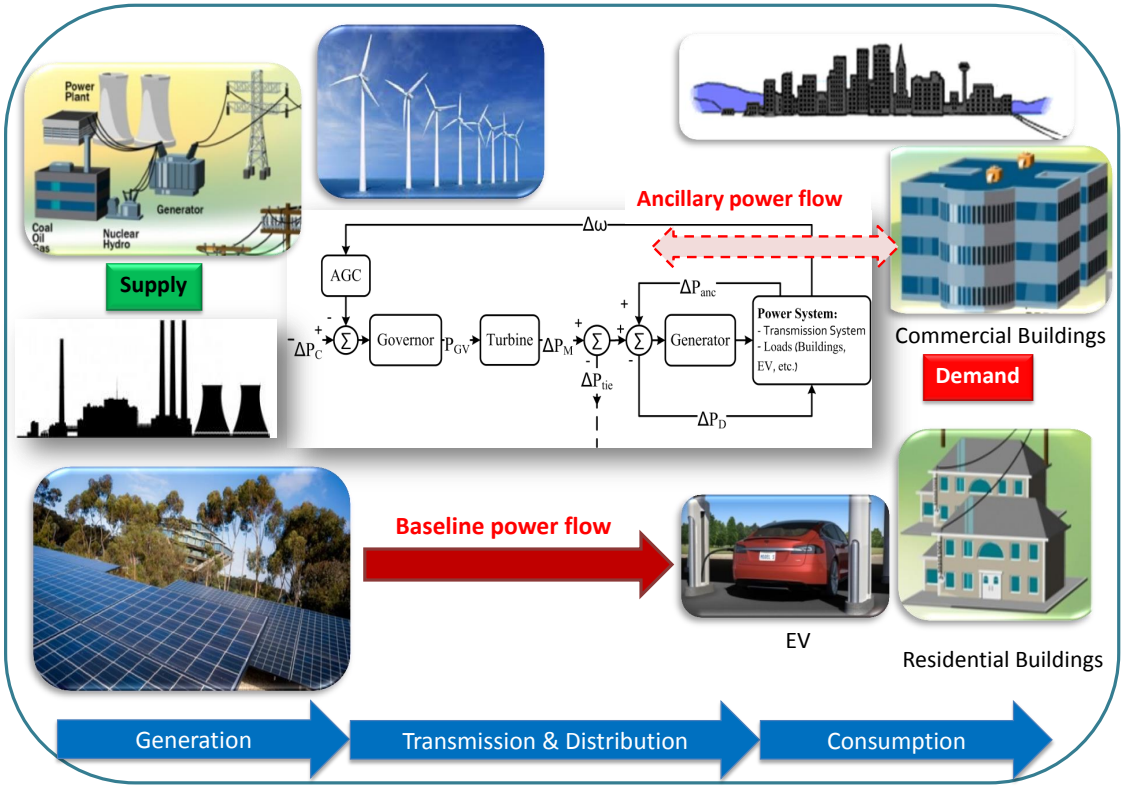

Figure 1.4: As influential players in the smart grid domain, buildings have a significant role in its operation. One of the services that buildings will provide to enhance the operation of the smart grid is ancillary services to help frequency regulation through automated demand response events.

an MPC scheme to direct the ancillary service power flow from buildings to improve upon the classical AGC practice. We show how constraints such as slow and fast ramping rates for various ancillary service providers, and short-term load forecast information can be integrated into the proposed MPC framework. Finally, we provide extensive simulation results to illustrate the effectiveness of the proposed methodology for enhancing grid frequency regulation practice.

1.3 Organization

The remaining chapters of this dissertation are organized as follows:

Chapter 2: Mathematical Modeling

We start from describing the fundamental Heat Transfer and Thermodynamics phenomena such as Convection, Conduction and Radiation which influence the temperature dynamics in a building in Chapter 2. We then present an RC model of the heat transfer in the building and extend it to the whole building to create a large RC model. Unmodelled dynamics such as internal and external heat gains are random, time-varying and hard to accurately model and estimate. In order to account for such dynamics, we use an affine mapping from measurable quantities such as CO2 concentration level and outside air temperature, respectively, to obtain an estimate of such unmodelled dynamics. Using historical data, we calibrate the model, and show the effectiveness of this methodology through modeling a real building and comparing the results with the measurements.

Chapter 3: Parameter-Adaptive Building (PAB) Model

The modeling framework developed in Chapter 2 works fine for most buildings. However, the methodology is not well scalable. From one building to another, one needs to repeat all the calibration process. The modeling framework of Chapter 2 on the other hand, does not address the time-varying behavior of the building and its indoor and outdoor environment. In Chapter 3 we improve the modeling framework developed in Chapter 2 by introducing a Parameter Adaptive Building (PAB) model. We present the architecture of the PAB model and its components including its Kalman filter based estimation algorithm and validate the effectiveness of the proposed approach through simulations.

Chapter 4: Control Design

We use the dynamic models developed in Chapters 2, and 3 to design optimal controllers for building HVAC system in Chapter 4. We first provide an overview of the classical building HVAC controllers. We then present a hierarchical control scheme in which the high-level controller optimizes a cost function and send the optimal setpoint to the local low-level PID controllers. The majority of Chapter 4 is devoted to obtaining and studying MPC, RMPC, and studying performance of each in the presence of model uncertainty. At the end of this Chapter we provide a guideline to selecting the most appropriate control strategy based on the accuracy of the building model.

Chapter 5: Co-Design Problem

After presenting various control strategies in Chapter 4, we present a framework to co-design the control algorithm and the embedded platform for building HVAC systems in Chapter 5. The goal of this chapter is to highlight energy efficient buildings as a cyber-physical system. As complex cyber-physical systems, HVAC systems

involve three closely-related subsystems - the control algorithm, the physical environment and the embedded implementation platform. In Chapter 5, we propose a co-design approach that analyzes the interaction between the control algorithm and the embedded platform through a set of interface variables in particular the sensing accuracy. Based on the proposed models, we explore the co-design of the control algorithm and the embedded platform to optimize a system with respect to energy cost and monetary cost while satisfying the constraints for user comfort level.

Chapter 6: Building Flexibility

In Chapter 6, we address the role of energy-efficient buildings within the context of the smart grid. We first propose a means to define and quantify the flexibility of a commercial building. We then propose a contractual framework that could be used by the building operator and the utility to declare flexibility on the one side and reward structure on the other side. We then design a control mechanism for the building to decide its flexibility for the next contractual period to maximize the reward, given the contractual framework. Finally, we perform at-scale experiments to demonstrate the feasibility of the proposed algorithm.

Chapter 7: Ancillary Control

After we defined, quantified and presented an algorithm to compute the flexibility of commercial buildings in Chapter 6, we show how this flexibility in power consumption of building HVAC system can be leveraged for providing regulation service, in Chapter 7. In this chapter, we consider a simplified model of the power grid with uncertain demand and generation. We present an MPC scheme to direct the ancillary service power flow from buildings to improve upon the classical Automatic Generation Control (AGC) practice. We show how constraints such as slow and fast ramping rates for various ancillary service providers, and short-term load forecast information can be integrated into the proposed MPC framework. Finally, we provide extensive simulation results to illustrate the effectiveness of the proposed methodology for enhancing grid frequency regulation practice.

Chapter 8: Conclusion

Finally, Chapter 8 draws conclusion of the dissertation with a discussion on the possible directions for future work.

Chapter 2

Mathematical Modeling

This chapter serves as a foundation for the rest of the Thesis. We discuss modeling techniques which are used by the researchers in the domain of building simulation and building climate control. This chapter includes a review of Thermodynamics extracted form [36], and a review of building thermal model extracted from [56, 53, 55].

2.1 Principles of Building Thermal Models

Heat storage capacity and *heat transmissibility* are the fundamental thermal properties of building elements. Walls, ceilings, floors and the air inside enclosed spaces are building components that can store energy. The capacity of these elements in storing energy is a function of their mass and their specific heat capacity. Heat is not only stored, but it can be transmitted through building elements in different ways. A useful representation of a thermal network is by means of a circuit analog where heat storage is represented by capacitors and heat transmission by resistors. We develop a model for building thermal elements such as rooms and walls using the *lumped-capacitance* method. To be useful for control design, the model has to be simple yet accurate enough so that relevant dynamic behaviors of thermal elements are retained.

2.1.1 Heat Storage

A basic property of materials is specific heat capacity c_p, which is the measurable physical quantity of heat or thermal energy required to change the temperature of a unit quantity of a substance by one unit. More heat is required to increase the temperature of a substance with high specific heat capacity than one with low specific heat capacity. For an object with mass m and specific heat capacity c_p , a rate of change of temperature $\dot{T}$ corresponds to the heat flow, denoted by Q, as shown

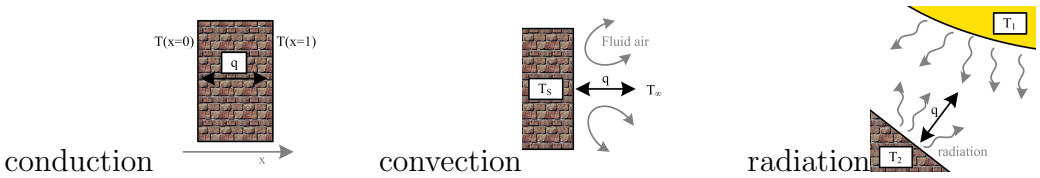

Figure 2.1: Mechanisms of heat transfer extracted from [36].

in equation (2.1). In the more familiar parlance of electrical engineering, mc_p is capacitance, $\dot{T}$ is the rate of change of electric potential (voltage) and Q is current.

$$Q = mc_p\dot{T} \tag{2.1}$$

2.1.2 Heat Transfer

Heat transfer takes place via the mechanisms of conduction, convection, and radiation as shown in Figure 2.1.

2.1.3 Conduction

When there is a temperature gradient in a stationary medium, we use the term *conduction* to refer to the heat transfer that occurs across the medium. Conduction may be viewed as the transfer of energy from the more energetic to the less energetic particles of a substance due to the interactions between the particles [36].

It is possible to quantify the heat transfer process in terms of appropriate *rate equations*. These equations may be used to compute the amount of energy being transfered per unit time. For heat conduction, the rate equation is known as *Fourier's law*. For the one-dimensional plane wall shown in Figure 2.1 having a temperature distribution $T(x)$, the rate equation is expressed as

$$q_x = -kA\frac{dT}{dx} \tag{2.2}$$

The heat q_x (W) is the heat transfer rate in the x direction and is proportional to the *temperature gradient*, dT/dx, in this direction. The proportionality constant k is a *transport* property known as the *thermal conductivity* $(W/m.K)$ and is a characteristic of the wall material. The minus sign is a consequence of the fact that heat is transferred in the direction of decreasing temperature. Under the *steady state* conditions the temperature distribution is *linear*, and the temperature gradient may be expressed as

$$\frac{dT}{dx} = \frac{T_2 - T_1}{L} \tag{2.3}$$

Table 2.1: Nomenclature

Parameter	Definition
A_i	Area of wall i
A_{win_i}	Total area of window on walls surrounding room i
α_i	Absorption coefficient of surface of wall i
τ_{win_i}	Transmissivity of glass of window i
q''_{rad_i}	Radiative heat flux density radiated to node i
$\dot{q}_{int_1}$	Internal heat generation in thermal zone i
c_a	Specific heat capacity of air
c_w	Specific heat capacity of wall material
C_{r_i}	Capacitance of thermal zone i
C_{w_i}	Capacitance of wall i
h	Convection heat transfer coefficient
k	Conduction heat transfer coefficient
$\dot{m}_{r_i}$	Mass flow rate of conditioned air entering thermal zone i
T_{r_i}	Temperature of room i
T_{s_i}	Supply air temperature into thermal zone i
T_{w_i}	Temperature of wall i
R'_{ij}	Thermal resistance between node i and node j
$Rval_w$	R-value of wall
$Rval_{gl}$	R-value of glass window
$Rval_{in}$	R-value of inside air film
$Rval_{out}$	R-value of outside air film

and the heat flow is then

$$q = \frac{kA}{L}(T_1 - T_2) \tag{2.4}$$

In the context of buildings, conduction occurs through solid walls that are not in thermal equilibrium.

2.1.4 Convection

The convection heat transfer mode is comprised of two mechanisms. In addition to energy transfer due to random molecular motion (diffusion), energy is also transferred by the bulk, or macroscopic motion of the fluid. Therefore we can describe the

convection heat transfer mode as energy transfer occurring within a fluid due to the combined effects of conduction and bulk fluid motion [36].

Regardless of the particular nature of the convection heat transfer process, the appropriate rate equation is of the form

$$q = hA(T_s - T_\infty) \tag{2.5}$$

Where q, the convective heat transfer (W), is proportional to the difference between the surface and the fluid temperatures, T_s and T_∞, respectively. This expression is known as *Newton's law of cooling*, and the proportionality constant $h(W/m^2.K)$ is termed the *convection heat transfer coefficient*. It depends on conditions in the boundary layer, which are influenced by surface geometry, the nature of the fluid motion, and an assortment of fluid thermodynamics and transport properties.

When Equation (2.5) is used, the convection heat flow is presumed to be *positive* if heat is transferred from the surface ($T_s > T\infty$) and *negative* if heat is transferred to the surface ($T_\infty > T_s$).

2.1.5 Radiation

Thermal radiation is the energy *emitted* by matter that is at a finite temperature. The energy of the radiation field is transported by electromagnetic waves (or alternatively, photons) [36]. While the transfer of energy by conduction or convection requires the presence of a material medium, radiation does not. In fact radiation transfer occurs most efficiently in a vacuum. Consider radiation transfer processes for the surface of Figure 2.1. Radiation that is *emitted* by the surface originates from the thermal energy of matter bounded by the surface, and the rate at which energy is released per unit area (W/m^2) is termed the surface *emissive power E*. There is an upper limit to the emissive power, which is prescribed by the *Stefan-Boltzmann law*

$$E_b = \sigma T_s^4 \tag{2.6}$$

Where T_s is the *absolute temperature (K)* of the surface and σ is the *Stefan-Boltzmann constant* ($\sigma = 5.67 \times 10^{-8} \quad W/m^2.K$). Such a surface is called an ideal radiator or *blackbody*. The heat flux emitted by a real surface is less than that of a blackbody at the same temperature and is given by

$$E = \varepsilon \sigma T_s^4 \tag{2.7}$$

Where ε is a relative property of the surface termed the *emissivity*. With values in the range $0 \leq \varepsilon \leq 1$. This property measures how efficiently a surface emits energy relative to a blackbody. It depends strongly on the surface material and finish.

Radiation may also be *incident* on a surface from its surroundings. The radiation may originate from a special source, such as the sun, or from other surfaces to which the surface of interest is exposed. Irrespective of the source(s), we designate the rate at which all such radiation is incident on a unit area of the surface as the *irradiation* G.

A portion or all of the the irradiation may be *absorbed* by the surface, thereby increasing the thermal energy of the material. The rate at which radiant energy is absorbed per unit surface area may be evaluated from the knowledge of surface radiative property termed *absorptivity* α. That is,

$$G_{abs} = \alpha G \tag{2.8}$$

Where $0 \leq \alpha \leq 1$ and the surface is *opaque*, portions of the irradiation are $reflected$. If the surface is *semitransparent*, portions of the irradiation may also be *transmitted*. However, while absorbed and emitted radiation increase and reduce, respectively, the thermal energy of matter, reflected and transmitted radiation have no effect on this energy. Note that the value of α depends on the nature of the irradiation, as well as on the surface itself. For example, the absorptivity of a surface to solar radiation may differ from its absorptivity to radiation emitted by the walls of a furnace.

A special case that occurs frequently involves radiation exchange between a small surface at T_s and a much larger, isothermal surface that completely surrounds the smaller one [36]. The *surroundings* could, for example be the walls of a room or a furnace whose temperature T_{sur} differs from that of an enclosed surface ($T_s \neq T_{sur}$). If the surface is assumed to be one for which $\alpha = \varepsilon$ (a gray surface), the net rate of radiation heat transfer from the surface, expressed per unit area of the surface, is

$$q''_{rad} = \frac{q}{A} = \varepsilon E_b(T_s) - \alpha G = \varepsilon\sigma(T_s^4 - T_{sur}^4) \tag{2.9}$$

This expression provides the difference between thermal energy that is released due to radiation emission and that which is gained due to radiation absorption.

In the context of building thermal analysis, we will ignore the radiation heat transfer among the internal walls in the building due to relative low range of temperatures inside the building, but we will consider the irradiation from the sun on the external sides of the walls and through the windows to the interior space of the building, in deriving the differential equations of the temperature distribution in different walls and rooms of the building.

2.2 Equivalent Thermal Circuit

2.2.1 Thermal Resistance

At this point we note that a very important concept is suggested by (2.4). In particular there exists an analogy between the diffusion of heat and electrical charge. Just as an electrical resistance is associated with the conduction of electricity, a thermal resistance may be associated with the conduction of heat [36]. Defining resistance as the ratio of a driving potential to the corresponding transfer rate, it follows from (2.4) that the *thermal resistance* for *conduction* in a plane wall is

$$R_{t,cond} = \frac{T_{s,1} - T_{s,2}}{q_x} = \frac{L}{kA} \tag{2.10}$$

Similarly for electrical conduction in the same system, Ohm's law provides an electrical resistance of the form

$$R_e = \frac{E_{s,1} - E_{s,2}}{I} = \frac{L}{\sigma A} \tag{2.11}$$

The analogy between Equations (2.10) and (2.11) is obvious. A thermal resistance may also be associated with heat transfer by convection at a surface. From Newton's law of cooling,

$$q = hA(T_s - T_\infty) \tag{2.12}$$

the *thermal resistance for convection* is then

$$R_{t,conv} = \frac{T_s - T_\infty}{q} = \frac{1}{hA} \tag{2.13}$$

Circuit representations provide a useful tool for both conceptualizing and quantifying heat transfer problems. The *equivalent thermal circuit* for the plane wall with convection surface conditions is shown in Figure 2.2. The heat transfer rate may be determined from separate consideration of each element in the network. Since q_x is constant through the network, it follows that

$$q_x = \frac{T_{\infty,1} - T_{s,1}}{1/h_1 A} = \frac{T_{s,1} - T_{s,2}}{L/kA} - \frac{T_{s,2} - T_{\infty,2}}{1/h_2 A} \tag{2.14}$$

In terms of the *overall temperature difference*, $T_{\infty,1} - T_{\infty,2}$, and the *total thermal resistance*, R_{tot}, the heat transfer rate may be may also be expressed as

$$q_x = \frac{T_{\infty,1} - T_{\infty,2}}{R_{tot}} \tag{2.15}$$

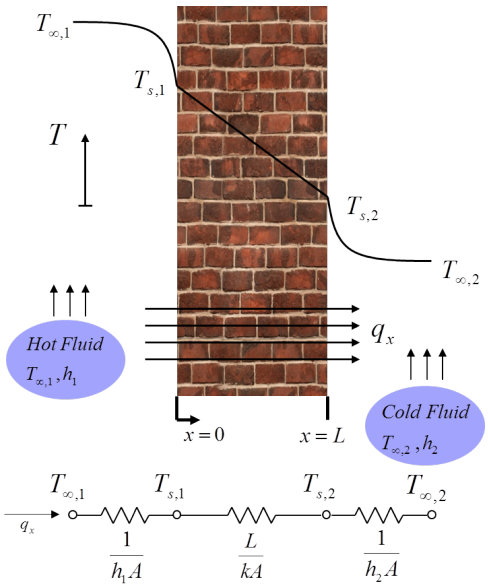

Figure 2.2: Heat transfer through a plane wall. Temperature distribution and equivalent thermal circuit

Because the conduction and convection resistances are in series and may be summed, it follows that

$$R_{tot} = \frac{1}{h_1 A} + \frac{L}{kA} + \frac{1}{h_2 A} \tag{2.16}$$

2.2.2 Thermal Potential

As it was discussed above, in *steady state* conditions we can define thermal resistances for different heat transfer modes such as conduction and convection. Accordingly, we can construct an equivalent thermal circuit to analyze the thermal behavior of the system. It was also shown that the equations derived here are analogous to the corresponding equations in an electrical circuit.

The other similarity that is noticed is the notion of *thermal potential* or *temperature* in thermal circuits which is analogous to the concept of *electrical potential* in electrical circuits. The temperature (thermal potential) of a point is fixed in steady state heat transfer, while it varies with time in transient heat transfer or heat storage.

2.2.3 Thermal Capacitance

In order to analyze the transient thermal behavior of the building model, we need to introduce the concept of *thermal capacitance*. During transient heat transfer the internal energy (and accordingly temperature) of the materials change with time. Thermal capacitance or heat capacity is the capacity of a body to store heat. It is typically measured in units of $(J/^\circ C)$ or (J/K) (which are equivalent). If the body consists of a homogeneous material with sufficiently known physical properties, the thermal mass is simply the mass of material times the specific heat capacity of that material. For bodies made of many materials, the sum of heat capacities for their pure components may be used in the calculation.

In the context of building design, thermal mass provides "inertia" against temperature fluctuations, sometimes known as the thermal flywheel effect. For example, when outside temperatures are fluctuating throughout the day, a large thermal mass within the insulated portion of a house can serve to "flatten out" the daily temperature fluctuations, since the thermal mass will absorb heat when the surroundings are hotter than the mass, and give heat back when the surroundings are cooler. This is distinct from a material's insulative value, which reduces a building's thermal conductivity, allowing it to be heated or cooled relatively separate from the outside, or even just retain the occupants' body heat longer.

In order to capture the evolution of temperature of walls and rooms we assign a capacitance with capacity $C = mc_p$ to each node in the thermal circuit. Notice that bodies of distributed mass like walls and air are considered as *nodes* in our modeling. This approximation is done based on some assumptions that will be presented in Section 2.3.

Example 2.2.3.1 Peripheral Wall
In this example we consider a peripheral wall (i.e. one side of the wall is exposed to the outside air and to the sun, and the other side is exposed to the inside air) as shown in Figure 2.3. The wall has a window with area A_w, thickness t and conductive heat transfer coefficient k_w. The total area of the wall, not including the window, is A. The circuit model for this example has three nodes with potentials T_1, T_2 and T_3 corresponding to the outside air, the inside air and the wall, respectively. The nodes are connected to ground via capacitors with capacitance value $C_1 = m_{a_1}c_a$ for the outside air, $C_2 = m_{a_2}c_a$ for air in in the room, and $C_3 = m_w c_w$ for wall material where m_{a_1}, m_{a_2}, and m_w are the masses fo each element, and c_a and c_w are specific heat capacitance of air and wall material respectively.

Heat propagates from the outside to the inside through two parallel paths: the walls and the window. The path through the walls is modeled by convective thermal resistances $R_1' = \frac{1}{h_1 A}$ between the outside air and the wall, $R_2' = \frac{1}{h_2 A}$ between the inside air and the wall, and a conductive thermal resistance $R_3' = \frac{L}{kA}$ of the wall. The

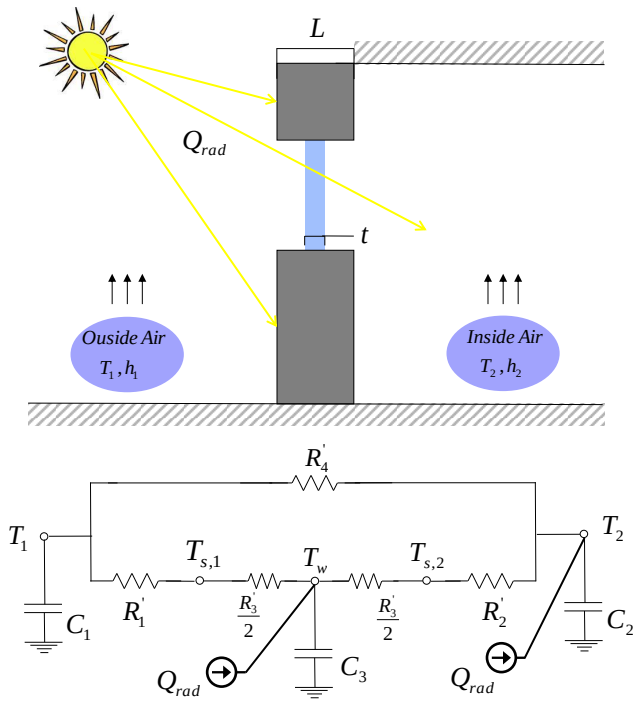

Figure 2.3: Thermal and circuit network for a peripheral wall with window

path through the window is modeled by a resistance $R_4' = \frac{1}{h_1 A_w} + \frac{t}{k_w A_w} + \frac{1}{h_2 A_w}$. The radiative heat gain from the sun Q_{rad} is also shown on the circuit network by a variable *current source*. The output of the current source that calculates the corresponding sun radiation is a function of the *altitude* and *azimuth* angle of the location of the building on the Earth, orientation of the considered wall or window, day of the year, time of the day, outside weather and sky condition, and etc.

Remark. One advantage of the proposed model to the other models that can be found in the literature is that the parameters of the proposed model have physical meanings and interpretations. This feature makes it possible to modify the model very easily when the parameters of the real building are changed from one building to another. For example if the glazing of the windows are changed this change can be applied to the model by only correcting the transmissivity of the windows in the model and keeping other parameters intact. Also when analyzing two buildings with the same wall materials and different wall thicknesses, we know that the $Rval_w$ of the two buildings are the same, therefore R_{ij} between any two neighboring nodes for the new building can be obtained by using the $Rval_w$ and $Rval_{in}$ of the old building and the dimensions of the new building.

2.3 Building Thermal Modeling

Using the heat transfer equations that was reviewed in Sections 2.1, and 2.2, we are now ready to derive the governing heat transfer equations for the temperature distribution in walls and rooms of a simple building. The heat transfer and storage equations compose a simple plant model representing a three room building Figure 2.4. Here are the simplifying assumptions made in deriving the equations:

- The air in a room has one temperature across its volume (lumped model) [29]. A more accurate model of temperature is significantly more complex and it does not facilitate the derivation of control laws.
- The specific heat of air, c_p, is constant at 1.007. In reality, c_p is 1.006 at *250 K* and 1.007 at *300 K*, so our assumption is accurate to within 0.1% error over the range of temperatures that would occur in a building.
- All rooms are at the same pressure used in the heating and cooling ducts. Air exchange between a room and vent is then *isobaric*, so the air mass in the room will not change in the process. We denote the air mass in the room by m and the rate of air mass entering the room, and also leaving the room, by $\dot{m}$.
- Radiative heating for each building face $(\mathcal{N}, \mathcal{S}, \mathcal{E}, \mathcal{W})$ is an input to the plant model. In a real building, the changing position of the sun through the day, and variations in atmospheric attenuation, will affect the radiation [28]. Here due to lack of exact data for the intensity of irradiation from the sun for a given time in a day, we use a sinusoidal input for the sun irradiation.
- We ignore radiative coupling between inner building walls; as the temperature difference between pairs of walls should be small, the effects of interior radiative coupling are likely to be minimal.

For a single room, the thermal model that results from our simplifying assumptions is presented as Figure 2.4. Also the detailed view of room number 1, coupled to its four surrounding walls, is given in detail. The temperature of room 1 is called T_1 while the temperature of the adjacent rooms 2 and 3 are called T_2 and T_3 respectively. The thermal capacity or thermal mass of room i is denoted by C_{ri} which is equal to the mass of the air in room i, m_i times the specific heat capacity of air, c_p, i.e.

$$C_{ri} = m_i c_{p_a} \tag{2.17}$$

where the mass of air in each room is obtained from the following equation

$$m_i = \rho_a V_i \tag{2.18}$$

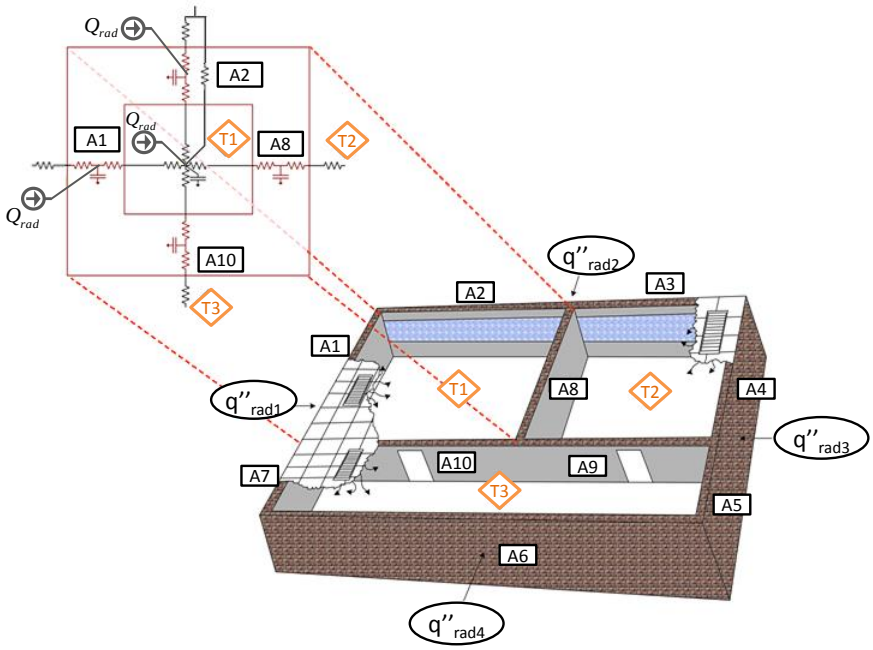

Figure 2.4: Simple three-room building with heat transfer through exterior and interior walls.

where ρ_a is the density of air at room temperature and V_i is the volume of room i.

As shown in Figure 2.4, the thermal capacity of each room is inserted in the thermal circuit representation of the building by a capacitor, C_{ri} which is placed between the node representing the temperature of the room and the ground.

Notice that the temperature assigned to every node in the thermal circuit is analogous to the voltage of the corresponding node in the electrical circuit. Therefore by placing the capacitor in the mentioned location, the effect of increase of internal energy of the room air is reflected to the temperature of the room by rising the temperature of the room by $\Delta T = (\Delta Q/mc_p)$, which is analogous to the increase of the voltage of the corresponding node in the electrical circuit by $\Delta V = \Delta q/C$, where ΔV, Δq and C are the increase in the voltage of the node, increase in the electrical charge on the capacitor's plates and the capacity of the capacitor, respectively.

Other than the rooms the walls are also the main elements, that affect the thermal behavior of a building. In our simple 3-room building model, there are 10 walls which are identified by $w_1, w_2, \ldots, w_{10}$. The *area* and the *temperature* of wall i is called A_i and T_{wi} respectively. The temperature of the wall is assigned to its centerline, separating the wall into two parts. The thermal capacity of a wall which is denoted by C_{wi} may be defined as

$$C_{wi} = m_{wi} c_{p_w} \tag{2.19}$$

where the mass of wall i, m_i can be obtained from the following equation

$$m_{wi} = \rho_w V_{wi} \tag{2.20}$$

where ρ_w is the density of the walls and V_{wi} is the volume of wall i which is the area of the wall times its thickness.

Now we have one node for the air inside the room and four nodes for the surrounding walls. These nodes should be linked to each other using the thermal resistances that were defined in Section 5.2. having the walls separated into two sides, we can define the thermal resistance for conduction for both sides of the wall. Therefore the thermal resistance for conduction for each side of the wall can be defined as

$$R_{cond,half} = \frac{R_w}{2} \tag{2.21}$$

where R_w is the total thermal resistance of the wall, which can be expressed as

$$R_w = \frac{L}{kA} \tag{2.22}$$

where L is the thickness of the wall, k is the *thermal conductivity* of the wall material, and A is the area of the wall.

We can define thermal resistance for the convection heat transfer on both sides of the walls by using the equations presented in Section 2.2. Since h, the *convective heat transfer coefficient* depends on the *type of fluid*, *flow properties* and *temperature properties*, it will have different values for the two sides of the walls depending on the factors mentioned above for each side[44]. For simplicity, we only consider two different convective heat transfer coefficients, one for the internal and one for the external sides of the peripheral walls. Notice that the internal walls have the same convective heat transfer coefficient on their both sides. We denote the internal convective heat transfer coefficient, by h_i and the external convective heat transfer coefficient, by h_o. Accordingly the thermal resistance for convection on the internal and external sides of the peripheral walls denoted by (R_i) and (R_o), respectively, can be defined as follows

$$R_i = \frac{1}{h_i A} \tag{2.23}$$

$$R_o = \frac{1}{h_o A} \tag{2.24}$$

Now we can derive the governing equation for the temperature evolution in walls and rooms of the building, using the resistances and capacitors defined above. By performing *nodal analysis* we can get the following equation for the temperature of walls and rooms [63]. For wall w_1 in Figure (2.4) we have

$$\frac{T_\infty - T_{w_1}}{(R_o + \frac{R_w}{2})_1} + \frac{T_1 - T_{w_1}}{(R_i + \frac{R_w}{2})_1} + \alpha A_1 q''_{rad_1} = C_{w1}\frac{d(T_{w1})}{dt} \tag{2.25}$$

Where the subscripts of the parentheses refer to the number of the wall, for which the equation is written and hence the wall that the resistances should be calculated for. The first term in the above equation accounts for the heat that is transferred form outside to the wall. The second term represents the heat transfer from the air in room number 1 to the wall. The term αq_{rad_1} accounts for the portion of the radiation heat from the sun, that is absorbed by the wall, where α is the *absorptivity coefficient* of the wall and q_{rad} is the total radiation heat that reaches the wall. Notice that the rest of the radiation heat that is not absorbed by the wall, is reflected. T_∞ refers to the outside temperature. A similar equation can be written for wall 2:

$$\frac{T_\infty - T_{w_2}}{(R_o + \frac{R_w}{2})_2} + \frac{T_1 - T_{w_2}}{(R_i + \frac{R_w}{2})_2} + \alpha A_2 q''_{rad_2} = C_{w2}\frac{d(T_{w2})}{dt} \tag{2.26}$$

We can write this equation for all of the walls of the building. So we have 10 equations governing the temperature evolution in the walls [20]. By doing the same $Nodal Analysis$ for each room in the building we can get the following equations:

For room 1 we have:

$$\frac{T_{w_1} - T_1}{(R_i + \frac{R_w}{2})_1} + \frac{T_{w_2} - T_1}{(R_i + \frac{R_w}{2})_2} + \frac{T_{w_8} - T_1}{(R_i + \frac{R_w}{2})_8} + \frac{T_{w_{10}} - T_1}{(R_i + \frac{R_w}{2})_{10}} + \dot{m}_1 c_{p_a}(T_0 - T_1) + q_{int1} = C_{r1}\frac{d(T_1)}{dt} \tag{2.27}$$

Where $\dot{m}_1$ is the air mass flow through the ducts into room number 1, c_p is the specific heat of air, T_0 is the temperature of the chilled air or hot air that comes into the rooms through the ducts, and q_{int} is the heat generation inside the rooms which can be from electrical devices such as computers, or from humans, lighting and etc.

The same equation can be written for room 2 and 3 as follows.

Room 2:

$$\frac{T_{w_8}-T_2}{(R_i+\frac{R_w}{2})_8}+\frac{T_{w_3}-T_2}{(R_i+\frac{R_w}{2})_3}+\frac{T_{w_4}-T_2}{(R_i+\frac{R_w}{2})_4}+\frac{T_{w_9}-T_2}{(R_i+\frac{R_w}{2})_9} + \dot{m}_2 c_{p_a}(T_0-T_2)+q_{int2}=C_{r2}\frac{d(T_2)}{dt} \tag{2.28}$$

Room 3:

$$\frac{T_{w_7}-T_3}{(R_i+\frac{R_w}{2})_7}+\frac{T_{w_{10}}-T_3}{(R_i+\frac{R_w}{2})_{10}}+\frac{T_{w_9}-T_3}{(R_i+\frac{R_w}{2})_9}+\frac{T_{w_5}-T_3}{(R_i+\frac{R_w}{2})_5}+\frac{T_{w_6}-T_3}{(R_i+\frac{R_w}{2})_6} + \dot{m}_3 c_{p_a}(T_0-T_3)+q_{int3}=C_{r3}\frac{d(T_3)}{dt} \tag{2.29}$$

If we write the heat transfer equation for every wall and room in the building and represent the equations in a state space form we get the following form of equation.

$$\dot{x}=Ax+f(x,u) \tag{2.30}$$
$$y=Cx \tag{2.31}$$

where x is the state, u is the input and y is the output of the system. The matrices A, C and the vector x and $f(x,u)$ are defined as follows:

$$x=\begin{bmatrix}T_{w_1} & T_{w_2} & T_{w_3} & \dots & T_{w_{10}} & T_1 & T_2 & T_3\end{bmatrix}^T \tag{2.32}$$

$$A=[M \quad N]$$

Where M and N are as follows

$$M = \begin{bmatrix}
\frac{-1}{R'_1 C_{w_1}} & 0 & 0 & 0 & 0 & 0 & 0 & 0 & 0 & 0 \\
0 & \frac{-1}{R'_2 C_{w_2}} & 0 & 0 & 0 & 0 & 0 & 0 & 0 & 0 \\
0 & 0 & \frac{-1}{R'_3 C_{w_3}} & 0 & 0 & 0 & 0 & 0 & 0 & 0 \\
0 & 0 & 0 & \frac{-1}{R'_4 C_{w_4}} & 0 & 0 & 0 & 0 & 0 & 0 \\
0 & 0 & 0 & 0 & \frac{-1}{R'_5 C_{w_5}} & 0 & 0 & 0 & 0 & 0 \\
0 & 0 & 0 & 0 & 0 & \frac{-1}{R'_6 C_{w_6}} & 0 & 0 & 0 & 0 \\
0 & 0 & 0 & 0 & 0 & 0 & \frac{-1}{R'_7 C_{w_7}} & 0 & 0 & 0 \\
0 & 0 & 0 & 0 & 0 & 0 & 0 & \frac{-1}{R'_8 C_{w_8}} & 0 & 0 \\
0 & 0 & 0 & 0 & 0 & 0 & 0 & 0 & \frac{-1}{R'_9 C_{w_9}} & 0 \\
0 & 0 & 0 & 0 & 0 & 0 & 0 & 0 & 0 & \frac{-1}{R'_{10} C_{w_{10}}} \\
\frac{1}{R_1 C_{r_1}} & \frac{1}{R_2 C_{r_1}} & 0 & 0 & 0 & 0 & 0 & \frac{1}{R_8 C_{r_1}} & 0 & \frac{1}{R_{10} C_{r_1}} \\
0 & 0 & \frac{1}{R_3 C_{r_2}} & \frac{1}{R_4 C_{r_2}} & 0 & 0 & 0 & \frac{1}{R_8 C_{r_2}} & \frac{1}{R_9 C_{r_2}} & 0 \\
0 & 0 & 0 & 0 & \frac{1}{R_5 C_{r_3}} & \frac{1}{R_6 C_{r_3}} & \frac{1}{R_7 C_{r_3}} & 0 & \frac{1}{R_9 C_{r_3}} & \frac{1}{R_{10} C_{r_3}}
\end{bmatrix}$$

$$N = \begin{bmatrix}
\frac{1}{R_1 C_{w_1}} & 0 & 0 \\
\frac{1}{R_2 C_{w_2}} & 0 & 0 \\
0 & \frac{1}{R_3 C_{w_3}} & 0 \\
0 & \frac{1}{R_4 C_{w_4}} & 0 \\
0 & 0 & \frac{1}{R_5 C_{w_5}} \\
0 & 0 & \frac{1}{R_6 C_{w_6}} \\
0 & 0 & \frac{1}{R_7 C_{w_7}} \\
\frac{1}{R_8 C_{w_8}} & \frac{1}{R_8 C_{w_8}} & 0 \\
0 & \frac{1}{R_9 C_{w_9}} & \frac{1}{R_9 C_{w_9}} \\
\frac{1}{R_{10} C_{w_{10}}} & 0 & \frac{1}{R_{10} C_{w_{10}}} \\
a & 0 & 0 \\
0 & b & 0 \\
0 & 0 & c
\end{bmatrix}$$

where the constants R, R', a, b and c are defined as follows:

$$\frac{1}{R} = \frac{1}{R_i + R_w/2} \tag{2.33}$$

$$\frac{1}{R'} = \frac{1}{R_o + R_w/2} + \frac{1}{R_i + R_w/2} \tag{2.34}$$

$$a = \frac{-1}{C_{r_1}}(\frac{1}{R_1} + \frac{1}{R_2} + \frac{1}{R_8} + \frac{1}{R_{10}}) \tag{2.35}$$

$$b = \frac{-1}{C_{r_2}}(\frac{1}{R_3} + \frac{1}{R_4} + \frac{1}{R_9} + \frac{1}{R_8}) \tag{2.36}$$

$$c = \frac{-1}{C_{r_3}}(\frac{1}{R_5} + \frac{1}{R_6} + \frac{1}{R_7} + \frac{1}{R_{10}}) \tag{2.37}$$

Matrix C which determines the outputs is defined as

$$C = \begin{bmatrix} 0 & 0 & 0 & 0 & 0 & 0 & 0 & 0 & 0 & 0 & 1 & 0 & 0 \\ 0 & 0 & 0 & 0 & 0 & 0 & 0 & 0 & 0 & 0 & 0 & 1 & 0 \\ 0 & 0 & 0 & 0 & 0 & 0 & 0 & 0 & 0 & 0 & 0 & 0 & 1 \end{bmatrix} \tag{2.38}$$

and $f(x, u)$, the nonlinear part of the system equations is defined as follows:

$$f(x,u) = \begin{bmatrix} \frac{\alpha}{C_{w1}} q''_{rad_1} A_1 + \frac{T_\infty}{C_{w1} R_{o1}} \\ \frac{\alpha}{C_{w2}} q''_{rad_2} A_2 + \frac{T_\infty}{C_{w2} R_{o2}} \\ \frac{\alpha}{C_{w3}} q''_{rad_3} A_3 + \frac{T_\infty}{C_{w3} R_{o3}} \\ \frac{\alpha}{C_{w4}} q''_{rad_4} A_4 + \frac{T_\infty}{C_{w4} R_{o4}} \\ \frac{\alpha}{C_{w5}} q''_{rad_5} A_5 + \frac{T_\infty}{C_{w5} R_{o5}} \\ \frac{\alpha}{C_{w6}} q''_{rad_6} A_6 + \frac{T_\infty}{C_{w6} R_{o6}} \\ \frac{\alpha}{C_{w7}} q''_{rad_7} A_7 + \frac{T_\infty}{C_{w7} R_{o7}} \\ 0 \\ 0 \\ 0 \\ \frac{1}{C_{r1}} \left[\dot{m}_1 c_{p_a} (T_0 - T_1) + q_{int_1} \right] \\ \frac{1}{C_{r2}} \left[\dot{m}_2 c_{p_a} (T_0 - T_2) + q_{int_2} \right] \\ \frac{1}{C_{r3}} \left[\dot{m}_3 c_{p_a} (T_0 - T_3) + q_{int_3} \right] \end{bmatrix} \tag{2.39}$$

As you can see in $f(x,u)$ the control input ($\dot{m}_i$) is multiplied by the state (x_i) which makes the dynamics of the system nonlinear. This f vector is actually composed of both the input and the disturbance to the system model. In order to be able to study the dynamics of the system more rigorously, we decompose vector f into the *input* vector and the *disturbance* vector, i.e.

$$f(x,u) = g(x,u) + d(t) \tag{2.40}$$

Where $g(x,u)$ which contains the input terms is

$$g(x,u) = \begin{bmatrix} 0 \\ 0 \\ 0 \\ 0 \\ 0 \\ 0 \\ 0 \\ 0 \\ 0 \\ 0 \\ \frac{1}{C_{r1}}\left[\dot{m}_1 c_{p_a}(T_0 - T_1)\right] \\ \frac{1}{C_{r2}}\left[\dot{m}_2 c_{p_a}(T_0 - T_2)\right] \\ \frac{1}{C_{r3}}\left[\dot{m}_3 c_{p_a}(T_0 - T_3)\right] \end{bmatrix} \tag{2.41}$$

Which can be written in the form below. Note that the following form, the state space representation for a dynamical system, is the form we will use for the control purposes.

$$g(x,u) = \begin{bmatrix} 0 & 0 & 0 \\ 0 & 0 & 0 \\ 0 & 0 & 0 \\ 0 & 0 & 0 \\ 0 & 0 & 0 \\ 0 & 0 & 0 \\ 0 & 0 & 0 \\ 0 & 0 & 0 \\ 0 & 0 & 0 \\ 0 & 0 & 0 \\ \frac{c_p}{C_{r1}}(T_0 - T_1) & 0 & 0 \\ 0 & \frac{c_p}{C_{r2}}(T_0 - T_2) & 0 \\ 0 & 0 & \frac{c_p}{C_{r3}}(T_0 - T_3) \end{bmatrix} \cdot \begin{bmatrix} \dot{m}_1 \\ \dot{m}_2 \\ \dot{m}_3 \end{bmatrix} \tag{2.42}$$

and the disturbance term is as follows

$$d(t) = \begin{bmatrix} \frac{\alpha}{C_{w1}} q''_{rad_1} A_1 + \frac{T_\infty}{C_{w1} R_{o1}} \\ \frac{\alpha}{C_{w2}} q''_{rad_2} A_2 + \frac{T_\infty}{C_{w2} R_{o2}} \\ \frac{\alpha}{C_{w3}} q''_{rad_3} A_3 + \frac{T_\infty}{C_{w3} R_{o3}} \\ \frac{\alpha}{C_{w4}} q''_{rad_4} A_4 + \frac{T_\infty}{C_{w4} R_{o4}} \\ \frac{\alpha}{C_{w5}} q''_{rad_5} A_5 + \frac{T_\infty}{C_{w5} R_{o5}} \\ \frac{\alpha}{C_{w6}} q''_{rad_6} A_6 + \frac{T_\infty}{C_{w6} R_{o6}} \\ \frac{\alpha}{C_{w7}} q''_{rad_7} A_7 + \frac{T_\infty}{C_{w7} R_{o7}} \\ 0 \\ 0 \\ 0 \\ \frac{1}{C_{r_1}} q_{int_1} \\ \frac{1}{C_{r_2}} q_{int_2} \\ \frac{1}{C_{r_3}} q_{int_3} \end{bmatrix} \tag{2.43}$$

The nonlinearity in the system is of the form xu (i.e. the product of state and input) and it is only seen in the input vector. There are some techniques such as feedback linearization including Input/Output Linearization or Input/State Linearization

techniques which can be used to deal with the nonlinearities of the system. It can be shown that due to the high order of the system these linearization techniques lead to very messy calculations, and the *internal dynamics* is of very high order with respect to the order of the transformed linearized state dynamics.

Therefore, we use the conventional *Jacobian Linearization* approach to take the system dynamics into the standard state space realization. it can be shown that due to the small range of temperatures in the building, the Jacobian linearization which is done about a certain *equilibrium point* is fairly accurate for our control purposes.

2.4 Model Validation

For validating the model that was developed in section 2.3, we have used the data of zone temperature of a specific zone at Bancroft library of UC Berkeley campus along with airflow, discharge air temperature (DAT) and outside air temperature (OAT) data to simulate the thermal behavior of that specific zone and then compare the simulation results with the measured temperature of the zone. We have used the WebCTRL of Automated Logic Corporation (ALC) to download the temperature data.

2.4.1 Parameter Identification

In order to estimate the parameters of the model such as the overall thermal resistance of each wall we have used some typical R-values for walls from ASHRAE handbook [77] as the initial guesses and then we have used the *fmincon* function in MATLAB to solve for the optimal parameters by minimizing the error between the measured temperature and the simulated temperature of the zone with respect to constraints on the parameters. The results of model validation is shown in Figure 2.5. In this optimization problem, the optimization parameters include the thermal resistances of the walls and the masses in the energy balance equation. The parameters of the model are reported in Table 2.2.

Note that since the presence of people in the room is very random and has not been considered in the modeling we have used the data of a weekend in order to minimize the disturbance effect of internal heat gains by the people in the system.

2.4.2 Parameter Validation

In order to validate the parameters listed in Table 2.2 we have simulated the temperature of the same thermal zone using the data of next weekend (Oct 24). The results of the simulation is presented in Figure 2.6.

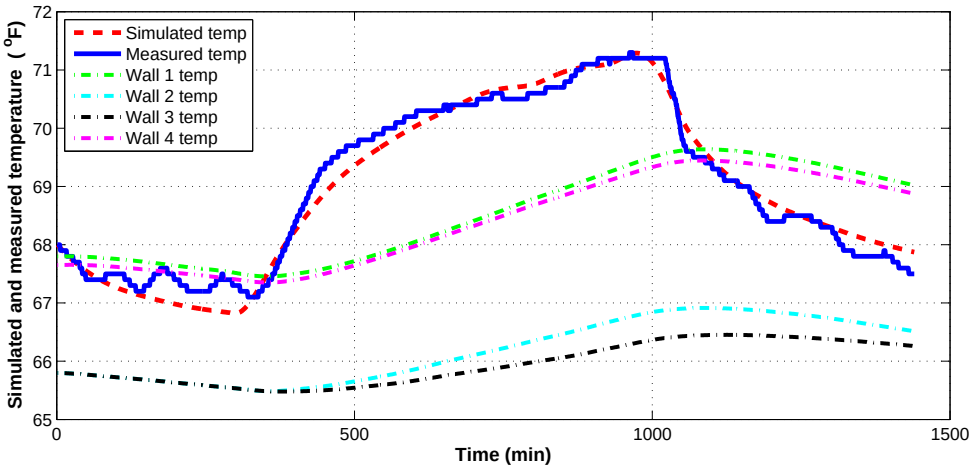

Figure 2.5: Simulated temperature versus measured temperature of zone 8 of Bancroft library on the campus of UC Berkeley (Oct 17, 2010).

Table 2.2: Parameter identification results.

Parameter	Value (kJ/K)	Parameter	Value (m.K/W)
C_{r_1}	1.673×10^3	$Rval_w$	1.659
C_{w_1}	2.707×10^4	$Rval_{gl}$	0.124
C_{w_2}	2.730×10^4	$Rval_{in}$	0.062
C_{w_3}	1.895×10^4	$Rval_{out}$	2.149
C_{w_4}	3.898×10^4		

Note that zone 8 is located in the north east corner of second floor of DOE library building. The walls on North and East side of the building face outside and have windows. There are two points in dealing with walls with windows. First, we have to take into account the R-value of windows which is in parallel with the R-value of the wall, and also we have to take into account the effect of radiation gain from the sun during the day and the radiation loss due to heat transfer between the room and the sky at night. We have assumed an additive sinusoidal disturbance to the model to represent the effect of solar radiation gain and heat loss to the sky at night. The amplitude of the sinusoidal wave and the transmissivity of the windows are the optimization variables that are obtained in the identification process.

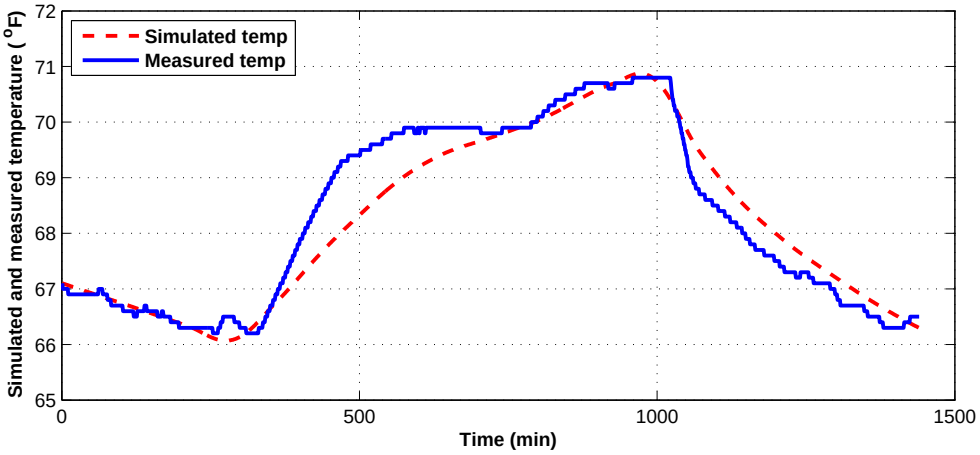

Figure 2.6: Simulated temperature versus measured temperature of zone 8 of Bancroft library on the campus of UC Berkeley (Oct 24, 2010).

2.5 Jacobian Linearization

In modeling systems, we see that nearly all systems are nonlinear, in that the differential equations governing the evolution of the system's variables are nonlinear. However, most of the theory we have developed has centered on linear systems. So, a question arises: "In what limited sense can a nonlinear system be viewed as a linear system?" In this section we review the concept of *Jacobian linearization* of a nonlinear system, about a specific operating point, called an *equilibrium point* [14].

2.5.1 Equilibrium Points

Consider a nonlinear differential equation:

$$\dot{x} = f(x(t), u(t)) \tag{2.44}$$

where f is a function mapping $R^n \times R^m \to R^n$. A point $\bar{x} \in R^n$ is called an *equilibrium point* if there is a specific $\bar{u} \in R^m$ (called the *equilibrium input*) such that

$$f(\bar{x}, \bar{u}) = 0_n \tag{2.45}$$

Suppose $\bar{x}$ is an equilibrium point with the equilibrium input $\bar{u}$. Consider starting the system (2.44) from initial condition $x(t_0) = \bar{x}$, and applying the input $u(t) \equiv \bar{u}$ for all $t \geq t_0$. The resulting solution $x(t)$ satisfies

$$x(t) = \bar{x} \tag{2.46}$$

for all $t \geq t_0$. That is why it is called an *equilibrium point.*

2.5.2 Deviation Variables

Suppose $(\bar{x}, \bar{u})$ is an equilibrium point and input. We know that if we start the system at $x(t_0) = \bar{x}$, and apply the constant input $u(t) = \bar{u}$, then the state of the system will remain fixed at $x(t) = \bar{x}$ for all t. What happens if we start a little bit away from $\bar{x}$, and we apply a slightly different input from $\bar{u}$. Define deviation variables to measure the difference.

$$\delta_x(t) := x(t) - \bar{x} \tag{2.47}$$
$$\delta_u(t) := u(t) - \bar{u} \tag{2.48}$$

Here, we are simply relabeling where we call 0. Now, the variables $x(t)$ and $u(t)$ are related by the differential equation

$$\dot{x}(t) = f(x(t), u(t)) \tag{2.49}$$

substituting in, using the constant and deviation variables, we get

$$\dot{\delta}_x(t) = f(\bar{x} + \delta_x(t), \bar{u} + \delta_u(t)) \tag{2.50}$$

This is exact. Now perform a *Taylor expansion* of the right hand side, and neglect all higher (higher than 1^{st}) order terms

$$\dot{\delta}_x(t) \approx f(\bar{x}, \bar{u}) + \left.\frac{\partial f}{\partial x}\right|_{\substack{x=\bar{x} \\ u=\bar{u}}} \tag{2.51}$$

Considering that $f(\bar{x}, \bar{u}) = 0$, we have:

$$\dot{\delta}_x(t) \approx \left.\frac{\partial f}{\partial x}\right|_{\substack{x=\bar{x} \\ u=\bar{u}}} \tag{2.52}$$

This differential equation approximately (we are neglecting 2^{nd} order and higher terms) describes the behavior of the deviation variables $\delta_x(t)$ and $\delta_u(t)$, as long as they remain small. It is a linear, time-invariant, differential equation, since the derivatives of δ_x are linear combinations of the δ_x variables and the deviation inputs, δ_u. The matrices

$$A := \left.\frac{\partial f}{\partial x}\right|_{\substack{x=\bar{x} \\ u=\bar{u}}} \in R^{n \times n} \qquad B := \left.\frac{\partial f}{\partial u}\right|_{\substack{x=\bar{x} \\ u=\bar{u}}} \in R^{n \times m} \tag{2.53}$$

are constant matrices. With the matrices A and B as defined in (2.53), the linear system

$$\dot{\delta}_x(t) = A\delta_x(t) + B\delta_u(t) \tag{2.54}$$

is called the **Jacobian Linearization** of the original nonlinear system (2.44), about the equilibrium point $(\bar{x}, \bar{u})$. For "small" values of δ_x and δ_u, the linear equation approximately governs the exact relationship between the deviation variables δ_u and δx.

If we design a controller that effectively controls the deviations δ_x, then we have designed a controller that works well when the system is operating near the equilibrium point $(\bar{x}, \bar{u})$. This is a common, and effective way of dealing with nonlinear systems approximating them with a linear system.

To implement this method, we need to find the equilibrium points of the system. The equilibrium points are obtained by fixing the input, $\bar{u}$ and then solving for $\bar{x}$. In this system there are infinite equilibrium points which can be obtained by assuming different equilibrium inputs. However we are only interested in one equilibrium point in which the system is working most of the time.

That equilibrium point is obtained by setting the temperature of the rooms equal to the set point temperatures that are assigned by the users (building occupants), and then solving for the equilibrium temperature of the walls and the equilibrium inputs. Here we have ignored the disturbance terms. The equilibrium point is achieved only by setting the nonlinear differential equation (2.44) equal to zero. We have solved for an equilibrium point near the setpoint $T_{stpnti} \quad \forall i = 1, 2, 3$. By solving the equation we find the equilibrium point to be

$$X_e = \begin{bmatrix} 0.0058 \\ 0.0058 \\ 0.0058 \\ 0.0058 \\ 0.0058 \\ 0.0014 \\ 0.0058 \\ 0.0116 \\ 0.0116 \\ 0.0116 \\ 22.0666 \\ 22.0666 \\ 22.0292 \end{bmatrix} \qquad u_e = \begin{bmatrix} 0.000333 \\ 0.000333 \\ 0.000665 \end{bmatrix} \tag{2.55}$$

Now we can find the linearized system by evaluating the matrices A and B from

equation (2.53). Therefore the linearized state space realization of the system is as follows

$$\dot{x} = Ax + Bu + d(t) \tag{2.56}$$

where matrix A stays the same as before but matrix B is as follows

$$B = \begin{bmatrix} 0 & 0 & 0 \\ 0 & 0 & 0 \\ 0 & 0 & 0 \\ 0 & 0 & 0 \\ 0 & 0 & 0 \\ 0 & 0 & 0 \\ 0 & 0 & 0 \\ 0 & 0 & 0 \\ 0 & 0 & 0 \\ 0 & 0 & 0 \\ \frac{c_p}{C_{r1}}(T_0 - T_{stpnt1}) & 0 & 0 \\ 0 & \frac{c_p}{C_{r2}}(T_0 - T_{stpnt2}) & 0 \\ 0 & 0 & \frac{c_p}{C_{r3}}(T_0 - T_{stpnt3}) \end{bmatrix} \tag{2.57}$$

Where T_0 is the temperature of the chilled or hot air which comes into the room from the HVAC ducts, which is assumed to be constant, and T_{stpnti} $\forall i = 1, 2, 3$ are the set point temperatures that the occupants set for each room in the building. Now that we have the linearized state space representation of the system, we will introduce the control algorithm and implement it on the system in Chapter 4.

2.5.3 Linearization of a Generic Nonlinear Dynamic Model

For a generic nonlinear model of building, we linearize the system dynamics around the nearest equilibrium point to the specified operating point of the system (details in [56]). The algorithm to find the equilibrium point of the system starts from an initial point and searches, using a *sequential quadratic programming algorithm*, until it finds the nearest equilibrium point. First we linearize the model considering all the inputs to the model. Once the linearization is done, we divide the inputs into *manipulated variables* and *disturbance variables*. Discretizing the state space realization leads to $x_{k+1} = Ax_k + Bu_k + Ed_k$ where d_k stores the disturbance at time k and the original B obtained from linearization process is split into two parts. The new B keeps the columns corresponding to the manipulated variables and E stores the columns of the original B corresponding to the disturbance variables. In this study

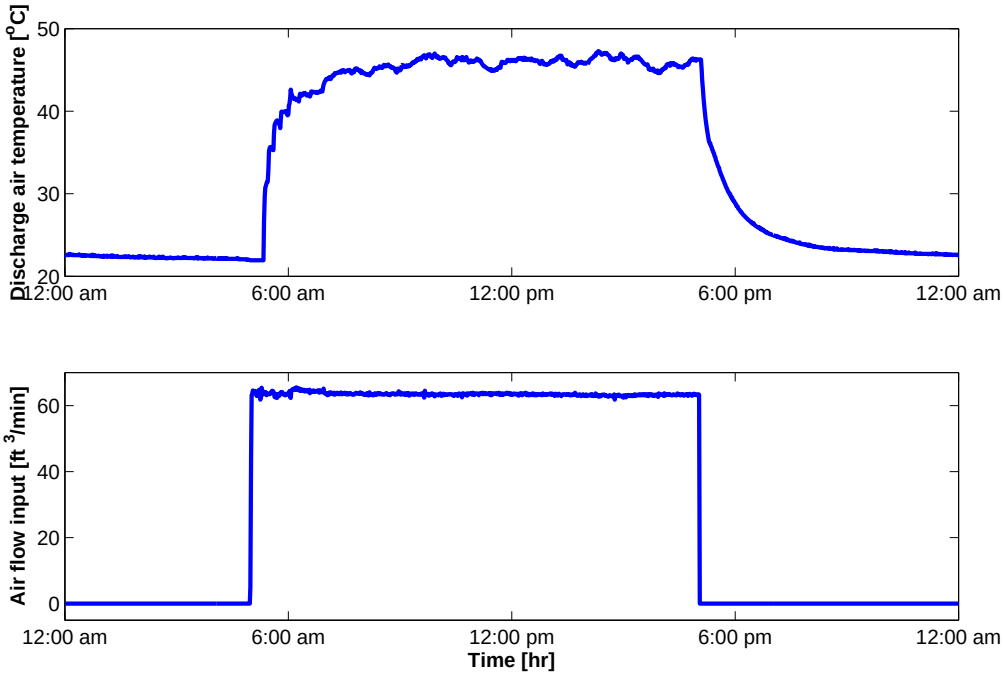

Figure 2.7: Measured data of air flow and discharge air temperature.

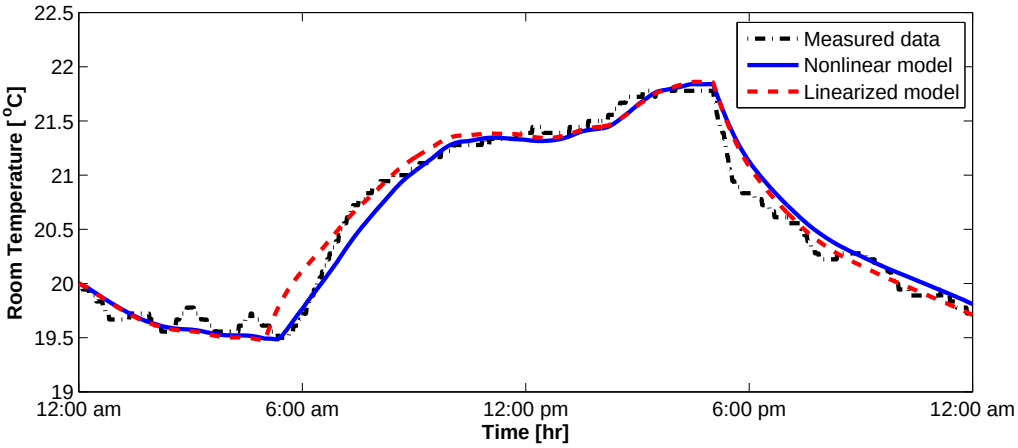

Figure 2.8: Temperature of room from measured data, nonlinear model and the linearized model.

we have kept the air flow as a manipulated variable and we regard the rest of the inputs as the disturbance input on which we don't have control. Note that since the

range of the variations of inputs as shown in Figure 2.7 during day (on-mode) and also the thermal zone temperature that the system experiences in the course of a day is not so wide (usually 20 - 22 ° C), linearizing about the equilibrium point does not introduce significant error as shown in Figure 2.8. On the other hand dealing with a linear system dramatically decreases the computational efforts. The results of the linearization is shown in Figure 2.8.

2.6 Unmodelled Dynamics Estimation

The model developed up to this point in this chapter works well as long as the internal heat generation, and heat transfer to the room from external sources such as sun radiation that are not captured in the model are negligible. However, this is not a good assumption in the case of almost every single building. Hence, these contributors to the temperature dynamics which are not captured by the model introduced earlier in Chapter 2, as we call them "unmodelled dynamics", should be accounted for by some means. In this section, we develop a methodology to estimate such unmodelled dynamics using measurable quantities such as CO2 concentration level and outside air temperature.

2.6.1 Estimating External Loads

Heat flux is radiated from the sun to the exposed walls and to the peripheral rooms through windows. This heat flux is a hard-to-estimate function of several variables including the *altitude* and *azimuth* angle of the location of the building on the Earth, orientation of the considered wall or window, day of the year, time of the day, outside weather and sky condition. However, to be able to estimate the heat flux at each time, we approximate it by assuming that this quantity is an affine function of the outside air temperature[1] given by

$$q''_{rad_i}(t) = \lambda T_{out}(t) + \gamma \tag{2.58}$$

where λ and γ will be obtained by the parameter estimation algorithm detailed later. Hence, we parameterize $q''_{rad_i}(t)$ and then identify all of the parameters using nonlinear regression. Note that this method does not cover all the uncertainties associated with external loads to the building, however it leads to a decent estimation as shown later in Section 2.7.

[1]Note that other quantities such as global horizontal irradiance (GHI) data either from the *California Irrigation Management Information System*, CIMIS [1] or METAR data [7] from nearby airports archived in the *National Climatic Data Center*, can be used for the purpose of this parameterization as well.

2.6.2 Estimating Internal Loads

Internal loads in the building are usually related to occupants and electrical devices. The heat emitted from electrical devices is easy to identify based on the electrical characteristics of the device with high precision; the main uncertainty in identifying the internal loads is due to the load associated to the building occupants. We propose a parameterization of the internal loads by occupants using the CO_2 sensor data (current CO_2 concentration in the room) which yields

$$\dot{q}_{int}(t) = \mu\Psi(t) + \nu \tag{2.59}$$

where $\Psi(t)$ is the CO_2 concentration in the room in (ppm). μ and ν are constants to be obtained from the identification process.

2.7 Unmodelled Dynamics Identification

We use historical data to identify the parameters of the system along with the unmodelled dynamics described in Section 2.3. The identification process is done through an optimization problem over the parameters given in (2.60).

$$\min_{C_{[.]},R_{[.]},\lambda,\gamma,\mu,\nu} \|Y^m - Y^s\|_2^2 \tag{2.60}$$
$$\text{s.t.} \begin{cases} x^s_{t+1} = Ax^s_t + f(x^s_t, u^m_t, d^m_t) & t = 0, ..., N-1 \\ y^s_t = Cx^s_t & t = 0, ..., N \end{cases}$$

Where the subscript t refers to time and the superscript m and s refer to measured and simulated data, respectively. The vector $Y \in \mathbb{R}^{N\times 1}$ stores the values of y_t for $t = 1, \cdots, N$.

2.7.1 Parameter Identification

For identifying the parameters of the model we have used the data of zone temperature of a specific zone at Bancroft library of UC Berkeley campus along with airflow, discharge air temperature (DAT) and outside air temperature (OAT) data to simulate the thermal behavior of that specific zone and then compare the simulation results with the measured temperature of the zone. We have used the WebCTRL of Automated Logic Corporation (ALC) to download the temperature data. The results of model validation is shown in Figure 2.9. We store the unmodelled dynamics in a time-varying vector called disturbance d_t.

Note that there are two peaks in the unmodelled dynamics values, one around 9 $a.m.$ and another around 3 $p.m.$ which are due to occupants and outside radiation.

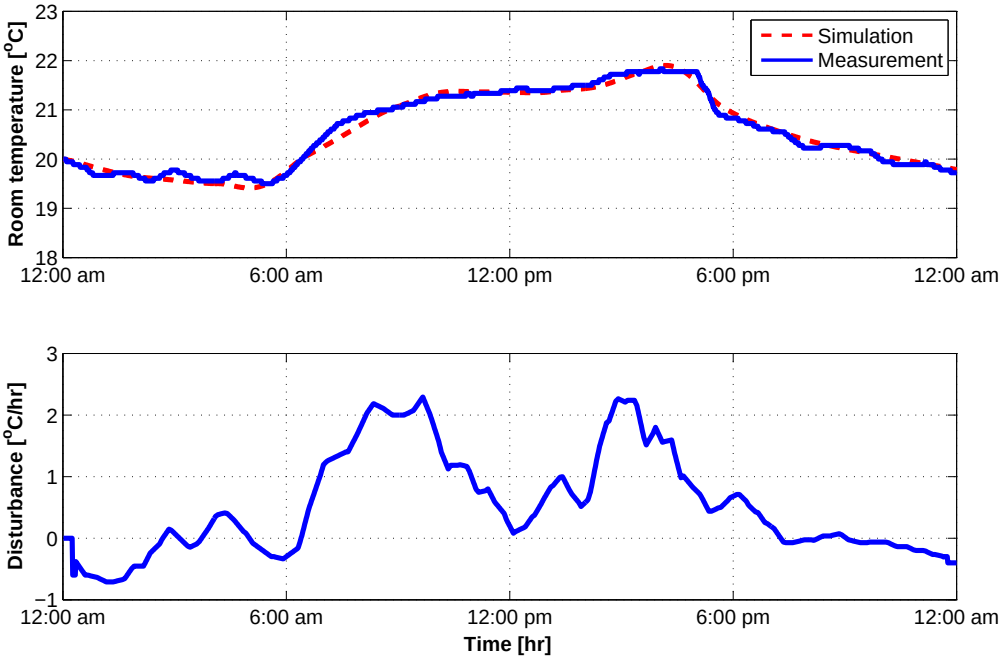

Figure 2.9: Simulated temperature and measured temperature of zone 8 of Bancroft library (Oct 24, 2010) and unmodelled dynamics.

The interesting observation is that the first peak of disturbance load does not cause as much temperature increase in the room as opposed to the second disturbance peak. The reason is that in the morning the walls which represent the slow-dynamic masses in the system are cold due to low temperature at night. Therefore part of the heating load, earlier in the day, goes toward warming up the slow-dynamic thermal masses in the building (e.g. walls and furniture). However in the afternoon the slow-dynamic thermal masses absorb heat at a slower rate and therefore, cause faster increase to the temperature of the fast-dynamic thermal mass of the system which is the air in the room. Also a decrease in the values of the unmodelled dynamics is observed which can be due to the people leaving the room around noon for lunch and/or cloudy sky. The optimal parameters of the model are reported in [53].

2.7.2 Parameter Validation

In order to validate the parameters of the model, we have simulated the temperature of the same thermal zone using the data of next weekend. The results of the simulation are presented in [53].

Chapter 3

Parameter Adaptive Building (PAB) Model

Model-based control of building energy offers an attractive way to minimize energy consumption in buildings. Model-based controllers require mathematical models that can accurately predict the behavior of the system. For buildings, specifically, these models are difficult to obtain due to highly time varying, and nonlinear nature of building dynamics. Also, model-based controllers often need information of all states, while not all the states of a building model are measurable. In addition, it is challenging to accurately estimate building model parameters (e.g. convective heat transfer coefficient of varying outside air). In this chapter, we propose a modeling framework for "*online estimation*" of states and unknown parameters of buildings models, leading to the Parameter-Adaptive Building (PAB) model. Extended Kalman filter (EKF) and unscented Kalman filter (UKF) techniques are used to design the PAB model which simultaneously tunes the parameters of the model and provides an estimate for all states of the model. The proposed PAB model is tested against experimental data collected from Lakeshore Center building at Michigan Tech University. Our results indicate that the new framework can accurately predict states and parameters of the building thermal model. The material of this chapter is extracted from [57].

3.1 Why Parameter Adaptive Building Model?

Buildings are dynamical systems with uncertain and time-varying plant and occupant characteristics. The heat transfer characteristics of a building are highly dependent on the ambient conditions. For instance, heat transfer properties such as convective heat transfer coefficient h, of peripheral walls is dependent on outside temperature, wind speed and direction. Also, unmodelled dynamics of a building (See [55]). is

function of 1) *external factors*: ambient weather conditions such as radiative heat flux into the walls and windows, and cloudiness of the sky, and 2) *internal factors:* such as occupancy level, internal heat generation from lighting, and computers. These quantities are highly time-varying and therefore the dynamics of the building and, consequently, parameters of the mathematical model describing the dynamics of the buildings are constantly changing with time. Accordingly, the estimation algorithms utilized to identify these parameters should take the *time-varying* aspect of buildings into account and be *adaptive* in this respect.

Reliable dynamical models are crucial to model predictive control strategies. Modeling and system identification are the most challenging and time-consuming parts of building predictive control [71]. To address this challenge, over the last few years numerous mathematical models of building thermal dynamics have been proposed in the literature. Resistor-capacitor (RC) models with disturbances to capture unmodelled dynamics have been proposed in [56, 55, 53]. A bilinear version of an RC model is presented in [67] that takes into account weather predictions to increase building energy efficiency. In [15], the authors found that time varying properties such as occupancy can significantly change the dynamic thermal model and influence how building models are identified. While modeling a multi-zone building, the authors observed that the experimental data often did not have sufficient quality for system identification and hence, proposed a closed-loop architecture for active system identification using prediction-error identification method (PEM). Other modeling techniques with application in building predictive control include: *subspace methods*, *MPC relevant identification (MRI)*, *deterministic semi-physical modeling (DSPM)*, and *probabilistic semi-physical modeling (PSPM)*. In this paper we focus on DSPM. In a recent work, unscented Kalman filtering has been used for online estimation of building thermal parameter estimation [72], although the model used in that work is over-simplified and the state estimation is not performed.

Building models can be linear or nonlinear. While nonlinear models typically provide better prediction of building thermal dynamics, they are computationally intensive when incorporated in building controller algorithms. On the other hand, linear models are less computationally intensive for use in building controllers but they are limited to the operating zones they have been tuned for. One approach to increase the accuracy of the linear building models is to use an adaptive parameter estimation technique such that the building parameters are updated as the environment changes. This leads to an adaptive modeling framework for building predictive control. Although this technique has been adopted for simultaneous state-parameter estimation in other applications [69, 64, 73], to the best of the authors' knowledge, this paper is the first study on developing adaptive modeling framework for simultaneous estimation of building *parameter*, *states* and *unmodelled dynamics*.

The contributions of this chapter are twofold: a novel adaptive modeling frame-

work for building predictive control and the application of extended Kalman filter (EKF) and unscented Kalman filter (UKF) techniques for building online parameter identification and state estimation using historical data from a test-bed.

3.2 Mathematical Model

We utilize the same model that we developed in Chapter 2, and build on top of that model. For consistency of notation throughout this chapter we first present a summary of the model developed in Chapter 2 with appropriate notation geared towards the purpose of this chapter.

Figure 3.1 depicts the schematic of a typical room which will be studied. We use lumped model analysis to reduce the complexity, and obtain a low order model, suitable for control purposes. Note that due to having forced convection inside the room, the temperature is assumed uniform inside the room. We use the RC model from Chapter 2, in which the building is considered as a network. Then we modify the representation of the system dynamics to account for *time varying* parameters by *augmenting* the parameters into the state vector.

3.2.1 Conductive and Convective Heat Transfer

There are two types of nodes in the building network: walls and rooms. There are in total n nodes, m of which represent rooms and the remaining $n-m$ nodes represent walls. We assign a number $i = 1, ..., m$ to each room, and denote the temperature of the room with T_{r_i}. The wall node and temperature of the wall between room i and j is denoted by (i, j) and $T_{w_{i,j}}$, respectively, and is governed by the following equation:

$$C^w_{i,j}\frac{dT_{w_{i,j}}}{dt} = \sum_{k\in\mathcal{N}_{w_{i,j}}} \frac{T_{r_k} - T_{w_{i,j}}}{R_{i,j_k}} + r_{i,j}\alpha_{i,j}A_{w_{i,j}}Q_{rad_{i,j}} \tag{3.1}$$

where $C^w_{i,j}$, $\alpha_{i,j}$ and $A_{w_{i,j}}$ are heat capacity, radiation heat absorption coefficient and area of wall between room i and j, respectively. R_{i,j_k} is the total thermal resistance between the centerline of wall (i, j) and the side of the wall where node k is located. $Q_{rad_{i,j}}$ is the radiative heat flux density on wall (i, j). $\mathcal{N}_{w_{i,j}}$ is the set of all of neighboring nodes to node $w_{i,j}$. $r_{i,j}$ is equal to 0 for internal walls, and equal to 1 for peripheral walls (*i.e.* either i or j is the outside node). Temperature of the i^{th} room is governed by the following equation:

$$C^r_i\frac{dT_{r_i}}{dt} = \sum_{k\in\mathcal{N}_{r_i}} \frac{T_k - T_{r_i}}{R_{i,k_i}} + \dot{m}_{r_i}c_a(T_{s_i} - T_{r_i}) + w_i\tau_{w_i}A_{win_i}Q_{rad_i} + \dot{Q}_{int_i} \tag{3.2}$$

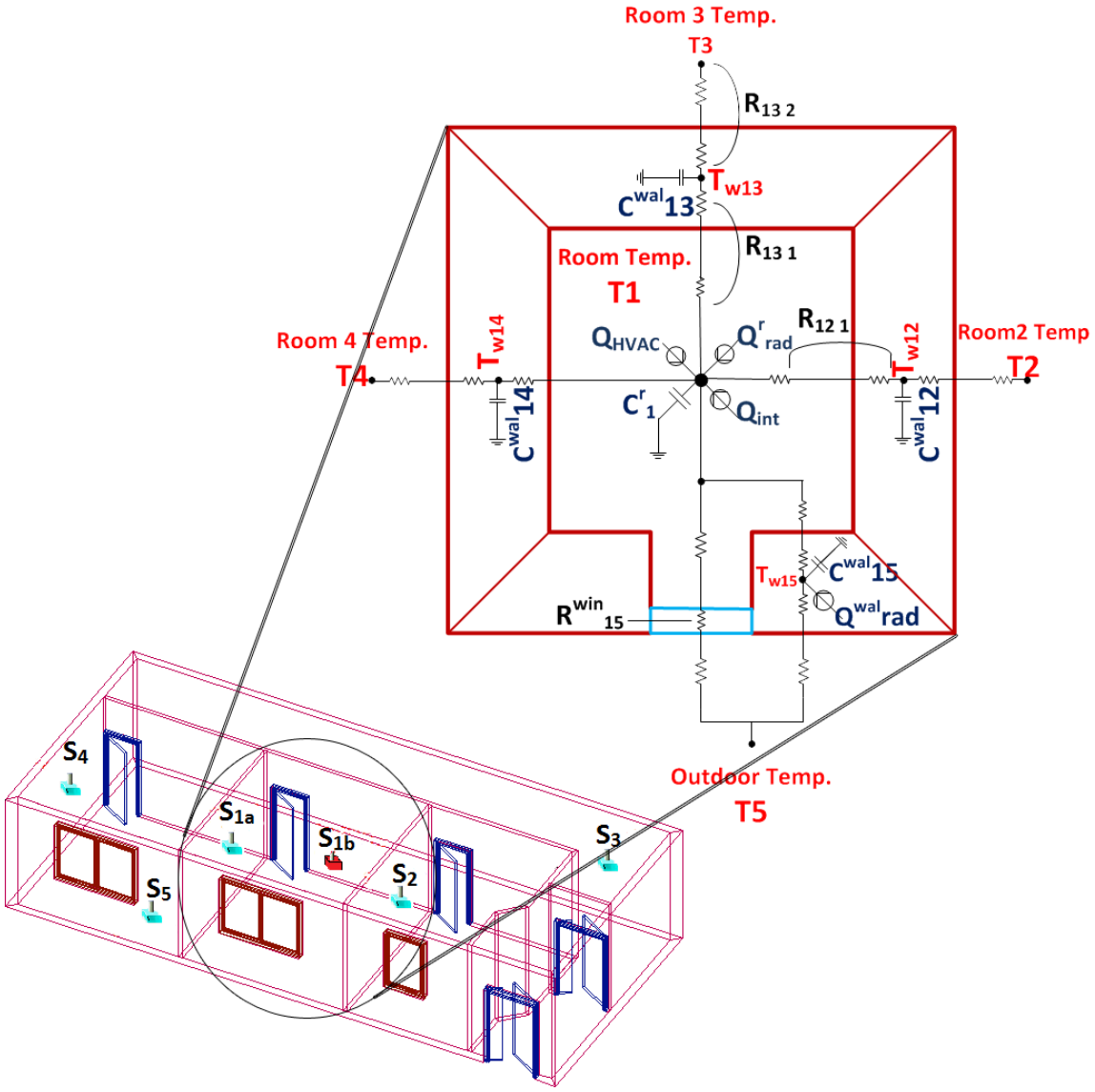

Figure 3.1: Schematic of a typical room with a window. Temperature sensors are denoted by "S" in this figure.

where T_{r_i}, C_i^r and $\dot{m}_{r_i}$ are the temperature, heat capacity and air mass flow into the room i, respectively. c_a is the specific heat capacity of air. T_{s_i} is the temperature of the supply air to room i. w_i is equal to 0 if none of the walls surrounding room i have window, and is equal to 1 if at least one of them has a window. τ_{w_i} is the transmissivity of glass of window i, A_{win_i} is the total area of window on walls surrounding room i,

Q_{rad_i} is the radiative heat flux density per unit area radiated to room i, and $\dot{Q}_{int_i}$ is the internal heat generation in room i. $\mathcal{N}_{r_i}$ is the set of all of the neighboring "room" nodes to room i. The details of building thermal modeling and estimation of the unmodelled dynamics is available in [56, 53, 55]. Note that we approximate the values of $Q_{rad_i}(t)$ and $\dot{Q}_{int}(t)$ based on the following equations:

$$Q_{rad_i}(t) = \tau T_{out}(t) + \zeta \tag{3.3}$$

$$\dot{Q}_{int}(t) = \mu \Psi(t) + \nu \tag{3.4}$$

where T_{out} and Ψ are the outside air temperature and CO_2 concentration in the room, respectively. Parameters τ, ζ, μ and ν are obtained by the parameter estimation algorithm detailed in Section 3.3.

3.2.2 Radiative Heat Transfer

We compute the radiative heat transfer between building and ambient environment as proposed in [30]. The amount of heat transferred from the building to the environment is given by the Stefan-Boltzmann law:

$$Q_{bldg} = \epsilon \sigma T_{bldg}^4 \tag{3.5}$$

where T_{bldg} is the average temperature of the building.

We also consider solar radiation heat transfer, Q_{solar} emitted on the walls, and inside the room through the windows. The data used in this paper is based on the past 30 years monthly average of solar radiation for flat-plate collectors facing south (resembling the south facing flat vertical walls of the building), and is obtained from NREL (National Renewable Energy Laboratory) [8] database for Houghton, MI in January.

Furthermore, we take into account the radiation cooling at night (*i.e.* sky thermal radiation to the building) based on the proposed relation in [30]:

$$Q_{sky} = (1 + KC^2) 8.78 \times 10^{-13} T_{out}^{5.852} RH^{0.07195} \tag{3.6}$$

where K is the coefficient related to the cloud height and C is a function of cloud coverage. We use $K = 0.34$ and $C = 0.8$ for simulations, as explained in [30]. T_{out} is the outside air temperature, and RH is the air relative humidity percentage.

The total radiation exchange between building and ambient environment is then given by:

$$Q_{rad} = Q_{sky} + Q_{solar} - Q_{bldg} \tag{3.7}$$

Note that Q_{sky} and Q_{solar} are heat flow *into* the building, and Q_{bldg}, is the heat flow *from* the building *to* the environment.

The heat transfer equations for each wall and room yield the following system dynamics:

$$\begin{aligned} \dot{x}_t &= f(x_t, u_t, d_t, t) \\ y_t &= Cx_t \end{aligned} \tag{3.8}$$

where $x_t \in \mathbb{R}^n$ is the state vector representing the temperature of the nodes in the thermal network, $u_t \in \mathbb{R}^{lm}$ is the input vector representing the air mass flow rate and discharge air temperature of conditioned air into each thermal zone, and $y_t \in \mathbb{R}^m$ is the output vector of the system which represents the temperature of the thermal zones. l is the number of inputs to each thermal zone (e.g., air mass flow and supply air temperature). C is a matrix of proper dimension and the disturbance vector is given by $d_t = g(Q_{rad_i}(t), \dot{Q}_{int}(t), T_{out}(t))$.

3.2.3 Disturbance

Following the intuitive linear relation between T_{out}, $\dot{Q}_{int}$ and Q_{rad}, we approximate g with an affine function of these quantities, leading to:

$$d_t = aQ_{rad_i}(t) + b\dot{Q}_{int}(t) + cT_{out}(t) + e \tag{3.9}$$

where e is a constant to be estimated. By substituting (5.3) and (5.4) into (5.6) and rearranging the terms, we get:

$$\begin{aligned} d_t &= (a\tau + c)T_{out}(t) + b\mu\Psi(t) + a\zeta + b\nu + e \\ &= \bar{a}T_{out}(t) + \bar{b}\Psi(t) + \bar{e} \end{aligned} \tag{3.10}$$

where $\bar{a} = a\tau + c$, $\bar{b} = b\mu$, and $\bar{e} = a\zeta + b\nu + e$. Therefore, only measurements of outside air temperature and CO_2 concentration level are needed to determine the disturbance. The values of $\bar{a}$, $\bar{b}$, and $\bar{e}$ are estimated along with other parameters of the model.

3.2.4 State-Parameter Estimation

State space form of the system is required for state-parameter estimation. Here, the state space form of building equations is presented, using (3.1) for each wall and (3.2)

for each room node in the building network.

$$\begin{aligned}\dot{x}_1 = \frac{1}{C_1^r} \cdot \Bigg(\Bigg(& \frac{1}{R_{12_1}} - \frac{1}{R_{13_1}} - \frac{1}{R_{14_1}} - \frac{1}{R_{15_1}} - \frac{1}{R_{15}^{win}} - \dot{m}_{r1} c_a \Bigg) x_1 \\ & + \frac{x_2}{R_{12_1}} + \frac{x_3}{R_{13_1}} + \frac{x_4}{R_{14_1}} + \frac{x_5}{R_{15_1}} + c_a T_{s1} \dot{m}_{r1} \\ & + \frac{T_5}{R_{15}^{win}} + A_{win} \tau Q_{rad} + \dot{Q}_{int_1} \Bigg) \end{aligned} \tag{3.11a}$$

$$\dot{x}_2 = \frac{1}{C_{21}^w} . \left(\frac{x_1}{R_{21_1}} - \left(\frac{1}{R_{21_1}} + \frac{1}{R_{21_2}} \right) x_2 + \frac{T_2}{R_{21_2}} \right) \tag{3.11b}$$

$$\dot{x}_3 = \frac{1}{C_{31}^w} . \left(\frac{x_1}{R_{31_1}} - \left(\frac{1}{R_{31_1}} + \frac{1}{R_{31_3}} \right) x_3 + \frac{T_3}{R_{31_3}} \right) \tag{3.11c}$$

$$\dot{x}_4 = \frac{1}{C_{41}^w} . \left(\frac{x_1}{R_{41_1}} - \left(\frac{1}{R_{41_1}} + \frac{1}{R_{41_4}} \right) x_4 + \frac{T_4}{R_{41_4}} \right) \tag{3.11d}$$

$$\dot{x}_5 = \frac{1}{C_{51}^w} . \left(\frac{x_1}{R_{51_1}} - \left(\frac{1}{R_{51_1}} + \frac{1}{R_{51_5}} \right) x_5 + \frac{T_5}{R_{51_5}} + A_{w_{51}} \alpha Q_{rad} \right) \tag{3.11e}$$

where T_2, T_3, T_4, T_5 are the temperatures of the surrounding zones, as shown in Figure 3.1. These temperatures act as disturbance to the system dynamics for a single zone thermal model, and x is the state vector:

$$x = \left[T_{r1}, T_{w12}, T_{w13}, T_{w14}, T_{w15} \right]^T \tag{3.12}$$

One way to adapt the model to account for time varying parameters is to assume that all the parameters of the model are independent, and hence define a state corresponding to each state. However, this would lead to excessive number of states. We take a different approach. Note that thermal properties of wall material (e.g. specific heat capacity and conductive heat transfer coefficient) are the same across the building. In addition, the thickness of internal walls and thickness of peripheral walls are the same throughout the building. Thus, we can reduce the number of independent parameters from 18 to 10. Hence we re-write the thermal equations of the wall, *i.e.* (3.11b)-(3.11d) as follows:

$$\dot{x}_2 = \frac{x_1}{C^w R^w} - \frac{2}{C^w R^w} x_2 + \frac{T_2}{C^w R^w} \tag{3.13}$$

$$\dot{x}_3 = \frac{x_1}{C^w R^w} - \frac{2}{C^w R^w} x_3 + \frac{T_3}{C^w R^w} \tag{3.14}$$

$$\dot{x}_4 = \frac{x_1}{C^w R^w} - \frac{2}{C^w R^w} x_4 + \frac{T_4}{C^w R^w} \tag{3.15}$$

$$\dot{x}_5 = \frac{x_1}{C^w_{51} R_{51_1}} - \left(\frac{1}{C^w_{51} R_{51_1}} + \frac{1}{C^w_{51} R_{51_5}} \right) x_5 + \frac{T_5}{C^w_{51} R_{51_5}} + \frac{A_{w_{51}} \alpha Q_{rad}}{C^w_{51}} \tag{3.16}$$

As shown in (3.17), $C_w R_w$ is not a function of the area of each wall:

$$C^w R_w = (c_w A_w L_w)(\frac{L_w/2}{k_w A_w} + \frac{1}{h_{in} A_w}) = \frac{c_w L_w^2}{2k_w} + \frac{c_w L_w}{h_{in}} \tag{3.17}$$

where c_w, k_w, A_w and L_w are the specific heat capacity, conductive heat transfer coefficient of wall material, area and thickness of wall, respectively, and h_{in} is the indoor convective heat transfer coefficient. Hence, we can use one common term to express thermal capacitance-resistance between centerline of each wall and the node on each side of the wall for the equations of walls in the building.

In order to use Kalman filtering for parameter estimation along with state estimation we augment the parameter vector into state vector and define the new state update equation accordingly. Effectively, we augment the following *time-varying* parameters to the state vector:

$$x_6 = \frac{1}{C^r_1 R_{12_1}} \qquad x_7 = \frac{1}{C^r_1 R_{13_1}} \tag{3.18}$$

$$x_8 = \frac{1}{C^r_1 R_{14_1}} \qquad x_9 = \frac{1}{C^r_1 R_{15_1}} \tag{3.19}$$

$$x_{10} = \frac{1}{C^r_1} \qquad x_{11} = \frac{1}{C_w R_w} \tag{3.20}$$

$$x_{12} = \frac{1}{C^w_{51} R_{51_1}} \qquad x_{13} = \frac{1}{C^w_{51} R_{51_5}} \tag{3.21}$$

$$x_{14} = \frac{\alpha}{C^w_{51}} \qquad x_{15} = \frac{1}{R^{win}_{15}} \tag{3.22}$$

As it can be seen in the continuous state space form, rate of change of these augmented states is equal to zero. We later add a low-magnitude *fictitious noise* to the dynamics of parameters to allow slow changes in the values of parameters over time.

$$\dot{x}_1 = (x_6 - x_7 - x_8 - x_9 - x_{10}x_{15} - x_{10}u_2c_a)x_1 + x_6x_2 + x_7x_3 + x_8x_4 + x_9x_5 + (c_au_1u_2 + T_5x_{15} + A_{win}\tau Q_{rad} + \dot{Q}_{int}).x_{10} \quad (3.23)$$

$$\dot{x}_2 = (x_1 - 2x_2 + T_2).x_{11} \quad (3.24)$$

$$\dot{x}_3 = (x_1 - 2x_3 + T_3).x_{11} \quad (3.25)$$

$$\dot{x}_4 = (x_1 - 2x_4 + T_4).x_{11} \quad (3.26)$$

$$\dot{x}_5 = x_1x_{12} - (x_{12} + x_{13})x_5 + T_5x_{13} + A^{w_{51}}x_{14}Q_{rad} \quad (3.27)$$

$$\dot{x}_i = 0 \qquad \forall i = 6, 7, ...15. \quad (3.28)$$

where u is the input vector:

$$u = \begin{bmatrix} T_{s1} \\ \dot{m}_{r1} \end{bmatrix} \quad (3.29)$$

In summary, we express the dynamics of the system using state space model below:

$$\begin{aligned} x_k &= f(x_{k-1}, u_{k-1}, d_{k-1}, w_{k-1}) \\ z_k &= h(x_k) + v_k \end{aligned} \quad (3.30)$$

where w_k and v_k are the process and measurement noise and are assumed to be zero mean multivariate Gaussian process with covariance W_k and V_k, (i.e. $w_k \sim N(0, W_k)$ and $v_k \sim N(0, V_k)$), respectively.

3.3 Combined State-Parameter Estimation

In order to estimate the unknown parameters of the system we augment the states of the system with a vector p_k which stores the parameters of the system, with a time evolution dynamics of $p_{k+1} = p_k$, as explained in Section 3.2. Nonlinear estimation algorithms can then be exploited to simultaneously estimate the states and the parameters of the system. Here we exploit the extended Kalman filter (EKF) and unscented Kalman filter (UKF) techniques. Simulation results are compared in Section 3.5. The architecture of the proposed Parameter-Adaptive Building (PAB) model [57] is shown in Figure 3.2.

3.3.1 Extended Kalman Filter

In the EKF, the state transition and observation models need not be linear functions of the state but may instead be differentiable functions. The Kalman filter algorithm

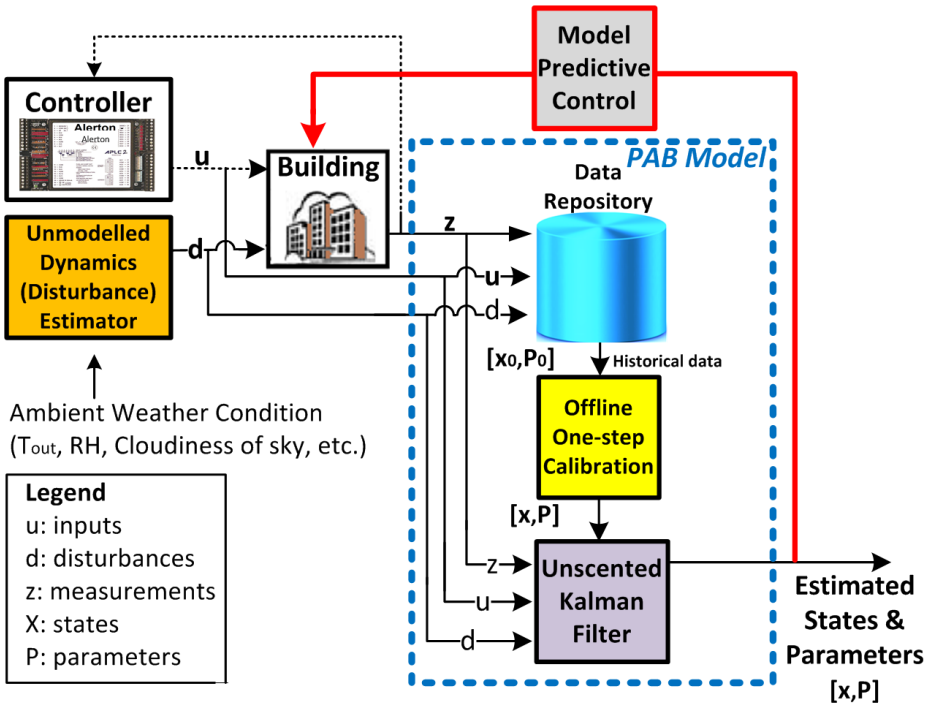

Figure 3.2: Architecture of the building control system utilizing the PAB model. Updated model parameters are obtained form UKF estimation process at each time step. At the next time step, the controller (in tis case, MPC) uses the model with updated parameters to calculate the optimal inputs. Inputs are implemented on the system and at the next sampling time new states (temperatures) are measured and sent to the PAB model, and this process repeats. Black dotted lines connecting the traditional control system to the building are replaced by the red solid lines connecting the estimation module to the MPC block and the MPC block to the building. Comprehensive study of MPC is provided in Section 4.4.

consists of two steps – *prediction* followed by *update*. The states of the system are approximated by a Gaussian random variable. In the prediction step, the filter propagates the *a-priori* state estimate through the nonlinear state update equation from time step $k-1$ to the current time step k, and the state estimation error covariance is propagated through the linearized approximation of the state equations to compute the *a-priori* state estimation error covariance. In the *update* step, the *a-posteriori* state estimate and state estimation error covariance are computed.

With the stochastic state update equation given in (5.17), and the following no-

tations

$$\hat{x}_{k|k-1} = \mathbb{E}[x_k|z_0, z_1, ..., z_{k-1}] \tag{3.31}$$
$$\hat{x}_{k|k} = \mathbb{E}[x_k|z_0, z_1, ..., z_k] \tag{3.32}$$
$$P_{k|k-1} = \mathbb{E}[(x_k - \hat{x}_{k|k-1})(x_k - \hat{x}_{k|k-1})^T|z_0, z_1, ..., z_{k-1}] \tag{3.33}$$
$$P_{k|k} = \mathbb{E}[(x_k - \hat{x}_{k|k})(x_k - \hat{x}_{k|k})^T|z_0, z_1, ..., z_k] \tag{3.34}$$

where $\mathbb{E}[x|y]$ represents mean of variable x, given measurement y. Each iteration of the EKF is presented in [37, 39] and is summarized here as follows:

Extended Kalman Filter Algorithm

Prediction:

A-priori state estimate: $\hat{x}_{k|k-1} = f(\hat{x}_{k-1|k-1}, u_{k-1}, d_{k-1}, 0)$
State transition and observation matrices:

$$F_{k-1} = \frac{\partial f}{\partial x}|_{\hat{x}_{k-1|k-1}, u_{k-1}} \qquad H_k = \frac{\partial h}{\partial x}|_{\hat{x}_{k|k-1}}$$

A-priori state estimation error covariance:

$$P_{k|k-1} = F_{k-1}P_{k-1|k-1}F_{k-1}^T + W_{k-1}$$

Update:

A-priori output estimation error:	$\tilde{y}_k = z_k - h(\hat{x}_{k|k-1})$
Innovation or residual covariance:	$S_k = H_k P_{k|k-1} H_k^T + V_k$
Near-optimal Kalman gain:	$K_k = P_{k|k-1} H_k^T S_k^{-1}$
A-posteriori state estimate:	$\hat{x}_{k|k} = \hat{x}_{k|k-1} + K_k \tilde{y}_k$
A-posteriori state estimation error covariance:	$P_{k|k} = (I - K_k H_k) P_{k|k-1}$

3.3.2 Unscented Kalman Filter

A nonlinear KF that shows promise as an improvement over the EKF is the unscented Kalman filter (UKF). The basic premise behind the UKF is that it is easier to approximate a Gaussian distribution than to approximate an arbitrary nonlinear function. The UKF addresses the approximation issues of the EKF. Instead of using Jacobian matrix, UKF uses a deterministic sampling approach to capture the

mean and covariance estimates with a minimal set of sample points [81]. As with the EKF, we present an algorithmic description of the UKF, omitting some theoretical considerations. More details can be found in [37, 39].

The state distribution is represented by a Gaussian random variable (GRV), but is now specified using a minimal set of carefully chosen sample points. These sample points completely capture the true mean and covariance of the GRV, and when propagating through the true nonlinear system, capture the posterior mean and covariance accurately to the 3rd order (Taylor series expansion) for any nonlinearity. Unscented Transformation (UT) is a method used for calculating the statistics of a random variable which undergoes a nonlinear transformation [37]. We conduct the following initialization:

$$\hat{x}_0 = \mathbb{E}[x_0] \tag{3.35}$$

$$P_0 = \mathbb{E}[(x_0 - \hat{x}_0)(x_0 - \hat{x}_0)^T] \tag{3.36}$$

Each step of the UKF is presented in [37, 39] and is summarized here as follows:

Unscented Kalman Filter Algorithm

Prediction:
Calculate sigma points:

$$\mathcal{X}_{k-1} = [\hat{x}_{k-1} \quad \hat{x}_{k-1} + \gamma\sqrt{P_{k-1}} \quad \hat{x}_{k-1} - \gamma\sqrt{P_{k-1}}]$$

Propagate each column of $\mathcal{X}_{k-1}$ through time:

$$(\mathcal{X}_k)_i = f((\mathcal{X}_{k-1})_i) \qquad i = 0, 1, ..., 2L$$

A-priori state estimate: $\hat{x}_k^- = \sum_{i=0}^{2L} W_i^{(m)} (\mathcal{X}_k)_i$

A-priori error covariance:

$$P_k^- = \sum_{i=0}^{2L} W_i^{(c)} [(\mathcal{X}_k)_i - \hat{x}_k^-][(\mathcal{X}_k)_i - \hat{x}_k^-]^T + Q_k$$

Update:

Measurement estimate: $(\mathcal{Z}_k)_i = h((\mathcal{X}_k)_i) \quad i = 0, .., 2L$
$\hat{z}_k^- = \sum_{i=0}^{2L} W_i^{(m)} (\mathcal{Z}_k)_i$

A-posteriori state estimate: $\hat{x}_k = \hat{x}_k^- + K_k(z_k - \hat{z}_k^-)$

where: $K_k = P_{\hat{x}_k \hat{z}_k} P_{\hat{z}_k \hat{z}_k}^{-1}$

A-posteriori estimate of the error covariance: $P_k = P_k^- - K_k P_{\hat{z}_k \hat{z}_k} K_k^T$

where:

$$P_{\hat{x}_k \hat{z}_k} = W_i^{(c)} [(\mathcal{X}_k)_i - \hat{x}_k^-][(\mathcal{Z}_k)_i - \hat{z}_k^-]^T$$

$$P_{\hat{z}_k \hat{z}_k} = \sum_{i=0}^{2L} W_i^{(c)} [(\mathcal{Z}_k)_i - \hat{z}_k^-][(\mathcal{Z}_k)_i - \hat{z}_k^-]^T + R_k$$

where $\hat{x}^-$ denotes a-priori estimate of x. $\gamma = \sqrt{(L + \lambda)}$, and $\lambda = \alpha^2(L + \delta) - L$ are the composite scaling parameters. α is a scaling parameter that determines the spread of the sigma points around $\hat{x}$, and is usually set to a small positive value (e.g. $1e - 4 \leq \alpha \leq 1$). δ is a secondary scaling parameter which is usually set to 0 or $3 - L$ [39]. Q_k is the process error covariance matrix and R_k is the measurement noise

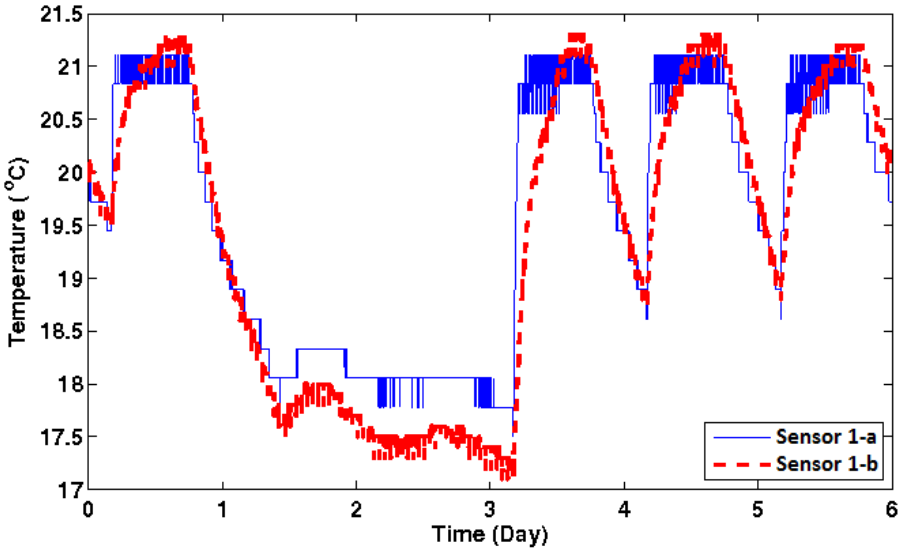

Figure 3.3: Data logger and BMS sensor temperature readings

covariance matrix. $W_i^{(m)}$ and $W_i^{(c)}$ weights are defined by:

$$W_i^{(m)} = \begin{cases} \frac{\lambda}{(L+\lambda)}, & \text{if } i = 0 \\ \frac{1}{2(L+\lambda)}, & \text{if } i = 1, 2, ..., 2L \end{cases} \tag{3.37}$$

and

$$W_i^{(c)} = \begin{cases} \frac{\lambda}{L+\lambda} + (1 - \alpha^2 + \beta), & \text{if } i = 0 \\ \frac{1}{2(L+\lambda)}, & \text{if } i = 1, 2, ..., 2L \end{cases} \tag{3.38}$$

where β is a parameter used to incorporate the prior knowledge of the distribution of x. We use $\beta = 2$ which is optimal for Gaussian distributions [82].

3.4 Test-Bed and Historical Data

The model studied in this paper is a model for an office with a simple structure in the Lakeshore building at Michigan Technological University. This room is surrounded by two rooms and a corridor in the building and connected to the outdoor area with a thick concrete wall and two south-oriented double-layered windows. Each room is equipped with temperature and humidity sensors (Uni-curve Type II) with the temperature accuracy of ± 0.2°C. We have installed a temperature data logger with accuracy of ± 0.8°C inside the main room to estimate measurement errors. Temperature readings from these two sensors are shown in Figure 3.3. We follow the

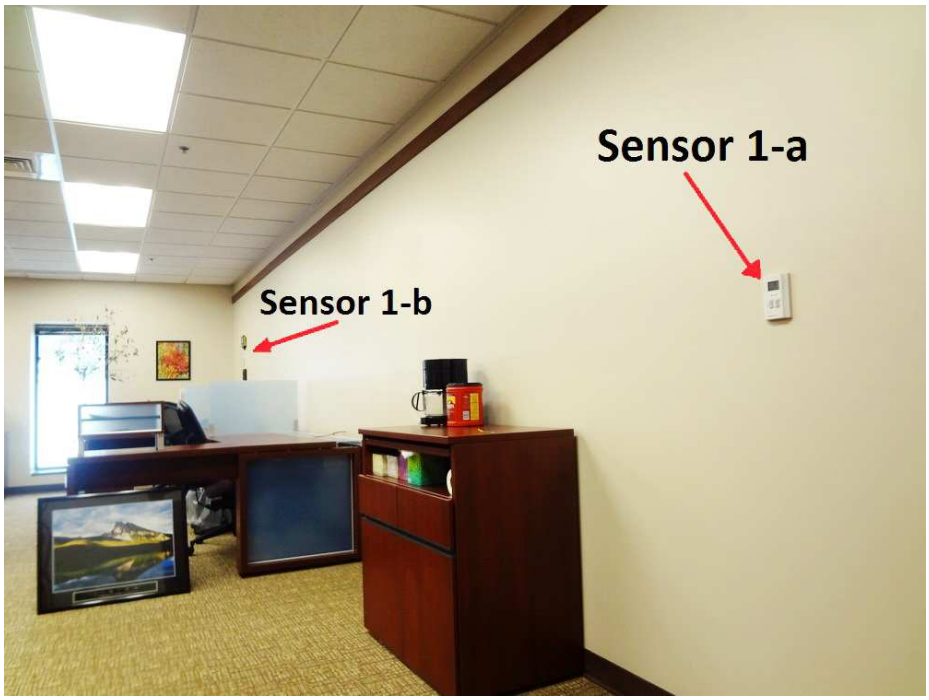

Figure 3.4: Location of the temperature sensors in the test-bed

methodology proposed in [61] to find the temperature measurement accuracy, which is obtained to be $\pm 0.82°C$, and is used in the EKF and UKF algorithms. There are also some other sensors throughout the university to measure and record the outdoor temperature. All the sensors' measurements for the building network are available through the Building Management System (BMS).

The HVAC system in the building uses Water-Source Heat-Pumps (WSHP) to maintain required energy for heating purposes. Each unit in this system provides heating for an individual zone. Therefore, a unit operates when heating is required for its zone and the set point can be defined independently based on the functionality of each zone. The HVAC system uses an on-off controller to provide a desired temperature for each zone. When the temperature goes below a set point by $0.28°C$ ($0.5\ °F$), the heating system is switched on until it reaches the adjusted set point. To maintain standard internal air quality (IAQ) for each zone, a supply fan with a constant mass flow rate of 0.52 (kg/ s) works between 4AM to 6 PM (except for holidays). Zone temperatures are measured with a sampling period of 60 seconds.

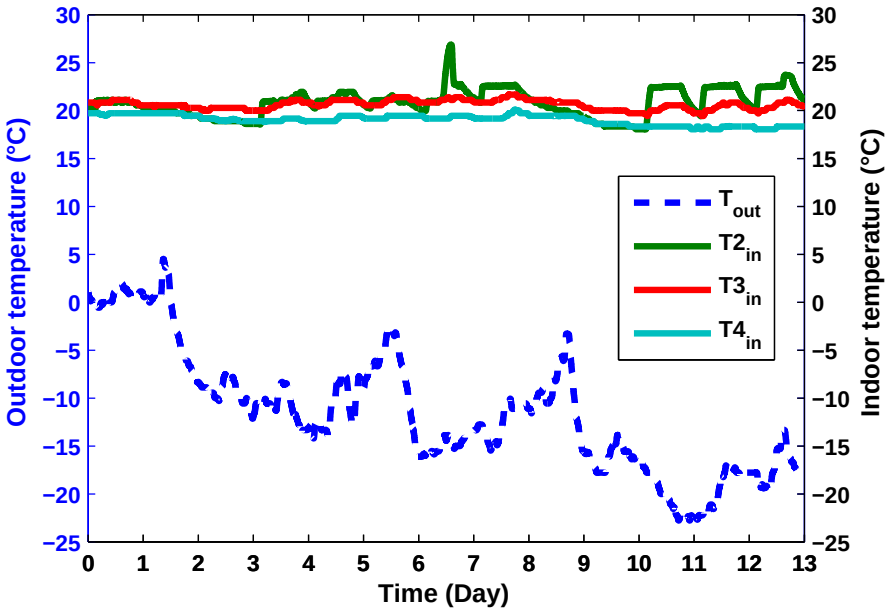

Figure 3.5: Disturbances to the PAB model.

3.5 Simulation Results

The test-bed from previous section was used to collect measurements from January 11 to January 24, 2013. To remove noise from the temperature measurements, a second order Butterworth lowpass filter with cutoff frequency of 0.001 Hz was used.

We implement both the EKF and the UKF and present the results of the simulations. Figure 7.6 shows the temperatures of the neighboring zones and the outside temperature which act as disturbance to the model. Figure 3.6 depicts the model inputs including the air mass flow rate and the supply air temperature. In order to obtain the best initial parameter values for the Kalman filter algorithms, we first perform a (static) parameter identification on the historical data. We consider the first part of the data as *training data set* (shown in red in Figure 3.7), and obtain the best parameters that minimize the error between the simulation and the measurement in least square sense. The result of this step is used to simulate the temperature evolution of the room air for the next three days (shown in black in Figure 3.7). Due to time-varying parameters and disturbance to the model, it is difficult to find a set of parameters for the model which results in good temperature tracking for all days, and hence, as shown in Figure 3.7, the results of simulations for the following days in the testing data set is even worse.

The obtained initial parameters from the off-line calibration step is used as initial

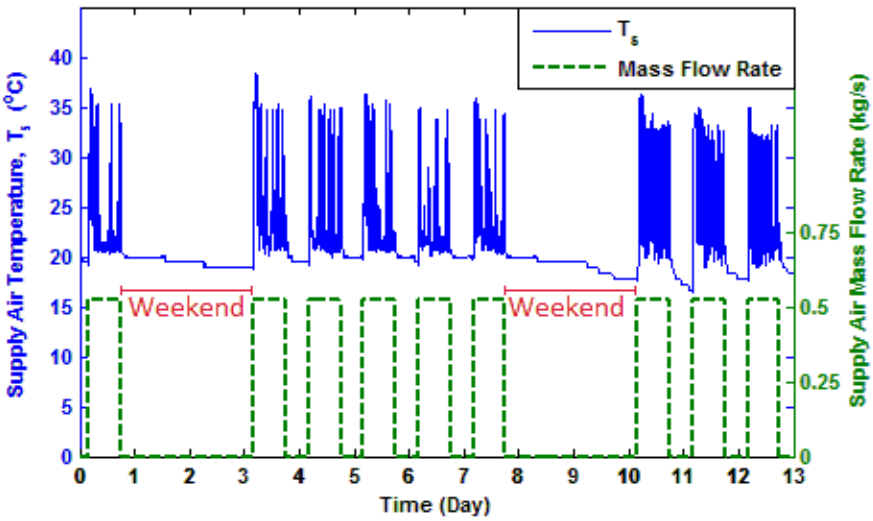

Figure 3.6: Inputs to the PAB model.

point for the EKF and UKF algorithms.

3.5.1 EKF Results

Temperature estimation of room and walls, using EKF are depicted in Figure 3.8 and Figure 3.9. The results show that although the initial parameters from the training data set is not necessarily optimal for future days, the PAB model manages to tune the parameters and leads to very good temperature tracking (Figure 3.8).

Figure 3.10 shows the evolution of parameters over time. In this case, EKF only temporarily changes the value of parameters when necessary, but the steady state values of the parameters are close to the initial values obtained from the one shot parameter identification using historical data.

Note that although the room temperature estimations are close to the actual room temperature, the temperature of walls are not realistic in the EKF case. Hence we also try UKF and report the results in what follows.

3.5.2 UKF Results

We follow the same steps to first acquire the best initial parameters by an off-line optimization and then use the obtained parameters as initial value for UKF. The temperature estimation of room and walls, using UKF are depicted in Figure 3.11 and Figure 3.12. The evolution of parameters over time is shown in Figure 3.13. In

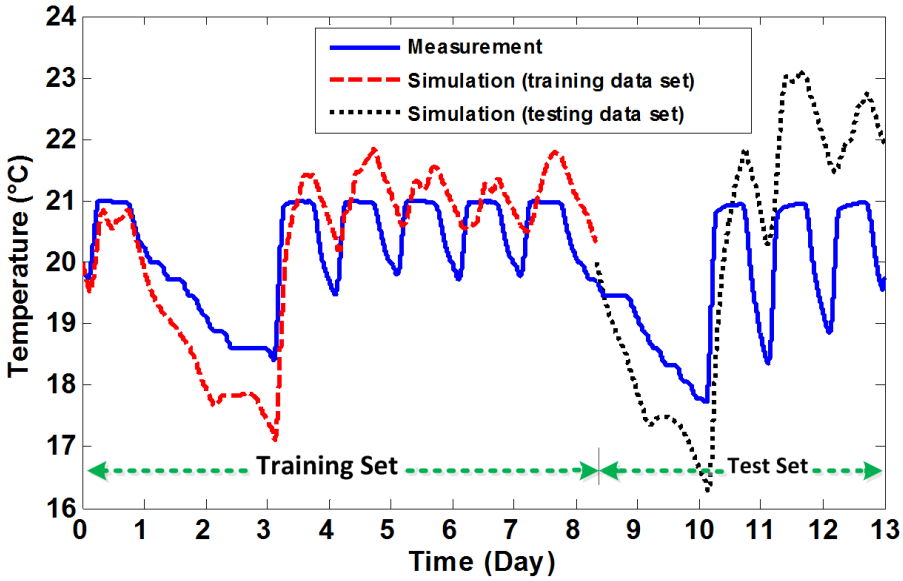

Figure 3.7: The first set of data (shown in red) is the training data. We identify the parameters in a one shot optimization by minimizing the l_2 norm of the error between simulation and measurement data. Then we used the obtained parameters from the training data set to predict the temperature evolution for the next days (shown in black).

this case, contrary to the EKF case, the parameters evolve over time and the steady state values are not necessarily close to the initial points.

Note that the first part of the estimation of wall temperature by UKF leads to overshoot in the wall temperature, however, this overshoot is quickly recovered as UKF uses more data to tune the parameters more accurately. Overall, the UKF outperforms the EKF in providing an accurate PAB mode because: 1) the estimation of room temperature is more accurate. 2) the estimated temperatures of walls are more realistic in the UKF case. High frequency oscillations in the wall temperature estimation of EKF is observed (Figure 3.9), but these fast temperature oscillations of walls are not realistic due to the large heat capacitance of the walls. The dynamics of wall temperatures determined by the UKF algorithm seem intuitive and correct, given the slower dynamics *i.e.* small frequency oscillations.

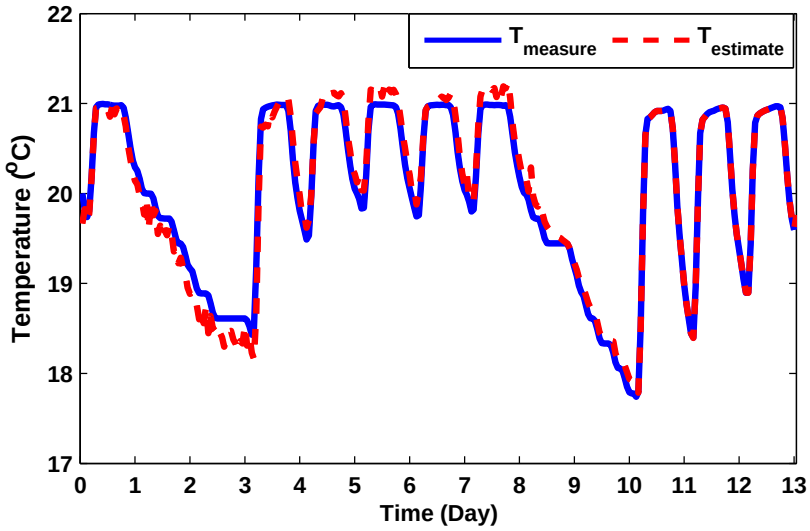

Figure 3.8: Estimated and measured room temperature using EKF.

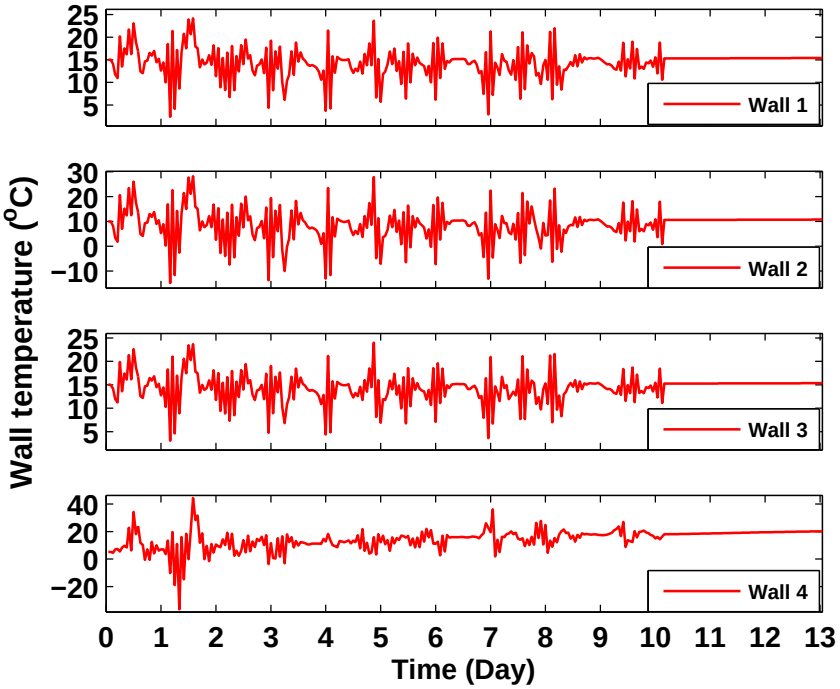

Figure 3.9: Estimated temperature of walls using EKF.

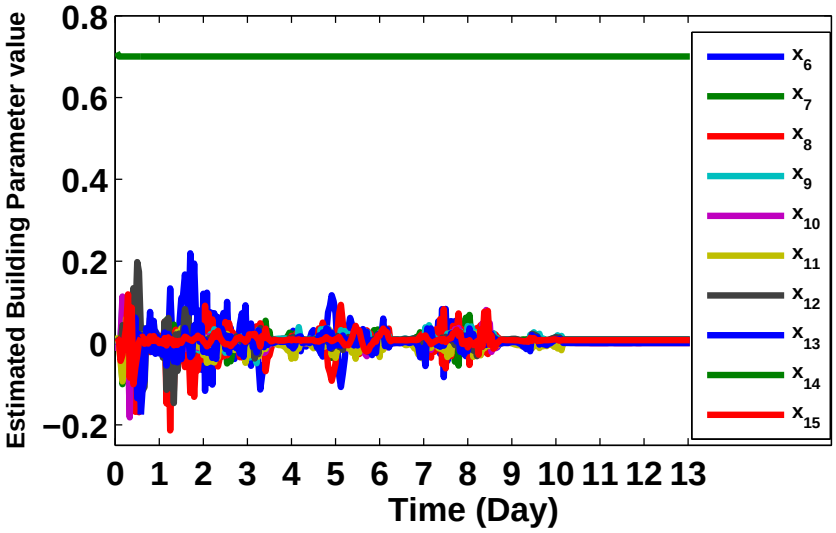

Figure 3.10: Estimated parameters of the system using EKF.

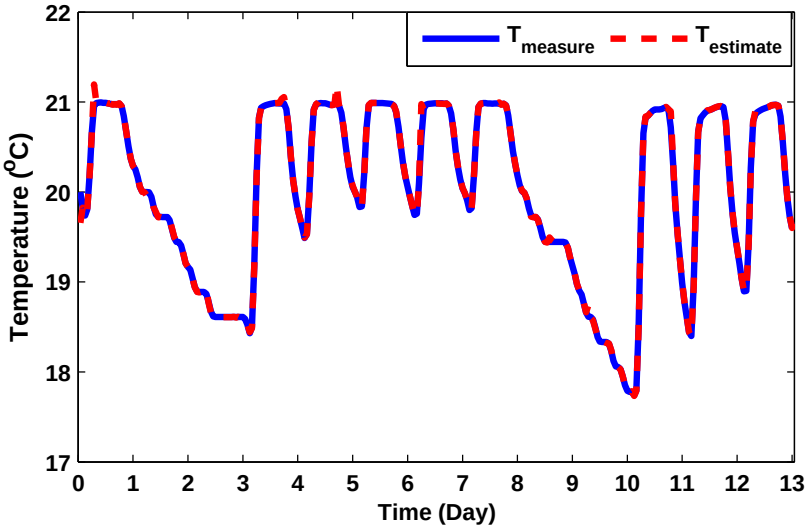

Figure 3.11: Estimated and filtered temperature of room using UKF.

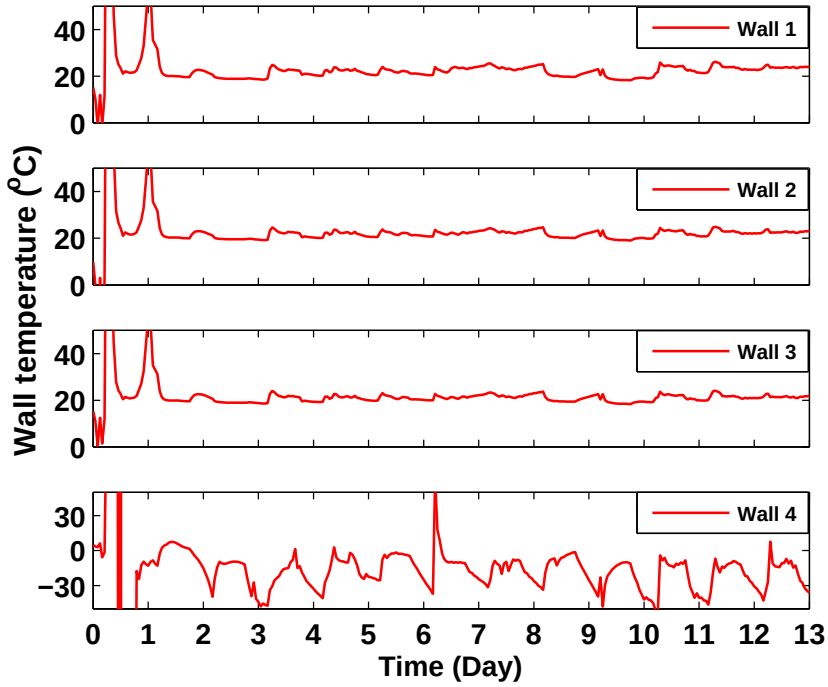

Figure 3.12: Estimated temperature of walls using UKF. We have zoomed the figures to focus on the more steady estimates of the walls rather than the first part transient behavior.

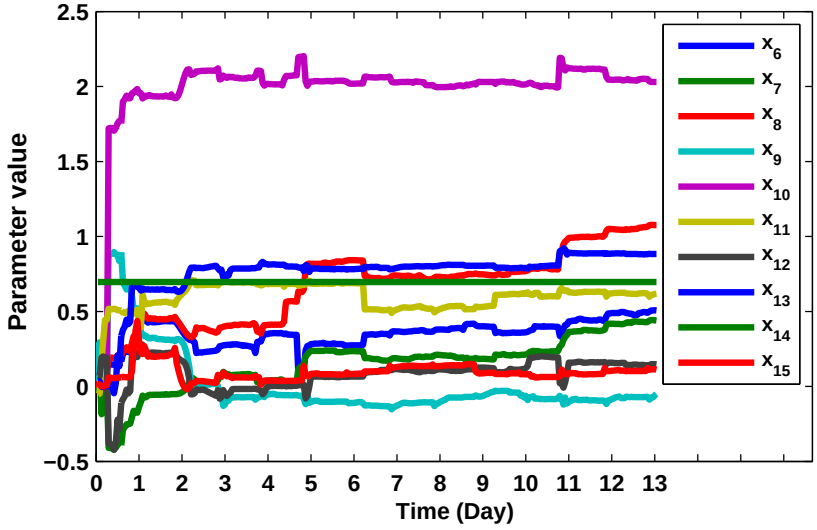

Figure 3.13: Estimated parameters of the system using UKF.

Chapter 4

Control Design

In this chapter different control strategies are presented. Each control algorithm has its own advantages and disadvantages and fits a particular set of application and implementation. The material of this chapter is extracted from [55, 54, 56]. In next chapter we present a co-design algorithm concerning control design with other subsystem design considerations such as various embedded platform, sensing system, communication network, etc.

In order to investigate how new control techniques can help improve energy efficiency of large buildings, a scalable thermal model for rooms and buildings was developed in Section 2 and 3. Scalability is important when analyzing the heat transfer behavior of large buildings. Thus we tried to keep the state space model representation of the system as general and standard as possible so that for example a model for a 3-room building can be easily extended to a model for a 30-room building. In this section, we introduce the classical controllers for HVAC systems and also the modern optimal controllers.

Although the model derived in the previous section is in continuous domain, here we discuss the control problem in the discrete domain. Usually when the plant model is in continuous domain, there are two possible approaches to design and implement the controller. The first approach is to use a continuous plant model and design a continuous controller but implement it digitally. The second approach is when we use a discretized plant model and design a discrete controller and implement it digitally. Each method has its own advantages and disadvantages, which depends on the time constants and the sampling time. Here, we have chosen to use the second method, i.e. discretizing the plant model and designing a discrete controller, and then implement it digitally.

4.1 Classical HVAC Control Techniques

Classical controllers for HVAC systems include on-off controller and Proportional-Integrator-Derivative (PID) controllers. These controllers have a simple structure and low initial cost. However in long term these controllers are expensive due to their low energy efficiency [17]. On-off controllers work either in the "on" or "off" state providing only two outputs, maximum (on) and zero (off). The limited functionality of on-off controller makes it inaccurate and not of high quality. PID controllers which have advantages such as disturbance rejection and zero steady state offset have been commonly used in many HVAC applications. The main drawback of classical air conditioning control systems is that most HVAC systems are set to operate at design thermal loads [17], while actual thermal loads are time varying and depend on the environmental factors like outside weather conditions, and the number of people in the building.

4.2 Hierarchical Control

In any control algorithm for HVAC systems, sensing and actuation are managed locally at the room-level. To achieve building-level energy-optimality, the rooms cannot act autonomously. To minimize building-level energy consumption, the actions relatives to the rooms must be coordinated. We introduce two levels of control over the system, consisting of PID as lower-level and an LQR as higher-level controller. Typically the controllers used for HVAC systems are PID controllers. Lower-level (PID) control governs sensing and actuation within a single room. The higher-level control is supposed to determine the optimal input to the system so that the cost function which is a combination of deviation from set point temperature set by the user and the control effort can achieve its minimum possible value. By applying the optimal input, cooling/heating air flow to the rooms, we still remain in the comfort zone defined according to the psychrometrics charts.

The difference of the proposed control algorithm in this chapter with the classical control techniques is that the desired temperature for every thermal zone is not directly fed into a local controller but into a higher level controller that has a global view of the current and desired state. The higher level controller determines the appropriate set points for the lower-level controllers of each room in a building. Higher-level and lower-level controllers can be referred to as room-level and building-level controllers, respectively.

4.2.1 Room-Level PID control

As mentioned above, the lower-level control is accomplished using a PID controller. A typical PID controller is shown in Figure 4.1. The dynamic of the room is described by Equation (2.56), in which x represents the states and u represents the inputs, which are the temperatures of the walls and rooms and the air flow mass into the rooms, respectively. Instead of allowing the set point to be controlled by a thermostat, the user setpoint and state of the room are sent to the higher level controller i.e. a linear-quadratic regulator which optimally calculates the set point for the lower-level controller and sends it back to the lower level PIDs. Therefore all the rooms are controlled locally by PID controllers which track the set point given by the higher-level controller. The task of the controller is to feed the optimal set point to the PID controllers.

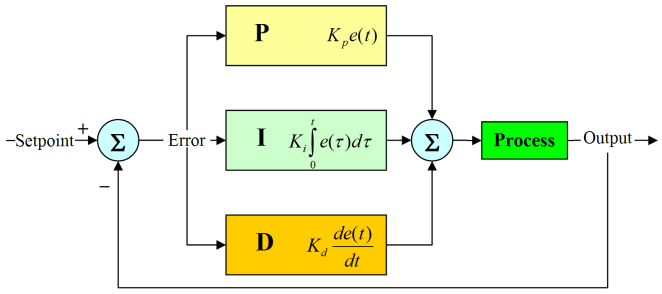

Figure 4.1: Typical PID controller block diagram.

4.2.2 Building-Level Optimal Control

In optimal control, one attempts to use a controller that provides the best possible performance with respect to some given measure of performance. For instance, we find the controller that uses the least amount of control-signal effort to take the output to zero. In this case the measure of performance (also called the optimality criterion) is the control-signal effort.

In general, optimality with respect to some criterion is not the only desirable property for a controller. One would also like stability of the closed-loop system, good gain and phase margins, robustness with respect to unmodelled dynamics, etc.

In this section we review the concept of Linear Quadratic Regulator (LQR) controllers that are optimal with respect to energy-like criteria. These are particularly interesting because the minimization procedure automatically produces controllers that are stable and somewhat robust. In fact, the controllers obtained with this procedure are generally so good that we often use them even when we do not necessarily

care about optimizing for energy. Moreover, this procedure is applicable to multiple-input/multiple-output (MIMO) processes for which classical designs are difficult to apply. All mentioned above are the reasons why we are using LQR as the higher level controller. We should also say that this higher level control can be implemented using other control techniques such as *model predictive control (MPC)* which we will cover in Section 4.4.

4.3 LQR Controller

LQR is appropriate for finding the optimal control input of a linear system according to a quadratic cost function to be minimized. The cost function is a quadratic function of states and inputs. The states and the inputs are assigned weight matrices called Q and R, respectively. Varying the weights associated with the cost function will cause the LQR to compute a new optimum input. Because LQR solves for the cost-optimal control, it should compare favorably against other possible high-level control schemes. The evolution of the state of the building is linearly determined by the current building state and the specified control law u as shown in Equation (2.56). The quadratic cost function for LQR is described by the following equations.

The state space representation of a discrete time LTI system is given as

$$x(k+1) = Ax(k) + Bu(k) \tag{4.1}$$

where $x \in \mathbb{R}^n$ and $u(k) \in \mathbb{R}^m$.

The optimal control that minimizes the finite horizon cost functional

$$J[x(0)] = \frac{1}{2}x^T(N)Sx(N) + \frac{1}{2}\sum_{k=0}^{N-1}\left\{x^T(k)C^TCx(k) + u^T(k)Ru(k)\right\}, \tag{4.2}$$

where $S = S^T \succeq 0$, $R = R^T \succ 0$ and $C^TC = Q \succeq 0$, is given by

$$u^o(k) = -K(k+1)x(k) \tag{4.3}$$

and the time varying gain matrix $K(k)$ is computed recursively (backwards) by the following Joseph Stabilized *Riccati* equation

$$K(k) = \left[R + B^TP(k)B\right]^{-1}B^TP(k)A \tag{4.4}$$

$$P(k-1) = C^TC + K^T(k)RK(k) + (A - BK(k))^TP(k)(A - BK(k)) \tag{4.5}$$

with boundary condition $P(N) = S$.

The necessary and sufficient condition for the existence of a steady state solution to the infinite horizon Riccati equation is that the pair $[A, B]$ be stabilizable. Then, as $N \to \infty$, for $P(N) = S = 0$, the Riccati equation converges to a bounded steady state solution P.

Other than the existence of a steady state solution to the infinite horizon Riccati equation we are also interested to know whether the solution to the Riccati equation is unique. The necessary and sufficient condition for the existence of a unique positive definite steady state solution to the infinite horizon Riccati equation and a stabilizing optimal control law is that the pair $[A, C]$ be detectable and the pair $[A, B]$ be stabilizable [16]. Here we check the stabilizability and detectability of the pairs $[A, B]$ and $[A, C]$(respectively), of the linearized system in its equilibrium point.

4.3.1 Controllability and Observability

The controllability check shows that the system is not fully controllable (i.e. the controllability matrix is not full rank), but if we analyze the stability of the uncontrollable modes, we find that all the uncontrollable modes are stable, hence the system is stabilizable. Similarly, the observability check shows that the system is not fully observable, but the stability analysis of the unobservable modes, shows that the unobservable modes are stable, hence the system is detectable.

4.3.2 Optimal Tracking Problem

To implement the LQR controller on our plant, we need to modify the controller so that it can track a desired set point. The general form of LQR is designed to take the states of the system to zero. However we need the output of the system (i.e. the temperature of the rooms) to track the desired temperature trajectories that are set by the occupants. So we need to manipulate the general LQR formulation so that it can take the output of the plant to the desired output. Here we derive the *Optimal Tracking Problem* using LQR technique. The LQ tracking problem is formulated as follows:

$$\min_{U_0}\{J\} \tag{4.6}$$

where

$$\begin{aligned} J := & \frac{1}{2}\left[y_d(N) - y(N)\right]^T S\left[y_d(N) - y(N)\right] \\ & + \frac{1}{2}\sum_{k=0}^{N-1}\left([y_d(k) - y(k)]^T Q[y_d(k) - y(k)] + u(k)^T R u(k)\right) \end{aligned} \tag{4.7}$$

subject to

$$x(k+1) = Ax(k) + Bu(k) \tag{4.8}$$

$$y(k) = cx(k) \tag{4.9}$$

$$x(0) = x_0 \tag{4.10}$$

with $y_d(k)$ specified for all k and

$$U_k := [u(k) \quad u(k+1) \quad \cdots \quad u(N-1)] \tag{4.11}$$

Define:

$$\begin{aligned} J_k = & \frac{1}{2}\left[y_d(N) - y(N)\right]^T S\left[y_d(N) - y(N)\right] \\ & + \frac{1}{2}\sum_{i=k}^{N-1}\{[y_d(i) - y(i)]^T Q[y_d(i) - y(i)] + u(i)^T R u(i)\} \end{aligned} \tag{4.12}$$

Using *Bellman's principle of optimality*, we can obtain a recursive relation between $J_k^o(x(k))$, i.e. the optimal cost to go from $x(k)$ to $x(N)$, and $J_{k+1}^o(x(k+1))$ as:

$$J_k^o(x(k)) = \min_{u(k)}\left\{\frac{1}{2}\left([y_d(k) - y(k)]^T Q[y_d(k) - y(k)] + u(k)^T R u(k) + J_{k+1}^o(x(k+1))\right)\right\}$$

Note that

$$\begin{aligned} J_N^o[x(N)] &= \frac{1}{2}[y_d(N) - y(N)]^T S[y_d() - y(N)] \\ &= \frac{1}{2}x^T(N)C^T SCx(N) - x^T(N)C^T S y_d(N) + \frac{1}{2}y_d(N) S y_d(N) \end{aligned} \tag{4.13}$$

defining

$$P(N) = C^T SC \tag{4.14}$$
$$b(N) = -C^T Sy^d(N) \tag{4.15}$$
$$c(N) = \frac{1}{2} y_d^T(N) S y_d^T(N) \tag{4.16}$$

gives

$$J_N^o[x(N)] = \frac{1}{2} x^T(N) P(N) x(N) + x^T(N) b(N) c(N) \tag{4.17}$$

Using Bellman's principle of optimality we can obtain a recursive relation between $J_{k-1}^o[x(k-1)]$, which is the optimal cost to go from $x(k-1)$ to $x(N)$, and $J_k^o[x(k)]$:

$$\begin{aligned} J_{k-1}^o[x(k-1)] = \min_{u(k)} \Big\{ & \frac{1}{2}[y_d(k-1) - y(k-1)]^T Q[y_d(k-1) - y(k-1)] \\ & + u(k-1)^T R u(k-1) + J_k^o(x(k)) \Big\} \end{aligned} \tag{4.18}$$

rearranging $J_{k-1}^o[x(k-1)]$ we have

$$\begin{aligned} J_{k-1}^o[x(k-1)] = \min_{u(k)} \Big\{ & \frac{1}{2} x^T(k-1)[C^T Q C + A^T P(K) A] x(k-1) \\ & + x^T(k-1)[A^T b(k) - C^T Q y_d(k-1)] \\ & + \frac{1}{2} u^T(k-1)[R + B^T P(k) B] u(k-1) \\ & + u^T(k-1) B^T [P(k) A x(k-1) + b(k)] \\ & + \frac{1}{2} y_d^T(k-1) Q y_d(k-1) + c(k) \Big\} \end{aligned} \tag{4.19}$$

Taking the derivative of the terms in the curly braces with respect to $u(k-1)$ and setting it equal to 0 gives

$$u^o(k-1) = -[R + B^T P(k) B]^{-1} B^T [P(k) A x(k-1) + b(k)] \tag{4.20}$$

by plugging the optimal value of $u(k-1)$, i.e. $u^o(k-1)$ into the equation for $J_{k-1}^o[x(k-1)]$ which is given above, and defining the following values for $P(k-1)$, $b(k-1)$ and $c(k-1)$ we have:

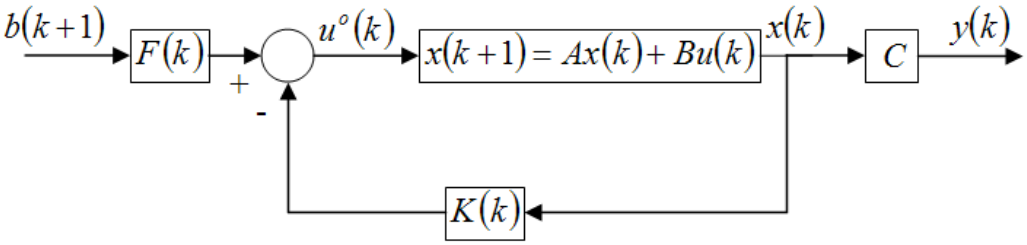

Figure 4.2: Block Diagram for the derived Optimal Control

$$P(k-1) = C^T QC + A^T P(k)A - A^T P(k)B[R + B^T P(k)B]^{-1} B^T P(k)A \quad (4.21)$$

$$b(k-1) = A^T b(k) - C^T Q y_d(k-1) - A^T P(k)B[R + B^T P(k)B]^{-1} B^T b(k) \quad (4.22)$$

$$c(k-1) = \frac{1}{2} y_d^T(k-1) Q y_d(k-1) + c(k) - \frac{1}{2} b^T(k)B[R + B^T P(k)B]^{-1} B^T b(k) \quad (4.23)$$

which results in the following expression for $J^o_{k-1}[x(k-1)]$:

$$J^o_{k-1}[x(k-1)] = \frac{1}{2} x^T(k-1)P(k-1)x(k-1) + x^T(k-1)b(k-1) + c(k-1) \quad (4.24)$$

thus, the optimal control law is given by the following equation

$$u^o(k) = F(k)b(k+1) - K(k)x(k) \quad (4.25)$$

where

$$K(k) = [R + B^T P(k+1)B]^{-1} B^T P(k+1)A \quad (4.26)$$

$$F(k) = -[R + B^T P(k+1)B]^{-1} B^T \quad (4.27)$$

$K(k)$ can be regarded as the feedback gain and $F(k)$ is the feed forward gain [16]. Figure 4.2 shows the block diagram of the system.

4.3.3 Control Algorithm Implementation

Here we will discuss more in detail the structure of the proposed control algorithm, and the implementation of the algorithm on the model. In summary, we have introduced a hierarchical control that consists of two layers of controllers. For the lower

level (room-level) we use PID controllers and for the higher level (building-level), LQR controller is used. The set point temperature for each room which is specified by the occupants are given to the Higher Level Controller (LQR). The LQR also needs the current temperature of the rooms. These temperatures are sensed by the temperature sensors which are mounted in specific locations in the building and are fed back to the LQR. The computations are done in the higher level controller (LQR) in order to calculate the optimal input. The optimal tracking problem is solved using a *Dynamic Programming* approach which requires the set point to be known (i.e. the temperature trajectory over time must be known ahead of time for the course of a day or any period in which the quadratic cost function is supposed to be minimized). The input to the model is in fact the air mass flow that should enter each room through the ducts. These inputs are given to the lower level PIDs as the set points for air mass flow in each local lower-level controller. The output of the PID which is a controlling signal is given to the fans to adjust the angle of each damper in order to control the amount of air which is blown into the room. Thus the output of the fan which is optimal air mass flow is given to the plant (room). The control is now closed by sensing the current temperature of the room and feeding it back to the higher level controller (LQR). The schematic representation of the hierarchical control discussed above in shown is Figure 4.3.

Modeling of the heat transfer system based on the equations derived in Section 2.3 and also the implementation of the control algorithm are done in Simulink. A library was also developed for future use which has some elements like the model of a wall and a room, which can be combined to make an arbitrary building. In Figure 4.4 we show the interconnection of two layers of controllers which was described above.

As we show in Figure 4.4 the system dynamics is solved in the left box labeled as "Three Room Plant Model" with the inputs of the block being the mass air flow inputs from the PIDs. This block simulates the dynamic behavior of the model and solves for the temperatures of the rooms. These temperatures are fed to the block in the middle labeled "LQR". In this block the optimal tracking problem is solved with Q and R matrices, as the weights for the output and the input terms defined in the quadratic cost function which is defined in the "LQR" block. The solution of the optimal tracking problem is the optimal input which is fed to the lower level PID controllers. The dynamics of the fan is considered in the block between the PID controllers and the Plant. The optimal input is fed to the PID controllers and the major task of the PID is to track this reference signal. The output of the PID is the controlling signal which is given to the fans to produce the required amount of air mass flow into the rooms. So, the loop is closed by feeding the input to the plant model. A detailed view of what takes place in the Plant block and the LQR block is shown in Figure 4.5.

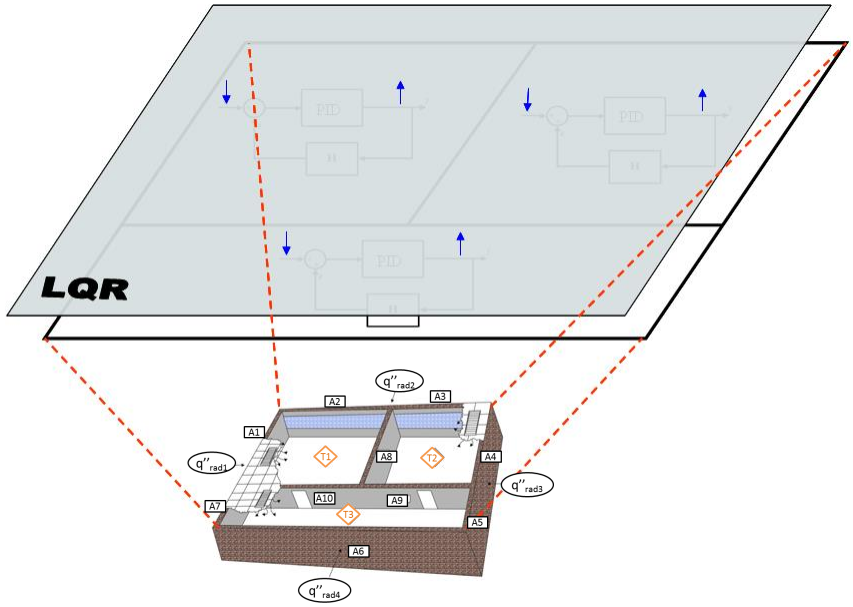

Figure 4.3: Hierarchical Control Algorithm including lower level PIDs and higher level LQR

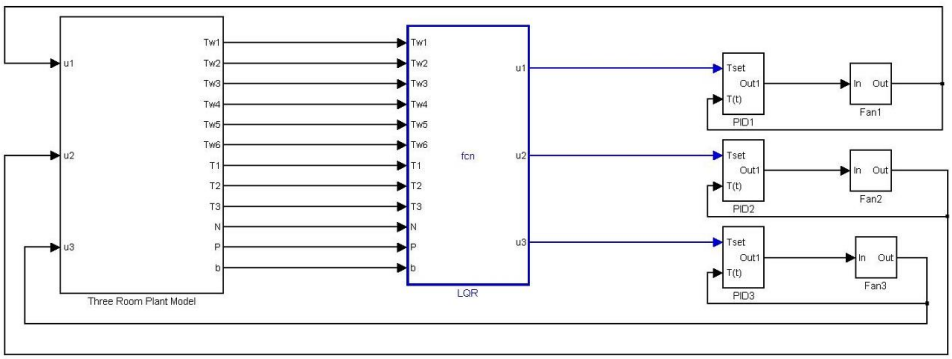

Figure 4.4: Interconnection of the Plant model, the lower level, and higher level controllers

4.3.4 Simulation Results

Having the model of the building ready in Simulink, we implement different controller strategies on the plant and compare the responses of the system, the comfort level of the occupants, and also the energy usage in each case. The final goal of the control design is to design the best controller which is able to keep the temperature

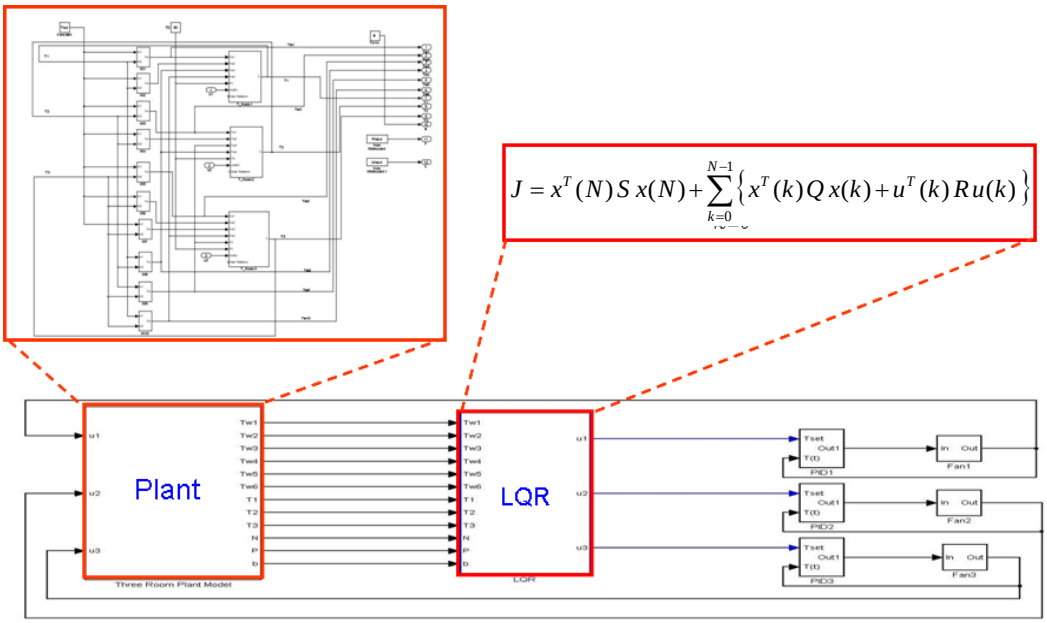

Figure 4.5: A detailed view of the inside of Plant and LQR blocks

of the rooms as close to the set point temperature for each room as possible while consuming the least amount of energy. The set point temperatures are set by the building occupants.

We define the concept of *comfort level* to be the closeness of the current temperature of the room to the temperature which is set for each room by the occupants. When the gap between the set point temperature for each room and the current temperature of that room is small we say the comfort level is higher than when this gap is larger.

The other factor that we consider to evaluate the performance of a controller, is *energy usage*. We want to have a specified level of comfort by using the least amount of energy possible. It is obvious that if we use more energy we can raise the level of comfort by more closely tracking the set point temperature of each room.

In order to make a balance between the two mentioned factors i.e. comfort level and energy usage, we have two *tuning parameters*. The Q and R matrices are the two parameters by which we can tune the performance of the LQR controller. Q is the weight matrix for the outputs and R is the weight matrix for the inputs in the cost

function. It means that if we want to put more constraint (tighten the constraint) on the output in the sense that the output tracks the desired output more closely, we can do it by increasing matrix Q, and if we want to loosen the constraint on the output, we can do it by decreasing matrix Q. The good point about this method is that different outputs are independent and we can at the same time tighten the constraint on one output and loosen the constraint on the other. Similarly, we can manipulate matrix R in order to tune the performance of the LQR controller. This can be done by increasing and decreasing matrix R when we want to tighten or loosen the constraints on the input, respectively. Note that loosening the constraint on the input gives the input more freedom to increase, and accordingly the desired output can be tracked more closely and vice versa.

The way take advantage of this property of the LQR controller, is that we can play with these two parameters to tune the controller. For example, when we know that there is going to be a conference in one room of a large building, and a crowd of people will be present in the room in a few hours, we can decrease the corresponding entry of that room in matrix R. Another example would be the case when it is very important for us that the temperature of one specific room be very close to the set point value for the temperature in that room. In this case we can increase the corresponding entry of that room in matrix Q. The other example which is very common is when a room is going to be unoccupied for a known period of time. In that case we set the corresponding entry of that room in matrix Q equal to "zero".

Results

Simulations were done for two different cases. In the first case we only simulated the local PID controllers. The temperature of the room is sensed and fed back to the PID controller. The PID controller just tries to track the given set point without having any idea of what the temperature trajectory is going to be like in the future. Thus in this model the input is given to the plant without any optimization process done in order to take into account the level of comfort for the occupants and also the energy which is used to reach the set points. Obviously the level of energy consumption will be higher than the case where the inputs are calculated in an optimal fashion.

In the second case we have applied both the PID controller and the LQR controller to optimally track the set point temperatures of the rooms. As discussed earlier in this case, the optimal tracking problem is solved backwards in time using dynamic programming. In this case we have two tuning parameters which can be varied to tune the performance of the controller in different situations.

For the following simulation results we have assumed the setpoint trajectory which is shown in Figure 4.6. The initial temperature of the walls and the air in the rooms and also the outside temperature are assumed to be $16(^oC)$ in the following simulation

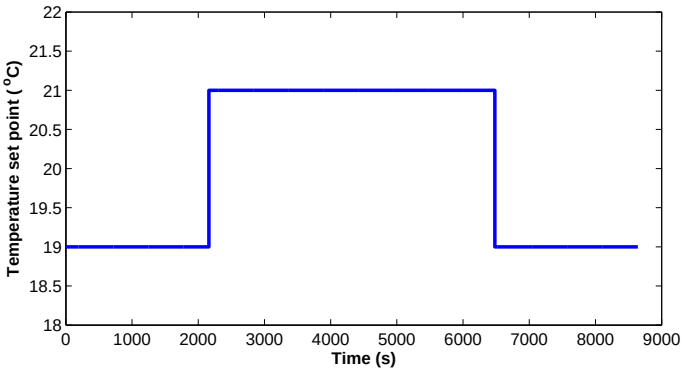

Figure 4.6: Temperature setpoint for the rooms

results.

Case 1

In this case we have set the following values for R and Q matrices:

$$R = \begin{pmatrix} 1 & 0 & 0 \\ 0 & 1 & 0 \\ 0 & 0 & 1 \end{pmatrix} \qquad Q = \begin{pmatrix} 1 & 0 & 0 \\ 0 & 1 & 0 \\ 0 & 0 & 1 \end{pmatrix}$$

We capture with these matrices the notion that we have no preference to either put more constraint on the output or on the input. The plots for the comfort and the energy usage comparing two different cases, one with only PID controller and the other with both PID and LQR is shown in Figure 4.7 and 4.8, respectively.

Case 2

In this case we have set the following values for R and Q matrices:

$$R = 0.01 \times \begin{pmatrix} 1 & 0 & 0 \\ 0 & 1 & 0 \\ 0 & 0 & 1 \end{pmatrix} \qquad Q = 1000 \times \begin{pmatrix} 1 & 0 & 0 \\ 0 & 1 & 0 \\ 0 & 0 & 1 \end{pmatrix}$$

In this case we have set more constraint on the output in order to have an output which is closer to the desired output, and also we have loosened the constraint on the input, meaning that we are allowing more control effort. The plots for the comfort and the energy usage comparing two different cases, one with only PID controller and the other with both PID and LQR is shown in Figure 4.9 and 4.10, respectively.

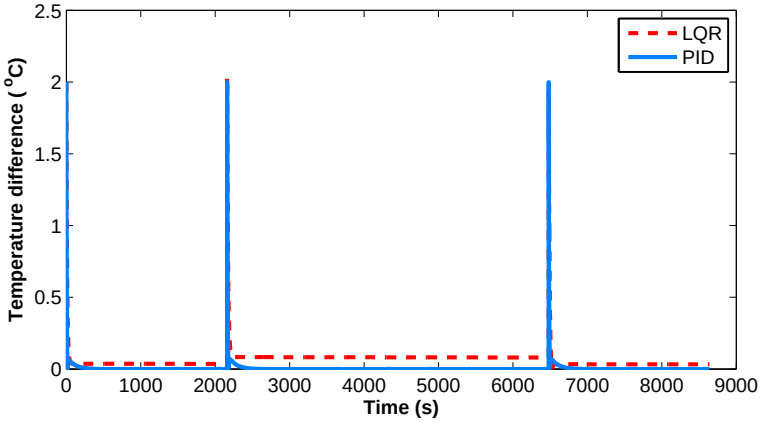

Figure 4.7: Comfort Plot for case 1

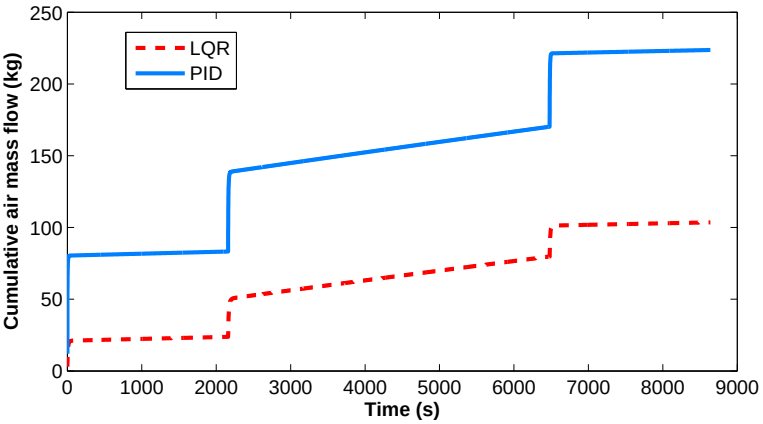

Figure 4.8: Energy Plot for case 1

Case 3

In this case we have set the same values for R and Q matrices as case 2, but we have rooms three times larger than the rooms in case 2. Larger rooms mean more energy consumption to take the temperature of the rooms to the set values. The plots for the comfort and the energy usage comparing two different cases, one with only PID controller and the other with both PID and LQR is shown in Figure 4.11 and 4.12, respectively.

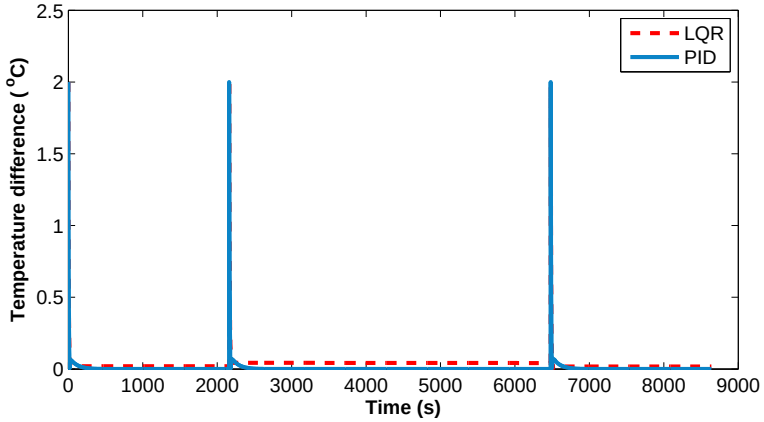

Figure 4.9: Comfort Plot for case 2

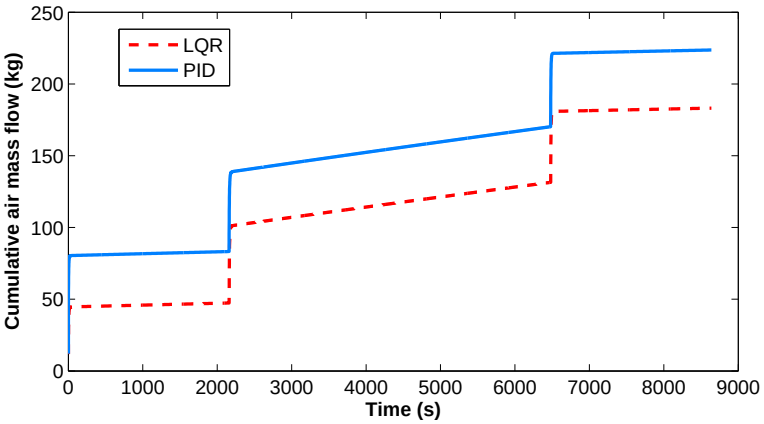

Figure 4.10: Energy Plot for case 2

4.3.5 Verification

In this section we are using Simscape from Mathworks^{TM} and the network node model approximation to model walls, rooms and buildings. The system allows a greater number of rooms or walls to be modeled without significant effort. Additionally, the Simscape model was verified using the analytical partial differential equations. This approach is an alternative to FemLab, Modelica and Matlab. The building model is entirely represented by electric elements using the libraries provided by Simscape. The system could be easier to scale, since there is no need to write analytical expressions.

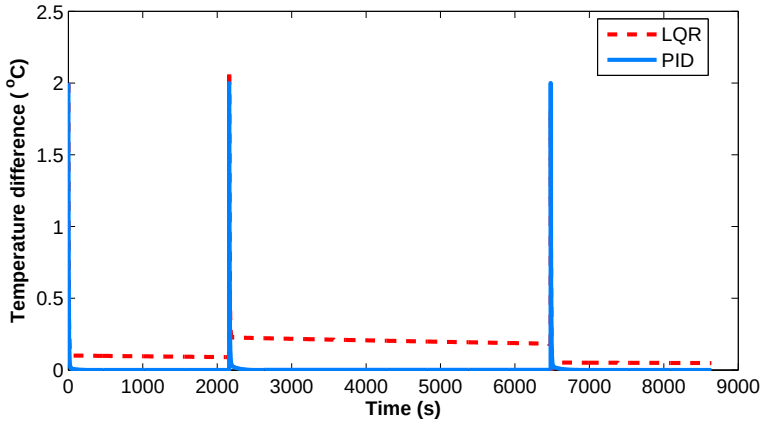

Figure 4.11: Comfort Plot for case 3

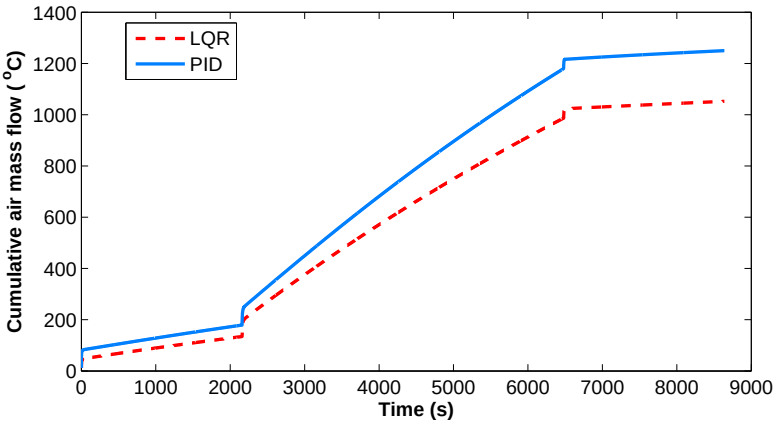

Figure 4.12: Energy Plot for case 3

Simscape

Simscape extends the Simulink with tools for modeling systems spanning mechanical, electrical, hydraulic and other physical domains as physical networks. It provides fundamental building blocks from these domains to let one create models of custom components. Engineers working towards an optimized design must develop their software and physical system together. MathWorks physical modeling tools bring accuracy and efficiency to this effort by enabling the assembly of system-level model that span multiple physical domains and include the control system in single environment, create reusable models of the physical system with physical ports, in addition to input and output signals and model custom physical components (in this case

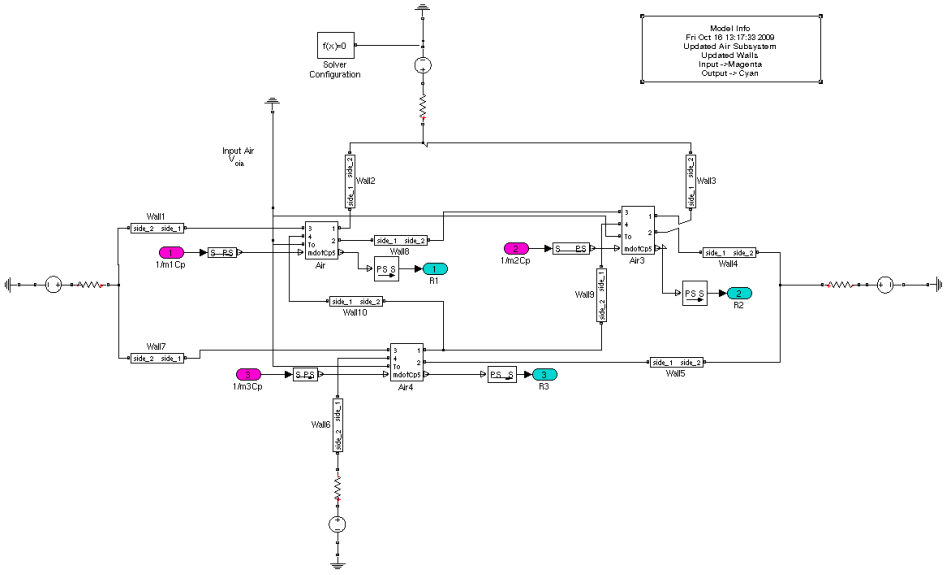

Figure 4.13: Thermal model in Simscape

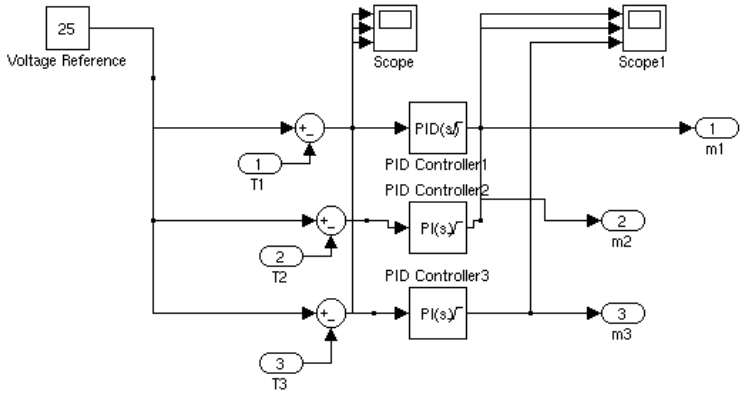

Figure 4.14: Control Implementation

electrical) using MATLAB based physical modeling language.

Figures 4.13 below show the Simscape representation for a building with three rooms.

Additionally, a simple PID controller has been implemented to start investigating control techniques (Figure 4.14). Each layer of the model can be implemented at any level. Figure 4.15 shows the comparison between the Simulink and the PDE model. The input was constant ($\dot{m} = 0$) and the temperature of the input air was $27(^oC)$. The error between the models is in the order of 10^{-9}, which is mainly due to numerical

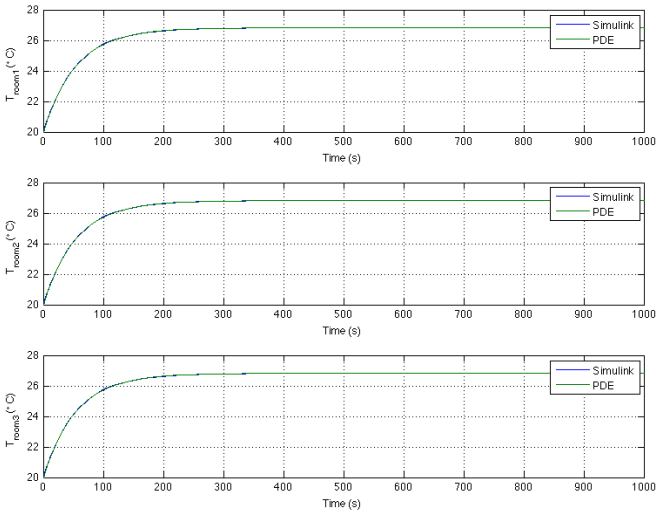

Figure 4.15: Model Comparison with Constant Input

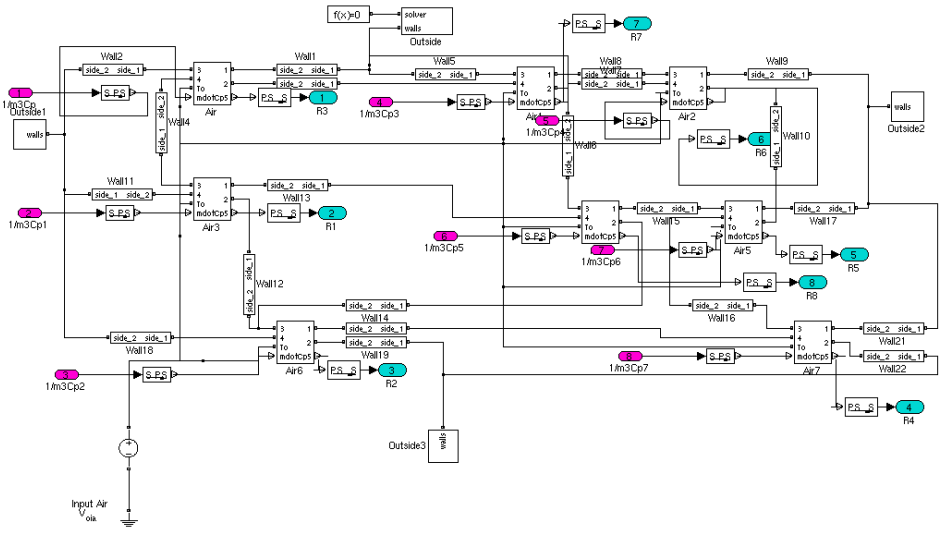

Figure 4.16: 8-Room Model

integration errors. Figure 4.16 shows the scaled eight room model. The model was easily scaled by keeping track of the relation between rooms.

4.4 Model Predictive Control

MPC offers an attractive framework for model-based optimal control of dynamical systems. MPC allows optimizing a cost function subject to state and input constraints. In the context of optimal control of building, we are interested in optimizing the cost function being the energy consumption or cost of energy and constraints are imposed on states such as room temperature, and on inputs such as air mass flow and operational limitations of HVAC components.

In this section we present an MPC problem tailored towards the model developed in Chapter 2 of the test bed in our study. We then compare the performance of the proposed controller with Rule-Based Control (RBC), and the existing controller of the test bed.

4.4.1 Controller Design

We presented the results of an optimal controller for the tracking case and compared the results with a PID controller in [53]. The introduced tracking LQR in [53] fits best to cases where a tight temperature tracking is required, e.g. data centers. However, the wider acceptable range of temperature for commercial buildings, especially during unoccupied hours, allows for more relaxed temperature boundaries. Accordingly, we have introduced new controllers to make the best use of this flexibility and achieve more savings. We study the performance of two different controllers on the temperature regulation problem. Here we have implemented two different controllers on the system and compared their performance with the original controller on the existing building. The way the original controller works is that the controller opens the valves of conditioned air flow to the thermal zones at *5:00 am* and keeps it fully opened till *5:00 pm*. The discharge air temperature is also kept constant at 47^oC during that time period.

We implement two controllers: an *on-off controller* and a *Model Predictive Controller*. For controller implementation, we assume that we can only manipulate the air flow valve while the discharge air temperature remains the same as before. Note that due to the weather condition at Berkeley, where the considered building is located, the HVAC system only needs to provide heating (according to Figure 4.17), and cooling is done naturally by turning off the heating mode of the HVAC system and by running the ventilation system. Note that even if no cooling is needed the rooms have to be ventilated for air quality reasons. For the two following controllers we consider a time-varying lower bound and upper bound for temperature which define the comfort zone to be between 20 and 22 ^oC during day and between 19 and 23 ^oC at night as shown in Figure 4.17.

4.4.2 On-off Controller

For the *on-off controller* we assume that the valves can have three states: fully opened, minimally opened (not fully closed due to air quality reasons) during occupied hours, or fully closed at night. and the duration of each state of the valve cannot be less than 1 hour, i.e. when the valve is set to open it has to remain open for at least 1 hour before it can close. The controller turns on the heating mode when the room temperature falls below the lower limit and turns it to either minimally open or fully closed (depending on whether it is occupied or unoccupied hours of the day) when the temperature is within the comfort zone. The performance of this controller is depicted in Figure 4.17.

4.4.3 Model Predictive Controller

A model predictive control problem is formulated with the objective of minimizing a linear combination of the total energy consumption and the peak airflow. An MPC with similar cost function is also used in [85] with a simple linear model. However, here we have modified the controller in order to reflect the constraints of the considered system, the system dynamics and etc. Also we have implemented the control inputs obtained from the MPC which utilizes the linearized system dynamics of the model on the original nonlinear model.

Note that the fan energy consumption is proportional to the *cubic* of the airflow. Hence minimizing the peak airflow would dramatically reduce fan energy consumption. We have considered a cost function for the MPC which comprises linear combination of the total heating power consumption (l_1 norm of input) and the peak of airflow (l_∞ norm of input). Also in order to guarantee feasibility (constraint satisfaction) at all times we have implemented soft constraints. The predictive controller solves at each time step the following problem

$$\min_{U_t,\overline{\epsilon},\underline{\epsilon}} \quad \{|U_t|_1 + \kappa|U_t|_\infty + \rho(|\overline{\epsilon}_t|_1 + |\underline{\epsilon}_t|_1)\} = \tag{4.28a}$$

$$\min_{U_t,\overline{\varepsilon},\underline{\varepsilon}} \quad \{\sum_{k=0}^{N-1} |u_{t+k|t}| + \kappa \max(|u_{t|t}|, \cdots, |u_{t+N-1|t}|) + \rho \sum_{k=1}^{N} (|\overline{\varepsilon}_{t+k|t}| + |\underline{\varepsilon}_{t+k|t}|)\} \tag{4.28b}$$

$$\text{s.t.} \quad x_{t+k+1|t} = Ax_{t+k|t} + Bu_{t+k|t} + Ed_{t+k|t}, \qquad k = 0, ..., N-1 \tag{4.28c}$$

$$y_{t+k|t} = Cx_{t+k|t}, \qquad k = 1, ..., N \tag{4.28d}$$

$$\underline{\mathcal{U}}_{t+k|t} \leq u_{t+k|t} \leq \overline{\mathcal{U}}, \qquad k = 0, ..., N-1 \tag{4.28e}$$

$$\underline{T}_{t+k|t} - \underline{\varepsilon}_{t+k|t} \leq y_{t+k|t} \leq \overline{T}_{t+k|t} + \overline{\varepsilon}_{t+k|t}, \qquad k = 1, ..., N \tag{4.28f}$$

$$\underline{\varepsilon}_{t+k|t}, \overline{\varepsilon}_{t+k|t} \geq 0, \qquad k = 1, ..., N \tag{4.28g}$$

Where $U_t = [u_{t|t}, u_{t+1|t}, \cdots, u_{t+N-1|t}]$ is the vector of control inputs, $\underline{\epsilon} = [\underline{\varepsilon}_{t+1|t}, \cdots, \underline{\varepsilon}_{t+N|t}]$ is the temperature violations from the lower bound, $\overline{\epsilon}$ is the temperature violation from the upper bound, $y_{t+k|t}$ is the thermal zone temperature vector, $d_{t+k|t}$ is the disturbance load prediction, and $\underline{T}_{t+k|t}$ and $\overline{T}_{t+k|t}$ for $k = 1, \cdots, N$ are the lower and upper bounds on the zone temperature, respectively. $\underline{\mathcal{U}}_{t+k|t}$ and $\overline{\mathcal{U}}$ are the lower and upper limit on the airflow input by the VAV damper, respectively. Note that based on ASHRAE requirements for *Air Change per Hour* (ACH) of rooms, there has to be a minimum non-zero airflow during occupied hours for ventilation purposes. ρ is the penalty on the comfort constraint violations, and κ is the penalty on peak power consumption.

Remark 1. Note that for predicting the *disturbance load*, we use the optimal solution $(\lambda^*, \gamma^*, \mu^*, \nu^*)$ to the optimization problem (2.60) along with the predictions of $T_{out}(t)$ and $\Psi(t)$ for future times. The predictive values for these two quantities can be obtained from weather forecasts and from the occupancy schedules of each thermal zone of the building, respectively. Although here we are assuming a *perfect* forecast for these quantities in this formulation, imperfect weather and occupancy predictions can potentially deteriorate the performance of MPC. The results of our study on the performance and effectiveness of MPC in the presence of forecast errors can be found in [54].

At each time step only the first entry of U_t is implemented on the plant. At the next time step the prediction horizon N is shifted leading to a new optimization problem. The prediction horizon is $N = 24$, and at each time step only the first entry of the input vector U_t is implemented on the model. This process is repeated over and over until the total time span of interest is covered. We use YALMIP [48] to set up the MPC problem in MATLAB.

We implement the hierarchical control algorithm proposed in [53]. At the lower level, each thermal zone is controlled by a PID controller while a model-based optimal control is used at the higher level for a group of thermal zones.

4.4.4 Simulation Results

Original Controller. The air flow valve is turned on from *5:00 am* until *5:00 pm* and remains off for the rest of the day. This approach results in a total airflow input of 45360 $[ft^3]$ per day and a maximum air flow rate of 63 $[ft^3/min]$.

On-off Controller. The airflow valve is turned on only for 4 hours in that specific day as shown in Figure 4.17. This reduces the total airflow input to 17520 $[ft^3]$ per day, which is 61.4% less than the original case and the maximum airflow rate remains at 63 $[ft^3/min]$.

MPC. The air flow valve is not just an on-off switch; rather any intermediate values can be set for the air flow into the room. The performance of the controller is shown

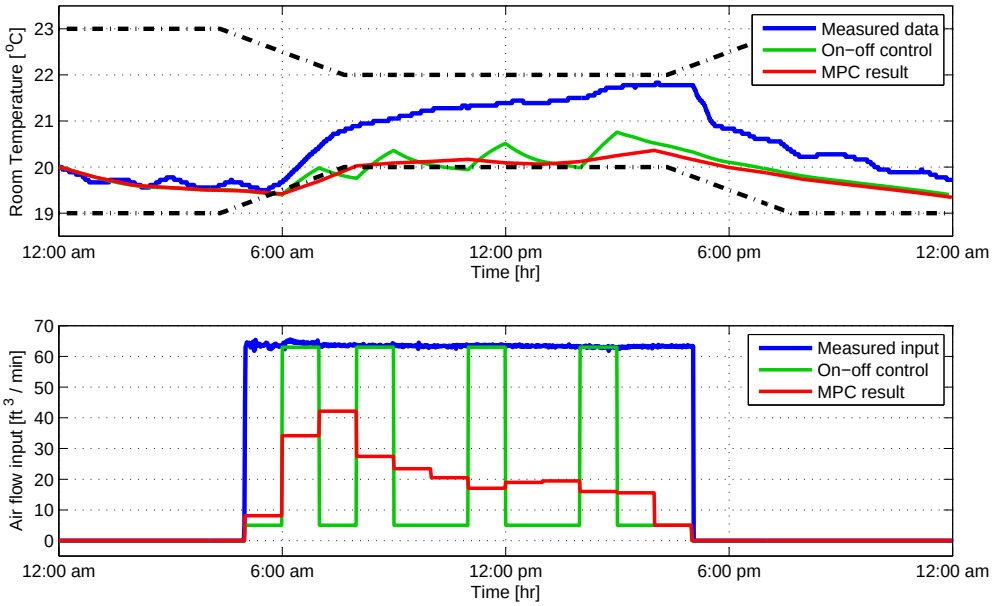

Figure 4.17: Measured data and the result of on-off controller and MPC.

in Figure 4.17. Implementation of MPC results in a total airflow input of 14870 $[ft^3]$ per day, which is 67.2% less than the original case and a maximum airflow rate of 42 $[ft^3/min]$ that is 33.3% less than the original case.

Remark 2. Note that the peak airflow required for a building is an important design parameter for sizing the HVAC system components at the design stage. A smaller Air Handling Unit (AHU) package (and hence a smaller fan) would, on top of the energy savings due to advanced control algorithms introduced here, lead to more electric power consumption reductions.

To compare the overall energy performance of the controllers we calculate the *total energy consumption* for each controller. The total energy consumption is given by

$$E_{tot} = \int_{t=0}^{24} [P_c(t) + P_h(t) + P_f(t)]\, dt \tag{4.29}$$

in which, the cooling power P_c, the heating power P_h and the fan power P_f are defined by

Table 4.1: Comparison of performance for three different controllers. The inputs are heating air flow to the room.

Controller	Total input $[ft^3]$	Peak input $[ft^3/min]$	Total energy $[kWh]$	Running time $[s]$
Original control	45360	63	12.46	-
On-off control	17520	63	4.62	1.8
MPC	14870	42	3.33	102.4

$$P_c(t) = \dot{m}_c(t)c_p[T_{out}(t) - T_c(t)] \tag{4.30}$$
$$P_h(t) = \dot{m}_h(t)c_p[T_h(t) - T_{out}(t)] \tag{4.31}$$
$$P_f(t) = \alpha\dot{m}^3(t) \tag{4.32}$$

where $c_p = 1.012[kJ/kg.^oC]$ is the specific heat capacity of air and $\alpha = 0.5[kW.s^3/kg^3]$ is the fan power constant. Using the above equations and constants results in fan power values in $[kW]$.

The comparisons of results are summarized in Table 4.1. MPC manages to reduce both the total and peak air mass flow, and total energy consumption as compared to the original controller of the test bed and an RBC such as On-off control.

4.5 Robust Model Predictive Control

Optimal control of HVAC components using model-based control techniques has shown promising results for achieving energy efficiency in buildings [55, 66, 85, 51, 67]. However, these control techniques rely heavily on a perfect (or almost perfect) mathematical model of the building or a perfect estimation of the unmodelled dynamics of the system [55].

Although a great deal of progress has been made in modeling the thermal behavior of building envelope and HVAC system [56, 53, 55, 27, 85, 51], the random nature of some components of these systems makes it very hard to predict, with high fidelity, the temperature evolution of the room using mathematical models. These random events and phenomena include building occupancy by people which along with other internal loads such as the heat emitted from electrical devices and lighting, account for the total internal heat generation of the building. The outside environment of the building is also subject to many random and hard-to-accurately-predict phenomena such as

the wind speed, solar radiation, cloudiness of the sky and outside air temperature. The aggregate effect of all these factors constitutes the total external heat gain of the building. The authors name these two heat gains of the building, the "unmodelled dynamics" and propose a methodology in [55] to estimate these loads which act as disturbance to the system dynamics. However, as mentioned earlier, it is difficult to obtain a *perfect* prediction of the loads in future times. On the other hand, model-based optimal controllers such as Model Predictive Control (MPC) are highly dependent on accurate predictions of these disturbances. In order to account for these modeling deficiencies, it is usually a reasonable assumption to consider an additive norm-bounded[1] uncertainty to the model. The question here is how to integrate this uncertainty information in the control design to achieve the desired comfort level while consuming *minimum* energy.

We present an overview of existing min-max formulations of Robust Model Predictive Control (RMPC) for uncertain constrained discrete-time systems. A min-max strategy for MPC tries to optimize the worst-case scenario cost function with respect to uncertainties. Standard min-max MPC schemes easily lead to conservative controllers because they typically deal with open-loop formulations. Moreover, Open-Loop Robust Model Predictive Control (OL-RMPC) is known to be unnecessarily overly conservative in most applications [74, 23]. The reason is that the optimal open-loop control sequence has to deal with all the future disturbances without using the information of the future measurements that will be obtained as the horizon window recedes. An extension to min-max MPC that resolves this problem is closed-loop min-max MPC or Closed-Loop Robust Model Predictive Control (CL-RMPC). However, CL-RMPC leads to an intractable problem which is much harder to solve [46]. Fortunately, approximation of closed-loop min-max MPC using a convex programming framework is possible by the use of semidefinite relaxations. The idea in CL-RMPC, is to approximate the intractable min-max problem by introducing new decision variables into the system and parameterize the future control sequence in the future states or disturbances [47, 19].

On the other hand, nominal MPC in practice is regarded as a state feedback controller. The reason is that, although MPC at each time step solves an *open-loop* optimal control problem, only the first entry of the resulting optimal control sequence is implemented on the plant at each time step, and this process is repeated as the prediction horizon recedes. This feedback of the measurement information to the optimization endows the whole procedure with a *robustness*, typical of closed-loop systems [23]. Therefore, nominal MPC is capable of rejecting some level of unmodelled or unpredictable disturbances due to its closed-loop nature.

Note that in the control of building climate, it is not extremely crucial to re-

[1] Refer to Section 4.5.1 for definition and more details.

spect temperature bounds at all times and based on some standards, some level of temperature constraint violations would be acceptable (e.g., the European standards state that the room temperature must be kept within a certain range with a certain probability [66].) and can be tolerated if it translates into considerable reductions in total or peak energy consumption of the whole HVAC system.

Based on the discussion of last three paragraphs, nominal MPC, OL-RMPC, and CL-RMPC, exhibit some level of robustness in their performances. In this section one of the questions that we will try to answer is: "*which of the above controllers would be the best choice for the building climate control, in the presence of uncertainty*?" We carry out a *quantitative* analysis of the performance of the above controllers. Through simulations we assess the performance of the controllers for a range of prediction accuracies.

A new disturbance feedback parameterization of the input is proposed. It is shown in this section that this parameterization reduces the number of decision variables of the optimization problem and hence results in a faster alternative than the existing parameterizations in the literature, while maintaining the performance level of the RMPC.

A number of related works can be found in the literature. A model predictive controller was implemented by the authors on the model utilized in this work, in [55]. It was shown that in the case of *perfect* disturbance load prediction the controller manages to maintain the temperature within the comfort zone for all times while reducing the total and peak conditioned air consumption with respect to the existing control strategy of the building, by 68% and 35%, respectively. In [67] the authors investigate a bilinear model under stochastic uncertainty with probabilistic, time varying constraints.

In this section we focus on optimal control design in the presence of *imperfect* disturbance predictions. Contribution of this section is twofold:

1. We propose a new disturbance feedback parameterization. Simulations show that the new parameterization enhances the computational and performance characteristics of the CL-RMPC. The new parameterization leads to a number of decision variables, *linear* in time horizon as opposed to *quadratic*, for the previously introduced parameterizations. The resulting sparse feedback gain matrix also reduces the simulation time by 30% with respect to the previous parameterization.

2. To validate our approach, we compare the performances of three different controllers for a range of prediction error values. Exhaustive *quantitative* analysis show how much the performance of the MPC will deteriorate in the case of *imperfect* predictions. We quantify how much the energy consumption and discomfort indices will degenerate as a function of *disturbance prediction error*.

4.5.1 Preliminaries

4.5.2 System Dynamics

We use the nonlinear system described in Chapter 2 and expressed in (5.5). The system dynamics is linearized around the nearest equilibrium point to the specified operating point of the system (details in [56]). The algorithm to find the equilibrium point of the system starts from an initial point and searches, using a *Sequential Quadratic Programming (SQP) algorithm*, until it finds the nearest equilibrium point. First we linearize the model considering all the inputs to the model. Once the system dynamics is linearized, we divide the inputs into *manipulated variables* and *disturbance variables*. Discretizing the state space realization leads to the following discrete time LTI system:

$$x_{k+1} = Ax_k + Bu_k + Ed_k \tag{4.33}$$

where $d_k \in \mathbb{R}^r$ stores the disturbance at time k and the original B obtained from linearization process is split into two parts $B' = [B \ E]$. Where B stores the columns corresponding to the *manipulated variables* and E stores the columns of B' corresponding to the *disturbance variables*. In this study, air mass flow is a *manipulated variable* and we regard the rest of the inputs as *disturbance variables* as they are not controlled.

4.5.3 State and Input Constraints

The system is subject to input constraints

$$\mathcal{U} := \{u \in \mathbb{R}^m | S^u u \leq s^u\} \tag{4.34}$$

where $S^u \in \mathbb{R}^{q \times l.m}$, $s^u \in \mathbb{R}^q$ and $\mathcal{U} \subset \mathbb{R}^{l.m}$ is a bounded polytopic set. The polytopic constraints on the state is given by

$$\mathcal{X} := \{x \in \mathbb{R}^n | S^x x \leq s^x\} \tag{4.35}$$

where $S^x \in \mathbb{R}^{p \times n}$, $s^x \in \mathbb{R}^p$ and $\mathcal{X} \subset \mathbb{R}^n$.

4.5.4 Additive Uncertainty

Consider the uncertain linearized system dynamics given by

$$x_{k+1} = Ax_k + Bu_k + E(d_k + w_k) \tag{4.36}$$

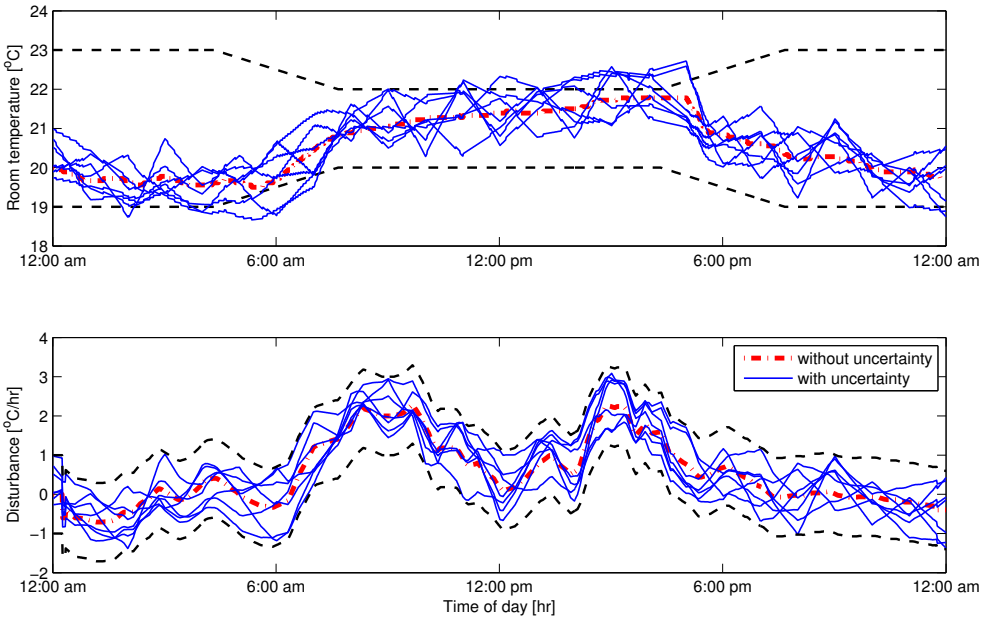

Figure 4.18: Room temperature and the corresponding unmodelled dynamics realization (in dashed red). Disturbance plus uncertainty and the corresponding room temperature for $\lambda = 1$ in the case of ECS is shown in solid blue. Note that although ECS is a rather conservative control strategy, it still fails to keep the temperature within the comfort zone at all times.

where the disturbance uncertainty $w_k \in \mathbb{R}^r$ is a stochastic disturbance. We assume it is only known to be bounded in some measure, but otherwise unknown. The set of possible disturbance uncertainties is denoted by $\mathcal{W}$ and $w_k \in \mathcal{W} \quad \forall k = 0, 1, ..., N-1$. The disturbance set $\mathcal{W}$ is one of the ingredients that determine the type of optimization problem we end up with. For an uncertain *Linear Programming* (LP) when the corresponding uncertainty set $\mathcal{W}$ is a polyhedron, then the robust counterpart is also an LP. When $\mathcal{W}$ is ellipsoidal, then the robust counterpart becomes a *second-Order Cone Programming* (SOCP) [22]. For this application we consider box-constrained disturbance uncertainties given by

$$\mathcal{W}_\lambda = \{w : ||w||_\infty \leq \lambda\} \tag{4.37}$$

As an example, Figure 4.18 depicts the temperature of the room from the validated model and the corresponding estimated unmodelled dynamics (in dashed red). The additive uncertainty to the system yields a temperature trajectory which is shown in

the same figure (in solid blue).

4.5.5 Disturbance Prediction Error

To illuminate the effectiveness of the controllers laid out in Section 4.2, we assess their performances for different *disturbance prediction error* values denoted by δ and defined as

$$\delta = \frac{\lambda}{||\mathbf{d}||_\infty} \tag{4.38}$$

where λ is the l_∞ norm bound of the uncertainty and $\mathbf{d} = [d_1', d_2', ..., d_N']'$ is the disturbance realization vector[2].

4.5.6 Chance Constraints

In this work we focus on uncertainty models given by (4.37). The results of this work can be easily extended to robust MPC problems with chance constraints such as [66]. Note that the uncertainty model used in [66] assumes independent and identically normally distributed random variables, i.e. $v \sim \mathcal{N}(0, I)$. However, the normally distributed disturbance v is approximated with a norm-bounded disturbance $w \in \mathbb{R}^p$, motivated with a work by the authors of [22] in which they show that a chance constraint of the form

$$\mathcal{X}_c = \{\mathbf{P}(\phi(x_0, U, \mathbf{d}, \mathbf{w}) \in \mathcal{X}) \geq 1 - \alpha\} \tag{4.39}$$

which requires that the condition $\phi(x_0, U, \mathbf{d}, \mathbf{w}) \in \mathcal{X}$ is fulfilled with a probability greater than or equal to $1 - \alpha$, can be approximated by a hard constraint if the uncertainty bound λ is chosen according to Theorem 5 in [66]. Note that $\phi(x_0, U, \mathbf{d}, \mathbf{w})$ denotes the solution to (4.36) given the initial state x_0, the control input $U = [u_1', u_2', ..., u_N']'$, the disturbance realization $\mathbf{d} = [d_1', d_2', ..., d_N']'$, and the uncertainty realization $\mathbf{w} = [w_1', w_2', ..., w_N']'$.

As introduced in Section 4.5.4 we consider l_∞ bounded additive uncertainties in the control derivation.

4.5.7 Robust MPC Against Additive Uncertainty

The crucial question in robust control is *how to exploit knowledge about uncertainty*. Typical knowledge can be bounds on uncertain parameters in the system, or bounds

[2]Note that x' represents the transpose of vector x.

on external disturbances, such as the disturbance load to the building. In this section we consider additive uncertainty to the system model as described in (4.36).

A typical robust strategy involves solving a min-max problem to optimize worst-case performance while enforcing input and state constraints for all possible disturbances. In this section we formulate a min-max robust constrained optimal control problem for the building air temperature regulation system affected by additive bounded input disturbances.

Open-Loop Predictions

A min-max strategy for MPC tries to optimize the worst-case scenario cost function with respect to uncertainties. Define the worst-case cost function as

$$\begin{aligned} J_0(x(0), U_0) \triangleq \max_{w_{[.]}} \quad & \{||Px_N||_p + \sum_{k=0}^{N-1} ||Qx_k||_p + ||Ru_k||_p\} \\ \text{s.t.} \quad & x_{k+1} = Ax_k + Bu_k + E(d_k + w_k) \\ & w_k \in \mathcal{W} \\ & \forall \quad k = 0, \cdots, N-1 \end{aligned} \tag{4.40}$$

Where $||.||_p$ can be any polytopic norm and N is the time horizon. The robust optimal control problem is formulated as follows

$$J_0^*(x(t)) \triangleq \min_{U_t} \quad J_0(x(t), U_t) \tag{4.41}$$

subject to:

$$x_{k+1} = Ax_k + Bu_k + E(d_k + w_k) \qquad k = 0, \cdots, N-1 \tag{4.42a}$$
$$y_k = Cx_k \qquad k = 1, \cdots, N \tag{4.42b}$$
$$u_k \in \mathcal{U} \qquad k = 0, \cdots, N-1 \tag{4.42c}$$
$$x_k \in \mathcal{X} \qquad k = 1, \cdots, N \tag{4.42d}$$
$$\forall \ w_k \in \mathcal{W} \qquad k = 0, \cdots, N-1 \tag{4.42e}$$

At each time step t, only the first entry of U_t is implemented on the plant. At the next time step the prediction horizon N is shifted leading to a new optimization problem. This process is repeated until the total time span of interest is covered.

Using the above formulation, we derive a robust counterpart of an uncertain optimization problem in which constraints are satisfied for all possible uncertainties,

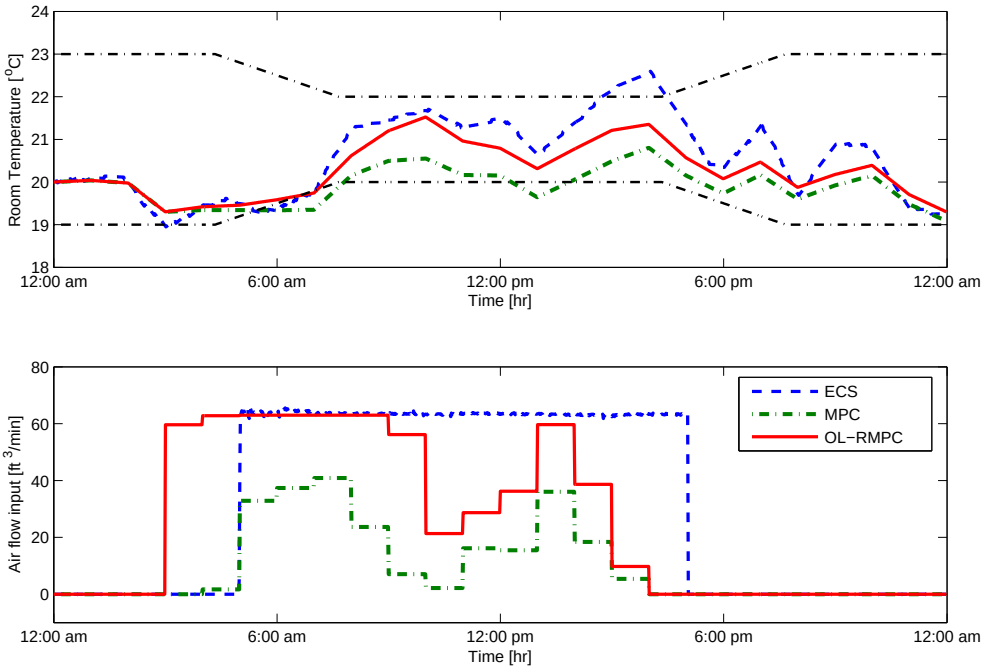

Figure 4.19: Performance of MPC and OL-RMPC in the presence of additive uncertainty with $\delta = 50\%$. It can be observed that the OL-RMPC yields an overly conservative control algorithm resulting in excessive energy consumption.

and worst-case objective is calculated. This system does not involve the uncertain variables anymore, and corresponds to the worst-case scenario model.

Performances of MPC and OL-RMPC are depicted in Figure 4.19. In the case of MPC, the controller is designed for the model with only disturbance d_k known a priori, and implemented on the model which has as input, both known disturbance d_k and the unknown additive uncertainty w_k.

4.5.8 Approximate Closed-Loop Min-Max MPC

It is shown in Figure 4.19 that the Open Loop Constrained Robust Optimal Control (OL-CROC) is conservative. This is because we are optimizing an open-loop control sequence that has to cope with all possible future disturbance realizations, without taking future measurements into account. The Closed-Loop Constrained Robust Optimal Control (CL-CROC) formulation overcomes this issue but it can quickly lead to an intractable problem [47]. There are some alternative approaches which introduce

feedback in the system and, in some cases, can be more efficient than CL-CROC.

Feedback Predictions

What we really would like to solve is the closed-loop min-max problem where we incorporate the notion that measurements will be obtained in the future times.

$$\min_{u_{k|k}} \max_{w_{k|k}} \cdots \min_{u_{k+N-1|k}} \max_{w_{k+N-1|k}} \sum_{j=0}^{N-1} p(x_{k+j|k}, u_{k+j|k}) \tag{4.43}$$

where $p(.)$ is the performance index. Instead of solving this intractable problem, the idea in feedback prediction, sometimes referred to as closed-loop predictions, is to introduce new decision variables $v_{k+j|k}$, and parameterize the future control sequences in the future states and $v_{k+j|k}$ such as $u_{k+j|k} = m_{k,j}x_{k+j|k} + v_{k+j|k}$. This way, there is at least some kind of feedback in the system, although not optimal. To incorporate feedback predictions, we write the feedback predictions in a vectorized form $U = \mathbf{M}X + \mathbf{v}$. Where $\mathbf{v}$ and X are given by $\mathbf{v} = [v_{k|k}^{'}, v_{k+1|k}^{'}, \cdots, v_{k+N-1|k}^{'}]^{'}$, and $X = [x_{k|k}^{'}, x_{k+1|k}^{'}, \cdots, x_{k+N-1|k}^{'}]^{'}$. The only requirement for matrix $\mathbf{M}$ is that this matrix is *causal* in the sense that $u_{k+j|k}$ only depends on $x_{k+i|k}$, $i \leq j$. Notice that feedback predictions introduce a new tuning knob in min-max MPC, which is matrix $\mathbf{M}$. However the choice of $\mathbf{M}$ is not obvious, and no guideline exists in the literature, on how to select its entries. In [47] it is shown through simulation examples that the choice of $\mathbf{M}$ is crucial for good performance of the min-max controller.

However sometimes $\mathbf{M}$ is incorporated as a decision variable in the online optimization problem. The obtained optimization problems are convex. Unfortunately, the optimization problem grows rapidly, although polynomially in the system dimension, the number of constraints and the prediction horizon. To resolve this problem, it is shown in [47] how the general solution can serve as a basis for off-line calculations, and approximations with a reduced degree of freedom, but with much better computational properties (we have somehow implemented this idea in constructing a better $\mathbf{M}$ in what follows).

The main problem with the min-max formulations based on these parameterizations is the excessive number of decision variables and constraints. The reason is the high-dimensional parameterization of matrix $\mathbf{M}$.

Alternative Parameterizations

To resolve this issue we study some other parameterizations that have been introduced in the literature and also the parameterization that we introduce later in this section.

It is shown in [47] that the problem with the parameterization introduced previously, is that the mapping from $\mathbf{M}$ and $\mathbf{v}$ to X and U is nonlinear, hence optimization

over both $\mathbf{M}$ and $\mathbf{v}$ is likely to cause problem. At least, it is not obvious how this parameterization can be incorporated in a standard convex optimization framework. Due to this problem, alternative parameterizations are introduced. One of the parameterizations introduced in [47] is as follows:

1. Lower Triangular Structure (LTS): Define the affine disturbance feedback as:

$$u_i := \sum_{j=0}^{i-1} m_{i,j} w_j + v_i \qquad \forall i = 1, 2, ..., N-1 \tag{4.44}$$

where $M_{i,j} \in \mathbb{R}^{l.m \times r}$ and $v_i \in \mathbb{R}^{l.m}$ are given by

$$\mathbf{M} := \begin{bmatrix} 0 & \cdots & \cdots & 0 \\ m_{1,0} & 0 & \ddots & 0 \\ \vdots & \ddots & \ddots & \vdots \\ m_{N-1,0} & \cdots & m_{N-1,N-2} & 0 \end{bmatrix}, \quad \mathbf{v} := \begin{bmatrix} v_0 \\ \vdots \\ \vdots \\ v_{N-1} \end{bmatrix} \tag{4.45}$$

and $\mathbf{w} = [w_0 \quad w_1 \quad \cdots \quad w_{N-1}]'$ is the vector of disturbance. Therefore the input can be written as $U = \mathbf{M}\mathbf{w} + \mathbf{v}$. The control sequence is now parameterized directly in the uncertainty. The mapping from $\mathbf{M}$ and $\mathbf{v}$ to X and U is now bilinear. What we have here is basically a sub-optimal version of the closed-loop min-max solution [47].

Note that other parameterizations such as *Toeplitz* are also introduced in [47]. However, Toeplitz structure was shown to deteriorate the performance of the CL-RMPC in our simulations and therefore is not considered here.

2. Two Lower Diagonal Structure (TLDS): By analyzing the structure of the optimal matrix $\mathbf{M}$, we observed that the parameterization of the input need not consider feedback of more than past two values of $\mathbf{w}$ at each time, hence we propose the following disturbance feedback:

$$\begin{aligned} u_i &:= m_{i,i-2} w_{i-2} + m_{i,i-1} w_{i-1} + v_i \\ &= \sum_{j=i-2}^{i-1} m_{i,j} \omega_j + v_i \qquad \forall i = 1, 2, ..., N-1 \end{aligned} \tag{4.46}$$

and the corresponding parameterization matrix $\mathbf{M}$ is an $N \times N$ matrix that has the entries on the first and second diagonal of $\mathbf{M}$ below its main diagonal as decision variables and 0 elsewhere as given by

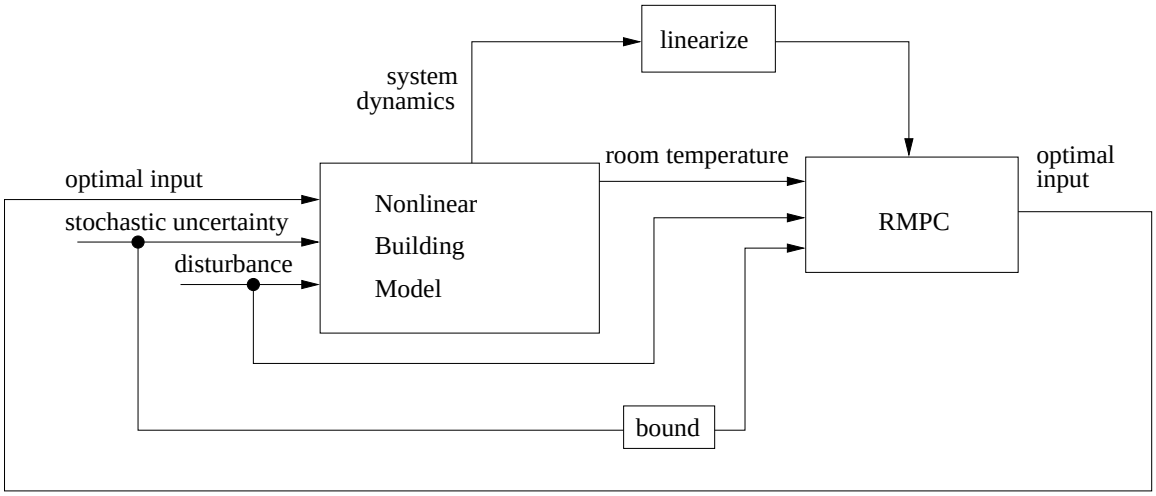

Figure 4.20: Schematic of the control implementation.

$$\mathbf{M} = \begin{bmatrix} 0 & 0 & \cdots & 0 & 0 & 0 \\ m_{21} & 0 & 0 & \cdots & 0 & 0 \\ m_{31} & m_{32} & \ddots & \vdots & \vdots & \vdots \\ 0 & m_{42} & \ddots & 0 & \vdots & \vdots \\ \vdots & \ddots & \ddots & m_{1,2} & 0 & 0 \\ 0 & \cdots & 0 & m_{N,N-2} & m_{N,N-1} & 0 \end{bmatrix} \tag{4.47}$$

and $\mathbf{v}$ remains as in the previous structure. Note that in this structure we exploit the sparsity of the feedback gain matrix to enhance the computational characteristics of the optimal problem.

A schematic of the robust optimal control implementation on the nonlinear building model is depicted in Figure 4.20.

4.5.9 Performance Indices

To compare the overall performance of the proposed controllers we define two indices to measure the energy consumption and comfort level provided by each controller.

The energy index I_e, is defined to be

$$I_e = \int_{t=0}^{24} [P_c(t) + P_h(t) + P_f(t)]\, dt \tag{4.48}$$

where cooling power P_c, heating power P_h and fan power P_f are defined as

$$P_c(t) = \dot{m}_c(t)c_p[T_{out}(t) - T_c(t)] \tag{4.49}$$
$$P_h(t) = \dot{m}_h(t)c_p[T_h(t) - T_{out}(t)] \tag{4.50}$$
$$P_f(t) = \alpha\dot{m}^3(t) \tag{4.51}$$

where $c_p = 1.012[kJ/kg.^oC]$ is the specific heat capacity of air and $\alpha = 0.5[kW.s^3/kg^3]$ is the fan power constant. Using the above equations and constants, results in fan power values in $[kW]$.

The discomfort index I_d, is defined as the sum of all the temperature violations during the course of a day.

$$I_d = \int_{t=0}^{24} \left[\min\left\{\left|T(t) - \overline{T}(t)\right|, |T(t) - \underline{T}(t)|\right\}.\mathbf{1}_{\mathcal{B}(t)^c}(T(t))\right] dt \tag{4.52}$$

where $\mathcal{B}(t) = [\underline{T}(t), \overline{T}(t)]$ is the allowable temperature boundary at time t and $\mathbf{1}$ is the indicator function.

4.5.10 Simulation Results

We implement the introduced controllers with a prediction horizon of $N = 24$. We observed a dramatic degradation of the performance for $N < 24$, and relatively long computational time for $N > 24$. We believe the choice of $N = 24$ leads to a good balance between performance and computational cost. The utilized cost function for the following simulations is given by

$$\min_{U_t, \bar{\varepsilon}, \underline{\varepsilon}} \quad \{||\mathbf{U_t}||_1 + c_1||\mathbf{U_t}||_\infty + c_2(||\overline{\epsilon}_\mathbf{t}||_1 + ||\underline{\epsilon}_\mathbf{t}||_1)\} \tag{4.53}$$

and the state and input constraints are as follows:

$$x_{t+k+1|t} = Ax_{t+k|t} + Bu_{t+k|t} + E(d_{t+k|t} + w_{t+k|t}) \tag{4.54a}$$
$$y_{t+k|t} = Cx_{t+k|t} \tag{4.54b}$$
$$\underline{T}_{t+k|t} - \underline{\varepsilon}_{t+k|t} \leq y_{t+k|t} \leq \overline{T}_{t+k|t} + \overline{\varepsilon}_{t+k|t} \tag{4.54c}$$
$$u_{t+k|t} \leq \overline{u} \tag{4.54d}$$
$$\underline{\varepsilon}_{t+k|t},\ \ \overline{\varepsilon}_{t+k|t} \geq 0 \tag{4.54e}$$
$$w_{t+k|t} \in \mathcal{W} \tag{4.54f}$$

where $\overline{u} = 63\ \ [ft^3/min]$ is the higher limit on air mass flow, $[\underline{T}_{.|t}\ \ \overline{T}_{.|t}] = [20\ \ 22]^oC$ during occupied hours and $[\underline{T}_{.|t}\ \ \overline{T}_{.|t}] = [19\ \ 23]^oC$ during unoccupied hours. We utilize

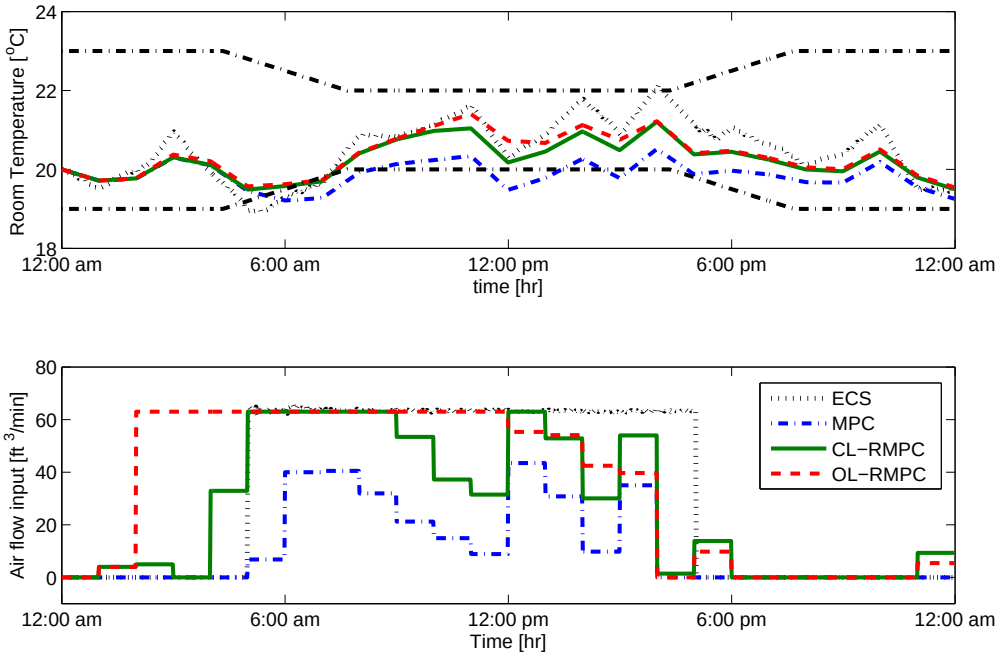

Figure 4.21: Control input and resulting temperature profile for original controller, open-loop, closed-loop and regular MPC. The additive uncertainty bound is considered $\delta = 60\%$ in this case.

soft constraints to guarantee feasibility of the problem at all time steps. For the simulations we use $c_1 = 0.75$ and $c_2 = 50$.

The optimal controller and the resulting room temperature with the presence of a box-constrained uncertainty in four cases is depicted in Figure 4.24. ECS refers to the Existing Control Strategy implemented on the building. This case shows the behavior of the original controller of the building if there were a hypothetical extra additive load to the system. The next case shows the performance of an MPC algorithm with only the accurate a priori knowledge of the disturbance (i.e. unmodelled dynamics of the system) and not the uncertainty. The third case is OL-RMPC in which the algorithm has a priori knowledge of both the disturbance and the uncertainty bound. The fourth case algorithm is a CL-RMPC which exploits the same knowledge as the third case, with the difference that it utilizes the uncertainty feedback strategy of (4.44).

We consider stochastic uncertainties with different uncertainty bounds (λ) as introduced in (4.37). The MPC does not have any a priori information regarding the

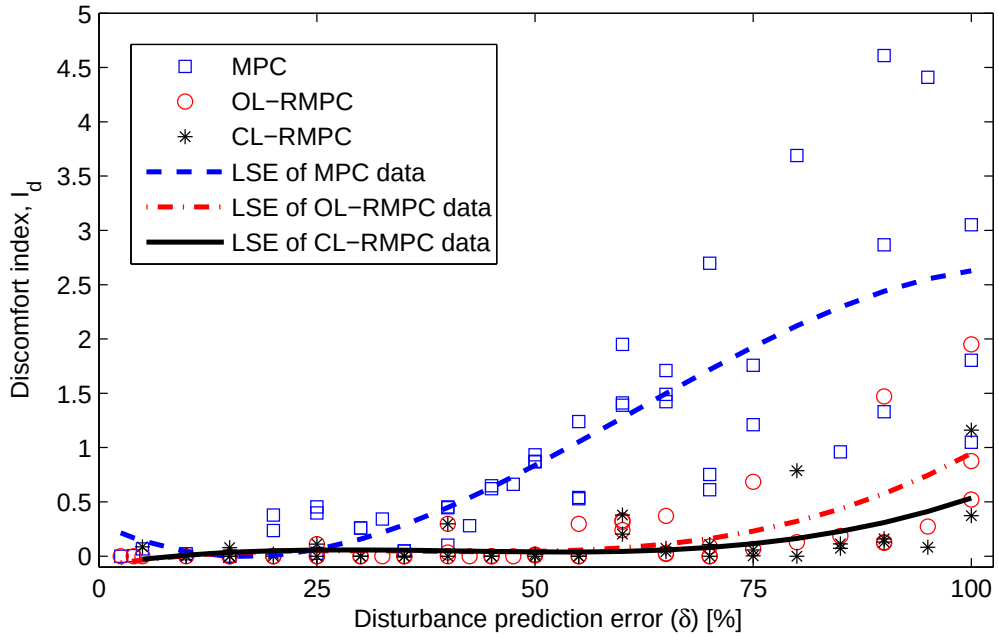

Figure 4.22: Discomfort index I_d $[^oCh]$ versus disturbance prediction error (δ). We generate a uniform random sequence based on the disturbance prediction error value δ. The generated random sequence is used in the simulations for making this graph. Note that different data points for one δ value refers to simulations with different random sequences. The reason for such wide deviation of the simulation results stems from the fact that depending on the value of the random variable at any time, the resulting disturbance vector can either lead to higher or lower temperature deviations with respect to the nominal disturbance value. LSE refers to Least Square Estimation.

additive uncertainty, and calculates the controller solely based on the deterministic system dynamics. However the RMPC integrates the uncertainty bound information in the control derivation. Controller performances are evaluated based on the energy and discomfort indices introduced in Section 4.5.9.

Remark 1. It can be observed from Figure 4.24, that the OL-RMPC and CL-RMPC are the only two controllers that are able to keep the temperature within the comfort zone, at all times, with the difference that the CL-RMPC leads to 36% reduction in energy index, I_e, while maintaining perfect level of comfort $(I_d = 0)$.

Figure 4.22 depicts how *Discomfort index* I_d, varies with disturbance prediction error δ for MPC, OL-RMPC and CL-RMPC. It is shown that both OL-RMPC and CL-RMPC manage to keep the perfect comfort level $(I_d = 0)$, for prediction errors up to $\delta = 60\%$ and $\delta = 75\%$ respectively, while the MPC maintains the perfect comfort

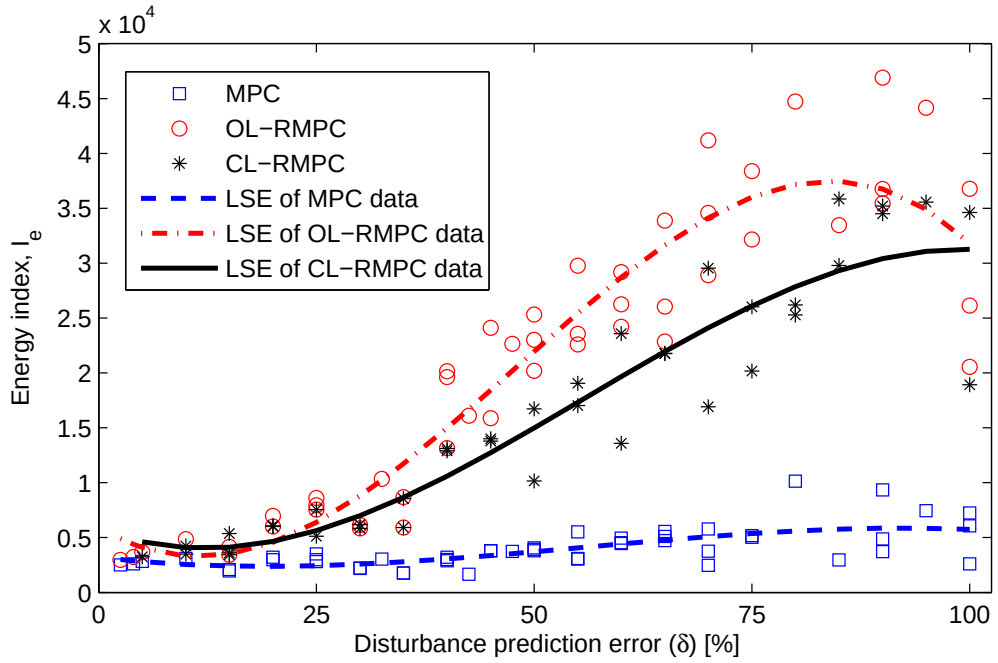

Figure 4.23: Energy index I_e $[kWh]$ versus disturbance prediction error (δ). The data points for this graph were generated using a similar technique as in Figure 4.22. LSE refers to Least Square Estimation.

level for uncertainty bounds up to $\delta = 20\%$. The discomfort index for MPC goes as high as 4.61 $[^oCh]$[3] while the value for CL-RMPC reaches 1.2 $[^oCh]$ in the worst case in the simulations corresponding to $\delta = 100\%$.

Figure 4.23 depicts the variations of *Energy index* I_e, versus the uncertainty bound on the unmodelled dynamics. It is clear that the energy index for RMPC increases dramatically with δ, while the energy index for MPC changes slightly. However, this comes with the drawback of increased discomfort index for MPC.

Remark 2. Exploiting the *TLDS* structure results in the same control law that was obtained from the *LTS* structure. Matrix $\mathbf{M}$ of *LTS* has $l.m.r\frac{N(N-1)}{2}$ variables (quadratic in N) while matrix $\mathbf{M}$ of *TLDS* has $l.m.r(2N-3)$ variables (linear in N), and hence exhibits faster computation characteristics. On average, the simulation time for *TLDS* is 30% less than the *LTS* structure, as shown in Table 4.2.

The problem is solved using CPLEX 12.2 [10] on a 2.67 GHz machine with 4 GB RAM. We observed about 33% reduction in the simulation time, in average, when we used CPLEX compared to the default solver of YALMIP [48], GLPK.

An important point to notice from Figure 4.23 is how much more energy needs

[3]degree Celsius hour.

Table 4.2: Comparison of LTS and TLDS uncertainty feedback parameterizations and Open Loop min-max results for the case of $\delta = 50\%$.

Controller	Number of feedback decision variables	Average simulation time for $N = 24$, in [s]	I_e $[kWh]$	I_d $[^oCh]$
LTS	$l.m.r(\frac{N(N+1)}{2})$	200	16467	0
TLDS	$3l.m.r(N-1)$	138	16467	0
OL	-	159	22592	0.84

to be supplied to the HVAC system to maintain the comfort level in the presence of imperfect and faulty unmodelled dynamics predictions. Consider the case where $\delta = 75\%$. MPC will lead to a discomfort index of 1.7^oCh on average, while the RMPC is able to maintain the temperature below a discomfort index of 0.016^oCh on average. However this level of comfort provided by the CL-RMPC comes at a cost of energy consumption of almost 5 times more than the MPC case.

Remark 3. Note that due to the trade-off between comfort and energy consumption, the choice of which controller to use is on the building HVAC operator, and depends on various factors such as criticality of meeting the temperature constraints for the considered thermal zone in the building, and availability and price of energy at that time of the day/year.

As observed from Figure 4.22 and 4.23 the behavior of controllers deviate considerably as the prediction error increases. For instance, The energy required to keep the same level of comfort for CL-RMPC in the case of $\delta = 75\%$ is almost 4 times the energy required to provide the same level of comfort when $\delta = 25\%$. Therefore, these two plots make it clear how precious a good model which *accurately* captures also the unmodelled dynamics of the system can be in minimizing the operation costs of HVAC systems of buildings.

4.6 Selecting Building Predictive Control Based on Model Uncertainty

MPC provides a potential building energy saving of 16%-41% compared to the commonly used rule-based HVAC controllers in the market as shown in [68, 51, 55, 71, 56]. At each iteration of MPC, a prediction of future states is obtained through for-

ward evolution of the system dynamics. The predictive cost is then calculated and constraints on future states and inputs are applied, leading to a large optimization problem, which is solved to obtain the optimal control action. MPC for building HVAC systems has desirable characteristics such as robustness, tunability, and flexibility [55]. Application of MPC for building energy control has been reported in [55, 71, 56, 53, 67, 84, 76, 50, 65, 52]. Different variations of nominal MPC such as distributed [65, 52], robust [84, 54] and stochastic [67, 66] model predictive control strategies have been also reported. All these MPC techniques rely on accurate building models to achieve optimal performance of HVAC system and provide sufficient comfort level.

Model uncertainty limits the utilization of Model Predictive Controllers (MPC) for minimizing building energy consumption. Hence, reducing *model uncertainty* is crucial for successful realization of building model-based controllers. However, uncertainty is an inevitable attribute of every model. For building models, model uncertainty is even more remarkable due to the substantial contribution of outside and inside thermal heats (realized as disturbance in our model) in the climate of the building, and unpredictability of the environment conditions such as wind speed and direction, ambient temperature, solar radiation and cloudiness of sky, and to some extent indoor factors such as human behavior.

In Sections 4.3, 4.4 and 4.5 we proposed several model-based controllers including Linear Quadratic Regulator (LQR), MPC, and RMPC, and compared their performance to simple RBC. RMPC provides a means to design a building controller robust to model uncertainty. In this section we compare the results from RMPC with those from a nominal MPC and a common building RBC. The results are then used to develop a methodology for selecting a controller type (i.e. RMPC, MPC, and RBC) as a function of building model uncertainty.

4.6.1 Performance Metrics

To compare the overall performance of the proposed controllers in Section 4.4, and 4.5, we defined indices to measure the energy consumption and comfort level provided by each controller. In addition, here we define a new index to evaluate the overall performance of each controller considering both the energy and comfort indices.

Overall Performance Index

A good control performance means not only low energy consumption, but also low resulting discomfort. To assess the overall performance of the controllers, we need to examine both I_e and I_d at the same time. Using the two indices defined above we define a third index called Overall Performance Index (I_{OP}). The intuition behind

this new index is to take into account the energy and discomfort index in one single term. I_{OP} is defined as:

$$I_{OP} = \frac{(I_d^* - I_d)/||I_d||_\infty}{I_e/||I_e||_\infty} \tag{4.55}$$

where I_d^* is the maximum allowed discomfort which is selected according to the required probability of maintaining room temperature within the comfort zone, and $||.||_\infty$ denotes infinity norm or the maximum value of energy indices among all three controllers. Negative value of I_{OP} means that the discomfort index is not within the preferred range. The lower the I_d and I_e are, the higher the I_{OP} will be. Therefore, the higher the I_{OP}, the better the overall performance. In this study, the limit on the allowed discomfort index is heuristically chosen to be $I_d^* = 0.5(^\circ\text{Ch})$ to ensure adequate comfort level.

4.6.2 Rule-Based Control (RBC)

The rule based controller use in this section is a conventional on-off HVAC controller. The time constant of the control implementation is Δt. The controller opens the dampers of conditioned air flow to the thermal zones when heating is required and keeps it fully open for the duration of Δt. In the next time step the controller checks the temperature again and adjusts the damper position if the room temperature is within the comfort zone, or keeps it open if the room air temperature is still outside the comfort zone. In on-off control, position of the dampers can be either the *min* value or the *max* value. When system goes to the cooling mode, supply air temperature changes accordingly. The experimental data presented here is for the heating mode only.

4.6.3 Simulation Results

To illustrate the effectiveness of the controllers proposed in Sections 4.4 and 4.5, we assess their performances for different *model uncertainty* values. In Section 4.5 we defined disturbance prediction error in (4.38). In this section we generalize this notion to "model uncertainty" value which is denoted by δ:

$$\delta = \frac{\lambda}{||\mathbf{d}||_\infty} \tag{4.56}$$

where λ is the l_∞ norm bound of the model uncertainty and $\mathbf{d} = [d_1', d_2', ..., d_N']'$ is the disturbance realization vector. In general, model uncertainty can be obtained by comparing the simulation results of a given model of a building for a period in the past, with historical data of same building over the same time period.

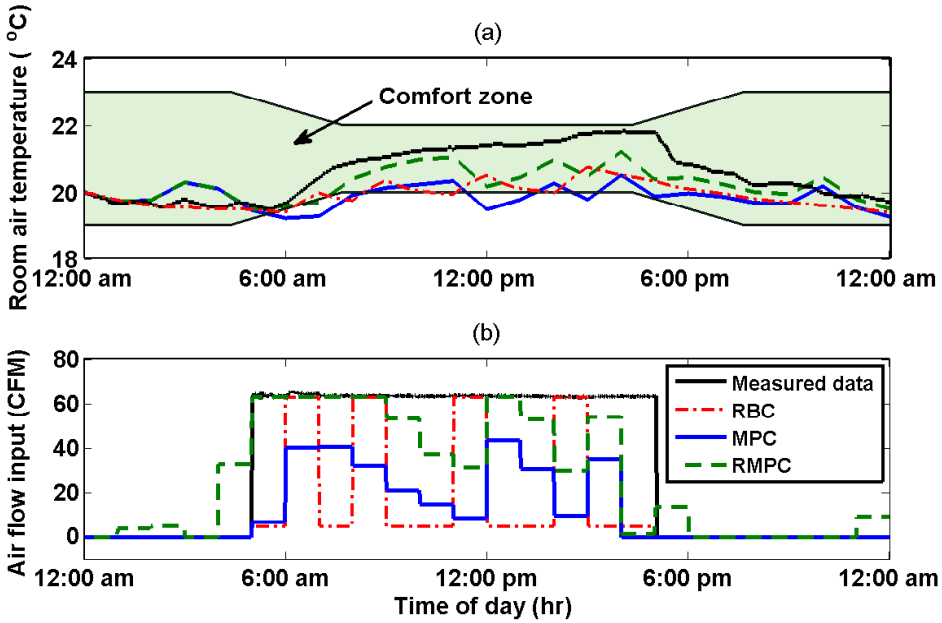

Figure 4.24: Control input and resulting temperature profile for the existing controller on the building (denoted as Measurements in the figure), RBC, MPC, and robust MPC controllers.($\delta = 60\%$)

Time constant $\Delta t = 1$ (hr) is used for all the following simulations. We implement the introduced model predictive controllers with a prediction horizon of $N = 24$. The choice of $N = 24$ is to provide a good balance between performance and computational cost for the MPC framework.

We use the following numerical values for parameters in (7.21). $\overline{\mathcal{U}} = 63$ CFM (0.03 m^3/s), and $\underline{\mathcal{U}} = 5$ CFM (0.002 m^3/s) are the lower and higher limit on air mass flow during occupied hours, $[\underline{T}_{.|t} \ \overline{T}_{.|t}] = [20 \ 22]^\circ\text{C}$ during occupied hours, and $[\underline{T}_{.|t} \ \overline{T}_{.|t}] = [19 \ 23]^\circ\text{C}$ is used during unoccupied hours. For the simulations we use $\kappa = 0.75$ and $\rho = 50$.

Optimal controller and the resulting room temperature with the presence of a box-constrained uncertainty in four cases are depicted in Figure 4.24. Measurements, as shown in black, shows the air mass flow and temperature recording for the room using a simple existing control policy of the building HVAC system which controls the fan speed by turning it on and off by the start and end time of occupancy hours. MPC and RMPC refer to algorithms described in Sections 4.4, and 4.5.

Controller performances are evaluated based on indices introduced in Sections 4.5.9, and 4.6.1 . We use YALMIP [48] to set up the MPC problem in MATLAB. Problem is solved using CPLEX 12.2 [10]. We performed mass simulations for different values of

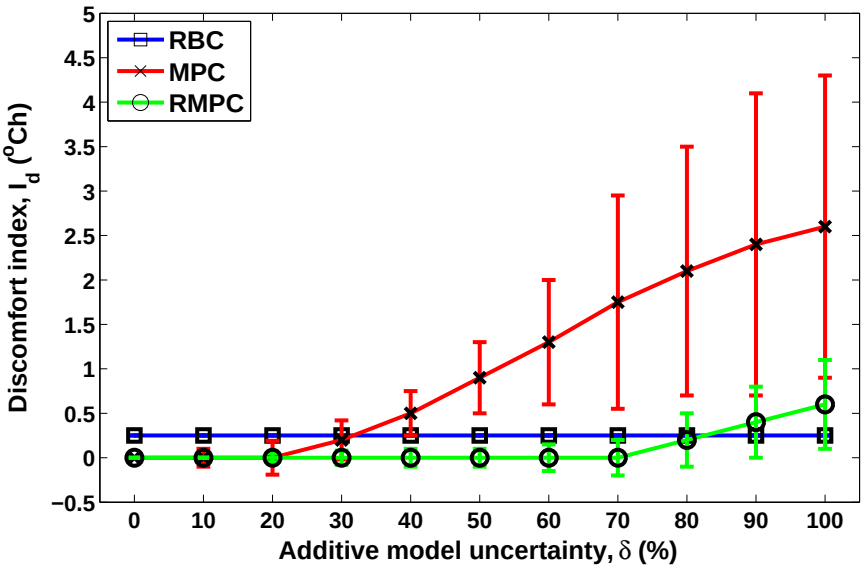

Figure 4.25: Discomfort index I_d versus additive model uncertainty (δ). We generate a uniform random sequences based on the model uncertainty value δ. The mean value (marker position) and standard deviation (error bar length) of discomfort are shown in the figure.

δ. Figure 4.25 and Figure 4.26 depict the results from these simulations. Monte Carlo simulations were performed to obtain the mean and standard deviation of energy and discomfort index for various values of model uncertainty.

Comfort: It can be observed from Figure 4.24 and Figure 4.25 that the RMPC is the only controller that is able to keep the temperature within the comfort zone, at all times, i.e. maintaining minimum level of discomfort ($I_d \leq I_d^*$) for all $\delta \leq 80\%$, while RBC still performs well, MPC fails to do so, resulting to $I_d > I_d^*$ for all $\delta \geq 40\%$. Figure 4.25 depicts how *discomfort index* I_d, varies with additive model uncertainty δ. As shown in Figure 4.25, RMPC manages to keep the perfect comfort level ($I_d = 0$), for additive model uncertainty up to $\delta = 70\%$, while the MPC maintains the perfect comfort level for uncertainty bounds up to $\delta = 20\%$. Since RBC is not a model-based control technique, its performance does not depend on values of δ, hence the straight horizontal line in Figure 4.25 ($I_d = 0.25$°Ch).

Energy Consumption: Figure 4.26 depicts the variations of *energy index* I_e, versus model uncertainty. It is clear that the energy index for RMPC increases dramatically with δ, while the energy index for MPC only changes slightly. However, this comes with the drawback of increased discomfort index for MPC. Figure 4.26 also shows energy consumption of RBC ($I_e = 1.43 \times 10^4$ kWh). MPC for all values

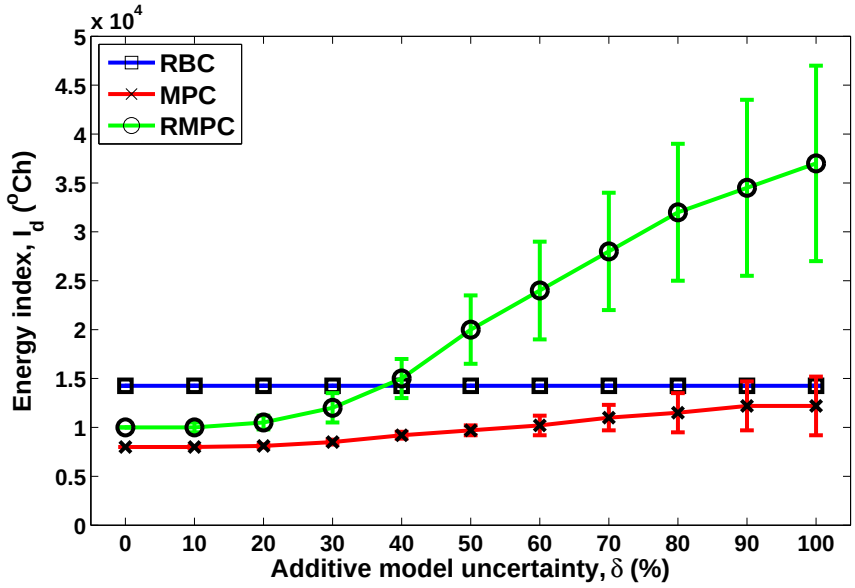

Figure 4.26: Energy index I_e versus additive model uncertainty (δ). We generate data with similar approach as in Figure 4.25.

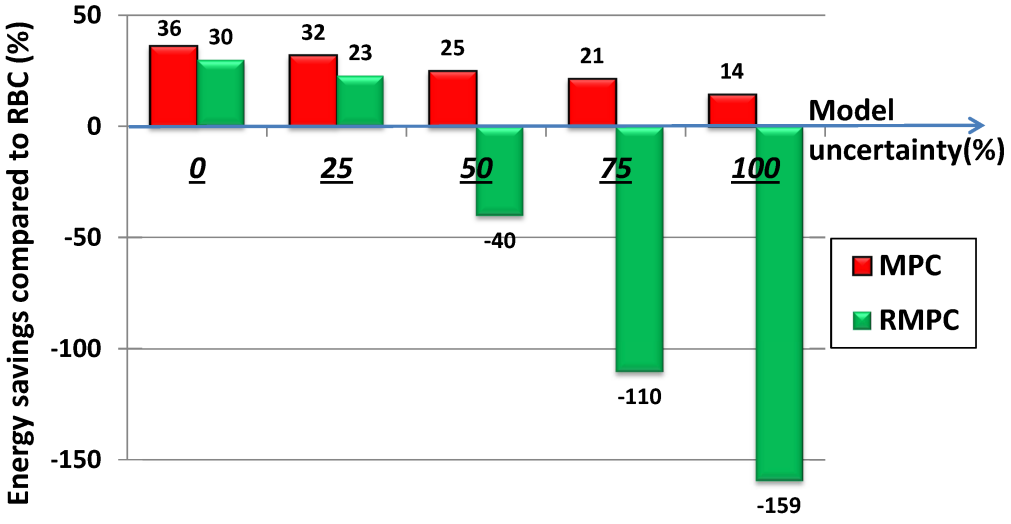

Figure 4.27: Energy saving of MPC and RMPC compared to RBC as a function of model uncertainty.

of δ leads to a lower amount of energy consumption than RBC, but RMPC leads to more energy consumption than RBC soon after $\delta = 40\%$.

Consider the case where $\delta = 70\%$. MPC will lead to a discomfort index of 1.7°Ch

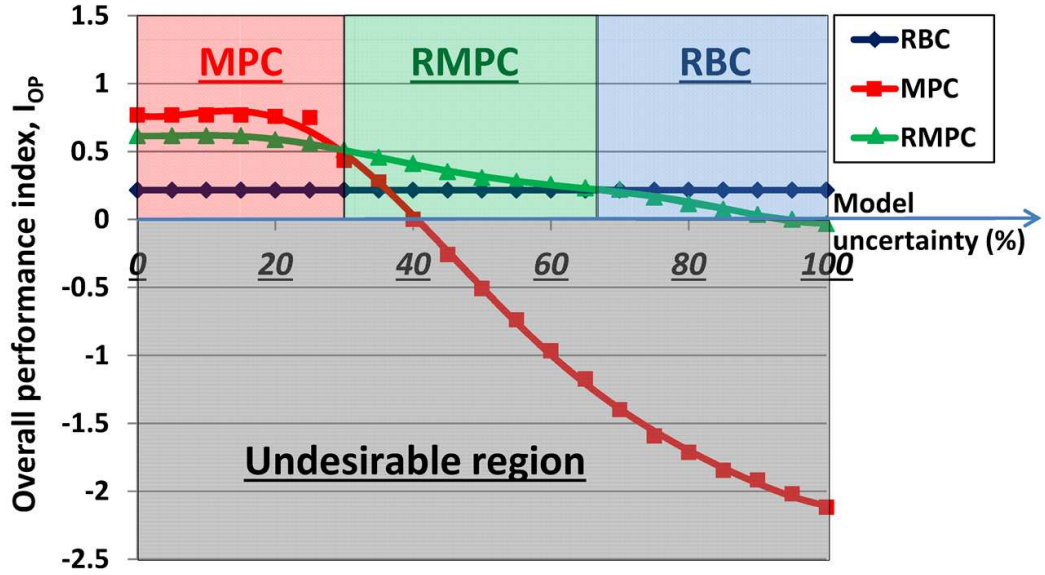

Figure 4.28: Overall performance index for RBC, MPC and RMPC as a function of model uncertainty. The red zone demonstrates the region which MPC outperforms RMPC and RBC as it yields a higher I_{OP}. The green zone represents the region that I_{OP} of RMPC is higher than that of MPC and RBC. RBC dominates in terms of I_{OP} in the blue zone. In the gray zone the resulting discomfort index is not acceptable.

on average, while the RMPC is able to maintain the temperature below a discomfort index of 0.016^oCh on average. However this level of comfort provided by the RMPC comes at a cost of energy consumption of more than 2 times of the MPC case.

Due to the trade-off between comfort and energy consumption, the choice of which controller to pick is not obvious, and depends on various factors such as criticality of meeting the temperature constraints for the considered thermal zone in the building, and price of energy at that time of the day/year, as well as uncertainty level of the model.

MPC and RMPC versus RBC: Figure 4.27 demonstrates savings of MPC and RMPC versus RBC. As shown, the maximum theoretical energy saving of MPC compared to RBC is 36%, and that of RMPC is 30% for the building studied. These saving values decrease as model uncertainty increases. Energy saving of MPC versus RBC stays positive for all values of model uncertainty, while energy saving of RMPC versus RBC is positive only for model uncertainty values up to about 34%, and is negative for larger model uncertainties (i.e. RMPC consumes more energy than RBC).

The result of an extensive study in [31] shows that MPC HVAC control can potentially provide 16%-41% building energy saving compared to rule-based controllers,

which complies with our findings. The saving also depends on various factors including climate zone, insulation level, and construction type.

For evaluation of energy consumption and provided comfort level, we have compared the overall performance of the three controllers using the overall performance index, I_{OP}. The results, as shown in Figure 4.28, suggest that for model uncertainties less than 30% MPC performs best among the three controllers studied here. For model uncertainties between 30% and 67% RMPC is the best, and for model uncertainties larger than 67%, RBC leads to better overall performance than model-based control techniques. This information can be of utility for choosing a controller type for building HVAC system based on how detailed and accurate the building model is, in capturing time-varying dynamics of a building.

Chapter 5

Co-Design of Controller and Embedded Platform

The design of heating, ventilation and air conditioning (HVAC) systems is crucial for reducing energy consumption in buildings. As complex cyber-physical systems, HVAC systems involve three closely-related subsystems – the control algorithm, the physical building and environment and the embedded implementation platform. In the traditional top-down approach, the control algorithm and the embedded platform are in general designed separately leading to sub-optimal systems. We propose a co-design approach that analyzes the interaction between the control algorithm and the embedded platform through a set of interface variables (in this paper we address in particular sensing accuracy). We present six control algorithms that take into account the sensing error, and model the relation of control performance and cost versus sensing error. We also capture the relation of embedded platform cost versus sensing error by analysis of the collected data from a testbed. Based on these models, we explore the co-design of the control algorithm and the temperature sensing subsystem of the embedded platform to optimize with respect to energy cost and monetary cost while satisfying the constraints for user comfort level. The material of this chapter is extracted from [61].

5.1 Introduction

Smart buildings today have sophisticated and distributed control systems as part of a Building Automation System (BAS). The task of a BAS is to maintain building climate within a specified range, control the lighting based on the occupancy schedule, and monitor the system performance and failures. To accomplish these tasks, a BAS has to deal with computation and communication non-idealities stemming from the

distributed nature of the implementation platform.

The design of HVAC systems involves three main subsystems – the physical building and its environment, the control algorithm that determines the system operations based on sensing inputs from the building and the environment, and the embedded platform that implements the control algorithm. In the traditional top-down approach, the design of the HVAC control algorithm is done without explicit consideration of the embedded platform. The underlying assumption is that the computation and communication capabilities of the embedded platform are sufficiently performing for any type of control mechanism. However, with the advent of more complex HVAC control algorithms for energy efficiency, the use of distributed networked platforms, and the imposition of tighter requirements for user comfort, this assumption on the embedded platform is no longer valid. Various aspects of the platform, including sensor accuracy and availability, communication channel reliability, and computing power of embedded processors, may have a significant impact on the quality and cost of a BAS. Thus, the design of the control algorithm should take into account the configuration of the implementation platform and *vice versa*, i.e., the control algorithm and the embedded platform should be *co-designed*.

In this chapter, we analyze the performance and energy cost of six HVAC control algorithms under different assumptions on temperature sensing accuracy. Indeed, we observed in our experiments that the accuracy of sensing data has significant impact on the control algorithms, to the extent that *different algorithms should be chosen depending on the different sensing accuracy of the implementation platform* . Based on this observation, we propose a framework to co-design the HVAC control algorithm with the part of the embedded platform that directly affects sensing accuracy – specifically the choices of sensor locations and the number of sensors. We believe this approach can be extended to a general framework for co-designing the control algorithm and the entire embedded platform. Figure 5.1 shows the structure of the co-design framework, with blocks in parentheses representing the focus of this paper.

As shown in Figure 5.1, the key aspects of the co-design process are 1) identifying the *interface variables* that are significant to both the control algorithm and the embedded platform, 2) designing the control algorithm with consideration of the interface variables and modeling the relation of control metrics (e.g. control performance) versus the interface variables, 3) capturing the relation of platform metrics (e.g. platform monetary cost) versus the interface variables, and 4) co-exploring the design of the control algorithm and the platform through the interface variables.

In this chapter, we focus on temperature sensing accuracy, which on one side significantly affects the control algorithm and on the other directly relates to the design of the sensing system. During the exploration of the design space, for any given monetary budget, we find the optimal choice of sensor locations and the number of sensors to maximize the accuracy of sensing data. Sensing accuracy is then used for

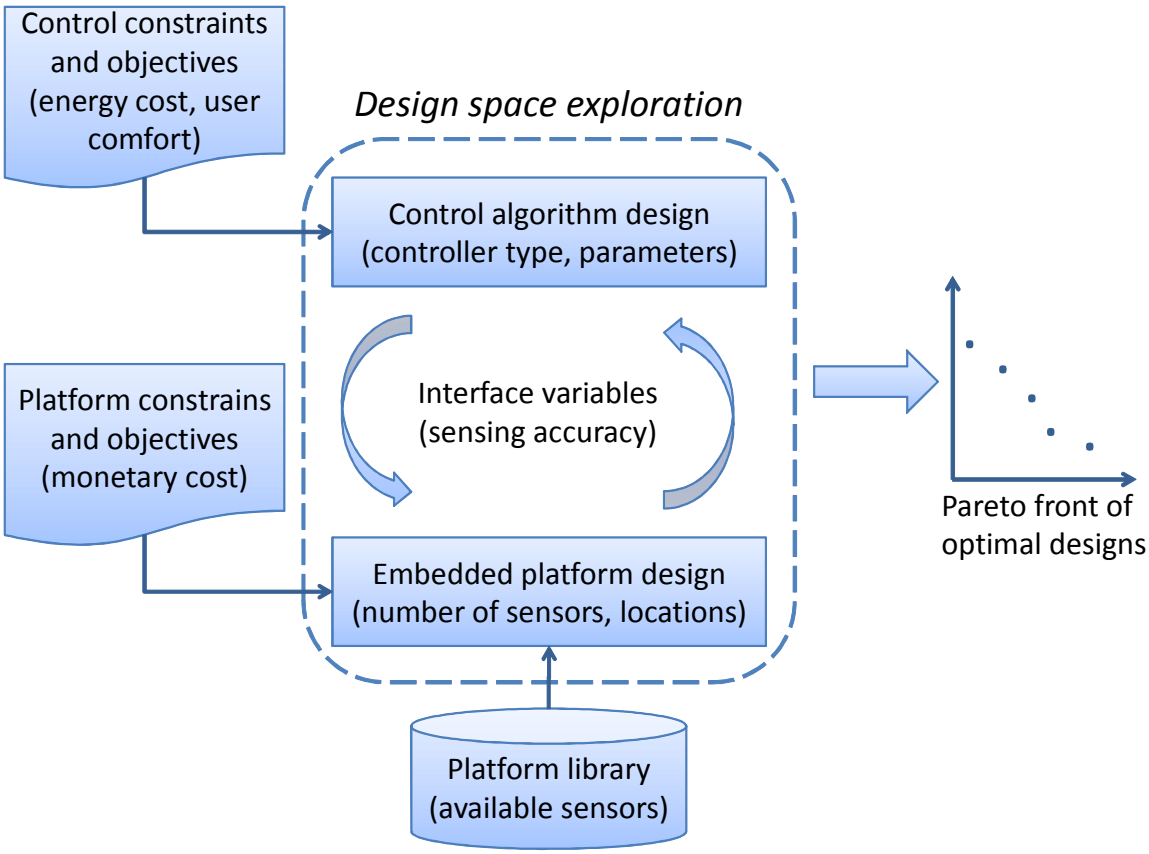

Figure 5.1: Co-design framework for HVAC systems

the selection of the HVAC control algorithm (from the six candidate controllers) to minimize energy cost while satisfying user comfort requirements. We set the monetary budget to a range of different values, and find the design that consumes the minimal energy for each given budget. The result of this design space exploration is a Pareto front of optimal monetary cost and energy cost.

Various models and control algorithms have been proposed in the literature for HVAC systems [56, 85, 67, 55, 53]. In a recent work, unscented Kalman filtering has been used for online estimation of building thermal parameter estimation [72]. The focus of these papers is on physical modeling and control design without taking into account the limitations of the embedded platform. For instance, in [54], weather and occupancy prediction uncertainties are considered in the control design process, and a robust model predictive control mechanism against prediction uncertainties is derived. However, the uncertainties (errors) from the embedded platform measurements are not addressed. Another set of papers [86, 87] focuses on the design of the embedded software and hardware for a given control algorithm, thus not addressing design space

exploration for optimal HVAC system design.

The main contributions of this chapter are the following:

- We propose six different control algorithms that take into account sensing accuracy, including two on-off controllers, two model predictive controllers (MPC) and two robust model predictive controllers (RMPC), each type with either extended Kalman filter (EKF) or unscented Kalman filter (UKF). We capture the relation between the control performance/cost and sensing accuracy in Simulink models for simulation.
- We establish the relation between sensing accuracy and the number and locations of temperature sensors, based on the analysis of measurement data collected from a well-instrumented testbed.
- We propose a framework for co-designing the control algorithm and the embedded platform, and apply it to a specific co-design case of the HVAC control algorithm (by choosing from the six candidate controllers) and the sensing system (by choosing the temperature sensor number and locations) to optimize energy and monetary cost.

The remainder of the chapter is organized as follows. Section 5.2 presents preliminaries. Section 5.3 addresses the modeling of sensing and prediction accuracy in the system dynamics. Section 5.4 presents the design of the control algorithms with EKF and UKF to address sensing accuracy, and demonstrate the impact of sensing accuracy on the control performance and cost. Section 5.5 introduces an approach for determining the relation between sensing accuracy and the number and locations of sensors. Section 5.6 explores the design space for both control algorithm and sensing system, based on the models we build in Section 5.4 and 5.5.

5.2 Preliminaries

We use the model that was proposed in Chapter 2, and [53] where a building is considered as a network. There are two types of nodes in the network: walls and rooms. There are in total n nodes, m of which represent rooms and the remaining $n-m$ nodes represent walls. The temperature of the i-th wall is governed by the following equation:

$$C_{w_i}\frac{dT_{w_i}}{dt} = \sum_{j\in\mathcal{N}_{w_i}}\frac{T_j - T_{w_i}}{R'_{ij}} + r_i\alpha_i A_i q''_{rad_i} \tag{5.1}$$

where T_{w_i}, C_{w_i}, α_i and A_i are the temperature, heat capacity, absorption coefficient and area of wall i, respectively. R'_{ij} is the total resistance between wall i and node j. q''_{rad_i} is the radiative heat flux density on wall i. $\mathcal{N}_{w_i}$ is the set of all of neighboring nodes to node w_i and, r_i is equal to 0 for internal walls, and to 1 for peripheral walls.

The temperature of the i-th room is governed by the following equation:

$$\begin{aligned} C_{r_i}\frac{dT_{r_i}}{dt} = &\sum_{j\in\mathcal{N}_{r_i}}\frac{T_j - T_{r_i}}{R'_{ij}} + \dot{m}_{r_i}c_a(T_{s_i} - T_{r_i}) \\ &+ w_i\tau_{w_i}A_{w_i}q''_{rad_i} + \dot{q}_{int_i} \end{aligned} \tag{5.2}$$

where T_{r_i}, C_{r_i} and $\dot{m}_{r_i}$ are the temperature, heat capacity and air mass flow into the room i, respectively. c_a is the specific heat capacity of air, A_{w_i} is the total area of window on walls surrounding room i, τ_{w_i} is the transmissivity of glass of window i, q''_{rad_i} is the radiative heat flux density radiated to room i, and $\dot{q}_{int_i}$ is the internal heat generation in room i. $\mathcal{N}_{r_i}$ is the set of all of the neighboring nodes to room i. w_i is equal to 0 if none of the walls surrounding room i has window, and is equal to 1 if at least one of them has. The details of building thermal modeling and estimation of the un-modeled dynamics is presented in [56, 53, 55]. Note that we estimate the values of $q''_{rad_i}(t)$ and $\dot{q}_{int}(t)$ based on the following equations.

$$q''_{rad_i}(t) = \tau\hat{T}_{out}(t) + \zeta \tag{5.3}$$

$$\dot{q}_{int}(t) = \mu\hat{\Psi}(t) + \nu \tag{5.4}$$

where $\hat{T}_{out}$ and $\hat{\Psi}$ are the (actual) outside air temperature and CO_2 concentration in the room. Parameters τ, ζ, μ and ν are obtained by the parameter estimation algorithm detailed in [55].

The heat transfer equations for each wall and room yields tothe following state space form of the system dynamics

$$\begin{aligned} \dot{x}_t &= f(x_t, u_t, \hat{d}_t) \\ y_t &= Cx_t \end{aligned} \tag{5.5}$$

where $x_t \in \mathbb{R}^n$ is the state vector representing the temperature of the nodes in the thermal network, $u_t \in \mathbb{R}^{lm}$ is the input vector representing the air mass flow rate and discharge air temperature of conditioned air into each thermal zone, and $y_t \in \mathbb{R}^m$ is the output vector of the system which represents the temperature of the thermal zones. l is the number of inputs to each thermal zone (e.g., air mass flow and supply air temperature). C is a matrix of proper dimension and the disturbance vector is $\hat{d}_t = g(q''_{rad_i}(t), \dot{q}_{int}(t), \hat{T}_{out}(t))$, where g is approximated as a linear function. This leads to

$$\hat{d}_t = aq''_{rad_i}(t) + b\dot{q}_{int}(t) + c\hat{T}_{out}(t) + e \tag{5.6}$$

By substituting (5.3) and (5.4) into (5.6) and massaging the resulting equation we get

$$\begin{aligned}\hat{d}_t &= (a\tau + c)\hat{T}_{out}(t) + b\mu\hat{\Psi}(t) + a\zeta + b\nu + e \\ &= \bar{a}\hat{T}_{out}(t) + \bar{b}\hat{\Psi}(t) + \bar{e}\end{aligned} \tag{5.7}$$

where $\bar{a} = a\tau + c$, $\bar{b} = b\mu$, and $\bar{e} = a\zeta + b\nu + e$.

In what follows we use linearized system dynamics for control design. However, the original non-linear model is used for state estimation and filtering and as the plant to compute the actual temperature evolution. System dynamics is linearized around the nearest equilibrium point, by starting from an initial point and searching, using a *Sequential Quadratic Programming (SQP) algorithm*, until it finds the nearest equilibrium point to the specified operating point of the system (details in [56]). Discretizing the state space realization using zero-order hold leads to the following discrete time LTI system:

$$\begin{aligned}x_{k+1} &= Ax_k + Bu_k + E\hat{d}_k \\ y_k &= Cx_k\end{aligned} \tag{5.8}$$

From this equation, we introduce the modeling of sensing and prediction accuracy, as shown in Section 5.3.

5.3 Sensing and Prediction Accuracy Modeling

5.3.1 Sensing Accuracy

In this paper, we focus on temperature sensing accuracy to determine the noise characteristics of the indoor temperature (x_k in (5.8)), which drives the design of the control algorithms (see Section 5.4).

Measurement inaccuracies of individual sensors can be categorized into the following three types: no information, completely incorrect information, and incorrect but in-range information. The error of the indoor temperature estimation, denoted by ϵ^{rt}, is affected by accuracy of individual sensors, number and locations of sensors in a thermal zone, and physical properties of the building. Statistics of ϵ^{rt} may be extracted from historical data as shown in Section 5.5.2, and we assume it is additive to the temperature measurement. Accordingly, the temperature measurement in (5.8) is updated as $z_k = Cx_k + F\epsilon_k^{rt}$. Where F is a matrix of proper dimension and z_k is the temperature reading at time k.

5.3.2 Prediction Accuracy

Disturbance prediction ($\hat{d}_k$ in (5.8)) in our model depends on the prediction of CO2 concentration level in the room (Ψ) and on the prediction of ambient air temperature (T_{out}) as shown in (5.7). We use ϵ_k^c to denote the error in CO2 level prediction, and hence the predicted CO2 level is

$$\Psi(k) = \hat{\Psi}(k) + \epsilon_k^c \tag{5.9}$$

and ϵ_k^{ot} to denote the error in ambient air temperature prediction, and hence the predicted ambient temperature is

$$T_{out}(k) = \hat{T}_{out}(k) + \epsilon_k^{ot} \tag{5.10}$$

Based on (5.7), disturbance prediction can be expressed using CO2 and ambient temperature prediction errors

$$\begin{aligned} \hat{d}_k &= \bar{a}\hat{T}_{out}(k) + \bar{b}\hat{\Psi}(k) + \bar{e} \\ &= \bar{a}(T_{out}(k) - \epsilon_k^{ot}) + \bar{b}(\Psi(k) - \epsilon_k^c) + \bar{e} \\ &= d_k - (\bar{a}\epsilon_k^{ot} + \bar{b}\epsilon_k^c) \end{aligned} \tag{5.11}$$

where d_k denotes the predicted disturbance at time step k. The above equation suggests that the disturbance prediction error, denoted by w_k, is a linear combination of the CO2 prediction error, ϵ_k^c, and the ambient air temperature prediction error, ϵ_k^{ot}. This leads to the following state update and output measurement equation (modified from (5.8))

$$\begin{aligned} x_{k+1} &= Ax_k + Bu_k + E(d_k - w_k) \\ z_k &= Cx_k + Fv_k \end{aligned} \tag{5.12}$$

where $w_k = -\xi(\bar{a}\epsilon_k^{ot} + \bar{b}\epsilon_k^c)$ and the constant ξ is a function of the discretization method and step of the continuous system dynamics, and $v_k = \epsilon_k^{rt}$ (i.e. the temperature measurement error). The CO2 and ambient air temperature forecast errors are *uncorrelated* random variables with variance σ_c and σ_{ot}, respectively. Hence, variance of w_k is calculated by

$$\begin{aligned} \sigma_w &= \mathbb{E}[(w - \hat{w})(w - \hat{w})^T] \\ &= \mathbb{E}\left\{[-\xi(\bar{a}\tilde{\epsilon}^{ot} + \bar{b}\tilde{\epsilon}^c)][-\xi(\bar{a}\tilde{\epsilon}^{ot} + \bar{b}\tilde{\epsilon}^c)]^T\right\} \\ &= \xi^2(\bar{a}^2\sigma_c + \bar{b}^2\sigma_{ot}) \end{aligned} \tag{5.13}$$

where $\tilde{\epsilon}^{ot} = \epsilon^{ot} - \hat{\epsilon}^{ot}$ and $\tilde{\epsilon}^c = \epsilon^c - \hat{\epsilon}^c$. In this paper, we assume typical values for σ_{ot}, σ_c and other constants in simulations: $\sigma_{ot} = 2$, $\sigma_c = 50$, $\bar{a} = 0.01$, $\bar{b} = 0.06$ and $\xi = 10$.

If CO2 and temperature sensors are deployed to facilitate the predictions of CO2 level and ambient air temperature, the values of σ_{ot} and σ_c will be largely affected by the choice of CO2 and temperature sensor type, number and locations.

5.4 Control Algorithms

5.4.1 Controller Design

In typical buildings, the temperature of air in rooms and in AC ducts is measured. These measurements are normally inaccurate and noisy due to the effects enumerated in Section 5.3.1. Also temperatures of the *slow dynamic* states, which include walls, ceiling and furniture, are not easy to measure. For simpler controllers such as on-off controllers, just filtering the measurement may be sufficient for control purposes. However, in the case of more sophisticated controllers such as model predictive controllers (MPC), estimation of temperature of all the states is required, including the states whose temperature cannot be measured. In this paper we use Kalman filtering technique to estimate and filter the states of system using available measurements. To the best of our knowledge, the effectiveness of Kalman filtering for *state* estimation and control applications in the presence of noisy data in buildings has not been explored. We consider three controllers: On-off[1], MPC and RMPC.

On-off Controller

The on-off controller is designed in a way that the valves can have three states: fully opened, minimally opened[2] during occupied hours, or fully closed at night. The duration of each state of the valve cannot be less than 1 hour, in order to be consistent with the actuation time step of other controllers. The controller turns on the heating mode when the room temperature falls below the lower limit and turns it to either minimally open or fully closed (depending on whether it is occupied or unoccupied hours of the day) when the temperature is within the comfort zone, and turns on the cooling mode if the temperature goes above the higher limit.

MPC Formulation

A model predictive control problem is formulated with the objective of minimizing a linear combination of total energy consumption and peak airflow. The fan energy consumption is proportional to the *cube* of the airflow, hence minimizing the peak airflow would dramatically reduce fan energy consumption. We consider a cost function for the MPC which includes a linear combination of the total heating flow into the building in the form of hot air (given by l_1-norm of input) and the peak of airflow (given by l_∞-norm of input)[3]. To guarantee feasibility (constraint satisfaction) at all

[1] Other controllers such as PI could also be used here.

[2] Not fully closed due to ventilation and air quality reasons.

[3] Note that using l_1 and l_∞ norms in the cost function, leads to an LP which can be solved very efficiently for even very large dimensions.

times we use soft constraints. The predictive controller solves at each time step the following problem

$$\begin{aligned}
\min_{U_t,\bar{\Theta}_t,\underline{\Theta}_t} \quad & \{|U_t|_1 + \kappa|U_t|_\infty + \rho(|\overline{\Theta}_t|_1 + |\underline{\Theta}_t|_1)\} \\
\text{s.t.} \quad & x_{t+k+1|t} = Ax_{t+k|t} + Bu_{t+k|t} + Ed_{t+k|t} \\
& y_{t+k|t} = Cx_{t+k|t} \\
& \underline{\mathcal{U}}_{t+k|t} \leq u_{t+k|t} \leq \overline{\mathcal{U}}_{t+k|t} \\
& \underline{T}_{t+k|t} - \underline{\theta}_{t+k|t} \leq y_{t+k|t} \leq \overline{T}_{t+k|t} + \overline{\theta}_{t+k|t} \\
& \underline{\theta}_{t+k|t}, \overline{\theta}_{t+k|t} \geq 0
\end{aligned} \tag{5.14}$$

where $U_t = [u_{t|t}, u_{t+1|t}, \cdots, u_{t+N-1|t}]$ stores the control inputs, $\underline{\Theta}_t = [\underline{\theta}_{t+1|t}, \cdots, \underline{\theta}_{t+N|t}]$ and $\overline{\Theta}_t = [\overline{\theta}_{t+1|t}, \cdots, \overline{\theta}_{t+N|t}]$ are the temperature violations from the lower and upper bounds, respectively. $y_{t+k|t}$ is the thermal zone temperature, and $d_{t+k|t}$ is the disturbance load prediction. $\underline{T}_{t+k|t}$ and $\overline{T}_{t+k|t}$ are the lower and upper bounds on the zone temperature, respectively. $\underline{\mathcal{U}}_{t+k|t}$ and $\overline{\mathcal{U}}_{t+k|t}$ are the lower and upper limit on airflow input by the VAV damper, respectively. Note that based on American Society of Heating Refrigeration and Air conditioning Engineers (ASHRAE) requirements for *air change per hour* (ACH) of rooms, there has to be a minimum *non-zero* airflow during occupied hours for ventilation purposes. ρ is the penalty on the comfort constraint violations, and κ is the penalty on peak power consumption. We use $\rho = 1000$ and $\kappa = 15$, and prediction horizon of N=24 for simulations.

RMPC Formulation

A typical robust strategy involves solving a min-max problem to optimize worst-case performance, while enforcing input and state constraints for all possible disturbances. In particular, we formulate the RMPC to minimize energy consumption of the HVAC system and satisfy the temperature and input constraints against additive bounded input uncertainties. Define the worst-case cost function as

$$\begin{aligned}
& J_t(x(t), U_t) \triangleq \\
& \max_{w_{[.]}} \{||Pz_{t+N|t}||_p + \sum_{k=0}^{N-1} ||Qz_{t+k|t}||_p + ||Ru_{t+k|t}||_p\} \\
\text{s.t.} \quad & x_{t+k+1|t} = Ax_{t+k|t} + Bu_{t+k|t} + E(d_{t+k|t} - w_{t+k|t}) \\
& z_{t+k|t} = Cx_{t+k|t} + Fv_{t+k|t} \\
& w_{t+k|t} \in \mathcal{W} \quad \& \quad v_{t+k|t} \in \mathcal{V} \\
& \forall \quad k = 0, 1, \cdots, N-1
\end{aligned} \tag{5.15}$$

where $||.||_p$ can be any polytopic norm. The robust optimal control problem is formulated as follows

$$\begin{aligned} J_t^*(x(t)) \triangleq \quad & \min_{U_t} \quad J_t(x(t), U_t) \\ \text{s.t.} \quad & x_{t+k+1|t} = Ax_{t+k|t} + Bu_{t+k|t} + Ed_{t+k|t} \\ & z_{t+k|t} = Cx_{t+k|t} + Fv_{t+k|t} \\ & u_{t+k|t} \in \mathcal{U} \quad \& \quad x_{t+k|t} \in \mathcal{X} \\ & \forall \ w_{t+k|t} \in \mathcal{W} \quad \& \quad \forall \ v_{t+k|t} \in \mathcal{V} \\ & \forall \quad k = 0, 1, \cdots, N-1 \end{aligned} \tag{5.16}$$

At each time step t, the first entry of U_t is implemented on the plant. At the next time step the prediction horizon N is shifted leading to a new optimization problem. This process is repeated until the time span of interest is covered.

We utilize Closed-Loop (CL) formulation, which is less conservative than the Open-Loop (OL) [54]. Performance improvement (less conservativeness) is gained due to the fact that in CL, future measurements are taken into account for calculating the control policy. We use the feedback predictions to approximate the solution to the CL problem. We utilize the TLDS parameterization introduced in [54].

Extended Kalman Filter

Due to the nonlinearity of the state update equations for the HVAC system, we use the Extended Kalman Filter (EKF)[4]. Note that EKF can be used due to the differentiability of the state update model.

The KF design requires state-space model of the system and two design parameters: the covariances of the *process noise* and the *measurement noise*, which in our problem correspond to the covariances of the prediction error w_k and the temperature measurement error v_k.

EKF Formulation In EKF, the state transition and observation models need not be linear functions, but may instead be differentiable functions. the stochastic state-space model is given by

$$\begin{aligned} x_k &= f(x_{k-1}, u_{k-1}, d_{k-1}, w_{k-1}) \\ z_k &= h(x_k) + v_k \end{aligned} \tag{5.17}$$

[4]The extended Kalman filter (EKF) is probably the most widely used estimation algorithm for nonlinear systems [38].

where w_k and v_k are the process and measurement noise which are assumed to be zero mean, independent and identically distributed (IID) multivariate Gaussian with covariance W_k and V_k respectively (i.e. $w_k \sim \mathcal{N}(0, W_k)$ and $v_k \sim \mathcal{N}(0, V_k)$).

Function f is used to compute the predicted state from the previous estimate and function h is used to compute predicted measurement from predicted state. However, nonlinear functions f and h cannot be applied to the covariance directly. Instead the Jacobian of these functions which is a matrix of partial derivatives is computed.

EKF Algorithm The KF consists of two steps – *prediction* followed by *update*. In the prediction step, the filter propagates the estimate from a previous time step $k-1$ to the current time step k. The EKF algorithm is as follows. At each time step, first the *a-priori* state estimate is predicted

$$\hat{x}_{k|k-1} = f(\hat{x}_{k-1|k-1}, u_{k-1}, d_{k-1}, 0) \tag{5.18}$$

and then state transition and observation matrices are computed using the *a-priori* state estimation

$$F_{k-1} = \frac{\partial f}{\partial x}|_{\hat{x}_{k-1|k-1}, u_{k-1}} \qquad H_k = \frac{\partial h}{\partial x}|_{\hat{x}_{k|k-1}} \tag{5.19}$$

then *a-priori* state estimation error covariance is predicted

$$P_{k|k-1} = F_{k-1} P_{k-1|k-1} F_{k-1}^T + W_{k-1} \tag{5.20}$$

and also the *a-priori* output estimation error (i.e. innovation or measurement residual) is computed

$$\tilde{y}_k = z_k - h(\hat{x}_{k|k-1}) \tag{5.21}$$

innovation or residual covariance is computed using the *a-priori* state estimation error covariance given by (5.20)

$$S_k = H_k P_{k|k-1} H_k^T + V_k \tag{5.22}$$

the near-optimal Kalman gain is obtained by using the value of S_k

$$K_k = P_{k|k-1} H_k^T S_k^{-1} \tag{5.23}$$

and finally *a-posteriori* state estimate and the *a-posteriori* state estimation error covariance are updated using

$$\hat{x}_{k|k} = \hat{x}_{k|k-1} + K_k \tilde{y}_k \tag{5.24}$$

$$P_{k|k} = (I - K_k H_k) P_{k|k-1} \tag{5.25}$$

Note that matrix inversion can be computationally expensive for large matrices. Therefore, in order to make the computations more efficient, from both an execution time and numerical accuracy standpoint, we utilize the *back substitution* technique with the help of the *Cholesky factorization* and perform the following operations (5.26), (5.27), (5.28), (5.29) substituting the steps explained in (5.23), (5.24). This method solves the problem using Gaussian elimination, without forming the inverse of the matrix.

$$R_k = chol(S_k) \tag{5.26}$$
$$U_k = P_{k|k-1}H_k^T/V_k \tag{5.27}$$
$$\hat{x}_{k|k} = \hat{x}_{k|k-1} + U_k(V_k^T \backslash \tilde{y}_k) \tag{5.28}$$
$$P_{k|k} = P_{k|k-1} - U_k U_k^T \tag{5.29}$$

where the $chol()$ operator performs the Cholesky factorization of its argument resulting in an upper triangular matrix. / and \ perform right and left matrix division, respectively.

Once the state is estimated and filtered, the state estimate $\hat{x}_{k|k}$ is used in the control design, for all the cases of On-off, MPC and RMPC. Then the control action u_k is computed based on this estimate. At the next time step, $\hat{x}_{k|k}$ and u_k are fed to the EKF algorithm to estimate the state at the next time step, and this process is repeated over.

Simulation results Figure 5.2 illustrates the simulated room temperature and air flow inputs of the MPC with EKF over one day period. The prediction error and the temperature measurement error are assumed to be $||w||_\infty = 0.9$ and $||v||_\infty = 0.8$, respectively.

Unscented Kalman Filter

A nonlinear KF that shows promise as an improvement over the EKF is the unscented Kalman filter (UKF). The basic premise behind the UKF is that it is easier to approximate a Gaussian distribution than to approximate an arbitrary nonlinear function. The UKF addresses the approximation issues of the EKF. Instead of using Jacobian matrix, UKF uses a deterministic sampling approach to capture the mean and covariance estimates with a minimal set of sample points [81]. As with the EKF, we present an algorithmic description of the UKF, omitting some theoretical considerations. More details can be found in [37, 39].

UKF Formulation The state distribution is represented by a Gaussian random variable (GRV), but is now specified using a minimal set of carefully chosen sample

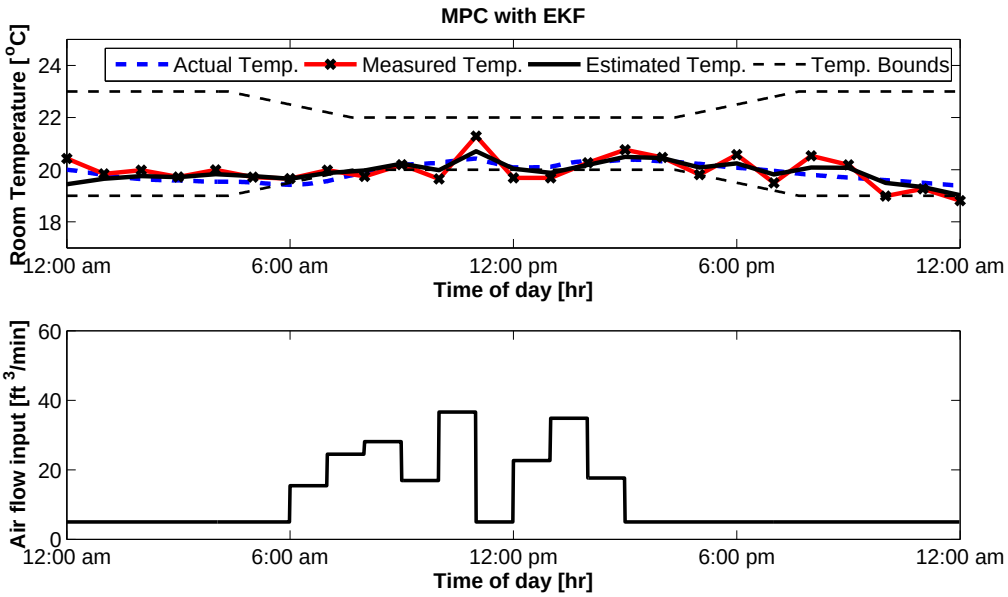

Figure 5.2: MPC with EKF for estimation and filtering. Performance of EKF-MPC over a range of temperature measurement error values are presented in Figure 5.4 and Figure 5.5.

points. These sample points completely capture the true mean and covariance of the GRV, and when propagating through the true nonlinear system, capture the posterior mean and covariance accurately to the 3rd order (Taylor series expansion) for any nonlinearity. To elaborate on this, we start by first explaining the Unscented Transformation(UT). The UT is a method for calculating the statistics of a random variable which undergoes a nonlinear transformation[37].

UKF Algorithm First, we conduct the following initialization

$$\hat{x}_0 = \mathbb{E}[x_0] \tag{5.30}$$

$$P_0 = \mathbb{E}[(x_0 - \hat{x}_0)(x_0 - \hat{x}_0)^T] \tag{5.31}$$

Given the state vector at step $k-1$, we then compute a collection of sigma points, stored in the columns of the $L \times (2L+1)$ sigma point matrix $\mathcal{X}_{k-1}$, where L is the dimension of the state vector.

$$\mathcal{X}_{k-1} = [\hat{x}_{k-1} \quad \hat{x}_{k-1} + \gamma\sqrt{P_{k-1}} \quad \hat{x}_{k-1} - \gamma\sqrt{P_{k-1}}] \tag{5.32}$$

where $\gamma = \sqrt{(L+\lambda)}$, and $\lambda = \alpha^2(L+\delta) - L$ is the composite scaling parameter. α is a scaling parameter that determines the spread of the sigma points around $\hat{x}$, and

is usually set to a small positive value (e.g. $1e-4 \leq \alpha \leq 1$). δ is a secondary scaling parameter which is usually set to 0 or $3-L$ [39]. Then we propagate each column of $\mathcal{X}_{k-1}$ through time by Δt using the system dynamics, i.e. $(\mathcal{X}_k)_i = f((\mathcal{X}_{k-1})_i)$ for $i = 0, 1, ..., 2L$, where f is given by (5.5). Having calculated $\mathcal{X}_i$, the *a-priori* state estimate is given by

$$\hat{x}_k^- = \sum_{i=0}^{2L} W_i^{(m)} (\mathcal{X}_k)_i \tag{5.33}$$

where $W_i^{(m)}$ are weights defined by

$$W_i^{(m)} = \begin{cases} \frac{\lambda}{(L+\lambda)}, & \text{if } i = 0 \\ \frac{1}{2(L+\lambda)}, & \text{if } i = 1, 2, ..., 2L \end{cases}$$

and the *a-priori* error covariance is calculated by

$$P_k^- = \sum_{i=0}^{2L} W_i^c [(\mathcal{X}_k)_i - \hat{x}_k^-][(\mathcal{X}_k)_i - \hat{x}_k^-]^T + Q_k \tag{5.34}$$

where Q_k is the process error covariance matrix. The $W_i^{(c)}$ weights are defined by

$$W_i^{(c)} = \begin{cases} \frac{\lambda}{L+\lambda} + (1 - \alpha^2 + \beta), & \text{if } i = 0 \\ \frac{1}{2(L+\lambda)}, & \text{if } i = 1, 2, ..., 2L \end{cases}$$

where β is a parameter used to incorporate the prior knowledge of the distribution of x. We use $\beta = 2$ which is optimal for Gaussian distributions [82].

In the *update* step, we fist transform the columns of $\mathcal{X}_k$ through the measurement function. Hence

$$(\mathcal{Z}_k)_i = h((\mathcal{X}_k)_i) \quad i = 0, .., 2L \tag{5.35}$$

$$\hat{z}_k^- = \sum_{i=0}^{2L} W_i^{(m)} (\mathcal{Z}_k)_i \tag{5.36}$$

then we compute the *a-posteriori* state estimate using $\hat{x}_k = \hat{x}_k^- + K_k(z_k - \hat{z}_k^-)$ where K_k is the Kalman gain defined by

$$K_k = P_{\hat{x}_k \hat{z}_k} P_{\hat{z}_k \hat{z}_k}^{-1} \tag{5.37}$$

$$P_{\hat{x}_k \hat{z}_k} = W_i^c [(\mathcal{X}_k)_i - \hat{x}_k^-][(\mathcal{Z}_k)_i - \hat{z}_k^-]^T \tag{5.38}$$

$$P_{\hat{z}_k \hat{z}_k} = \sum_{i=0}^{2L} W_i^c [(\mathcal{Z}_k)_i - \hat{z}_k^-][(\mathcal{Z}_k)_i - \hat{z}_k^-]^T + R_k \tag{5.39}$$

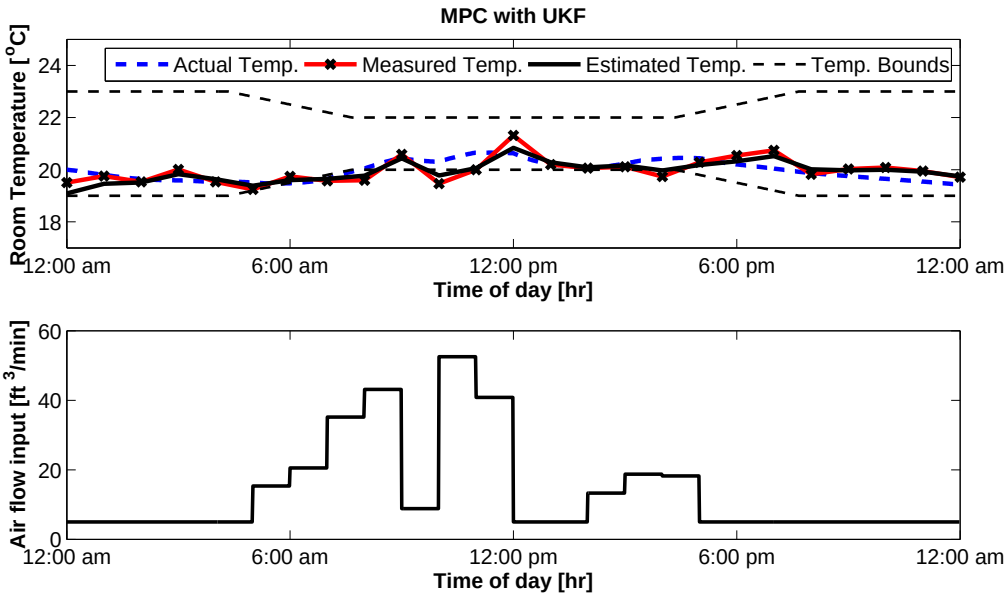

Figure 5.3: MPC with UKF for estimation and filtering. Performance of UKF-MPC over a range of temperature measurement error values are presented in Figure 5.4 and Figure 5.5.

where R_k is the measurement noise covariance matrix. The *a-posteriori* estimate of the error covariance is given by

$$P_k = P_k^- - K_k P_{\hat{z}_k \hat{z}_k} K_k^T \tag{5.40}$$

Simulation Results Figure 5.3 illustrates the simulated room temperature and air flow inputs of the MPC with UKF over one day period. The prediction error and the temperature measurement error values are assumed to be $||w||_\infty = 0.9$ and $||v||_\infty = 0.8$, respectively.

5.4.2 Control Cost and Performance vs. Sensing Accuracy

For each controller designed in Section 5.4.1, we simulate the energy cost and performance (measured by a discomfort index)[5] with respect to different levels of sensing accuracy.

Figure 5.4 and Figure 5.5 show the energy cost and discomfort index of the six controllers with either EKF or UKF under different levels of sensing accuracy from 0% to 100%. Note that we use a normalized uncertainty based on the maximum

[5]For detailed discussion on *energy cost* and *discomfort index*, refer to [55].

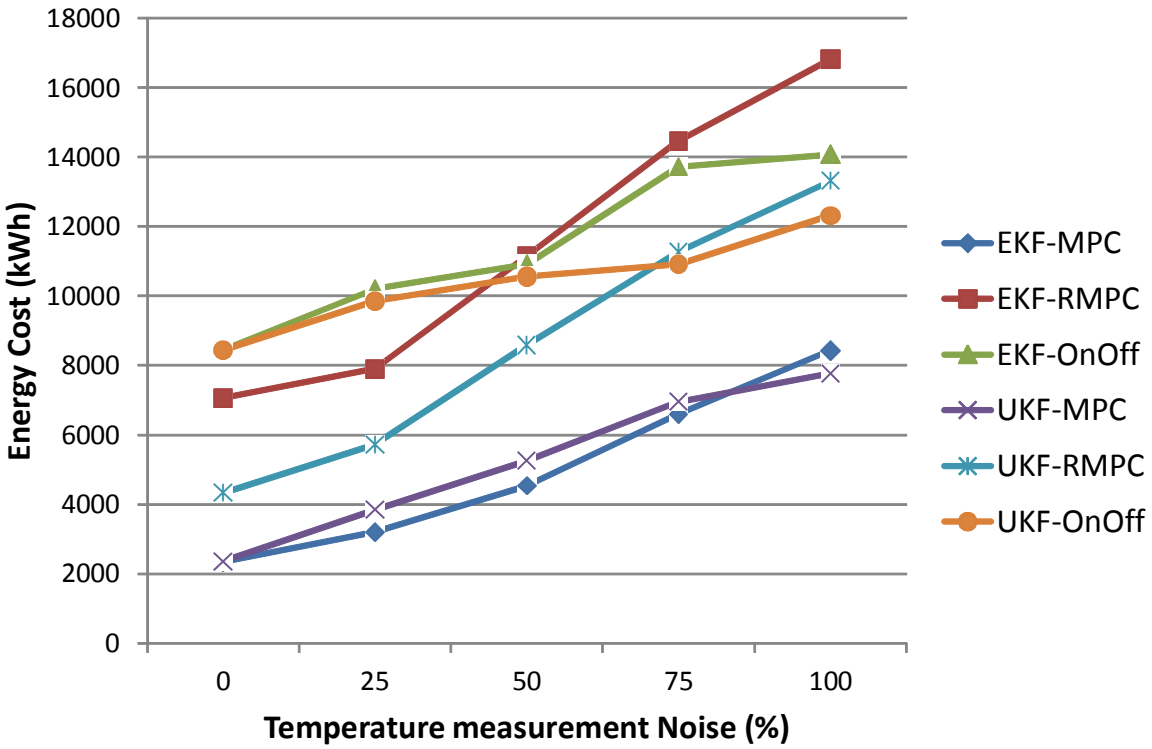

Figure 5.4: Energy cost vs. measurement noise

value of the disturbance. For instance, measurement error of 50% corresponds to $||w||_\infty = 0.5 * ||\hat{d}||_\infty$. More details can be found in [54].

From these results, we can see that some controllers are always superior to some other controllers in terms of both energy cost and discomfort index. For instance, the two MPC controllers are better than the two On-Off controllers. However, in other cases, particularly among MPC and RMPC controllers, choosing which controller to use depends on *the design requirements and the measurement noise and error (which is affected by the embedded platform)*. For instance, let us assume there is a requirement that the maximum discomfort level should be under 0.3. If we choose a number of accurate sensors and we estimate that noise will be under 25%, then we select EKF-MPC since it consumes the least amount of energy while satisfying the requirement. If we choose less accurate (or fewer) sensors to reduce platform cost and we estimate that noise will be around 75% , then we select UKF-RMPC since it consumes the least energy among the schemes that satisfy the comfort level requirement (the other being EKF-RMPC).

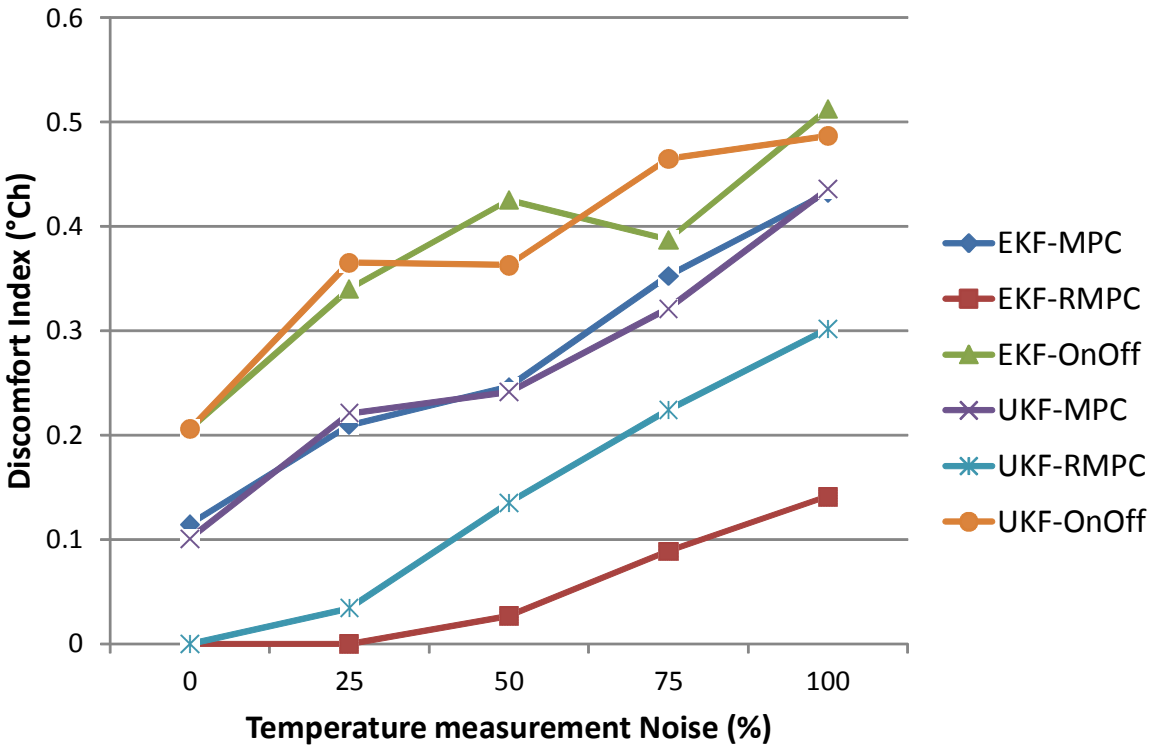

Figure 5.5: Discomfort index vs. measurement noise

5.5 Sensing System Design and Sensing Accuracy

The relation between sensing system design and temperature sensing accuracy, i.e. the temperature measurement error v_k in (5.12) is quite important in the overall performance of the HVAC system. In this paper, we collect measurements from multiple temperature sensors in a test-bed and analyze their statistics to estimate sensing accuracy under different number of sensors and locations. This approach may be applied in practice if the designer has access to the target building (or buildings/testbeds with similar characteristics) and can deploy sensors for testing, otherwise simulation approaches such as computational fluid dynamics (CFD) analysis may be applied.

5.5.1 BubbleZERO Test-bed Setup

Our test-bed BubbleZERO (shown in Figure 5.6) is an experimental building and laboratory, and is conceived as part of the Low Exergy Module development for Future Cities Laboratory (FCL) [2]. The BubbleZERO was constructed by ETH Zurich with concrete floor and ceiling as well as LowEx systems installed along with an experimental chiller. It is currently installed on the NUS campus in Singapore. It

Figure 5.6: BubbleZERO test-bed owned by Future Cities Lab of ETH Zurich, and located on the campus of National University of Singapore.

provides extensive opportunities to test and evaluate the performance of sensing and control systems as well as low energy systems.

Deployed instruments with a network of wireless sensors provides instant and interactive information on multiple dimensions of the building environment. The use of wireless sensor network systems is well suited for future building operation with its low-cost, low energy, easy-to-deploy, flexibility, and closed-loop sensing and control features. Figure 5.8 shows the system structure. The system is built based on the open source wireless sensor network platform Telosb [70], and the software is developed based on the TinyOS [45] operating system. Each sensor node is powered with an embedded CPU, equipped with a wireless communication module for intercommunication, and various interfaces and sensors.

The system contains 4 sub-systems as shown in Figure 5.8. The Environment Sensing System senses the indoor and outdoor ambient parameters. Temperature and humidity are monitored for both indoor and outdoor, while CO2 concentration is collected for indoor. The environment sense system includes 8 indoor sensors, 4 CO2 concentration sensors and 4 outdoor sensors. The 8 indoor sensors (Telosb41-

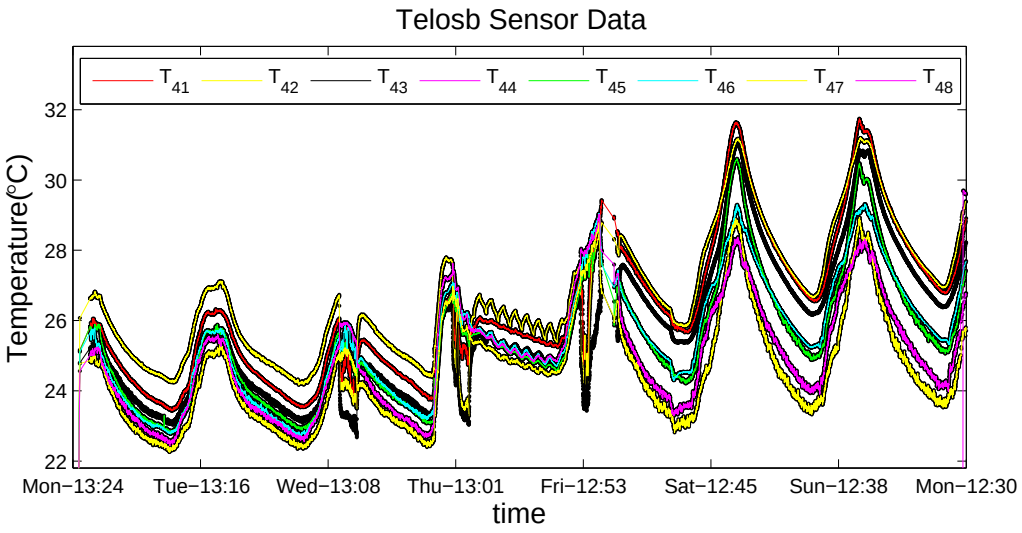

Figure 5.7: Temperature readings from 8 sensors

Telosb48) are hanged at the ceiling panels. They measure temperature and humidity at different locations in the room. The 4 CO2 flaps (CO2flap31-CO2flap34) are installed at the ceiling to measure the indoor CO2 concentration and also to control the air exhaust for the room.

5.5.2 Analysis of Historical Data

We collected the data from the test-bed for one week period (July 16-23, 2012). Figure 5.7 shows sensor readings from the 8 indoor temperature sensors located in the test-bed.

As shown in Figure 5.8, the 8 sensors are spread out to cover the entire area of BubbleZERO. The spatial sensor location variation leads to different levels of measurement accuracy from each sensor with respect to the average temperature in the space. To obtain the relation between sensing accuracy and choice of number and locations of sensors, we analyze the data collected from the test-bed. Note that sensor Telosb44 has only stored a few data points due to faulty behavior; consequently, we neglect that sensor in our analysis.

We consider the average of all the remaining 7 sensors as the actual temperature of the room. We then select a different number of sensors and calculate the *difference* between the average measure of the selected k sensors ($k = 1, 2, ..., 6$) and the average measure of all 7 sensors (i.e. the actual temperature of the room). This difference provides an estimation of the temperature sensing accuracy under certain selection of the sensors, and can be regarded as the measurement error of this set of sensors.

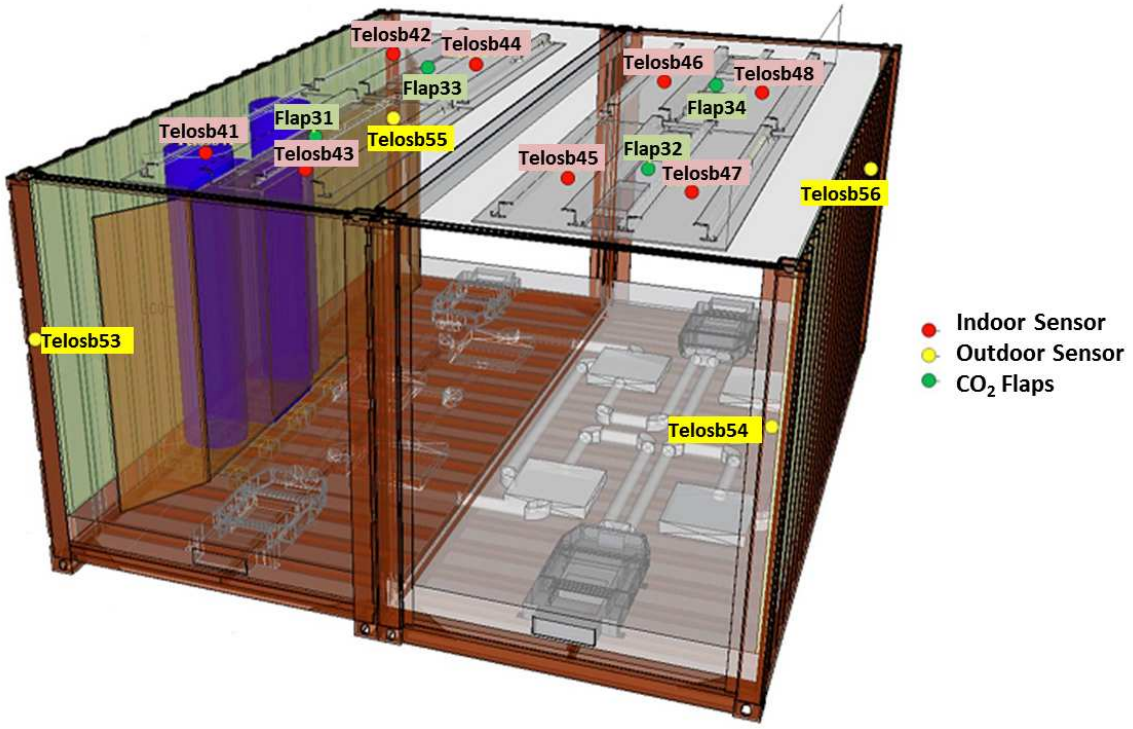

Figure 5.8: Sensor deployment in the test-bed

The root mean square (rms) of this difference is denoted by Δ_{rms}.

To further study the effect of sensor locations on sensing accuracy, for each k value, we enumerate all possible sets of sensors (with different locations) and pick the set that provides the minimal rms value of its measurement error, which is denoted by δ_m^b. We also calculate the measurement error of a randomly selected set (assuming equal probability for each sensor) and denote it by δ_m^r. The results of this analysis is shown in Figure 5.9. For instance, when $k = 1$, the best sensor (i.e. the one that provides the minimal rms value with respect to the average of all 7 sensors) is sensor T_{45}, which is located in the south eastern part of the bubble and provides $\Delta_{rms} = 0.29$. When $k = 2$, the best two sensors are T_{41} and T_{48}, which are the two sensors located in the two opposite corners, southwest and northeast of the bubble and leads to $\Delta_{rms} = 0.18$. In Figure 5.9, we also use the normal distribution to approximate the measurement error and calculate the corresponding mean and variance. The variance will then be used in the selection of control algorithms.

As mentioned in Section 5.3.2, in addition to the measurement error, the prediction error may also depend on the design of the sensing system, if CO2 sensors and outdoor temperature sensors are deployed to facilitate the prediction. The BubbleZERO test-bed provides CO2 and outdoor sensors that may enable this study, although currently

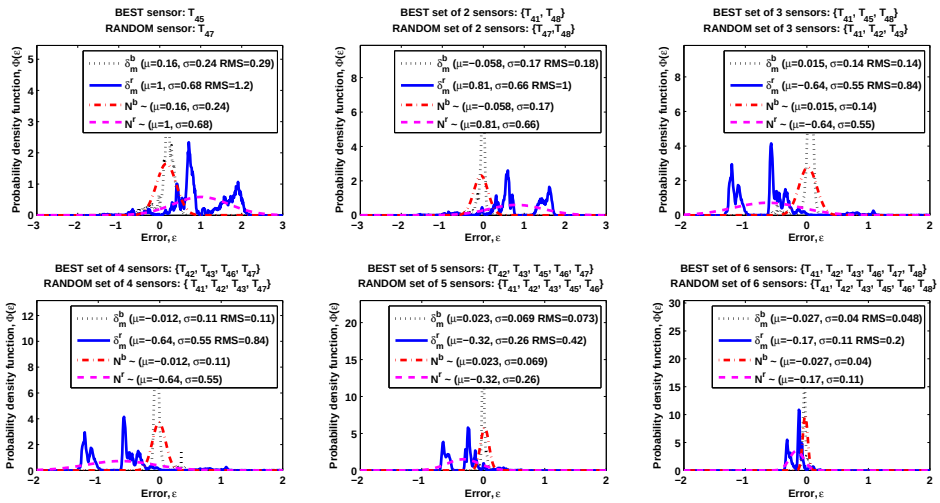

Figure 5.9: Average error of k sensors for the minimal error set of sensors and a random choose of sensors. Each figure lists in its title the best and random set of k sensors for k=1,2,...,6, and plots the pdf of its measurement error (i.e. the difference between the average of k sensor readings with the average of all 7 sensor readings), denoted by δ_m^b and δ_m^r, respectively. The best and random set of sensors are selected based on their resulting Δ_{rms}. N^b and N^r represent the normal distribution.

we do not have enough functional CO2 and outdoor sensors (e.g. only two CO2 sensors have readings available). We plan to conduct such study in the future.

5.6 Exploration of Control Algorithm and Sensing System

Based on the results presented above, we explore the design space for both control algorithm and sensing system to build a Pareto front of optimal energy and monetary cost under the constraint on user comfort level.

Specifically, we first choose the number of sensors based on a given monetary budget. We assume the best sensor locations are known to the designers (possibly through testing different location combinations) and decide the sensing data accuracy according to the statistics in Figure 5.9, i.e. the measurement error δ_m^b. Then by setting the measurement error v_k in (5.12) to σ_m^b, we conduct simulations for all six controllers and choose the one that minimizes the energy cost and satisfy the constraint on user comfort level as measured by the discomfort index. Results are shown in Figure 5.10.

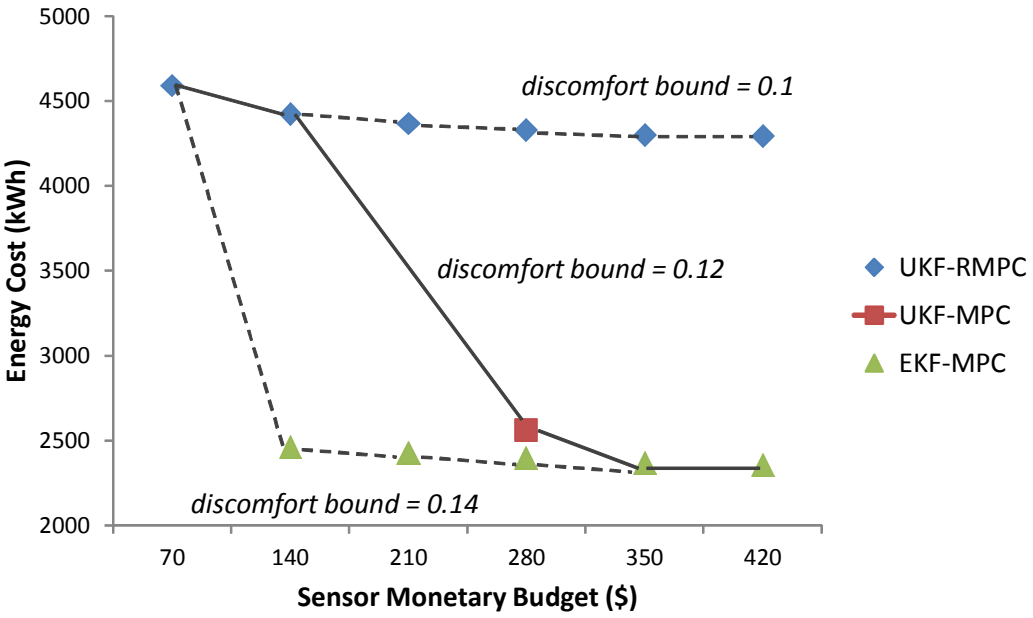

Figure 5.10: Pareto front under comfort constraints with best sensor locations

If it is required that the discomfort index be less than 0.12, the *Pareto front consists of different control algorithm choices depending on the sensor monetary budget.* In our platform, each Telosb unit costs about $70. When the budget is set to be under $140, we may choose 1 or 2 sensors, in which case the control algorithm that can satisfy the comfort level constraint and provide the minimal energy cost is UKF-RMPC (with energy cost around 4500). When the budget is set be more than 350, we may choose 5 or 6 sensors, in which case the control algorithm that has the minimal energy cost and satisfy the comfort constraint is EKF-MPC (with energy cost under 2500). When the budget is around 280, we may choose 4 sensors, in which case the best control algorithm is UKF-MPC.

Intuitively, when we have a small budget, the sensing data accuracy is lower and we need a more robust algorithm to satisfy the comfort level constraint; hence the RMPC controller (the MPC controllers do not satisfy the constraint in this case). When we have a large budget, the sensing accuracy is higher and we may choose the more energy-efficient algorithms, hence the MPC controllers. If the discomfort index is required to be less than 0.1, we will choose the UKF-RMPC controller under any budget, since the other controllers either do not satisfy the comfort constraint (i.e. EKF-MPC, UKF-MPC, OnOff controllers), or cost more energy (i.e. EKF-RMPC). If the discomfort index is set to be 0.14, we will choose EKF-MPC if there is budget for more than 1 sensor.

If the sensor locations are selected randomly (the theoretical best locations might

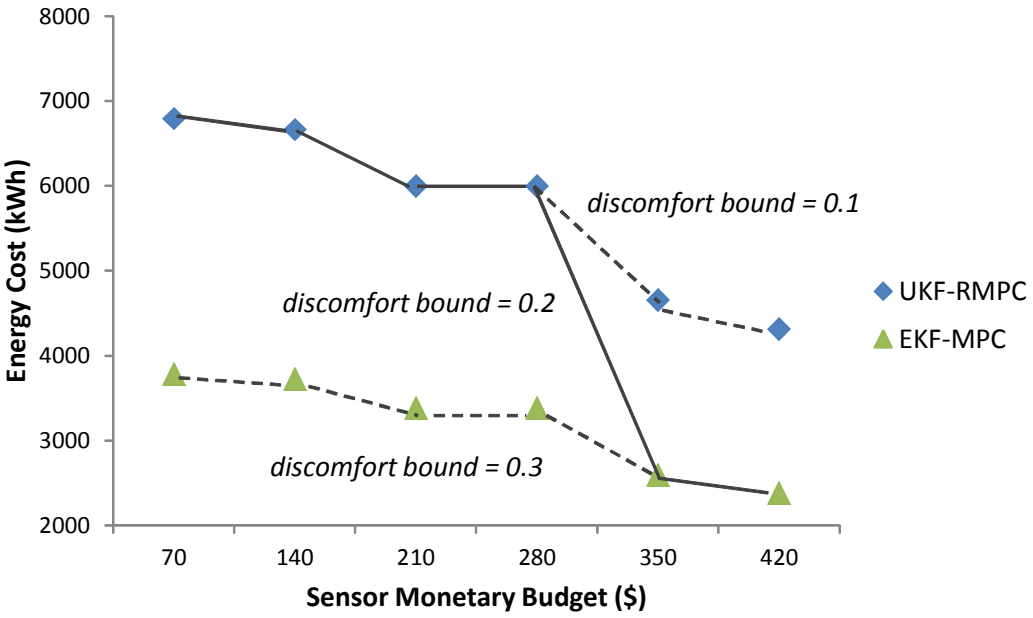

Figure 5.11: Pareto front under comfort constraints with random sensor locations

not be known or accessible in practice), the energy cost and performance of each controller under certain budget are different from the best location case. Figure 5.11 shows the exploration results with random sensor locations. We can see that similar to the best location case, *the selection of control algorithms depends on the number of sensors*. For instance, the solid line represents the case where the discomfort index is required to be less than 0.2. When the budget is under 280, we may select as most 4 sensors and the best control algorithm is UKF-RMPC (other controllers do not satisfy the comfort constraints except for EKF-RMPC but it has higher energy cost). When the budget is more than 350, the best control algorithm is EKF-MPC. If the discomfort index is required to be less than 0.1, the best control algorithm is always UKF-RMPC. Note that the energy cost under any number of sensors is also more than the energy cost in the best location case with the same number of sensors, which is to be expected.

Chapter 6

Building Flexibility for Supply Following

Commercial buildings have inherent flexibility in how their HVAC systems consume electricity. We investigate how to take advantage of this flexibility. We first propose a means to define and quantify the flexibility of a commercial building. We then propose a contractual framework that could be used by the building operator and the utility to declare flexibility on the one side and reward structure on the other side. We then design a control mechanism for the building to decide its flexibility for the next contractual period to maximize the reward, given the contractual framework. Finally, we perform at-scale experiments to demonstrate the feasibility of the proposed algorithm. The material of this chapter is extracted from [59].

6.0.1 Introduction

Consumers of energy usually do not pay attention to *when* they use energy. Demand for electricity tends to rise specially at times when it seems natural to use it; So natural in fact that we all tend to use it at the same time and in similar ways. On days when demand for electricity is high, extra power plants are needed to meet the demand.

There are environmentally-friendly alternatives to adding more generation. Electricity customers can voluntarily trim their electricity use during peak periods or choose to use electricity at a less congested time, a strategy called "Supply-Following" (SF). With SF programs, utilities provide *incentives* to encourage consumers to reduce their demand during peak periods. Smart grids are enabling the transformation from a demand-following strategy to a supply-following one.

Smart buildings are essential elements of the smart grid and can play a significant role in its operation. A building has some inherent flexibility in the way its HVAC

system consumes electricity while respecting the comfort of its occupants. This flexibility could be used to reduce costs if the electricity price is time-varying, or could be traded (i.e., sold to the utility) if a proper contractual framework exists. Typically the electricity consumption of a commercial building is controlled by a process that aims at reducing costs. Among the many possible ways to design such a process, Model Predictive Control (MPC) stands out. In order to use the potential of commercial buildings as providers of *flexibility* to the smart grid, we need to fundamentally redesign the way a building, and in particular its HVAC, is controlled. In this paper, we identify and quantify "flexibility". Then, a contractual framework between the utility and the building operator is designed so that the building can "declare" its flexibility and be rewarded for it. Finally, a control algorithm is proposed that allows the operation of building under this framework and at-scale experiments are carried out to demonstrate the high potential of commercial buildings as a source of flexibility, and the feasibility of the developed algorithm.

6.1 Baseline System and Contract

We focus on commercial buildings due to the following reasons:

1. Commercial buildings account for more than 35% of electricity consumption in the US.

2. More than 30% of commercial buildings have adopted Building Energy Management System (BEMS) technology which facilitate the communication with the grid system operators for providing flexibility. The majority of these buildings are also equipped with variable frequency drives, which in coordination with BEMS, can modulate the heating, ventilation and air conditioning (HVAC) system power consumption frequently (in the order of seconds).

3. Compared to a typical residential building, commercial buildings typically have larger HVAC systems and therefore consume more electricity.

About 15% of electricity consumption in commercial buildings is related to the fans of HVAC systems. Fans are the main drivers to move the conditioned air from the air handling units (AHU) to the rooms for climate control. For instance, the main supply fans that feed Sutardja Dai Hall on UC Berkeley campus can spin at variable speeds, with the corresponding power consumption which is proportional to the cube of fan speed, with the maximum rated power of 134 KW or about 14% of the maximum power consumed in that building. Moreover, we can directly control

Table 6.1: Nomenclature

Parameter	Definition
τ	Sampling time for discretizing continuous system dynamics
H^m	Prediction horizon of MPC
H^c	Horizon (length) of the proposed contract
d_t	Disturbance to the system at time t which comprises outside temperature, occupancy, solar radiation, etc.
T_t^{out}	Outside air temperature at time t
T^s	Supply air temperature exiting air handling unit (AHU)
$\mathcal{X}_t$	Set of permissible states at time t
$\mathcal{U}_t$	Set of permissible inputs at time t
π_t^e	Per-unit price of electric energy at time t – ($\$/kWh$)
$\pi^{ne,c}$	Per-unit price of non-electric cooling energy – ($\$/kWh$)
$\pi^{ne,h}$	Per-unit price of non-electric heating energy – ($\$/kWh$)
COP_h	Coefficient of performance of heating system
COP_c	Coefficient of performance of cooling system
t_{cs}	Contract start time
t_{ce}	Contract end time
$\{\overline{\beta}_t, \underline{\beta}_t\}$	Reward paid from the utility to the building at time t for providing upward flexibility ($\overline{\beta}_t$),and down flexibility ($\underline{\beta}_t$) – ($\$/kW$)
Variable	**Definition**
x_t	State of the system at time t
u_t	Input to the system at time t
w_t	Uncertainty variable introduced to derive the worst-case (*robustified*) optimal control problem
e_k^u	Upper envelope for safe air mass flow
e_k^l	Lower envelope for safe air mass flow
$\{\overline{\varphi}_t, \underline{\varphi}_t\}$	Provided upward ($\overline{\varphi}$), and downward ($\underline{\varphi}$) flexibility by building at time t in unit of air flow
$\{\overline{\psi}_t, \underline{\psi}_t\}$	Provided upward ($\overline{\psi}$), and downward ($\underline{\psi}$) flexibility by building at time t in unit of power
$C_{\text{hvac}}(u_t, \pi_t^e)$	Total HVAC energy consumption cost at time t
P_f, P_h, P_c	Power consumption of fan, heating and cooling systems
$R(\Phi, \mathcal{B})$	Reward from utility to building for providing flexibility

their power, upward or downward making it an ideal candidate for ancillary demand-response. See [67, 51, 56, 53, 32] for more information about the physics and control of HVAC systems.

6.1.1 The Baseline System

We consider a commercial building that has an HVAC system controlled by an MPC as our baseline. The MPC has the objective of minimizing the total energy cost (in dollar value). Let the time be slotted with τ as the length of each time slot, and let H^m be the prediction horizon (in number of time-slots) of the MPC. System dynamics is also discretized with a sampling time of τ. Typical values for τ and H^m range from 15 min to 1 hr for τ and a few hours to a few days, e.g., 3 to 72 time slots (with the assumption of 1 hr for each time slot) for H^m. The choice of H^m depends on how far in the future the estimation of the predicted values have an acceptable accuracy, and also on how far in the future the required information (e.g. cost of energy) is available. In this chapter we use $\tau = 1$ hr and $H^m = 24$ hrs. At each time t, the predictive controller solves the following optimal control problem to compute the optimal vector $\vec{u}_t = [u_t, \ldots, u_{t+H^m-1}]$, where u_{t+k} is the air mass flow to the thermal zones of the building. The inputs to the optimal control problem are the states (i.e. zone temperatures) x_t (as initial condition), the set of *electric* energy prices $\{\pi^e_t, \ldots, \pi^e_{t+H^m-1}\}$, the *non-electric* and non-fan energy prices, such as gas price for heating $\pi^{ne,h}$, and cooling $\pi^{ne,c}$ which are considered time-invariant, a set of constraints $\mathcal{X}_{t+k}$ on the system states of the type: "x_{t+k} should be in $\mathcal{X}_{t+k}$ for all times $t+k$ where $k \in \{1, \ldots, H^m\}$)", a set of constraints $\mathcal{U}_{t+k}$ on system inputs for all $k \in \{0, \ldots, H^m - 1\}$, and an estimate on unmodelled disturbances d_{t+k} (e.g., outside temperature or building occupancy [55]) for all $k \in \{0, \ldots, H^m - 1\}$ for the next H^m time slots. The optimization problem is as follows:

$$
\begin{aligned}
\min_{\vec{u}_t} \quad & \sum_{k=0}^{H^m-1} C_{\text{hvac}}(u_{t+k}, \pi^e_{t+k}, \pi^{ne,c}, \pi^{ne,h}, T^{\text{out}}_{t+k}) && && (6.1)\\
\text{s.t.} \quad & x_{t+k+1} = f(x_{t+k}, u_{t+k}, d_{t+k}), && k = 0, ..., H^m - 1\\
& x_{t+k} \in \mathcal{X}_{t+k}, && k = 1, ..., H^m\\
& u_{t+k} \in \mathcal{U}_{t+k}, && k = 0, ..., H^m - 1
\end{aligned}
$$

where T^{out} is the outside air temperature, f captures the system dynamics, and the total HVAC power consumption cost $C_{\text{hvac}}(t)$ is the summation of fan power, cooling power and heating power, given by:

$$C_{\text{hvac}}(t) = \pi^e(t)P_f(t) + \pi^{ne,c}P_c(t) + \pi^{ne,h}P_h(t) \tag{6.2}$$

where with the assumption of no recirculation of air, and without loss of generality, these power consumptions for time slot $[t, t+1]$ (with the assumptions of constant

air mass flow and price of energy over $[t, t+1]$) are calculated as follows:

$$P_f(u_t) = c_1.u_t^3 + c_2.u_t^2 + c_3.u_t + c_4 \tag{6.3}$$
$$P_h(u_t, T_t^{out}) = c_p.u_t.(T^s - T_t^{out})/COP_{\mathrm{h}} \tag{6.4}$$
$$P_c(u_t, T_t^{out}) = c_p.u_t.(T_t^{out} - T^s)/COP_{\mathrm{c}} \tag{6.5}$$

where c_1, c_2, c_3, and c_4 are constants of the fan as shown in Figure 6.1, c_p is the specific heat of air, and COP_{h}, and COP_{c} are the coefficients of performance for the heating system and the cooling system, respectively, and the supply air temperature T^s is considered constant. To move the coolant fluid around, heating and cooling systems use pumps which consume electric power. However, we assume that electric power consumption of pumps is negligible compared to the non-electric heating and cooling powers of these systems.

Hence, the MPC solution to (6.1) is an optimal air mass flow trajectory (also called an air mass flow profile) $\vec{u}_t^* = [u_t^*, \ldots, u_{t+H^m-1}^*]$. Only the first entry of $\vec{u}_t^*$ is implemented at time t. At the next time step, $t+1$, the horizon of MPC is receded by one step, a new MPC is set up, and solved to obtain $\vec{u}_{t+1}^* = [u_{t+1}^*, \ldots, u_{t+H^m}^*]$. Again, the first entry is implemented on the system, and the horizon is receded, and this process repeats until the whole time frame of interest is covered. At each time t, the optimal air mass flow vector for the next H time steps is given by $\vec{u}_t^* = [u_t^*, \ldots, u_{t+H^m-1}^*]$, with corresponding fan power flow profile of $P_f(\vec{u}^*) = [P_f(u_t^*), \ldots, P_f(u_{t+H^m-1}^*)]$. In the following, we will omit the reference to t in the profile and define a power profile as a vector $P_f(\vec{u}^*) = [P_f(u_0^*), \ldots, P_f(u_{H^m-1}^*)]$.

6.1.2 The Baseline Contract

The *baseline contract* corresponding to this baseline system is very simple. Namely, the building can consume what it wants at all times and it pays π_t^e per unit of consumed electricity at time t (i.e., if the time span is of duration Δ, then it pays $\sum_{k=t}^{t+\Delta} \pi^e(k) P_f(k)$ for electric power). Hence, the only information being exchanged between the utility and the BM is the real-time price vector $[\pi_0^e, \ldots, \pi_{H^m-1}^e]$ in (\$/kWh) sent by the utility to the building ($\pi^{ne,c}$ and $\pi^{ne,h}$ are considered constant and known). Then the building solves the MPC (6.1) to compute what its electricity consumption profile/trajectory would be in the next H^m time slots. As described, this MPC would minimize its total cost in the next H^m time slots while respecting the building and the occupants (comfort) constraints. Let $\vec{u}^*$ denote the trajectory that is the solution to this MPC and let $C(\vec{u}^*)$ be its cost.

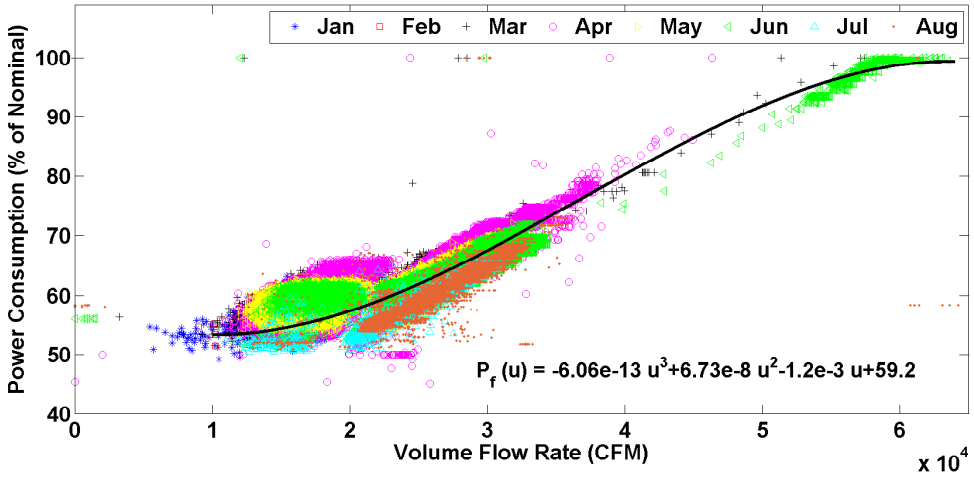

Figure 6.1: Fan power consumption versus volume flow rate. Data is for January through August of 2013.

6.2 Flexibility, Contractual Framework and Control Algorithm

6.2.1 Definition of Flexibility

We define flexibility in terms of two envelope air mass flow profiles $\vec{e^l} = [e^l_{t_{cs}}, \ldots, e^l_{t_{ce}}]$ a lower envelope, and $\vec{e^u} = [e^u_{t_{cs}}, \ldots, e^u_{t_{ce}}]$ an upper envelope. t_{cs} and t_{ce} are contract start and end times. Based on the requirement from the utility that flexibility of each building has to be determined ahead of time we pick t_{cs}, and consequently t_{cs} as follows:

$$t_{cs} \geq 1 \tag{6.6}$$

$$t_{cs} + 1 \leq t_{ce} \ll H^m - 1 \tag{6.7}$$

$$t_{ce} - t_{cs} = H^c \tag{6.8}$$

where H^c is the length of the contract. Typical values for H^c are much smaller than H^m, and can take values from one slot to a few time slots. The BEMS computes $\vec{e^l} = [e^l_0, \ldots, e^l_{H^m-1}]$ a lower envelope and $\vec{e^u} = [e^u_0, \ldots, e^u_{H^m-1}]$ an upper envelope (using the algorithm described later in the paper), so that any air mass flow profile $\vec{u} = [u_0, \ldots, u_{H^m-1}]$ such that for all $k \in \{0, \ldots, H^m - 1\}$, $e^l_k \leq u_k \leq e^u_k$ is feasible; i.e. no building constraints are violated at anytime. The corresponding fan power consumption envelopes are $P_f(\vec{e^l}) = [P_f(e^l_0), \ldots, \vec{P_f}(e^l_{H^m-1})]$ and $P_f(\vec{e^u}) = [P_f(e^u_0), \ldots, P_f(e^u_{H^m-1})]$. However the building only *declares* the first H^c values of

the envelope as flexibility, namely, $\vec{e^l} = [e^l_{t_{cs}}, \ldots, e^l_{t_{cs}+H^c}]$ a lower envelope, and $\vec{e^u} = [e^u_{t_{cs}}, \ldots, e^u_{t_{cs}+H^c}]$ an upper envelope, at the beginning of each contract. The reason for declaring a subset of the obtained envelopes is that due to model mismatch, imperfect predictions of disturbance and so on, the later values in the H^m-step envelopes may not be accurate and need to be updated in the next time step. By declaring these two envelopes, the building has essentially declared its flexibility for the next H^c time slots. Note that there is NO objective function and energy cost here, we define flexibility with respect to feasibility criteria.

By declaring these two envelopes, the building manager is telling the utility: "I allow you to select any power trajectory $P_f(\vec{u}) = [P_f(u_{t_{cs}}), \ldots, P_f(u_{t_{ce}})]$ such that for all $k \in \{t_{cs}, \ldots, t_{ce}\}$, $P_f(e^l_k) \leq P_f(u_k) \leq P_f(e^u_k)$".

To quantify the flexibility provided at each time step k, we need to define a single *metric*. The metric that is natural to use is the difference between the upper and lower power envelope that can be consumed by the building without violating any constraints. Hence,

$$\text{Flexibility}(k) \triangleq P_f(e^u_k) - P_f(e^l_k) \tag{6.9}$$

6.2.2 Contract Framework

In the proposed framework, the building operator can declare its flexibility contract to the utility. The flexibility declared by the building operator would only be significant if the reward is appropriate. It is important to understand that by allowing the utility to select any trajectory $P_f(\vec{u}) = [P_f(u_{t_{cs}}), \ldots, P_f(u_{t_{ce}})]$ or correspondingly $\vec{u} = [u_{t_{cs}}, \ldots, u_{t_{ce}}]$ such that for all $k \in \{t_{cs}, \ldots, t_{ce}\}$ $e^l_k \leq u_k \leq e^u_k$, the building might consume more or be in a worse state at the end of the H^c time slots. We define the "flexibility" contract as follows:

The utility charges the building operator for its baseline power consumption $P_f(\vec{u}^*)$ which is agreed upon at the time of the contract, irrespective of the deviations from the baseline power consumption due to flexibility signals from the utility, and the utility rewards the building operator for its declared flexibility.

Hence, this contract is deterministic in the sense that from the beginning of the contract, the utility and the building operator both know how much money each has to pay; the building pays for consuming $P_f(u^*_t)$ at rate π^e_t, and the utility pays the building for providing downward flexibility at rate $\underline{\beta}_t$ and for providing upward flexibility at rate $\overline{\beta}_t$.

In short, the contract implementation steps are as follows:

1. The building and the utility agree upon a contract length, H^c.
2. The utility declares $[\pi^e_0, \ \ldots, \ \pi^e_{H^m-1}]$, as per unit price of electric energy, $[\underline{\beta}_0, \ \ldots, \ \underline{\beta}_{H^m-1}]$ in ($/kW$), as reward for down flexibility, and $[\overline{\beta}_0, \ \ldots, \ \overline{\beta}_{H^m-1}]$

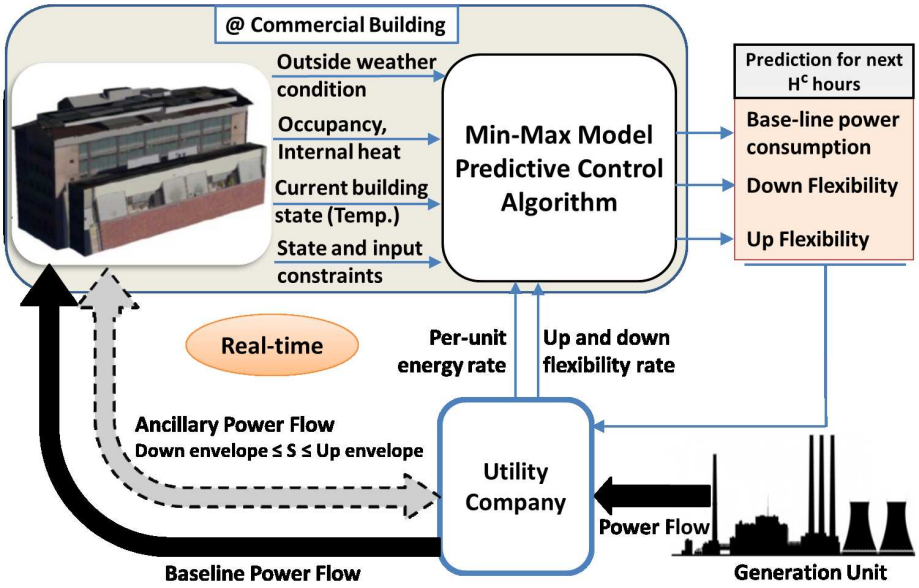

Figure 6.2: Schematic of the proposed architecture for contractual framework.

in ($\$/kW$), as reward for upward flexibility. If the utility is not willing to commit to the flexibility rates for the time span beyond the next immediate contract period, i.e. $[\underline{\beta}_{H^c+1}, \ \ldots, \ \underline{\beta}_{H^m-1}]$, and $[\overline{\beta}_{H^c+1}, \ \ldots, \ \overline{\beta}_{H^m-1}]$, the building operator can then obtain an estimate of these values from historical data.

3. The building operator computes the baseline air mass flow u_k^* and the two envelopes e_k^l and e_k^u, for the time frame $k = 0, 1, \ldots, H^m - 1$, with its overall cost if it uses the flexibility contract as follows:

$$C_f = \overbrace{\sum_{k=0}^{H^m-1} C_{\text{hvac}}(u_k, \pi_k^e)}^{\text{Building Operator Payment}} \underbrace{- \sum_{k=1}^{H^m-1} \underline{\beta}_k \underline{\psi}(u_k, e_k^l) - \sum_{k=1}^{H^m-1} \overline{\beta}_k \overline{\psi}(u_k, e_k^u)}_{\text{Reward for Providing Flexibility}} \tag{6.10}$$

where $\overline{\psi}$, and $\underline{\psi}$ are defined as:

$$\overline{\psi}(u_k, e_k^u) \triangleq P_f(e_k^u) - P_f(u_k) \tag{6.11a}$$

$$\underline{\psi}(u_k, e_k^l) \triangleq P_f(u_k) - P_f(e_k^l) \tag{6.11b}$$

4. The building operator then declares $P_f(\vec{e^l})$ and $P_f(\vec{e^u})$, the baseline profile $P_f(\vec{u}^*)$ that it will consume and the length of the contract H^c to the utility.

5. In the next H^c time slots, the utility will send signals (s_k)'s, such that $P_f(e^l_k) \leq s_k \leq P_f(e^u_k)$ and the building operator has to obey the signals, i.e., has to consume power in time slot k equal to s_k. Flexibility signal s_k may arrive as frequently as every few seconds, as mentioned earlier.

6.2.3 Proposed Control Mechanism

As discussed in Section 6.2.2, if the utility provides a vector $\vec{\pi}^e = [\pi^e_0, \ldots, \pi^e_{H^m-1}]$ of per-unit of energy prices per time slot, then BEMS could try to minimize its total energy cost $\sum_{k=0}^{H^m-1} C_{\text{hvac}}(u_k, \pi_k, T^{out}_k)$. In that case, BEMS uses building flexibility selfishly to minimize its cost. Hence, BEMS does value (and does use) its flexibility. If the utility values the flexibility that the building HVAC system can offer, it has to provide the right incentive and the right mechanism to declare this flexibility.

Formalizing Flexibility and Incentive in the MPC Framework

We say that the building can offer a flexibility $\Psi := \{\underline{\vec{\psi}}, \overline{\vec{\psi}}\}$ in fan power or equivalently a flexibility $\Phi := \{\underline{\vec{\varphi}}, \overline{\vec{\varphi}}\}$ in air mass flow which comprises down flexibility, $\underline{\vec{\varphi}}$, and upward flexibility $\overline{\vec{\varphi}}$, from the contract start time $t_{cs} = t+1$ to the contract end time $t_{ce} := t+1+H^c$ for $1 \leq H^c \leq H^m$ time slots (starting from x_0) if there exist two trajectories $\vec{e^l} = \vec{u} + \underline{\vec{\varphi}}$ and $\vec{e^u} = \vec{u} + \overline{\vec{\varphi}}$, that satisfy:

$$\underline{\varphi}_k \leq 0, \quad \overline{\varphi_k} \geq 0 \qquad \forall k \in \{t_{cs}, \ldots, t_{ce}\} \tag{6.12}$$

$$f(x_k, u_k + \underline{\varphi}_k, d_k) \in \mathcal{X}_{k+1} \qquad \forall k+1 \in \{t_{cs}, \ldots, t_{ce}\} \tag{6.13}$$

$$f(x_k, u_k + \overline{\varphi}_k, d_k) \in \mathcal{X}_{k+1} \qquad \forall k+1 \in \{t_{cs}, \ldots, t_{ce}\} \tag{6.14}$$

$$u_k + \underline{\varphi}_k \in \mathcal{U}_k \qquad \forall k \in \{t_{cs}, \ldots, t_{ce}\} \tag{6.15}$$

$$u_k + \overline{\varphi}_k \in \mathcal{U}_k \qquad \forall k \in \{t_{cs}, \ldots, t_{ce}\} \tag{6.16}$$

What we defined here is a flexibility over multiple time slots. Assume that BEMS declares $\underline{\vec{\varphi}}$ and $\overline{\vec{\varphi}}$ (i.e., the utility might choose any fan power (and consequently air flow $\hat{u}_k$) in time step $t_{cs} \leq k \leq t_{ce}$ as long as $u^*_k + \underline{\varphi}_k \leq \hat{u}_k \leq u^*_k + \overline{\varphi}_k$), where u^*_k is the *baseline* air mass flow. Hence, we "center" the flexibility around u^*.

The flexibility-aware optimal control problem should minimize the cost function which is composed of the *cost* for the baseline HVAC power consumption, C_{hvac}, (i.e., the cost of problem (6.1)), minus the *reward* for the flexibility, R, which is computed as follows:

$$R(\vec{\Phi}, \vec{\mathcal{B}}) = \overline{\vec{\beta}}^T . \overline{\vec{\psi}}(\vec{u}, \overline{\vec{\varphi}}) + \underline{\vec{\beta}}^T . \underline{\vec{\psi}}(\vec{u}, \underline{\vec{\varphi}}) \tag{6.17}$$

where $\vec{\mathcal{B}} := \{\vec{\underline{\beta}}, \vec{\overline{\beta}}\}$, and $\underline{\psi}(.)$, and $\overline{\psi}(.)$ are given by (6.11), in which $\vec{e^l} = \vec{u} + \vec{\underline{\varphi}}$ and $\vec{e^u} = \vec{u} + \vec{\overline{\varphi}}$.

MPC Formulation

We assume at each time step t, that the current state of the building is known. Furthermore, the prediction of the outside temperature, inside heat generation, and constraints on the system states and inputs are known. The outputs of the algorithm is the nominal power consumption of the building, u^*_{t+k} for $k \in \{0, ..., H^m - 1\}$, the flexibility that the building can provide, Φ^*_{t+k+1} for $k \in \{0, ..., H^m - 1\}$, for future time steps, without violating constraints. Based on this set of information, the BEMS can decide how much flexibility to offer. It may declare very small flexibility and hence get a cost close to C_{hvac}.

The algorithm described above can be formulated as a *min-max* MPC problem. At time t we are interested in solving the following robust optimal control problem:

Min-Max Problem

$$\min_{\vec{u}_t, \vec{\Phi}_{t+1}} \max_{\vec{\mathbf{w}}_t} \quad \sum_{k=0}^{H^m-1} C_{\text{hvac}}(u_{t+k}, \pi_{t+k}) - R(\Phi_{t+k+1}, \mathcal{B}_{t+k+1}) \tag{6.18a}$$

subject to:

$$x_{t+k+1} = f(x_{t+k}, u_{t+k} + w_{t+k}, d_k)$$

$$\forall \quad k = 0, ..., H^m - 1 \tag{6.18b}$$

$$\forall\ w_t \text{ s.t. : } \underline{\varphi}_t \leq w_t \leq \overline{\varphi}_t \tag{6.18c}$$

$$\forall\ w_{t+k} \text{ s.t. : } \underline{\varphi}_{t+k} \leq w_{t+k} \leq \overline{\varphi}_{t+k}$$

$$\forall k = 1, ..., H^m - 1 \tag{6.18d}$$

$$\overline{\varphi}_{t+k} \geq 0, \quad \forall\ k = 1, ...H^m - 1 \tag{6.18e}$$

$$\underline{\varphi}_{t+k} \leq 0, \quad \forall\ k = 1, ...H^m - 1 \tag{6.18f}$$

$$x_{t+k} \in \mathcal{X}_{t+k}\ \forall\ k = 1, ..., H^m \tag{6.18g}$$

$$u_{t+k} + w_{t+k} \in \mathcal{U}_{t+k}\ \forall\ k = 0, ..., H^m - 1 \tag{6.18h}$$

Note that $\underline{\varphi}_t$ and $\overline{\varphi}_t$ are computed in the previous time step and are constant values in this formulation, while $\underline{\varphi}_{t+k}$ and $\overline{\varphi}_{t+k}$ for $k \in \{1, \ldots, H^m - 1\}$ are optimization variables and will be computed in the current time step by solving the optimal control problem (6.18).

The inner maximization problem robustifies the optimization problem and derives the worst-case scenario cost and constraints. The outer minimization problem solves for its arguments $(\vec{u}_t, \vec{\Phi}_{t+1})$ while it is guaranteed that the constraints are satisfied for all values of uncertainty w, as long as it is within the range $\underline{\varphi}_{t+k} \leq w_{t+k} \leq \overline{\varphi}_{t+k}$

for $k \in \{1, \ldots, H^m - 1\}$.

Theorem [21]:

Let $\mathbb{C}$ be a closed convex set and let $f : \mathbb{C} \to \mathbb{R}$ be a convex function. Then if f attains a maximum over $\mathbb{C}$, it attains a maximum at some extreme point of $\mathbb{C}$.

According to the theorem above, the *analytic* worst-case solution can be obtained. Closed convex sets can be characterized as the intersections of closed half-spaces (i.e. sets of points in space that lie on and to one side of a hyperplane). The feasible set for states, i.e. the temperature of the rooms in the building and inputs, i.e. air mass flow into the thermal zones, are defined by:

$$\mathcal{X}_k := \{x \mid \underline{T}_k \leq x \leq \overline{T}_k\} \tag{6.19}$$

$$\mathcal{U}_k := \{u \mid \underline{U}_k \leq u \leq \overline{U}_k\} \tag{6.20}$$

where $\underline{T}_k$, and $\overline{T}_k$ are the upper and lower temperature limits and $\overline{U}_k$, and $\underline{U}_k$ are the upper and lower feasible air mass flow at time t. Therefore, the feasible set of (6.18) is closed and convex. The objective function is also convex on w, as the max is over variable w. In fact, w does not appear in the cost function. The objective function is a linear function on w and hence it is concave. We also consider a linearized state update equation as follows:

$$x_{t+1} = Ax_t + Bu_t + Ed_t \tag{6.21}$$

the nonlinear system dynamics has been linearized with the forward Euler integration formula with time-step $\tau = 1$ hr. Hence, the min-max problem (6.18) is equivalent to:

Minimization Problem

$$\min_{\vec{u}_t, \vec{\Phi}_{t+1}} \quad \sum_{k=0}^{H^m-1} C_{\text{hvac}}(u_{t+k}, \pi_{t+k}) - R(\Phi_{t+k+1}, \mathcal{B}_{t+k+1}) \tag{6.22a}$$

$$\text{s. t.:} \quad \underline{x}_{t+k+1} = f(x_{t+k}, u_{t+k} + \underline{\varphi}_{t+k}, d_{t+k}) \tag{6.22b}$$

$$\forall k = 0, ..., H^m - 1$$

$$\overline{x}_{t+k+1} = f(x_{t+k}, u_{t+k} + \overline{\varphi}_{t+k}, d_{t+k}) \tag{6.22c}$$

$$\forall k = 0, ..., H^m - 1$$

$$\overline{\varphi}_{t+k} \geq 0, \quad \forall\ k = 1, ...H^m - 1 \tag{6.22d}$$

$$\underline{\varphi}_{t+k} \leq 0, \quad \forall\ k = 1, ...H^m - 1 \tag{6.22e}$$

$$\underline{x}_{t+k} \in \mathcal{X}_{t+k} \quad \forall \quad k = 1, ..., H^m \tag{6.22f}$$

$$\overline{x}_{t+k} \in \mathcal{X}_{t+k} \quad \forall \quad k = 1, ..., H^m \tag{6.22g}$$

$$u_{t+k} + \underline{\varphi}_{t+k} \in \mathcal{U}_{t+k} \ \ \forall\ k = 0, ..., H^m - 1 \tag{6.22h}$$

$$u_{t+k} + \overline{\varphi}_{t+k} \in \mathcal{U}_{t+k} \ \ \forall\ k = 0, ..., H^m - 1 \tag{6.22i}$$

The *argmin* of the optimization problem (6.22) is the nominal power consumption, u^*_{t+k}, and the maximum available flexibility, Φ^*_{t+k}, $\forall\ k = 0, ..., H^m - 1$. The building declares u^*_{t+k}, and Φ^*_{t+1+k} for the time slots: $\forall\ k = 0, ..., H^c - 1$ to the utility. After H^c time slots, the BEMS collects the updated parameters such as new measurements and disturbance predictions, and sets up the new MPC algorithm for the time step $k = H^c, H^c + 1, \ldots, H^c + H^m - 1$, and solves the new MPC for this time frame and uses only the first H^c values of baseline power consumption and flexibility, i.e. for $k = H^c, \ldots, 2H^c - 1$, and this process repeats.

Figure 6.2 shows the schematic of the entire system architecture. The solid line power flow arrows correspond to the baseline system and contract. The ancillary power flow via the flexibility contract is shown with dashed line arrow. Real-time state of the system such as occupancy, internal heat, outside weather condition, building temperature, state and input constraints are passed as input to the algorithm. The utility also communicates information such as per-unit energy and upward and downward flexibility prices to the BEMS (or effectively to the algorithm). The output of the algorithm includes baseline power consumption, downward flexibility and upward flexibility values, and cost. Within the flexibility contract framework, this information is communicated to the utility. Consequently, a flexibility signal s_t is sent from the utility to the building to be tracked by the HVAC fan. Essentially, the utility has control of the building consumption for the next H_c time slots. The control strategy is actuated by sending flexibility signals (similar to frequency regulation signals). These signals can be sent as frequently as every few seconds. In

fact, we show through experiments on a real building in Section 6.4, that buildings with HVAC systems equipped with variable frequency drive (VFD) fans are capable of tracking such signals very fast (e.g. within a few seconds).

6.3 Computational Results

The algorithm presented in Section 6.2.3 was implemented on a building model developed and validated against historical data in [53, 55]. We used Yalmip [48], an interface to optimization solvers available as a MATLAB toolbox, for rapid prototyping of optimal control problems. The non-linear optimization problem solver Ipopt [80], was used to solve the resulting nonlinear optimization problem arising from the MPC approach. We use sampling time of $\tau = 1\ hr$. We assess the performance of the algorithm for the following scenarios.

Scenario I: Different reward rates have been considered for upward and downward flexibility at each time step. In particular, downward flexibility is rewarded more than upward flexibility ($\underline{\beta} > \overline{\beta}$), for most of the time. Since MPC maintains the comfort level using the least possible amount of energy, buildings that are operated under nominal MPC such as (6.1) have no down flexibility (for extended period of time, i.e. 1 hr or more). However we show that via proper incentives and by solving (6.22), it is possible to provide downward flexibility when most needed. The results of this scenario are shown in Figure 6.3 for the case when ancillary signals are received from the utility every minute: no system constraint (e.g. temperature being within the comfort zone) will be violated when the fan speed enforcement is performed for arbitrary values of fan speed as long as fan power consumption, and consequently fan speed is within the safe envelope calculated by the algorithm. It is shown in Figure 6.3 that maximum flexibility (100%) is provided at times when the room temperature is far from the boundaries of the comfort zone. The flexibility decreases as the temperature of the room approaches the comfort zone boundary, and is minimum (about 0-15% in this case) when room temperature is fairly close to the boundaries of the comfort zone, and the reward for flexibility is not high enough.

Scenario II: In this scenario we test the algorithm when no *reward* for providing flexibility is provided (i.e. $\overline{\beta} = \underline{\beta} = 0$). Results are shown in Figure 6.4. In this case the MPC "selfishly" uses the thermal capacitance of the building to minimize energy cost. This case yields to an MPC policy similar to nominal MPC (6.1). As expected, the resulting flexibility is very small throughout the day.

Scenario III: In this case, the amount of reward to the building for upward and downward flexibility is the same as Scenario I. Furthermore, the BM is encouraged to provide *equal* upward and downward flexibility as long as possible. This requirement

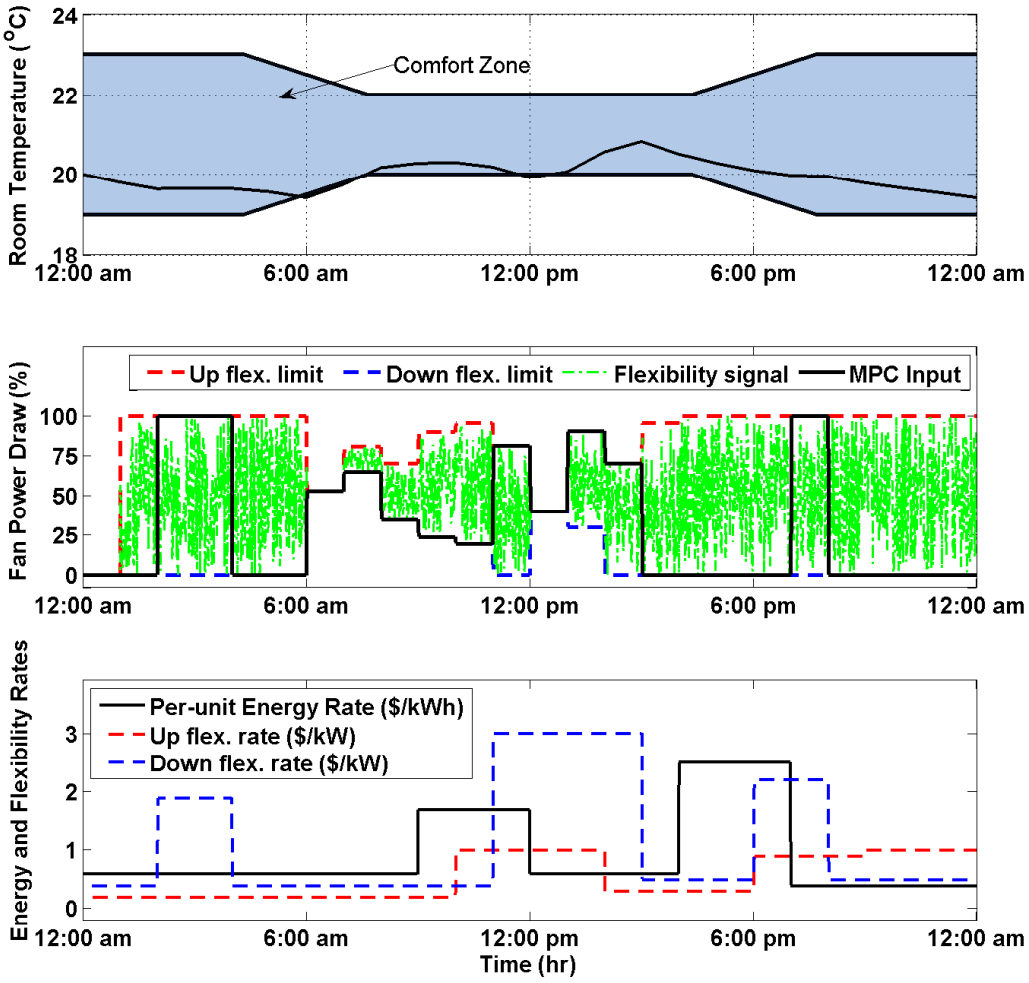

Figure 6.3: **Scenario I:** The Per-unit energy rate, and upward and downward flexibility reward are shown in the lowest figure. The middle figure shows the resulting flexibility at each time, and the top figure shows the resulting room temperature. Flexibility signals are sent every minute from the utility to the building.

has been enforced by adding an extra penalty term to the cost function as follows:

$$\text{cost} := \text{cost} + \gamma_t^T . |\overline{\varphi}_t - \underline{\varphi}_t| \tag{6.23}$$

where $\gamma \gg 0$ is a constant, and $|.|$ returns the absolute value of its argument. Larger value of γ makes the equality of upward and downward flexibility to hold for a longer

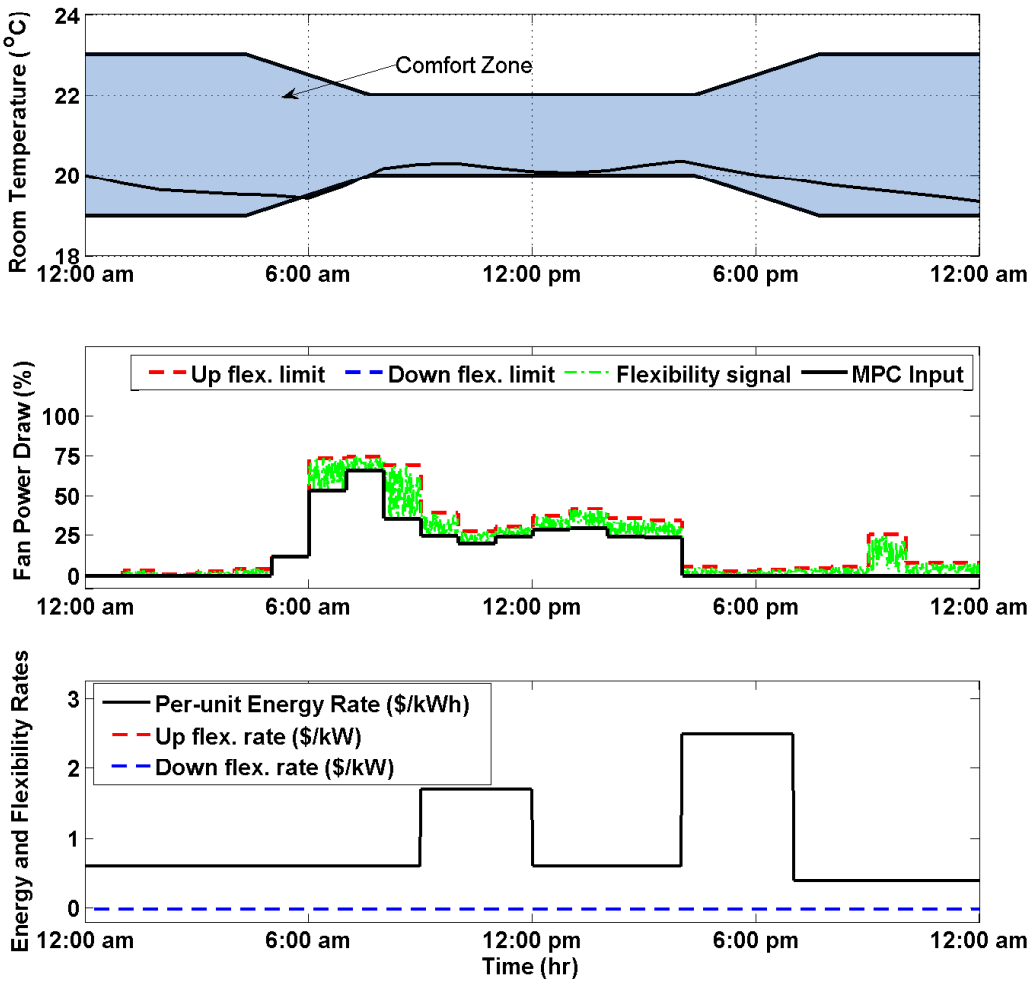

Figure 6.4: **Scenario II:** In this case we consider both upward and downward flexibility reward to be zero. This results into a performance similar to the one of the nominal MPC (6.1).

period. However, in this case, we lose the guaranteed maximization of the economic benefit of the building due to the newly added term in the cost function. Figure 6.5 shows the result for this scenario. Maximum flexibility (100%) happens during unoccupied hours and when the reward for flexibility is high. In this case minimum flexibility is 0% and it happens during 6 to 7 am, 9 to 10 am, and 12 to 1 pm. The room temperature is close to the comfort-zone boundary. The per-unit price of

electricity is high, and the reward for upward and downward flexibility is very small. Hence, the algorithm provides no flexibility at these time periods. In Figure 6.5 the frequency of flexibility signals is 1 hr. By picking a large value for the period of flexibility signal arrivals, we show that no system constraint will be violated when the fan speed is constrained even for long time periods, as long as the fan power consumption and consequently fan speed is within the safe envelope calculated by the algorithm.

6.4 Experimental Results

6.4.1 Tracking Ancillary Signals by VAV-Equipped Fans

We ran some experiments to demonstrate that it is indeed feasible to track the flexibility signals received from utility (s_k : where $e_k^l \leq s_k \leq e_k^u$) very fast. We run our experiments in a new building constructed four years ago (2009) on the UC Berkeley campus named Sutardja Dai Hall (SDH). It is a 141,000 square-foot modern building that houses several laboratories, including a nanofabrication lab, dozens of classrooms and collaborative work spaces. It contains a Siemens building management system called Apogee [3] which is connected to an sMAP server [25] co-located with the Apogee server. We run our experiments using a control platform built on sMAP, whereby control points are set programmatically upon approval from the building manager. The energy data of this building is stored in the cloud and is accessible to the public at [12].

The BEMS of the experiment set up is shown in Figure 6.6. There are two sets of 9 fans namely AH2A and AH2B with a total capacity of 180 hp (about 134 kW). The existing control mechanism is designed to maintain the pressure in the HVAC ducts at the set point value by setting the Supply Duct Static Pressure (SDSP) setpoint. If the pressure drops below the setpoint (e.g. due to the opening of more dampers at the room level, or to the increase of the SDSP setpoint) the two sets of fans will spin faster to compensate for the change in the system and increase the pressure in the duct work to reach the setpoint. And in the case that the pressure goes above the setpoint (e.g. due to the closing of more dampers or to the decrease of the SDSP setpoint), the fan speed will decrease to bring down the pressure to the setpoint. The air handling unit (AHU) maintains an almost constant supply temperature (T^s) in the supply air duct to be sent to the rooms. If one room needs more heating, the air is *reheated* locally at the Variable Air Volume (VAV) box designated for each room, to increase the supply air temperature for that specific room. The flow of air to each room ($\dot{m}_s$) is controlled by opening and closing of the dampers at the VAV level.

Several experiments were conducted on this test-bed to prove our hypothesis that it is indeed feasible to track the ancillary signal s_k received from the utility without

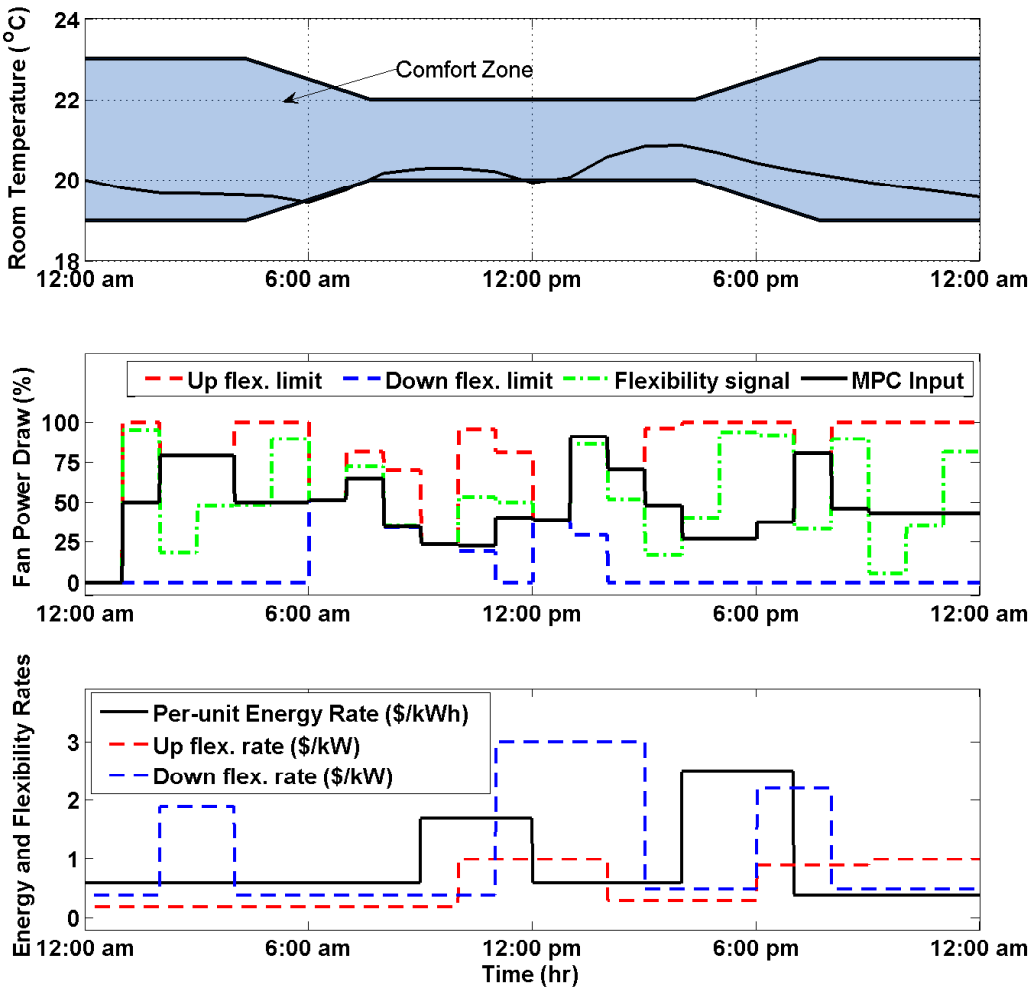

Figure 6.5: **Scenario III:** In this case we use the cost function presented in (6.23) to push the algorithm to produce equal up and downward flexibility as long as possible. Frequency of flexibility signals is 1 hr.

affecting the comfort of the occupants. Here we report the two experiments performed on May 17 of 2013. Experiment 1 was conducted from 12:45 pm to 13:15 pm. and Experiment 2 was performed from 5:30 pm to 6:15 pm of the same day. Experiments were done by frequently changing the SDSP setpoint. SDSP is normally kept at 1.75 inch WC (inch Water Column). Due to safety reasons it is advised to always keep the duct pressure within 1.2 and 1.9 inch WC. Hence, we perform the experiments

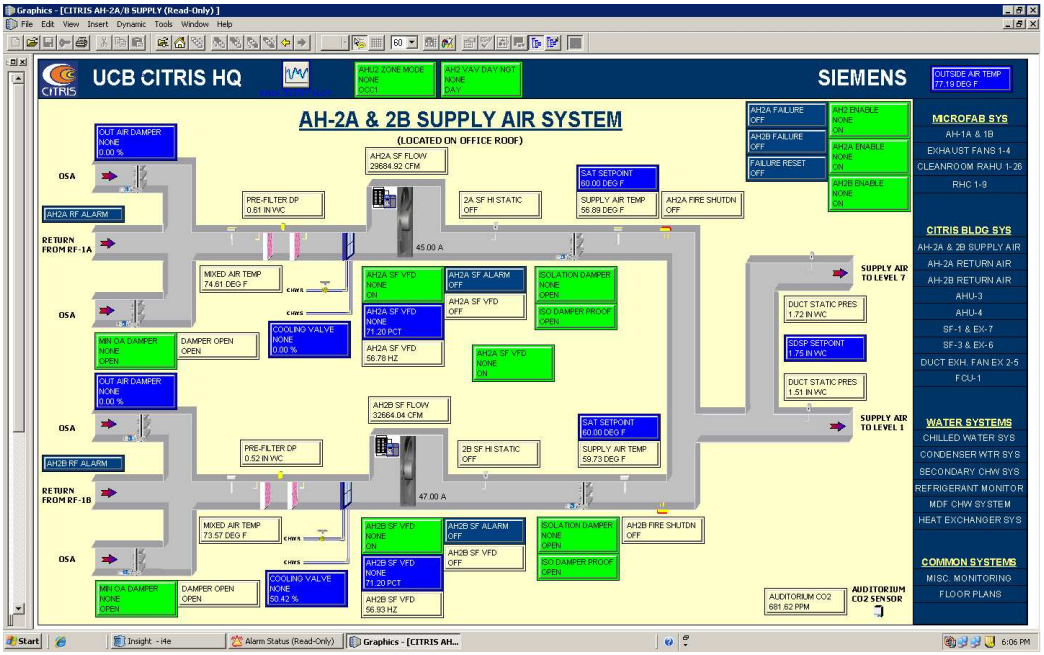

Figure 6.6: Building management system of the CITRIS hall, our experimental set up located on the campus of UC Berkeley.

by changing the SDSP between these two values. In Experiment 1 the set point was changed every minute to values randomly selected in the range $[1.2, 1.9]$ and held at that value for one minute. In Experiment 2, the same procedure was done but every three minutes, and the SDSP setpoint was kept at the new value for three minutes.

The results are shown in Figure 6.7 and Figure 6.8. In Figure 6.7 we present the SDSP setpoint signal, as input of the experiment and the power consumption of the fan, as output of the experiment. It can be observed that the fan power consumption can vary up to 25% within a few seconds around its nominal power consumption at the time of the experiment (which itself is prescribed by the control algorithm running the HVAC system). Figure 6.8 on the other hand shows the SDSP setpoint, the outside air temperature and temperature of 15 randomly selected rooms in the building. This figure is provided to show that the performed experiment created no significant and human-sensible change in the temperature of the building, and the building temperature was kept within the comfort zone at all times. Data of one day before the experiment (May 16) and the day of experiment (May 17) is provided for comparison.

Note that since this is a very large building with many occupants, we were not allowed to change the control algorithm of the building to test our algorithm for a long period of time. Nevertheless, the purpose of this experiment was to show that

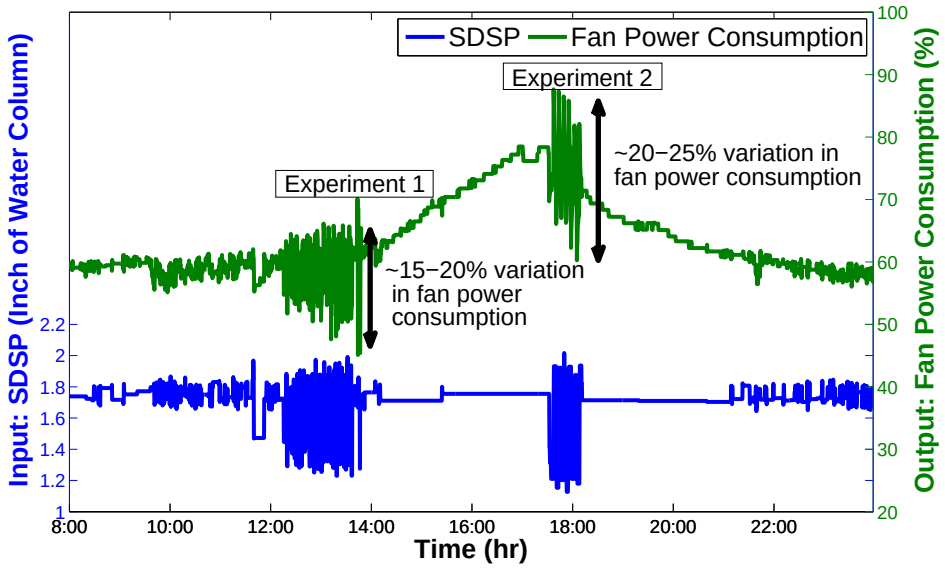

Figure 6.7: Fan power consumption can vary as quickly as in a few seconds by up to 25% by changing the SDSP setpoint.

the high frequency component of the flexibility signals from utility, can indeed be tracked using the already existing BEMS software in commercial buildings.

Further experiments were performed on June 6 and 7, 2013 [58]. It was shown that a maximum of 20% flexibility in fan power consumption can be obtained within a few seconds of changing the SDSP setpoint. It is shown in [58] that such modulations of fan speed does not lead to any sensible change in the room temperature and also the percentage of the time in which the reheat valve is open does not change compared to similar times of day in previous days.

6.4.2 Total Flexibility of Commercial Buildings in the US

Using the algorithm developed in this paper it was shown that a certain percentage of fan power consumption flexibility can be obtained from commercial buildings and used as fast regulation reserve at each time of the day. Consider a case when 50% flexibility in power consumption is available. 50% flexibility is equivalent to 67 kW of power. According to the latest survey on energy consumption of commercial buildings, performed in 2003 [5], there are 4.9 million commercial buildings in the US which cover a total area of about 72 billion square foot. Almost 30% of such buildings are equipped with variable frequency drive fans. Assuming the same fan power consumption flexibility per square foot to that of the SDH for all commercial buildings,

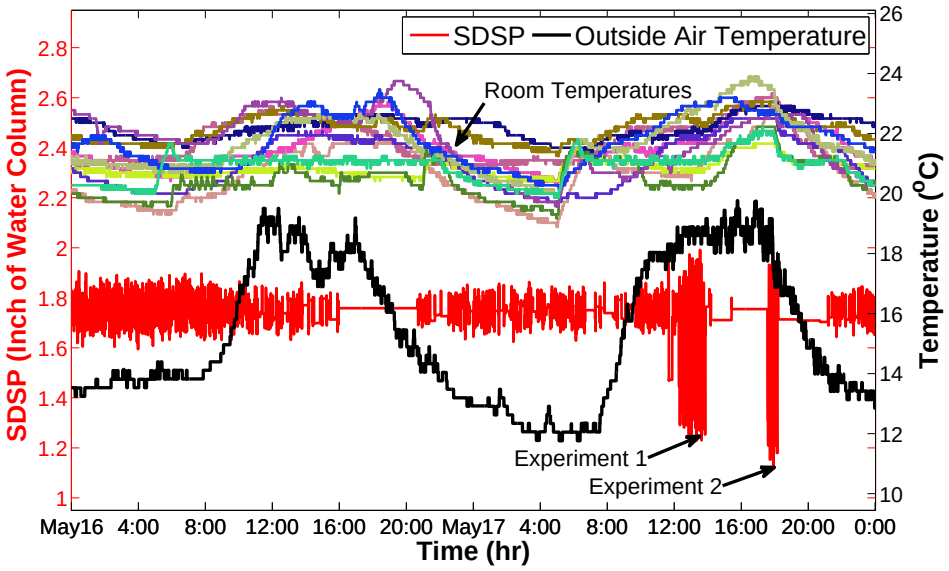

Figure 6.8: SDSP setpoint, outside air temperature, and temperature of 15 randomly selected rooms are shown for one day before (May 16, 2013) and the day of the experiment (May 17, 2013).

we estimate that at least 11.4 GW of fast ancillary service is readily available in the US at almost no cost, based on the 2003 data. Commercial building floor space is expected to reach 103 billion sq. ft. in 2035 [6]. With the same assumption of the above calculations, about 16.3 GW of regulation reserve will be available in 2035. Note that these numbers correspond to 50% flexibility. In the case of less or more percentage of available flexibility, these numbers will change proportionally.

Chapter 7

Ancillary Power Control

We first demonstrate that the demand-side flexibility of the Heating Ventilation and Air Conditioning (HVAC) system of a typical commercial building can be exploited for providing frequency regulation service to the power grid using at-scale experiments. We then show how this flexibility in power consumption of building HVAC system can be leveraged for providing regulation service. To this end, we consider a simplified model of the power grid with uncertain demand and generation. We present a Model Predictive Control (MPC) scheme to direct the ancillary service power flow from buildings to improve upon the classical Automatic Generation Control (AGC) practice. We show how constraints such as slow and fast ramping rates for various ancillary service providers, and short-term load forecast information can be integrated into the proposed MPC framework. Finally, we provide extensive simulation results to illustrate the effectiveness of the proposed methodology for enhancing grid frequency regulation. The material of this chapter is extracted from [60].

7.1 Introduction

A sustainable energy future requires widespread and significant penetration of Renewable Energy Sources (RESs). Several states in the U.S. and countries around the world have set ambitious targets for penetration of RESs by the next few years. The state of California, as an example, has targeted a 33% RES portfolio by 2020 [34]. However, volatility, uncertainty, and intermittency of RESs present a challenge for integrating such resources into the power grid in a large scale as proper functioning of the grid requires continuous power balance between supply and demand.

In addition to the need for maintaining balance between generation and load, the power flows through individual transmission lines and facilities should also be continuously controlled by adjusting generation or load. Instantaneous matching between

generation and load is even more challenging when considering uncertainties and randomness in demand. Short-term load variability results from a random switching of millions of individual loads. Longer-term variability results from predictable factors such as the daily and seasonal load patterns as well as less predictable events such as shifting weather patterns. Traditional generators may also cause unexpected fluctuations due to a range of equipment failures and aging [41].

Electricity storage is widely believed to be a solution to this problem by absorbing the variability associated with RESs. However, storage has two important drawbacks. It is expensive and it is not environmentally friendly. There is an emerging consensus that flexible loads with thermal storage capabilities such as Thermostatically Controlled Loads (TCLs) will play an important role in regulating the grid frequency and consequently in enabling deep penetration of RESs. It has been reported that about 20% of the total electricity consumption in the United States is used by residential TCLs such as air conditioners, heat pumps, water heaters, and refrigerators [4, 9]. Recently, [75, 33] showed that flexible loads such as TCLs are good candidates for providing ancillary services since their aggregate flexibility has the characteristic of a stochastic battery.

These recent papers also demonstrate that TCLs have a great potential for providing *fast* regulating reserve services; speed is indeed beneficial, especially in the context of recent regulations such as Federal Energy Regulatory Commission (FERC) Order 755 [13]. In fact, these new federal regulations require scheduling coordinators to procure and compensate more for regulation resources with *faster ramping rates*. There is an emerging consensus that future regulation services will be distinguished and compensated by *capabilities* of which ramping rate is one component.

Modeling, estimation, and control of aggregated heterogeneous TCLs for ancillary services have been discussed in [42, 62]. TCLs are particularly well-suited for Direct Load Control (DLC) and Demand Response (DR) programs that require loads to both decrease and increase power consumption because they are capable of storing thermal energy, much like a battery stores chemical energy. Fully responsive load control is highlighted in [24] in the context of TCLs and plug-in Electric Vehicles (EVs). Despite several challenges of using loads for system services, several key advantages include: 1) Reducing overall grid emissions by using loads to provide system services [78]. 2) Instantaneous response of loads to operator requests, versus slow response of generators to make significant output changes [40], and 3) Less variability associated to a very large number of small loads with respect to that of a small number of large generators [40]. It may soon be the case that the only technical impediment to reliable utilization of loads for system services is the development of the necessary load models and control strategies and the development of inexpensive and scalable communication and sensing infrastructure. [83].

In this paper, we first quantify (by means of empirical data analysis) the demand-

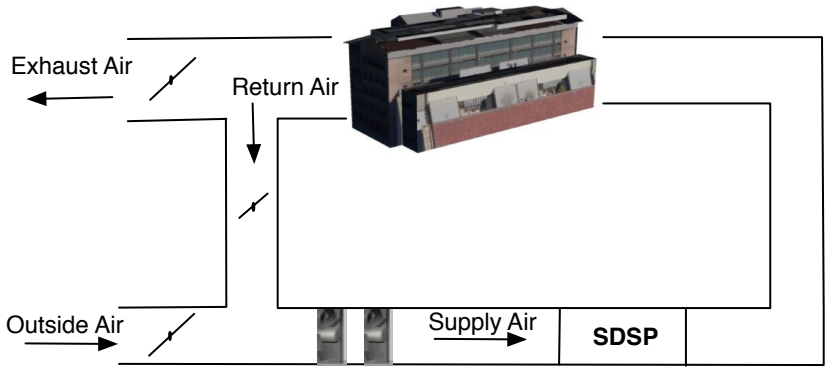

Figure 7.1: Schematics of the experiment testbed (Sutardja-Dai Hall on UC Berkeley campus).

side flexibility of a typical commercial building. Then we show that such flexibility can be tapped for providing fast frequency regulation service to the power grid. We then show the effectiveness of such "fast" ramping rates on the overall frequency regulation performance in the event of transient fluctuations in the load. To this end, we consider a simplified model of the power grid with uncertain demand and generation. We present a Model Predictive Control (MPC) scheme to control the ancillary service power flow from buildings to improve on the classical Automatic Generation Control (AGC) practice, by integrating information such as ramping rates of various sources of regulation services, and short term load forecast into the control algorithm. We provide extensive simulation results to illustrate the effectiveness of the proposed methodology for enhancing grid frequency regulation.

This chapter is organized as follows. A high-level description of the test bed, a summary and the results of the experiments performed on the test bed is provided in Section 7.2 which quantifies the amount of flexibility of the building power consumption. The mathematical model describing the dynamics of the power system is followed in Section 7.3. AGC is explained in Section 7.4. Our proposed MPC scheme is explained in details in Section 7.5. We provide extensive simulation results in Section 7.6.

7.2 Fast Ancillary Power from Buildings

Commercial buildings consume more than 35% percent of electricity in the US [5]. About 15% of electricity consumption in commercial buildings is related to the fans of the heating, ventilation and air conditioning (HVAC) systems. HVAC fans are essential parts of HVAC systems in buildings that move the conditioned air from the

air handling units (AHU) to the room level for ventilation, heating and cooling of building indoor climate [56, 67, 51]. For instance, the main supply fans that feed Sutardja-Dai Hall (SDH) on the UC Berkeley campus can spin at variable speeds. Power consumption is proportional to the cube of fan speed, with the maximum rated power of 134 KW or about 14% of the maximum power consumed in that building. Moreover, more than 30% of commercial buildings have adopted Building Energy Management System (BEMS) technology, which facilitates a fine control of the building HVAC components as well as the communication with the grid system operators. The majority of commercial buildings are also equipped with variable frequency drives, which in coordination with BEMS, can manipulate the HVAC system power consumption very frequently (in the order of seconds).

The supply fans to the building consume a large amount of power and have inherent flexibility in how they consume electricity. Hence, as shown in [59] we can directly modulate HVAC power consumption, within a safe envelope, without imposing extra cost to the building operation, and violating occupant comfort constraints. This flexibility in power consumption can be either upward (consuming more) or downward (consuming less), making it an ideal candidate for regulation services.

7.2.1 Experiment Results

To demonstrate this potential of commercial building HVAC system, we performed at-scale experiments on the HVAC system of Sutardja-Dai Hall on the UC Berkeley campus. The goal of the experiment was to quantify this flexibility, and to examine the effects of supply-fan speed modulation on the internal temperature of the rooms in the building. More details on the experiments is reported in [58]. Here we present a summary and the results of the experiments to set a foundation for the rest of the paper.

Figure 7.1 shows a high-level schematics of our experiment set-up including the main fans that feed Sutardja-Dai Hall. The speed of the fans is indirectly controlled by setting the Supply-Duct Static Pressure (SDSP) set-point value. The main challenges in performing this experiment include 1) keeping the pressure in the air ducts within a specific safety boundary and 2) minimizing the changes on the internal temperature that may make occupants uncomfortable. Because of the first concern, we used the SDSP set-point to control fan speed, instead of directly changing the fan speed by over-writing its control logic. The safety margin for the pressure set-point ranges between $[1.2 - 1.9]$ (Inch of Water Column). By changing the SDSP set-point, the fan speed either increased or decreased to adhere to the specified pressure value. We also tested the response speed of the fans to respond to changes to the pressure set-point and model the response. We run a number of experiments where we vary the speed of the fan at different rates and for different lengths of time. We show

that supply-fan speed modulation, over short time periods, has little effect on the comfort of the building occupants. In fact, the effects are not observable on the internal temperature of the spaces. We also show that the supply fan responds very quickly to a change in the pressure set-point, indicating that this is a viable option for providing grid-level ancillary response services.

The experiment results were shown in Chapter 6 in Figure 6.7 and Figure 6.8. Figure 6.7 shows the SDSP set-point signal, as the input of the experiment and the power consumption of the fan, as the output of the experiment. It is observed that the fan power consumption can vary by up to 25% within a few seconds around its nominal power consumption at each time (which itself is prescribed by the control logic running the HVAC system). Figure 6.8 on the other hand shows the SDSP set-point, the outside air temperature and temperature of 15 randomly selected rooms in the building. This figure is provided to show that the performed experiment created no significant and human-sensible change in the temperature of the building, and the building temperature was kept within the comfort zone at all times. Data of one day before the experiment (May 16) and the day of experiment (May 17) is provided for comparison. Based on the experiment results it was estimated in [58] that in average, each fan can provide about 18% of its nominal power as flexibility. This equals 12 kW out of 67 kW power draw for each fan, and in total 24 kW for the whole SDH building.

7.2.2 Estimation of Total Ancillary Power from All US Commercial Buildings

According to the latest survey on energy consumption of commercial buildings, performed in 2003 [5], there are 4.9 million commercial buildings in the US which cover a total area of about 72 billion square feet. Almost 30% of these buildings are equipped with variable frequency drive fans. Assuming the same fan power consumption flexibility per square foot for these buildings to that of SDH, we estimate that at least 4 GW of fast ancillary service is readily available in the US at almost no cost, based on the 2003 data. Commercial building floor space is expected to reach 103 billion sq. ft. in 2035 [6]. With the same assumption of the above calculations, about 5.6 GW of regulation reserve will be available in 2035.

We also identify a Single-Input Single-Output (SISO) Auto Regressive with eXogenous input (ARX) model of the fan with SDSP as input and fan power consumption as output based on the empirical data from SDH building. In order to track the SDSP signal, the two fans change their speeds and consequently their power consumption changes. A detailed description of the experiments and analysis on the results has been reported in [58].

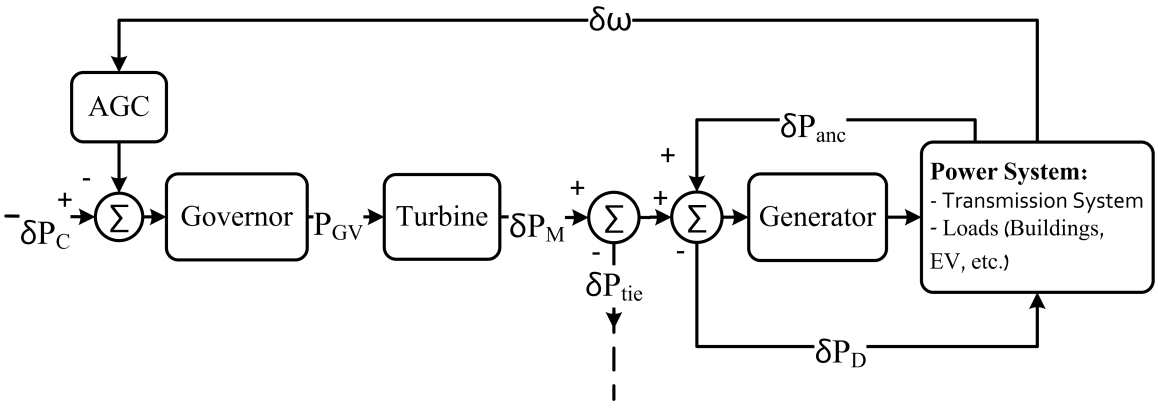

Figure 7.2: Block diagram of power system and its relation to governor, turbine, generator, and the AGC signal for each control area.

7.3 Mathematical Model of Power System Components

In this section, we develop mathematical models of power system components. These models, along with the estimations on the amount of available ancillary power from buildings, obtained from the experiment results of Section 7.2, and the proposed control algorithm of Section 7.5, will be used to demonstrate how commercial buildings flexibility can be utilized for frequency regulation provision in the smart grid.

Detailed models of power system elements have been developed in the literature. In this paper, we use the model developed by [26, 79, 43]. We present a detailed governor, turbine, and generator model in this section. The interconnection of these components of the power system is shown in the block diagram of Figure 7.2. δP_C is a control input which acts against increase or decrease in the power demand to regulate the system frequency. δP_D denotes the fluctuations in the power demand which is considered here as an exogenous input (disturbance). We present a model of the power system, with the following underlying assumptions:

- The resistance of the transmission lines are ignored.
- Transmission line between area i, and j is characterized by a reactance $X_{\text{tie}_{ij}}$.
- Reactive power flows are ignored.
- Voltage of bus i, denoted by V_i is considered constant.

Under steady state, we have: $\omega = \omega_o$, $V_t = V_t^o$, and $P_M = P_G = P_M^o$, where ω_o, V_t^o, and P_M^o are the nominal values for rated frequency, terminal voltage and mechanical

Table 7.1: Basic Power Systems Nomenclature

Variable	Description
P_M	Mechanical power input
P_M^o	Desired real power generation
P_G	Generated real electric power
δP_G	Increase in demand (at rated generator MVA)
V_t	Terminal voltage
P_D	Load (Power Demand)
δP_D	Input disturbance due to load changes
δP_C	Speed changer position feedback control signal
ω	Angular speed and frequency
ω_o	Rated (desired) frequency
Parameter	Description
D	Damping coefficient. Range: 0.01 - 0.1 [-]
M	Machine inertia constant. Range: 100 - 1000 [MW s]
R	Speed regulation constant. Range: 0.05 [p.u.]
T_i	Time constant for power system components. Range: {0,0.01-10} [s]
K_i	Fraction of total mechanical power outputs associated with different operating points of the turbine. Range: {0,0.1-1} [-]

power input. Basic variables of a power system which are used in the following formulations with a short description of each variable are reported in Table 7.1.

7.3.1 Governor Model

A general model of a governor contains three time constants. The overall input-output transfer function is given by

$$T_{Gov}(s) = \frac{(1 + sT_2)}{(1 + sT_1)(1 + sT_3)} \tag{7.1}$$

Mechanical-hydraulic governors have $T_2 = 0$ with typical values of $T_1 \in [0.2, 0.3]$ and $T_3 = 0.1$. Electro-hydraulic governors without steam feedback have typical time constants as follows: $T_1 = T_2 = 0$ and $T_3 \in [0.025, 0.1]$. Electro-hydraulic governors with steam feedback utilize a feed-forward mechanism. Typical time constant values under these assumptions are as follows: $T_1 = 2.8$, $T_2 = 1.0$, and $T_3 = 0.15$ [26].

7.3.2 Turbine Model

Turbines are grouped into steam and hydro turbines. The input-output transfer function model for turbines is given by

$$\frac{\delta P_M}{P_{GV}} = K_1F_1 + K_3F_1F_2 + K_5F_1F_2F_3 + K_7F_1F_2F_3F_4 \tag{7.2}$$

where F_1, F_2, F_3, and F_4 are transfer functions corresponding to steam chest, piping system, re-heaters, and cross-over mechanisms, respectively, and are given by

$$F_1(s) = \frac{1}{1+sT_4} \qquad F_2(s) = \frac{1}{1+sT_5} \tag{7.3}$$

$$F_3(s) = \frac{1}{1+sT_6} \qquad F_4(s) = \frac{1}{1+sT_7} \tag{7.4}$$

The basic time constant associated with steam turbines is T_4 which corresponds to that of the *steam chest*. For non-reheat steam turbines, this is the only time constant needed. The time constants T_5, T_6, and T_7, are associated with time delays of piping systems for re-heaters and cross-over mechanisms. The coefficients K_1, K_3, K_5, and K_7 represent fractions of total mechanical power outputs associated with *very high*, *high*, *intermediate*, and *low* pressure components, respectively. Typical values of steam turbine time constants and fractions are reported in [26].

7.3.3 Generator Model

The dynamics of the generator is given by the following transfer function

$$F_{Gen} = \frac{1}{D+sM} \tag{7.5}$$

where constants D and M represent the damping coefficient and the inertia of the governor, respectively.

7.3.4 Two Area System Model

Consider the interconnected system shown in Figure 7.3. It consists of two areas connected by a tie line with reactance X_{tie}. The power flow on the tie line from area 1 to area 2 is shown by P_{tie}. A positive δP_{tie} represents an increase in power transfer from area 1 to area 2. This in effect is equivalent to increasing the load of area 1 and decreasing the load of area 2. Each area consists of the subsystems shown in Figure 7.2.

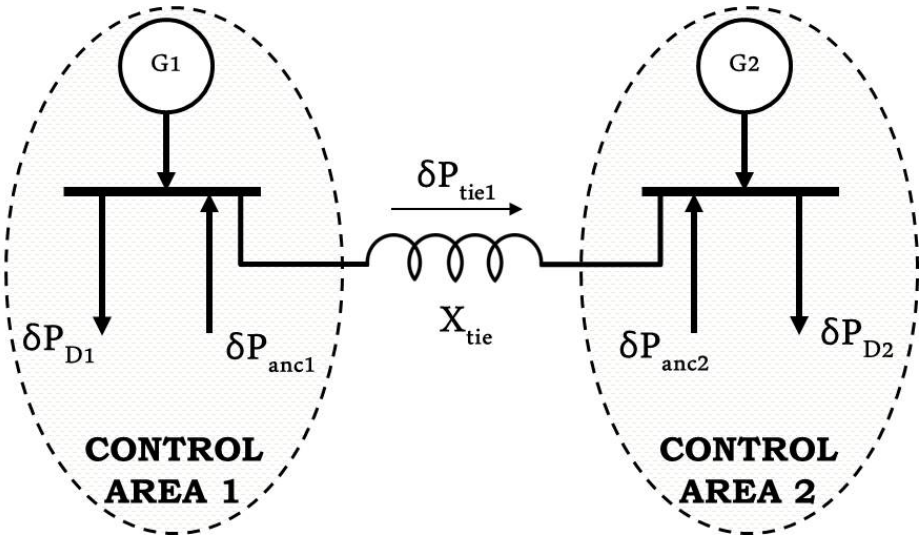

Figure 7.3: Two control area system. Each control area includes a generation unit. δP_{D_i} and δP_{anc_i} are load (demand) and ancillary power in area i.

Next, we present the mathematical model of the entire system. Note that the superscript refers to the control area (i or $j = 1, 2$ in the case of two interconnected areas), and the subscript indexes the state in each area.

$$\frac{dx_1^i}{dt} = \frac{(-D^i x_1^i + \delta P_M^i - \delta P_D^i - \delta P_{\text{tie}}^{ij} + \delta P_{\text{anc}}^i)}{M_x^i} \tag{7.6a}$$

$$\frac{dx_2^i}{dt} = \frac{(x_3^i - x_2^i)}{T_7^i} \tag{7.6b}$$

$$\frac{dx_3^i}{dt} = \frac{(x_4^i - x_3^i)}{T_6^i} \tag{7.6c}$$

$$\frac{dx_4^i}{dt} = \frac{(x_5^i - x_4^i)}{T_5^i} \tag{7.6d}$$

$$\frac{dx_5^i}{dt} = \frac{(P_{GV}^i - x_5^i)}{T_4^i} \tag{7.6e}$$

$$\frac{dx_6^i}{dt} = \frac{(x_7^i - x_6^i)}{T_3^i} \tag{7.6f}$$

$$\frac{dx_7^i}{dt} = \frac{(-x_7^i + \delta P_C^i - x_1^i/R^i)}{T_1^i} \tag{7.6g}$$

where

$$\delta P_M^i = K_1^i x_5^i + K_3^i x_4^i + K_5^i x_3^i + K_7^i x_2^i \tag{7.7}$$

$$P_{GV}^i = (1 - T_2/T_3)x_6^i + (T_2/T_3)x_7^i \tag{7.8}$$

In formulation (7.6), the first state represents the frequency increment, $x_1^i = \delta\omega_i$. All the seven states are derived using the mathematical model of each subsystem as presented in (7.1)–(7.5). Note that when the time constant representing the system pole is zero, the corresponding differential equation becomes an algebraic equation. For instance, when $T_5 = 0$, the equation $\frac{dx_4^i}{dt} = 1/T_5(x_5^i - x_4^i)$ becomes $x_5^i = x_4^i = 0$.

The real transferred power from bus i to bus j is governed by $P_{\text{tie}}^{ij} \approx V_i V_j b_{ij} cos(\theta_i - \theta_j)$. Since here we are concerned with incremental changes in all variables, the incremental change in P_{tie}^{ij} is given by $\delta P_{\text{tie}}^{ij} = \nu_{ij}(\theta_i - \theta_j)$ where at the nominal operating points, θ_i^o, $i = 1, 2$, the *transmission line stiffness* coefficient ν_{ij} is given by

$$\nu_{ij} = -V_i V_j b_{ij} cos(\theta_i^o - \theta_j^o). \tag{7.9}$$

In terms of the incremental state variables used, we have:

$$\delta P_{\text{tie}}^i = \sum_{j=1}^{n} \nu_{ij}(x_8^i - x_8^j), \tag{7.10}$$

where the state variable x_8^i is the integral of the frequency increment of area i, i.e.,

$$\frac{dx_8^i}{dt} = x_1^i. \tag{7.11}$$

The state space model (7.6)-(7.11) can be written in compact form as follows:

$$\frac{dx(t)}{dt} = A'x(t) + B_1' u_{sc}(t) + B_2' u_{anc}(t) + E'd(t). \tag{7.12}$$

In the case of two areas, states are stored in x, input signals to the speed changers are $u_{\text{sc}} = [\delta P_{C_1}\ \delta P_{C_2}]^T$, the ancillary inputs buildings are $u_{\text{anc}} = [\delta P_{\text{anc}_1}\ \delta P_{\text{anc}_2}]^T$, and the exogenous input (disturbance) (*i.e.* variations in demands) are denoted by $d = [\delta P_{D_1}\ \delta P_{D_2}]^T$.

7.3.5 Load Modeling

Many loads are frequency-sensitive. In this case, the incremental change in load will have a frequency-dependent part, i.e.

$$\delta P_D = \delta P_D^o + \bar{D}\delta\omega \tag{7.13}$$

where $\bar{D} = \frac{\partial P_D}{\partial \omega}$ represents the sensitivity of the load to frequency changes at the nominal value of the load. In this case, D^i in (7.6a) is replaced by $D^i + \bar{D}^i$, and δP_D is replaced by δP_D^o.

7.3.6 Discretization of the Continuous Model

We discretize the state space dynamics of the system using the forward Euler discretization scheme. We show the result of the equation for $\dot{x}_1^i$. The discretized dynamics for the rest of the states can be obtained in similar way. At time t_n we approximate the derivative of x_1^i by

$$\frac{dx_1^i(t_n)}{dt} \approx \frac{x_1^i(t_n + \delta t) - x_1^i(t_n)}{\delta t} \tag{7.14}$$

Hence the discretized version of (7.6a) is

$$x_1^i(t_{n+1}) = (1 - \frac{D_x^i \delta t}{M_x^i})x_1^i + \frac{\delta t}{M_x^i}\left[\delta P_M^i - \delta P_D^i - \delta P_{\text{tie}}^{ij} + \delta P_{\text{anc}}^i\right] \tag{7.15}$$

where $t_{n+1} = t_n + \delta t$ and δt is the discretization time step. The discrete-time state-space model is obtained as

$$x[k+1] = Ax[k] + B_1 u_{\text{sc}}[k] + B_2 u_{\text{anc}}[k] + Ed[k]. \tag{7.16}$$

We use this state update equation in Section 7.5 where we present the MPC formulation.

7.4 Automatic Generation Control

AGC is the main control function of a utility's energy control section. The purpose of an AGC is to track the load variations while maintaining the system frequency, net tie-line interchanges, and optimal generation level close to scheduled values [26]. This function is referred to as Load-Frequency Control (LFC). A secondary objective is to distribute the required change in generation among units to minimize operating cost [43]. In the case where several utilities are interconnected, each will perform its own AGC independent of the others.

With primary speed control action, a change in the system load will result in a steady-state frequency deviation, depending on the governor droop characteristics and frequency sensitivity to the load. All generating units on speed control will contribute to the overall change in generation, irrespective of the location of the load change. Restoration of system frequency to nominal value requires supplementary control action which adjusts the load reference set-point (through the speed-changer motor). Therefore, the basic means of controlling prime-mover power to match variations of system load in a desired manner is through control of the load reference set-points of selected generating units. As system load is continually changing, it is necessary to change the output of generators automatically.

7.4.1 AGC in Interconnected Power Systems

In the classical AGC, a simple PI control is utilized to regulate the frequency of the grid. The Area Control Error (ACE) is defined to be

$$ACE^i = \delta P^i_{tie} + \beta^i x^i_1, \tag{7.17}$$

where $\delta P^i_{\text{tie}} = P^i_{\text{tie}} - P^i_{\text{tie,scheduled}}$, and β^i is the bias coefficient of area i. The standard industry practice is to set the bias β^i at the so-called Area Frequency Response Characteristic (AFRC) which is defined as $\beta^i = D^i + 1/R^i$. The integral of the ACE is then used to construct the speed changer position (δP^i_C) feedback control signal. A new state x^i_9, is defined as

$$\frac{dx^i_9}{dt} = ACE^i. \tag{7.18}$$

Consequently the control input δP^i_C is given by

$$\delta P^i_C = -K^i x^i_9, \tag{7.19}$$

where K^i is the feedback gain. We propose a methodology for the ancillary services from buildings to help with the primary control of AGC as describe in 7.5.

7.5 Model Predictive Control of Ancillary Services

We present an MPC scheme to control the available ancillary service from commercial buildings to improve on the classical AGC practice. This optimization-based control framework is utilized as a *higher-level* control in a "hierarchical" fashion on top of the *low-level* classical AGC control. Consider the n-control area network shown in Figure 7.4.

7.5.1 Control Architecture

The schematic of the power system is depicted in Figure 7.5. Electric power is generated by the turbo-generators, and is fed to the power system. The power system transmits and distributes the power to the end use.

As mentioned earlier, the recent FERC Order 755 requires scheduling coordinators to procure and compensate more for regulation resources with *faster ramping rates*. To this end, we particularly address such constraints in our proposed MPC framework. In total, we consider the ramping rate constraint, $|P_{\text{anc}}[k+1] - P_{\text{anc}}[k]|$, the maximum capacity, $\max(P_{\text{anc}}[k]) > 0$, and the minimum capacity, $\min(P_{\text{anc}}[k]) < 0$, on the characteristics of the ancillary service signal from commercial buildings. We should mention that buildings can provide both positive and negative power flow to the

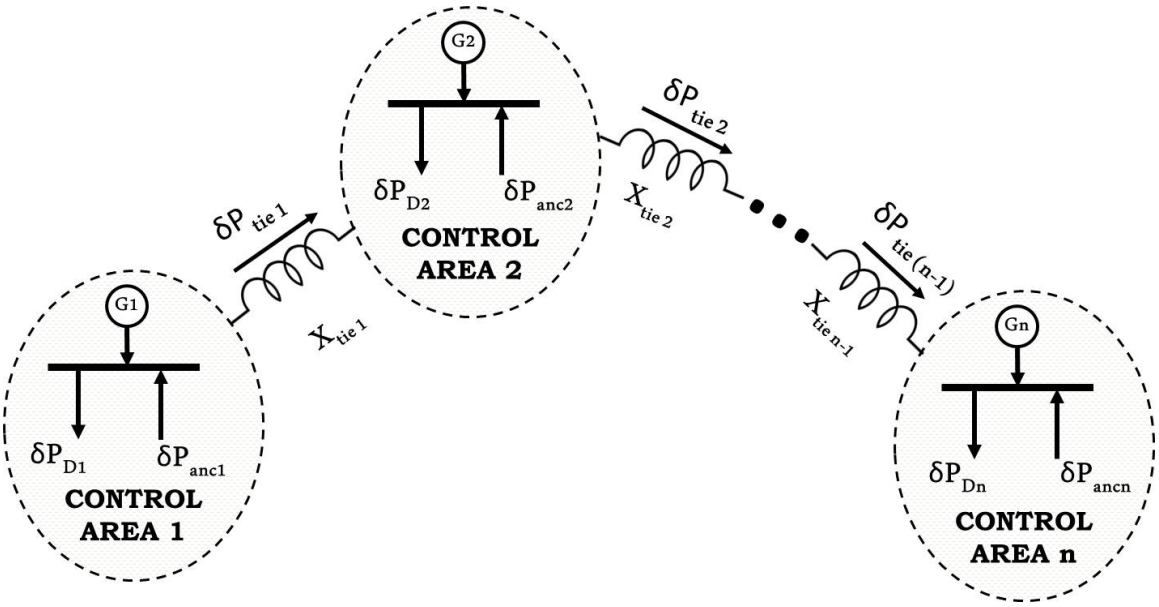

Figure 7.4: Schematic of n control areas with their corresponding tie power transfers and reactances.

grid, for frequency regulation purposes. When there is a power deficit, buildings will temporarily use less power, and when there is as surplus of power, they will temporarily use the extra power. We assume that the rate of power supply by the buildings is limited by

$$|\Delta P_{\text{anc}}| \leq \lambda, \tag{7.20}$$

where

$$\Delta P_{\text{anc}} := P_{\text{anc}}[k+1] - P_{\text{anc}}[k].$$

7.5.2 MPC Algorithm

At each time step k, we solve the following optimization problem:

$$\begin{aligned} \min_{U_{\text{anc}}[k]} \quad & \sum_{i=1}^{n} \sum_{j=0}^{H-1} (\text{ACE}^i[k+j|k])^2 \\ \text{s.t.} \quad & x[k+j+1|k] = Ax[k+j|k] + B_2 u_{\text{anc}}[k+j|k] + Ed[k+j|k] \\ & \underline{\pi}[k+j|k] \leq u_{\text{anc}}[k+j|k] \leq \overline{\pi}[k+j|k] \\ & |u_{\text{anc}}[k+j+1|k] - u_{\text{anc}}[k+j|k]| \leq \lambda[k+j|k] \end{aligned} \tag{7.21}$$

where

$$U_{\text{anc}}[k] = (u_{\text{anc}}[k|k], u_{\text{anc}}[k+1|k], \ \ldots, u_{\text{anc}}[k+H-1|k])$$

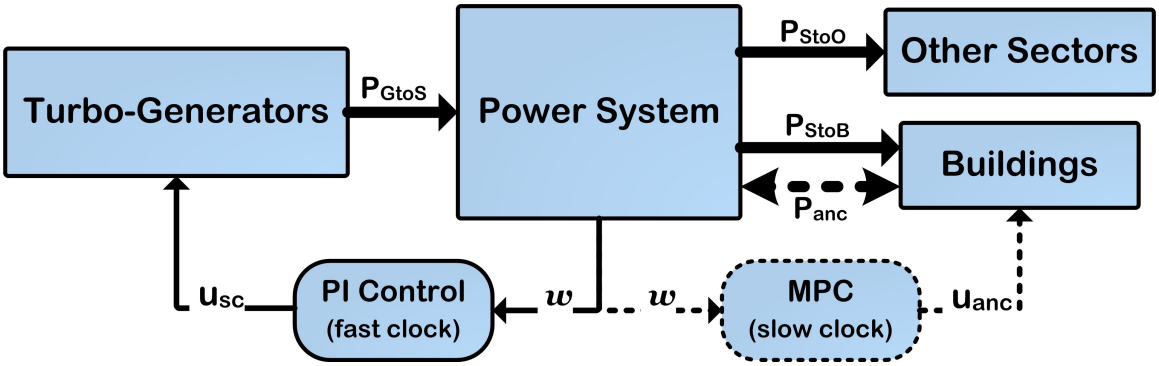

Figure 7.5: Schematic of power system and its relation to turbo-generator and and other sectors including the building sector, along with the control architecture. The thick arrows represent the flow of power and the thin arrows represent frequency and control signals. The dashed arrows indicate the additional signals and power flows proposed in this paper.

is the vector of inputs from k to $k+H$, n is the number of areas that participate in this regulation program, and H is the prediction horizon of MPC. Notation $x[k+j|k]$ means that at each time step k, predictions of x for future times $k+j$ are obtained at time k. All the constraints of problem (7.21) should hold for $j = 0, 1, \ldots, H-1$. The cost function of this optimization problem minimizes the ℓ_2 norm of the ACE signal in areas $i = 1, 2, ..., n$, by exploiting the ancillary service available form buildings, taking into account the system dynamics and constraints. The constraints of the optimization problem are $\overline{\pi}[k+j|k] > 0$ maximum positive power and $\underline{\pi}[k+j|k] < 0$ maximum negative power provided by the participating set of buildings in each area in the contract. Here, "positive" and "negative" refer to the flow of power from generation to consumption. These values are estimated on the building side and sent to the utility periodically. $\lambda[k+j|k]$ is the maximum limit on the rate of change of ancillary service provided by the building side. Note that in the state-space model used in the MPC problem, we do not incorporate $B_1 u_{sc}[k]$ as u_{sc} is assumed to be constant and is regulated by the local PI controller. Figure 7.5 illustrates the structure of our MPC implementation with regards to other components of the power system.

7.6 Simulation Results

We consider two interconnected control areas with parameters of their models presented in Table 7.2, and with inter-area stiffness coefficient of $\nu = 1.0$ $(p.u.)$. The main generation unit for area 1 is a non-reheat turbo generator (TG) system and the main generation unit for area 2 is a hydro TG system. Some metrics such as root mean square (rms) values of frequency and ACE signal are considered to compare the

Table 7.2: Parameters for the Two Areas Used in the Simulations

Control Area	Parameters
Area 1	$T_1 = 0.1$, $T_3 = 0.1$, $T_4 = 1.0$
	$K_1 = 1.0$
	$M = 132.6$ $(MW.sec)$
	$D = 0.0265$ $(p.u.)$
Area 2	$T_1 = 0.2$, $T_3 = 0.3$, $T_4 = 0.1$, $T_5 = 0.5$
	$K_1 = 0.2$, $K_3 = 3$
	$M = 663.13$ $(MW.sec)$
	$D = 0.1325$ $(p.u.)$

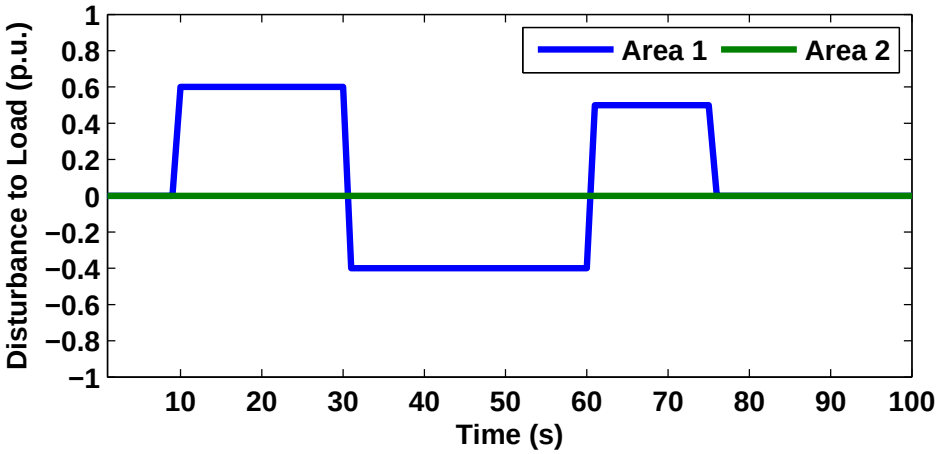

Figure 7.6: Disturbance to load in area 1 and 2.

performances of the proposed controller. We use time-invariant bounds on the maximum and minimum ancillary power $\overline{\pi}[k] = \underline{\pi}[k] = \pi$, and maximum rate of change of ancillary power $\lambda[k] = \lambda$, in the following simulations.

The resulting quadratic program (QP) obtained in Section 7.5.2 was formulated using YALMIP [49] and solved with ILOG CPLEX Barrier Optimizer [10] for a time horizon of 100 s and a sampling time $T_s = 1$ s. On a 4-core 2.67-GHz Intel processor with 3.86 GB of memory, the average and maximum solver times were 0.02 s and 0.03 s, respectively, for a prediction horizon of $H = 10$.

We consider a disturbance in the load of area 1, and no disturbance in the load of area 2, as shown in Figure 7.6. We assess the performance of the proposed controller considering the following scenarios:

Finally we present the results on the effect of integrating load forecast in the MPC framework. We consider a constant maximum available ancillary power of $\pi = 0.9$

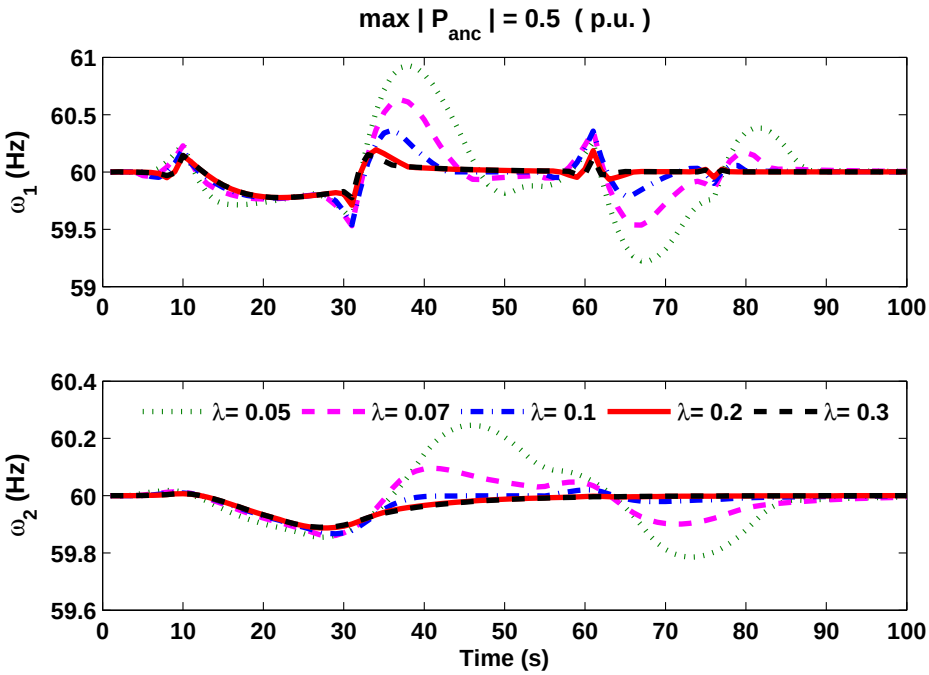

Figure 7.7: Frequency of areas 1 and 2 in response to the disturbance are shown. Prediction horizon is $H = 10$ and maximum ancillary power is $\max|P_{\text{anc}}| = 0.5$ $(p.u.)$. Results are for various values of rate of change of ancillary power such that $\max|\Delta P_{\text{anc}}| = \lambda$.

(p.u.) and present the results of rms of frequency deviation for various values of rate of change of ancillary power λ versus prediction horizon as shown in Figure 7.11. Short term load forecast can be very valuable and can dramatically improve the performance of the controller. for prediction values up to about $H = 10$, the performance keeps improving, while for longer load forecasts, the improvement is not as significant.

Scenario 1: The maximum ancillary service available in each area is 0.5 per unit (p.u.) of power. We consider a prediction horizon of H=10 time steps. As shown in Figure 7.7 by increasing the maximum rate of change of ancillary power (also known as ramping rate for generation units) the resulting frequency deviation decreases. Ramping rate of $\lambda = 0.05$ (p.u./s) is associated with large power generator size, ramping rate of $\lambda = 0.1$ (p.u./s) is associated with smaller size generators and high ramping rates such as $\lambda = 0.3$ (p.u./s) is associated with fast ancillary service such as the one provided by building HVAC system fan.

Scenario 2: We consider a fixed ancillary ramping rate of $\lambda = 0.9$ (p.u./s), and show the frequency deviations in cases with different maximum available ancillary power in each area. The ramping rate is considered very high to eliminate the effects of slow ramping rates on the results, so that we can perform a fair comparison which

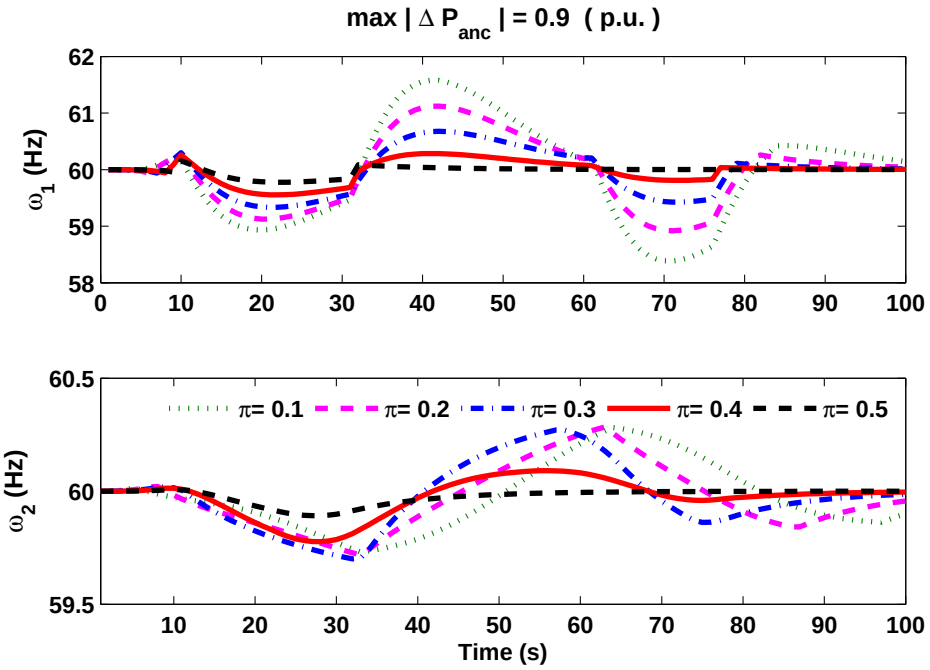

Figure 7.8: Prediction horizon is $H = 10$ and the maximum ancillary power is $\max|\Delta P_{\text{anc}}| = 0.9\ (p.u.)$. Figure shows frequency of control areas 1 and 2. In each case, we change $\max|P_{\text{anc}}| = \pi$.

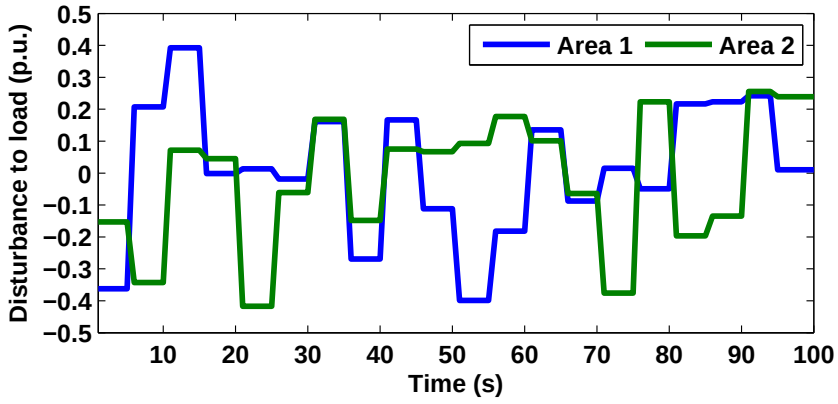

Figure 7.9: Disturbance in load of area 1 and 2 used for the mass simulations.

only concerns the effect of maximum ancillary power. As shown in Figure 7.8 by increasing the maximum available ancillary power, the frequency deviation decreases. Although the disturbance in load of area 1 affects both interconnected areas, the change of frequency in area 1 is larger than that of area 2.

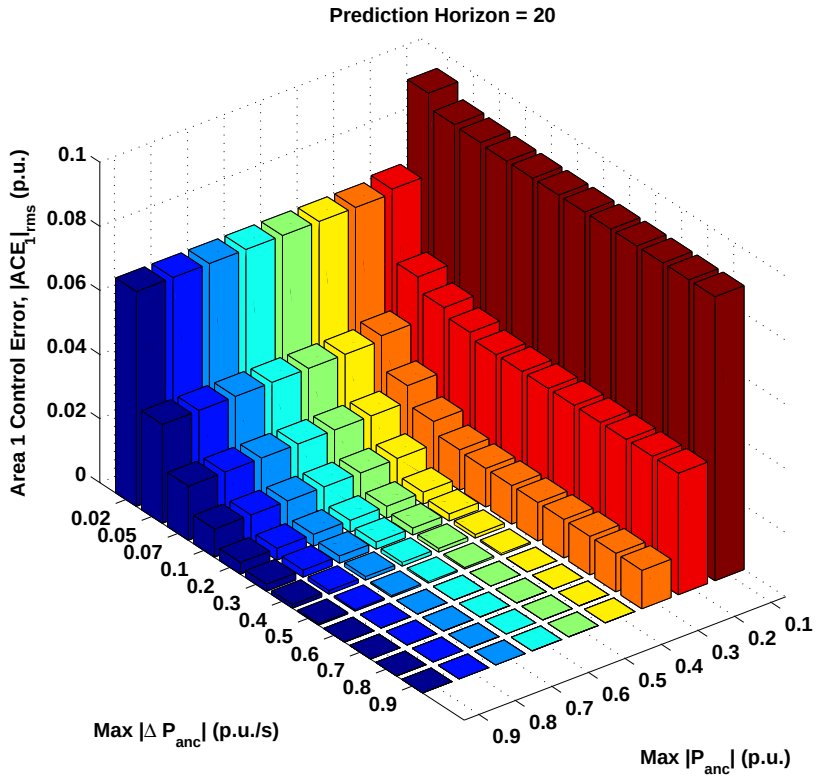

Figure 7.10: Result of mass simulation for various maximum ancillary power and maximum rate of change of ancillary power for prediction horizon of 20 time steps.

Scenario 3: We consider a stronger disturbance and compare the overall frequency and area control error in rms sense. We consider a zero mean disturbance to both areas with a maximum absolute value of ancillary power of $\pi = 0.4$ (p.u.) as shown in Figure 7.9. We then perform a mass simulation using various maximum ancillary power available in each area within the range [0.1 0.9] (p.u.), and various rate of change of ancillary service within the range [0.05 0.9] (p.u./s), and prediction horizons ranging from 1 to 20 time steps.

As shown in Figure 7.10, the highest and lowest ACE_{rms} are obtained for the set $\{\pi = 0.1,\ \lambda = 0.02\}$, and the set $\{\pi = 0.9,\ \lambda = 0.9\}$, respectively.

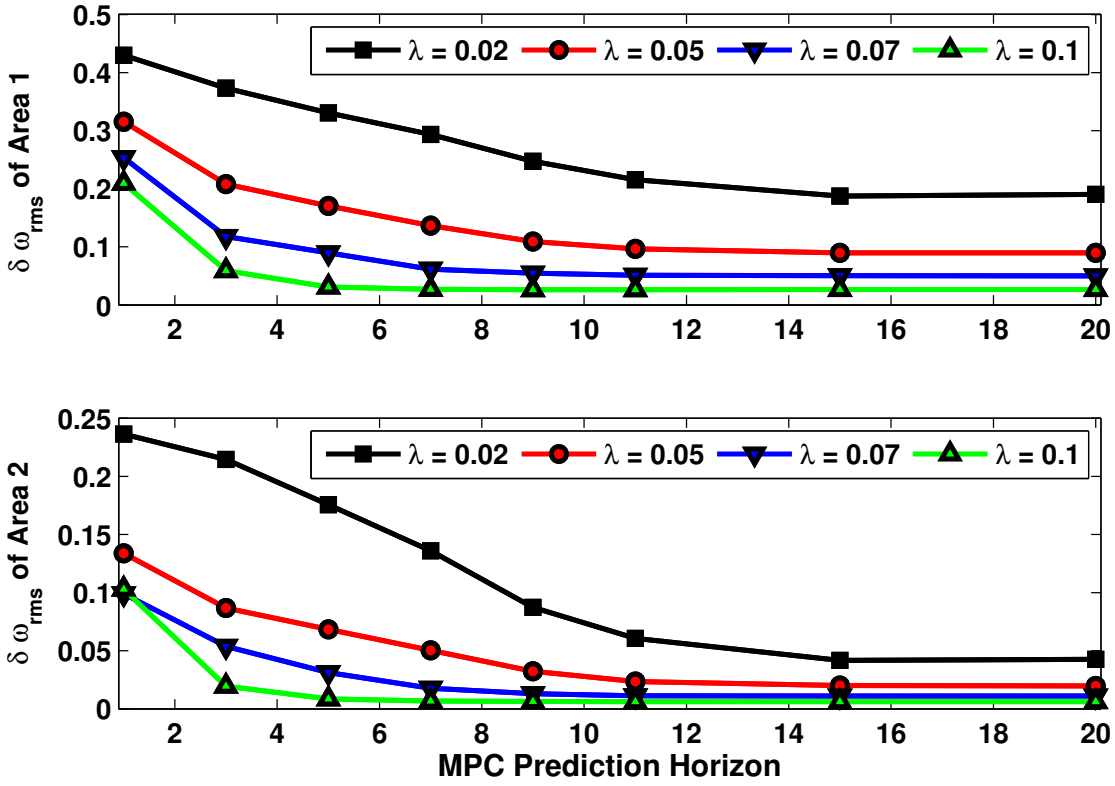

Figure 7.11: Root mean square of frequency deviation for various λ values for a constant $\pi = 0.9$ versus prediction horizon.

Chapter 8

Conclusion and Future Work

8.1 Conclusion

In this dissertation we presented a building model, obtained based on the buildings thermal characteristics and behavior that captures the relevant dynamics of the temperature for each room taking into account the interactions between rooms, external loads such as weather forecast, and building occupancy.

To enhance the performance of the proposed model, we introduced a framework to continuously update the parameters of the model. We called that model a Parameter-Adaptive Building (PAB) Model. Using the obtained building model, we then presented Model Predictive Control (MPC) to minimize the energy consumption of the building while satisfying thermal comfort, and constraints on other system states and inputs. As building models always inherit uncertainty, we proposed a Robust Model Predictive Control (RMPC) to obtain a control strategy that is robust against model uncertainties. We then addressed the trade-off between comfort and energy use.

We then proposed a framework to co-design the control algorithm and the embedded platform of building Heating, Ventilation and Air Conditioning (HVAC) systems of building, as a complex cyber-physical system. Based on the developed models, we explore the co-design of the control algorithm and the temperature sensing subsystem of the embedded platform to optimize with respect to energy cost and monetary cost while satisfying the constraints for user comfort level.

Leveraging the flexibility of commercial buildings in how their HVAC system consumes energy, we proposed a means to define and quantify the flexibility of a commercial building. We then proposed a contractual framework that could be used by the building operator and the utility to declare flexibility on the one side and reward structure on the other side. We then designed a control mechanism for the building to decide its flexibility for the next contractual period to maximize the reward, given the contractual framework.

Finally, we demonstrated that the demand-side flexibility of the HVAC system of a typical commercial building can be exploited for providing frequency regulation service to the power grid using at-scale experiments. We then showed how this flexibility in power consumption of building HVAC system can be leveraged for providing regulation service. We presented an MPC scheme to direct the ancillary service power flow from buildings to improve upon the classical Automatic Generation Control (AGC) practice. We showed how constraints such as slow and fast ramping rates for various ancillary service providers, and short-term load forecast information can be integrated into the proposed MPC framework.

8.2 Future Work

- We proposed a methodology and framework to adapt the parameters of a building model in an online fashion leading to the PAB Model. As future work, the PAB model can be utilized in an adaptive control framework to yield better control performance.

- The inter-dependencies between the HVAC control algorithm and the embedded platform can be studied as future work. In particular, one can analyze the relation between the prediction error and the design of the embedded platform (e.g. the choice of the CO2 and outdoor sensors), and leverage the findings in co-design. Our consideration of the embedded platform design can be also broadened from the sensing system to the computation and communication components, such as the impact of communication reliability on the control algorithm.

- In Chapter 6 where we discussed building flexibility, we assumed that the building operator communicates directly with the utility. However a more realistic scenario would be when an electricity broker, an aggregator, seeks rate offers from suppliers for "bundled" groups of customers and acts on their behalf. In the future work this scenario can be studied in details to generalize this approach appropriately.

- Chapter 7 where we discussed ancillary power control, was based on the assumption that the load in the power gird is accurately predictable. However, it is very difficult to accurately forecast power consumption. As future work, a robust MPC framework can be developed to address the uncertainties associated with imperfect predictions of load.

Bibliography

[1] CIMIS - California Irrigation Management Information System. http://www.cimis.water.ca.gov .

[2] FCL – Future Cities Lab. http://www.futurecities.ethz.ch/.

[3] Apogee Building Automation. https://www.hqs.sbt.siemens.com/gip/general/dlc /data/assets/hq/APOGEE–Building-Automation-A6V10301530-hq-en.pdf.

[4] Buildings energy data book. http://buildingsdatabook.eren.doe.gov/default.aspx.

[5] Commercial Buildings Energy Consumption survey (CBECS). http://www.eia.gov/consumption/commercial/data/2003/index.cfm? view=consumption.

[6] EIA – Annual energy Outlook 2012. www.eia.gov/forecasts/aeo/pdf/0383(2012).pdf .

[7] Metar - national climatic data center. http://www.ncdc.noaa.gov.

[8] National Renewable Energy Laboratory (Jan 2013). http://www.nrel.gov/.

[9] U.S. Energy Information Administration, annual energy review 2010. http://www.eia.gov/totalenergy/data/annual/consumption.

[10] IBM ILOG CPLEX Optimizer. http://www.ibm.com/software/integration/ optimization/cplex-optimizer/, February 2012.

[11] Building Energy Data Book of DOE. http://buildingsdatabook.eren.doe.gov/ default.aspx, February 2013.

[12] Openbms, a Berkeley campus energy portal., Sep 2013. http://berkeley.openbms.org/.

[13] Frequency energy regulation compensation - FERC order no. 755. Technical report, MISO, March 2013. https://www.midwestiso.org.

[14] K. Poolla A. Packard and R. Horowitz. Jacobian linearization, equilibrium points. ME 132 Notes, University of California, Berkeley.

[15] Clarence Agbi, Zhen Song, and Bruce Krogh. Parameter Identifiability for Multi-Zone Building Models. In *IEEE 51st Annual Conference on Decision and Control (CDC)*, pages 6951–6956, 2012.

[16] B.D.O. Anderson and J.B. Moore. *Linear optimal control*. Prentice-Hall Englewood Cliffs, NJ, 1971.

[17] B. Arguello-Serrano and M. Velez-Reyes. Nonlinear control of a heating, ventilating, and air conditioningsystem with thermal load estimation. *IEEE Transactions on Control Systems Technology*, 7(1):56–63, 1999.

[18] B. Arguello-Serrano and M. Velez-Reyes. Nonlinear control of a heating, ventilating, and air conditioning system with thermal load estimation. *Control Systems Technology, IEEE Transactions on*, 7(1):56–63, 2002.

[19] A. Bemporad and M. Morari. Robust model predictive control: A survey. *Robustness in identification and control*, pages 207–226, 1999.

[20] S. Bertagnolio and J. Lebrun. Simulation of a building and its HVAC system with an equation solver: application to benchmarking. In *Building Simulation*, volume 1, pages 234–250. Springer, 2008.

[21] Dimitri P Bertsekas. Nonlinear programming. 1999.

[22] D. Bertsimas and M. Sim. Tractable approximations to robust conic optimization problems. *Mathematical Programming*, 107(1):5–36, 2006.

[23] F. Borrelli, A. Bemporad, and M. Morari. Predictive control for linear and hybrid systems. to be published, April 2011.

[24] D.S. Callaway and I.A. Hiskens. Achieving controllability of electric loads. *Proceedings of the IEEE*, 99(1):184–199, 2011.

[25] Stephen Dawson-Haggerty, Xiaofan Jiang, Gilman Tolle, Jorge Ortiz, and David Culler. smap: a simple measurement and actuation profile for physical information. In *Proceedings of the 8th ACM Conference on Embedded Networked Sensor Systems*, SenSys'10, New York, USA, 2010. ACM.

[26] A.S. Debs. *Modern power systems control and operation*. Kluwer Academic Publishers, Norwell, MA, 1988.

[27] K. Deng, P. Barooah, P.G. Mehta, and S.P. Meyn. Building thermal model reduction via aggregation of states. In *American Control Conference (ACC), 2010*, pages 5118–5123. IEEE, 2010.

[28] F. Felgner, S. Agustina, R.C. Bohigas, R. Merz, and L. Litz. Simulation of thermal building behaviour in modelica. In *Proceedings of the 2nd International Modelica Conference*, volume 154. Citeseer, 2002.

[29] F. Felgner, R. Merz, and L. Litz. Modular modelling of thermal building behaviour using modelica. *Mathematical and Computer Modelling of Dynamical Systems*, 12(1):35–49, 2006.

[30] M.A. Goforth, G.W. Gilcrest, and J.D. Sirianni. Cloud Effect on Thermal Downwelling Sky Radiance. *Proc. SPIE, Society of Photo-Optical Instrumentation Engineers*, 4710–27(1):pp 203–213, 2002.

[31] D. Gyalistras and M. Gwerder. Use of weather and occupancy forecasts for optimal building climate control (OptiControl): Two years progress report. *Terrestrial Systems Ecology ETH Zurich, Switzerland and Building Technologies Division, Siemens Switzerland Ltd., Zug, Switzerland*, 2010.

[32] He Hao, Anupama Kowli, Yashen Lin, Prabir Barooah, and Sean Meyn. Ancillary service for the grid via control of commercial building hvac systems. In *American Control Conference (ACC)*, 2013.

[33] He Hao, Borhan M. Sanandaji, Kameshwar Poolla, and Tyrone L. Vincent. Aggregate flexibility of thermostatically controlled loads. *submitted to the IEEE Transactions of Power Systems*, 2013.

[34] Udi Helman. Resource and transmission planning to achieve a 33% RPS in California–ISO modeling tools and planning framework. In *FERC Technical Conference on Planning Models and Software*, 2010.

[35] G.P. Henze, C. Felsmann, and G. Knabe. Evaluation of optimal control for active and passive building thermal storage. *International Journal of Thermal Sciences*, 43(2):173–183, 2004.

[36] F.P. Incropera and D.P. DeWitt. *Introduction to heat transfer*. John Wiley & Sons New York, 1996.

[37] S.J. Julier and J.K. Uhlmann. A new extension of the kalman filter to nonlinear systems. In *Int. Symp. Aerospace/Defense Sensing, Simul. and Controls*, volume 3, page 26. Spie Bellingham, WA, 1997.

[38] S.J. Julier and J.K. Uhlmann. Unscented filtering and nonlinear estimation. *Proceedings of the IEEE*, 92(3):401–422, 2004.

[39] S.J. Julier, J.K. Uhlmann, and H.F. Durrant-Whyte. A new approach for filtering nonlinear systems. In *American Control Conference, 1995. Proceedings of the*, volume 3, pages 1628–1632. IEEE, 1995.

[40] B.J. Kirby. *Spinning reserve from responsive loads*. United States. Department of Energy, 2003.

[41] B.J. Kirby. *Frequency regulation basics and trends*. United States. Department of Energy, 2005.

[42] S. Koch, J.L. Mathieu, and D.S. Callaway. Modeling and control of aggregated heterogeneous thermostatically controlled loads for ancillary services. In *Proc. PSCC*, pages 1–7, 2011.

[43] P. Kundur, N.J. Balu, and M.G. Lauby. *Power system stability and control*, volume 4. McGraw-hill New York, 1994.

[44] S.F. Larsen, C. Filippín, and G. Lesino. Thermal behavior of building walls in summer: Comparison of available analytical methods and experimental results for a case study. In *Building Simulation*, volume 2, pages 3–18. Springer, 2009.

[45] P. Levis, S. Madden, J. Polastre, R. Szewczyk, E. Brewer, et al. Tinyos: An operating system for sensor networks. *Ambient intelligence*, 35, 2005.

[46] J. Lofberg. Approximations of closed-loop minimax mpc. In *Decision and Control, 2003. Proceedings. 42nd IEEE Conference on*, volume 2, pages 1438–1442. IEEE, 2003.

[47] J. Löfberg. *Minimax approaches to robust model predictive control*. Univ., 2003.

[48] J. Lofberg. Yalmip : A toolbox for modeling and optimization in MATLAB. In *Proceedings of the CACSD Conference*, Taipei, Taiwan, 2004.

[49] John Lofberg. Yalmip: A toolbox for modeling and optimization in matlab. In *Int. Symp. Computer Aided Control Systems Design*, pages 284–289, 2004.

[50] Jingran Ma, S Joe Qin, Bo Li, and Tim Salsbury. Economic model predictive control for building energy systems. In *Innovative Smart Grid Technologies (ISGT), 2011 IEEE PES*, pages 1–6. IEEE, 2011.

[51] Y. Ma, F. Borrelli, B. Hencey, B. Coffey, S. Bengea, and P. Haves. Model predictive control for the operation of building cooling systems. In *American Control Conference (ACC), 2010*, pages 5106–5111. IEEE, 2010.

[52] Yudong Ma, Garrett Anderson, and Francesco Borrelli. A distributed predictive control approach to building temperature regulation. In *American Control Conference (ACC), 2011*, pages 2089–2094. IEEE, 2011.

[53] M. Maasoumy, A. Pinto, and A. Sangiovanni-Vincentelli. Model-based hierarchical optimal control design for HVAC systems. In *Dynamic System Control Conference (DSCC), 2011*. ASME, 2011.

[54] M. Maasoumy and A. Sangiovanni-Vincentelli. Optimal control of HVAC systems in the presence of imperfect predictions. In *Dynamic System Control Conference (DSCC)*. ASME, 2012.

[55] M. Maasoumy and A. Sangiovanni-Vincentelli. Total and peak energy consumption minimization of building hvac systems using model predictive control. *IEEE Design and Test of Computers*, Jul-Aug 2012.

[56] Mehdi Maasoumy. Modeling and optimal control algorithm design for HVAC systems in energy efficient buildings. Master's thesis, EECS Department, University of California, Berkeley, Feb 2011.

[57] Mehdi Maasoumy, Barzin Moridian, Meysam Razmara, mahdi Shahbakhti, and Alberto Sangiovanni Vincentelli. "Online Simultaneous State Estimation and Parameter Adaptation for Building Predictive Control". In *DSCC*, Stanford, CA, May 2013.

[58] Mehdi Maasoumy, Jorge Ortiz, David Culler, and Alberto Sangiovanni-Vincentelli. Flexibility of commercial building hvac fan as ancillary service for smart grid. In *submitted to the IEEE Green Energy and Systems Conference (IGESC)*, 2013.

[59] Mehdi Maasoumy, Catherine Rosenberg, Alberto Sangiovanni-Vincentelli, and Duncan Callaway. Model predictive control approach to online computation of demand-side flexibility of commercial buildings hvac systems for supply following. In *submitted to the American Control Conference (ACC)*, 2014.

[60] Mehdi Maasoumy, Borhan Sanandaji, Kameshwar Poolla, and Alberto Sangiovanni-Vincentelli. Model predictive control of regulation services from commercial buildings to the smart grid. In *submitted to the American Control Conference (ACC)*, 2014.

[61] Mehdi Maasoumy, Qi Zhu, Cheng Li, Forrest Meggers, and Alberto Sangiovanni-Vincentelli. Co-Design of Control Algorithm and Embedded Platform for HVAC Systems. In *The 4th ACM/IEEE International Conference on Cyber-Physical Systems (ICCPS 2013)*, Philadelphia, USA, April 2013.

[62] J.L. Mathieu and D.S. Callaway. State estimation and control of heterogeneous thermostatically controlled loads for load following. In *System Science (HICSS), 2012 45th Hawaii International Conference on*, pages 2002–2011. IEEE, 2012.

[63] N. Mendes, G.H.C. Oliveira, and H.X. de Araújo. Building thermal performance analysis by using matlab/simulink. In *Seventh International IBPSA Conference, Rio de Janeiro, Brazil*, 2001.

[64] Hamid Moradkhani, Soroosh Sorooshian, Hoshin V. Gupta, and Paul R. Houser. Dual State-Parameter Estimation of Hydrological Models Using Ensemble Kalman Filter. *Advances in Water Resources*, 28(2):135–147, 2005.

[65] Petru-Daniel Moroşan, Romain Bourdais, Didier Dumur, and Jean Buisson. Building temperature regulation using a distributed model predictive control. *Energy and Buildings*, 42(9):1445–1452, 2010.

[66] F. Oldewurtel, C.N. Jones, and M. Morari. A tractable approximation of chance constrained stochastic mpc based on affine disturbance feedback. In *Decision and Control, 2008. CDC 2008. 47th IEEE Conference on*, pages 4731–4736. IEEE, 2008.

[67] F. Oldewurtel, A. Parisio, C.N. Jones, M. Morari, D. Gyalistras, M. Gwerder, V. Stauch, B. Lehmann, and K. Wirth. Energy efficient building climate control using stochastic model predictive control and weather predictions. In *American Control Conference (ACC), 2010*, pages 5100–5105. IEEE, 2010.

[68] F. Oldewurtel et al. "Use of Model Predictive Control and Weather Forecasts for Energy Efficient Building Climate Control". *Energy and Buildings*, vol. 45, pp. 15-27, 2012.

[69] Gregory L Plett. Sigma-Point Kalman Filtering for Battery Management Systems of LiPB-Based HEV Battery Packs: Part 2: Simultaneous State and Parameter Estimation. *Journal of Power Sources*, 161(2):1369–1384, 2006.

[70] J. Polastre, R. Szewczyk, and D. Culler. Telos: enabling ultra-low power wireless research. In *Information Processing in Sensor Networks, 2005. IPSN 2005. Fourth International Symposium on*, pages 364–369. IEEE, 2005.

[71] Samuel Prvara, Jir Cigler, Zdenek Vna, Frauke Oldewurtel, Carina Sagerschnig, and Eva cekov. Building Modeling as a Crucial Part for Building Predictive Control. *Energy and Buildings*, 56:8 – 22, 2013.

[72] P. Radecki and B. Hencey. Online building thermal parameter estimation via unscented kalman filtering. In *American Control Conference (ACC), 2012*, pages 3056–3062. IEEE, 2012.

[73] Mohammad Rafiee, Andrew Tinka, Jerome Thai, and Alexandre M Bayen. Combined state-parameter estimation for shallow water equations. In *American Control Conference (ACC)*, pages 1333–1339. IEEE, 2011.

[74] J.A. Rossiter. *Model-based predictive control: a practical approach*. CRC, 2003.

[75] Borhan M. Sanandaji, He Hao, and Kameshwar Poolla. Fast regulation service provision via aggregation of thermostatically controlled loads. *to appear in Proceedings of 47-th Hawaii International Conference on System Sciences – HICSS47*, 2014.

[76] Jan Širokỳ, Frauke Oldewurtel, Jiří Cigler, and Samuel Prívara. Experimental analysis of model predictive control for an energy efficient building heating system. *Applied Energy*, 88(9):3079–3087, 2011.

[77] A. Standard. 90.1-1989. *American Society of Heating, Refrigerating, and Air-Conditioning Engineers*, 1989.

[78] G. Strbac. Demand side management: Benefits and challenges. *Energy Policy*, 36(12):4419–4426, 2008.

[79] V. Vittal and A.R. Bergen. *Power systems analysis*. Prentice Hall, 1999.

[80] Andreas Wächter and Lorenz T Biegler. On the implementation of an interior-point filter line-search algorithm for large-scale nonlinear programming. *Mathematical programming*, 106(1):25–57, 2006.

[81] E.A. Wan and R. Van Der Merwe. "The Unscented Kalman Filter for Nonlinear Estimation". *Adaptive Systems for Signal Processing, Communications, and Control Symposium, AS-SPCC*, pp. 153-158, Alberta, Canada, 2000.

[82] E.A. Wan and R. Van Der Merwe. "The Unscented Kalman Filter". *kalman filtering and neural networks*. pp. 221-280, 2001.

[83] C.K. Woo, E. Kollman, R. Orans, S. Price, and B. Horii. Now that california has ami, what can the state do with it? *Energy Policy*, 36(4):1366–1374, 2008.

[84] Xinhua Xu, Shengwei Wang, and Gongsheng Huang. Robust mpc for temperature control of air-conditioning systems concerning on constraints and multitype uncertainties. *Building Services Engineering Research and Technology*, 31(1):39–55, 2010.

[85] A. Dally Y. Ma, A. Kelman and F. Borrelli. Model predictive control of thermal energy storage in building cooling systems. *IEEE Control System Magzine*, pages 1–65, 2011.

[86] Y. Yang, A. Pinto, A. Sangiovanni-Vincentelli, and Q. Zhu. A design flow for building automation and control systems. In *Real-Time Systems Symposium (RTSS), 2010 IEEE 31st*, pages 105–116. IEEE, 2010.

[87] Yang Yang, Qi Zhu, Mehdi Maasoumy, and Alberto Sangiovanni-Vincentelli. Development of building automation and control systems. *Design Test of Computers, IEEE*, 29(4):45 –55, aug. 2012.